AEDC-TR-77-103

FUNDAMENTAL STUDIES OF SUBSONIC AND TRANSONIC FLOW SEPARATION

PART II – SECOND PHASE SUMMARY REPORT

J. M. Wu et al.

GAS DYNAMICS DIVISION
THE UNIVERSITY OF TENNESSEE SPACE INSTITUTE
TULLAHOMA, TENNESSEE 37388

December 1977

Final Report - January 1974 - September 1975

Prepared for

ARNOLD ENGINEERING DEVELOPMENT CENTER/DOTR
ARNOLD AIR FORCE STATION, TENNESSEE 37389

NOTICES

When U. S. Government drawings, specifications, or other data are used for any purpose other than a definitely related Government procurement operation, the Government thereby incurs no responsibility nor any obligation whatsoever, and the fact that the Government may have formulated, furnished, or in any way supplied the said drawings, specifications, or other data, is not to be regarded by implication or otherwise, or in any manner licensing the holder or any other person or corporation, or conveying any rights or permission to manufacture, use, or sell any patented invention that may in any way be related thereto.

Qualified users may obtain copies of this report from the Defense Documentation Center.

References to named commerical products in this report are not to be considered in any sense as an indorsement of the product by the United States Air Force or the Government.

This final report was submitted by The University of Tennessee Space Institute, Tullahoma, Tennessee 37388, under contract F40600-74-C-0009, with the Arnold Engineering Development Center, Arnold Air Force Station, Tennessee 37389. Captain Carlos Tirres was the Air Force project engineer.

This report has been reviewed by the Information Office (OI) and is releasable to the National Technical Information Service (NTIS). At NTIS, it will be available to the general public, including foreign nations.

APPROVAL STATEMENT

This report has been reviewed and approved.

Stephen L. Lamkin

STEPHEN L. LAMKIN, Captain, USAF
Project Manager, Research Division
Directorate of Test Engineering

Approved for publication:

FOR THE COMMANDER

Marion L. Laster

MARION L. LASTER
Director of Test Engineering
Deputy for Operations

REPORT DOCUMENTATION PAGE

READ INSTRUCTIONS BEFORE COMPLETING FORM

1 REPORT NUMBER: AEDC-TR-77-103	2 GOVT ACCESSION NO.
3 RECIPIENT'S CATALOG NUMBER	
4 TITLE (and Subtitle): FUNDAMENTAL STUDIES OF SUBSONIC AND TRANSONIC FLOW SEPARATION, PART II - SECOND PHASE SUMMARY REPORT	5 TYPE OF REPORT & PERIOD COVERED: Final Report - January, 1974 - September 1975
	6 PERFORMING ORG REPORT NUMBER
7 AUTHOR(s): J. M. Wu, C. H. Chen, T. H. Moulden, K. C. Reddy, F. G. Collins, R. Nygaard, H. Kuwano, Ahmad Vakili-Dastjerd, and W. Sickles	8 CONTRACT OR GRANT NUMBER(s): F40600-74-C-0009
9 PERFORMING ORGANIZATION NAME AND ADDRESS: The University of Tennessee Space Institute Tullahoma, Tennessee 37388	10 PROGRAM ELEMENT, PROJECT, TASK AREA & WORK UNIT NUMBERS: Program Element 65807F
11 CONTROLLING OFFICE NAME AND ADDRESS: Arnold Engineering Development Center/DOS Air Force Systems Command Arnold Air Force Station, Tennessee 37389	12 REPORT DATE: December 1977
	13 NUMBER OF PAGES: 191
14 MONITORING AGENCY NAME & ADDRESS(if different from Controlling Office)	15 SECURITY CLASS (of this report): UNCLASSIFIED
	15a DECLASSIFICATION/DOWNGRADING SCHEDULE: N/A

16 DISTRIBUTION STATEMENT (of this Report)

Approved for public release; distribution unlimited.

17 DISTRIBUTION STATEMENT (of the abstract entered in Block 20, if different from Report)

18 SUPPLEMENTARY NOTES

Available in DDC

19 KEY WORDS (Continue on reverse side if necessary and identify by block number)

flow separation	cavities	computations
subsonic flow	flow	wind tunnel tests
transonic flow	Reynolds number	
turbulent flow	wake	
turbulent boundary layer	transonic wind tunnels	

20 ABSTRACT (Continue on reverse side if necessary and identify by block number)

The work reported herein represents the second phase of a fundamental study of subsonic and transonic flow separation. The detailed features of the turbulent boundary layer flow separation induced by a forward-facing step in transonic and high subsonic flow were studied. The influences of an upstream disturbance upon the downstream separation were simulated by several shallow-cavity models of different depth to length ratios. The free-stream conditions were varied over the ranges $M_\infty = 0.6 \sim 0.9$ and $Re/ft = 5 \times 10^6 \sim 30 \times 10^6$. It was shown

DD FORM 1 JAN 73 1473 EDITION OF 1 NOV 65 IS OBSOLETE

20. ABSTRACT (Continued)

that certain upstream disturbances can produce higher separation pressure and skin friction than those related to a single forward-facing step. A separation pressure correlation was established empirically from the cavity flow data. It was observed that a certain Reynolds number and depth-to-length-ratio cavity yielded a maximum separation pressure. At the same time, an increase of free-stream Mach number continuously increased the separation pressure. The flow relaxation along the cavity floor was explored by systematic measurements and analysis of surface pressures and velocity profiles. These studies revealed that the flow relaxation started from the floor and spread outward. Therefore, the lower portion of the outer layer of the shear flow contained a longer memory, carrying the influence of the upstream disturbance to the downstream separation. The law of the wall and the wake was used for the analysis of the velocity distributions and the estimation of the skin friction. It was found that the slope of the law of the wall is different for velocity profiles of different strengths of wake. The law of the wake did not perfectly fit the measured velocity profile if there existed a non-uniform adverse pressure gradient. The skin friction along the flat plate estimated by the law of the wall and the wake was quite accurate by comparison with other measured data.

Based on an inverse computation of an inviscid streamline corresponding to an experimentally measured pressure distribution for subsonic flow past a cavity, inviscid transonic flow computations have been carried out. The computed pressure distribution at transonic speeds agrees with the measured pressure data at transonic speeds. Also a new finite difference method has been developed for solving viscous-transonic equation which describes the small disturbance transonic inviscid flow with the effect of compressive viscosity included in regions of sharp gradients. The computations have successfully been carried out for supercritical flows with shocks and also with pre-described wake effects.

AFSC
Arnold AFS Tenn

PREFACE

The work reported herein was conducted at the University of Tennessee Space Institute, Tullahoma, Tennessee, and was supported by the Arnold Engineering Development Center under Contract Number F40600-74-C0009 for the period January 1974 to September 1975. The Air Force project engineer during this contract period was Capt. Carlos Tirres. The Program Element number was 65807F.

The reproducibles used in the reproduction of this report were supplied by the authors: J. M. Wu, C. H. Chen, T. H. Moulden, K. C. Reddy, F. G. Collins, R. Nygaard, H. Kuwano, Ahmad Vakili-Dastjerd and W. Sickles.

TABLE OF CONTENTS

ILLUSTRATIONS

Figure | Page

1.0 INTRODUCTION

Depending upon its nature, an upstream disturbance may induce, or suppress, a subsequent downstream flow separation. There are countless practical examples of such situations (from the golf ball to the airfoil). The present study is devoted to understanding such flows at transonic speeds. The motivation of this study is clearly explained in the first phase summary report (Ref. 1). However, it is still worthwhile to reiterate some crucial points so vital in understanding today's transonic flights.

It was Pearcey (Ref. 2) who pointed out, after an extensive experimental study, that the flow over a transonic airfoil or wing presents two kinds of distinguished flow separation patterns over the surface. One kind is a separation bubble which forms at the foot of a near-normal shock wave adjacent to the surface. The bubble will grow aft as either the free-stream Mach number or the angle of attack increases. He called this type of flow separation pattern, Type A. The other kind is a flow separation from the trailing edge, with or without the local shock induced separation near the midchord. This type of separation pattern is classified as Type B. In order to see more clearly these two types of flow field developments, Pearcey's original concept has been reillustrated as shown in Figure 1. Whether it belongs to Type A or Type B, the "upstream influence" to the downstream flow is very well explained. The problem becomes serious if it is Type B, because the downstream flow is associated with a flow separation. As is explained in this report, the upstream disturbance definitely affects the downstream flow condition and thus extends its influence to the flow separation.

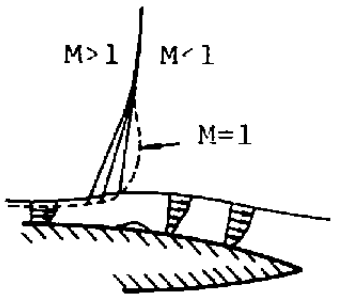

(a-1) Bubble initially induced

(a-2) Rear separation starting

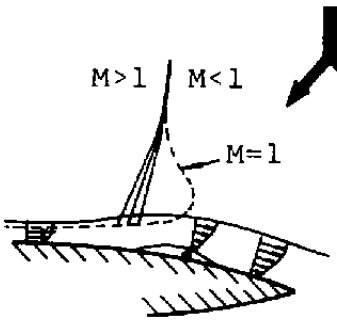

(b-1) Bubble expanding

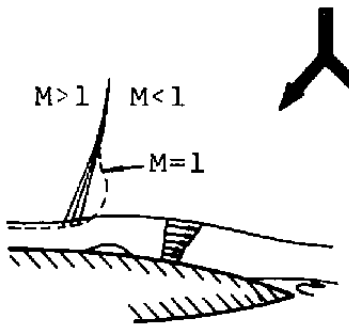

(b-2) Bubble in conjunction with rear separation

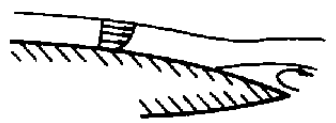

(b-3) Rear separation moving upstream

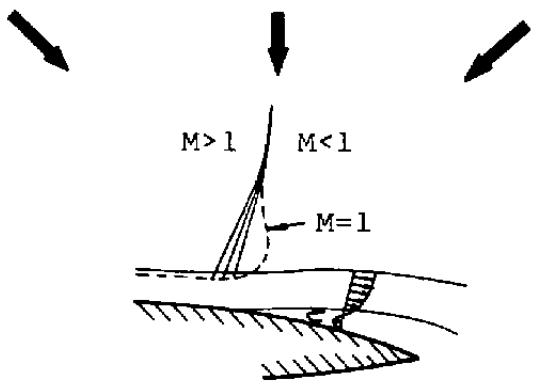

(c) Separation from shock to trailing edge

Figure 1. Schematic diagram of typical transonic flow inviscid/viscous interactions (adapted from Ref. 2).

Recently Yoshihara and Zonnars (Ref. 3) reported that the three-dimensional transonic shock-induced separation over a super-critical wing-fuselage configuration is very much a Type B pattern (See Figure 2). Whitcomb (Ref. 4) indicated also that for flow over a supercritical wing with a contoured fuselage (designed by area rule), the flow separation pattern definitely belongs to Type B. The surface oil flow trace showed that the flow started to separate from the trailing edge as the angle of attack was increased. This and the work of additional researchers indicate that the flow over a modern super-critical wing-fuselage configuration is of the Type B and that the upstream disturbance affects the downstream separation. Therefore, the present study is very timely in shedding some light in understanding this vital problem.

Whenever flow separation is influenced by some upstream disturbance, a large interaction can ensue. Both the rate of relaxation from the upstream disturbance and the upstream propagation from the separation will be modified due to the interaction between the two flow phenomena. The local flow taking place between the upstream disturbance and the downstream separation will also be changed. The extent of this change must evidently depend upon the following parameters:

1. Free stream conditions--Mach number, Reynolds Number, etc.

2. The strength of the upstream disturbance which can be characterized in many different ways. In the absence of a downstream separation, perhaps the most convenient parameters for the description of the strength of the upstream disturbance are: the magnitude of the maximum recovered pressure, the boundary layer integral thickness, and the intensity of the turbulence at certain locations downstream of the reattachment point.

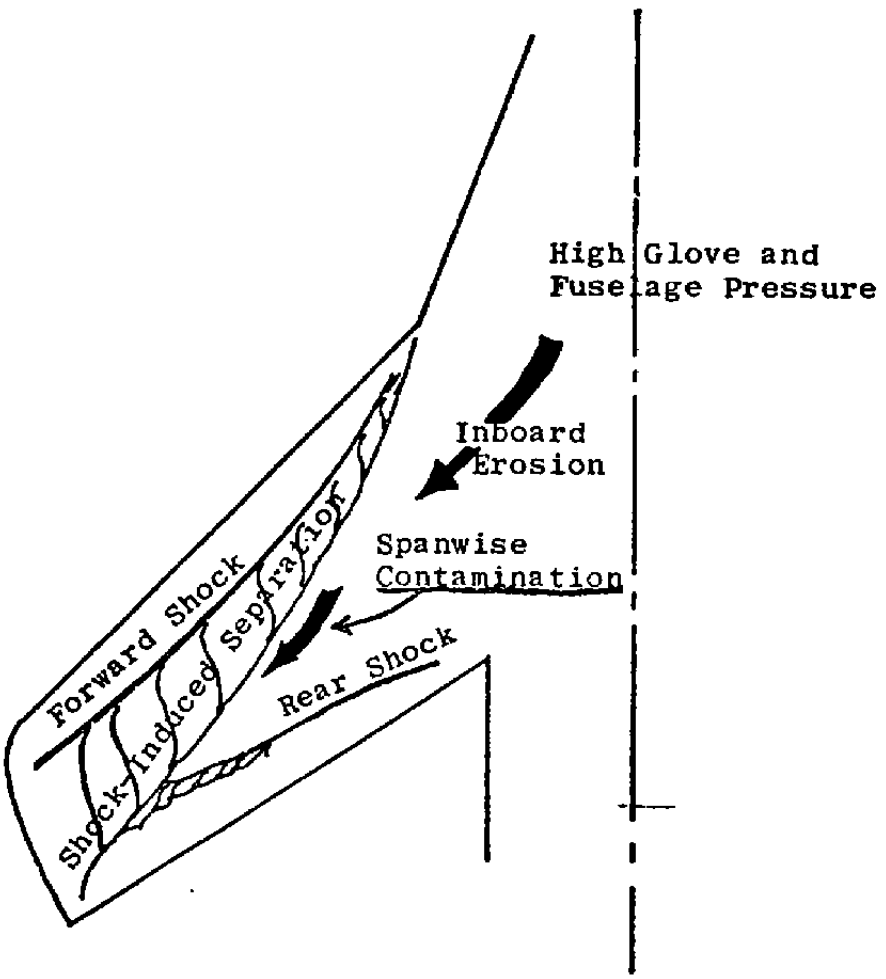

Figure 2. Shock and separation pattern at 45° sweep, M_∞ = 0.95 and α = 9° (Ref. 3).

3. The strength of the downstream separation which can be characterized by such parameters as the magnitude of the peak pressure in the separation region, the boundary layer integral thicknesses, and the intensity of the turbulence at the separation point.

4. The distance between the upstream disturbance and the downstream separation. The flow after the disturbance needs a certain relaxation distance to recover.

5. The manner of distortion in the pressure and the velocity profile as well as their recovery process.

The present interim report does not provide conclusive understanding of the influence of all the parameters listed above; however, some significant progress was obtained. For instance, the relaxation distance (as mentioned in point 4 above) for the pressure was found to be much shorter than that for the velocity profile and the pressure and skin friction recovered over different distances. Once the pressure and skin friction recovered, they reached higher values than the no disturbance condition. It has been observed by Whitcomb in wind tunnel tests (Ref. 4) that a constant pressure region for a small distance aft of the shock wave on a supercritical airfoil actually helps in preventing trailing edge separation (Figure 3). His observations can be clearly explained from the findings reported herein.

The basic configuration used for the experiments conducted in this study is shown in Figure 4. This figure shows the nomenclature used in this report and gives a schematic drawing of the pressure distribution and the flow over a shallow-cavity model.

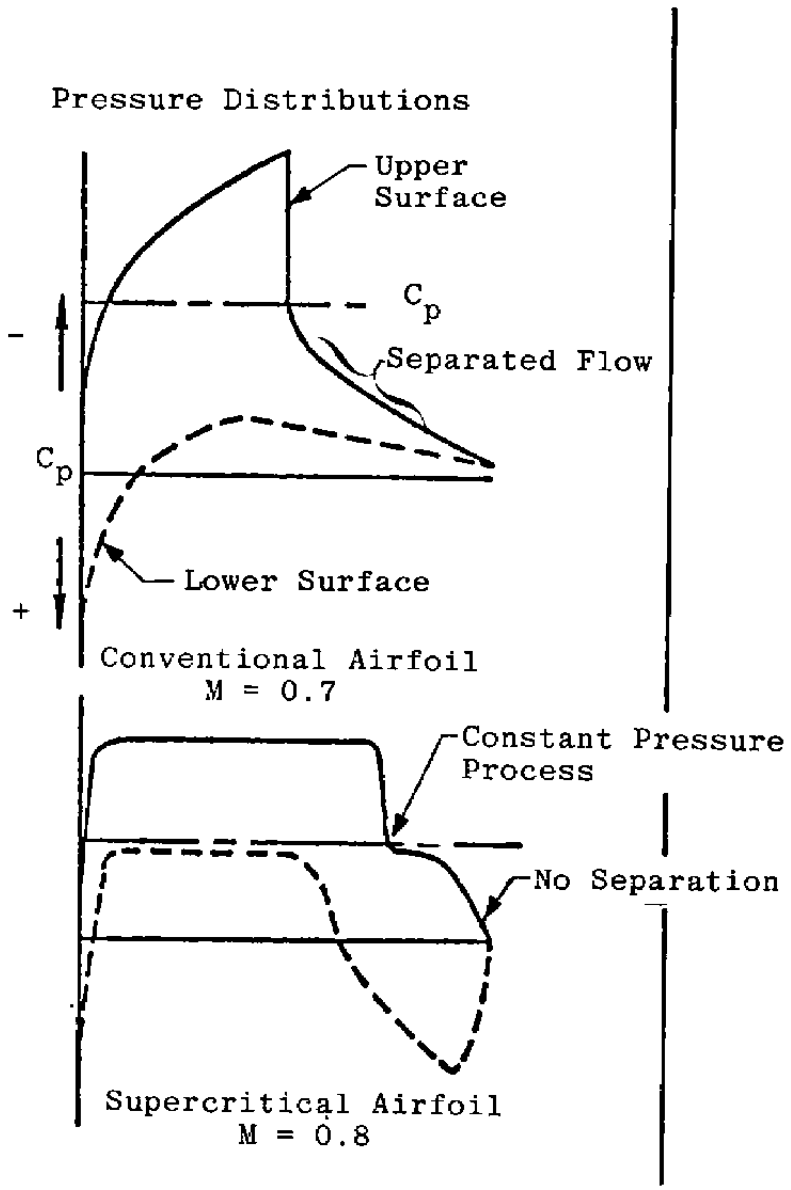

Figure 3. Comparison of pressure distribution on conventional and supercritical airfoils.

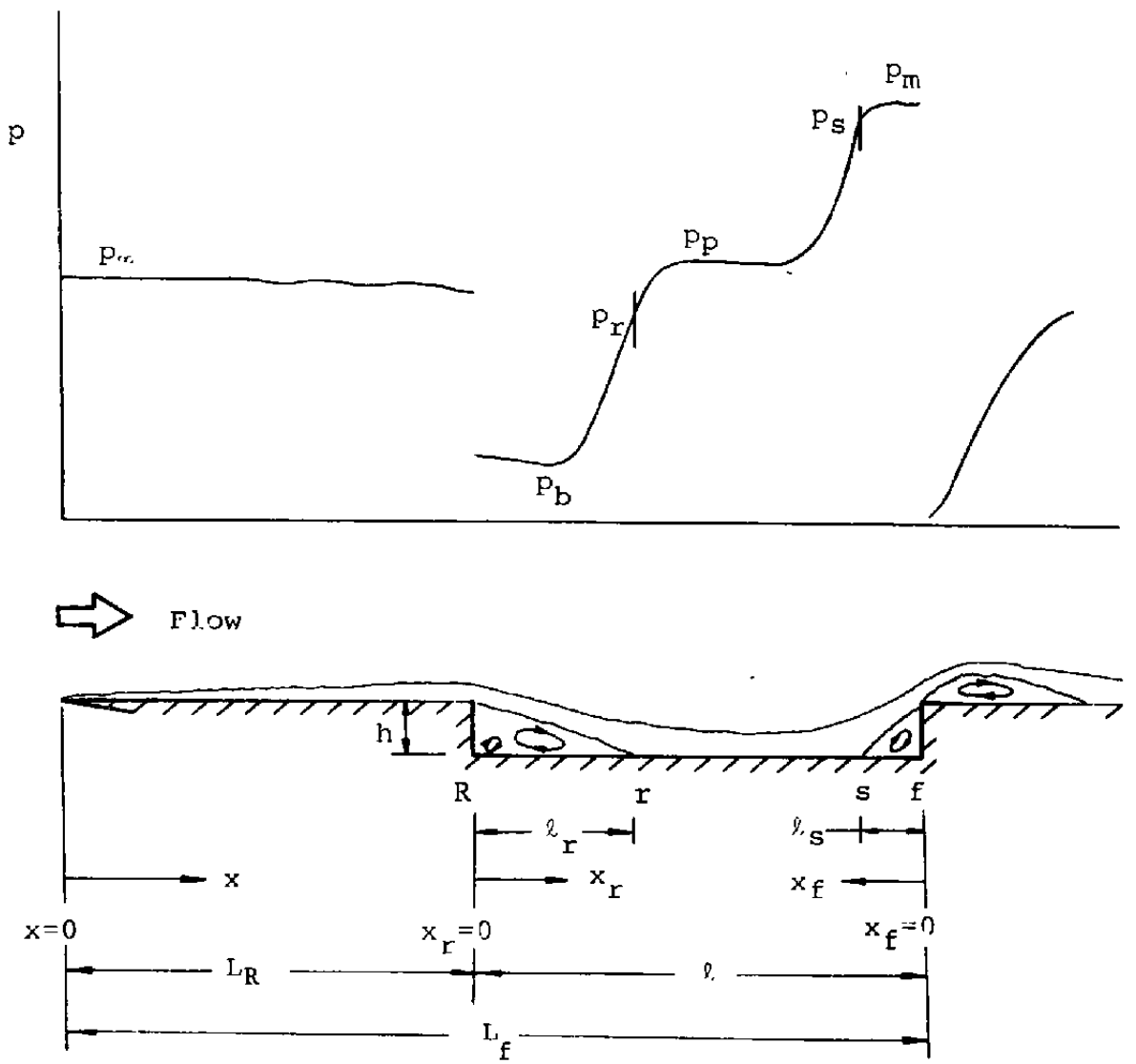

Figure 4. Nomenclature and schematic diagram of the pressure distribution and the flow over a shallow-cavity model.

2.0 FACILITIES AND EXPERIMENTAL TECHNIQUES

2.1 UTSI TRANSONIC WIND TUNNEL FACILITY

Testing in conventional wind tunnels usually results in the acceptance of some of the following drawbacks: (1) scaling effect, i.e., limited Reynolds number simulation, due to the limited model size and moderate air density; (2) channel flow effect; and (3) ill-defined integrated boundary-layer thicknesses if the model lacks a clear-cut leading edge or as a result of using a trip device. These drawbacks will become more significant for flows at transonic speeds.

In order to avoid these drawbacks, the present experiments were conducted in a specially designed transonic flow wind tunnel (see Refs. 1 and 5). The normal cross-sectional area of the test section is 12 x 11 inches (Figure 5). The divergence angle between the ceiling and the floor is approximately 0.8 degrees for the purpose of compensating for the increasing wall boundary layer along the tunnel length. In order to ensure that the flow is free from channel effects under different free-stream conditions, one adjustable boundary-layer suction device is mounted on each of the side walls at 94 inches downstream from the throat of the nozzle. These two devices are also movable along the flow direction when necessary. They are designed to suck away the excessive sidewall boundary-layer flow. The total exit area of the side suction devices can be varied from 0 to 18 in^2. The floor of the wind tunnel test section was designed as the test model (see Ref. 6). It has a total length of 144 inches, with a nominal width of 12 inches. The leading edge of the model is located 7 inches from the nozzle throat. A natural boundary layer starting from this leading edge is ensured by another adjustable boundary-layer suction device which is located beneath the model leading edge. The exit area of this leading-edge suction device can be varied from 0 to 9 in^2. The tunnel floor

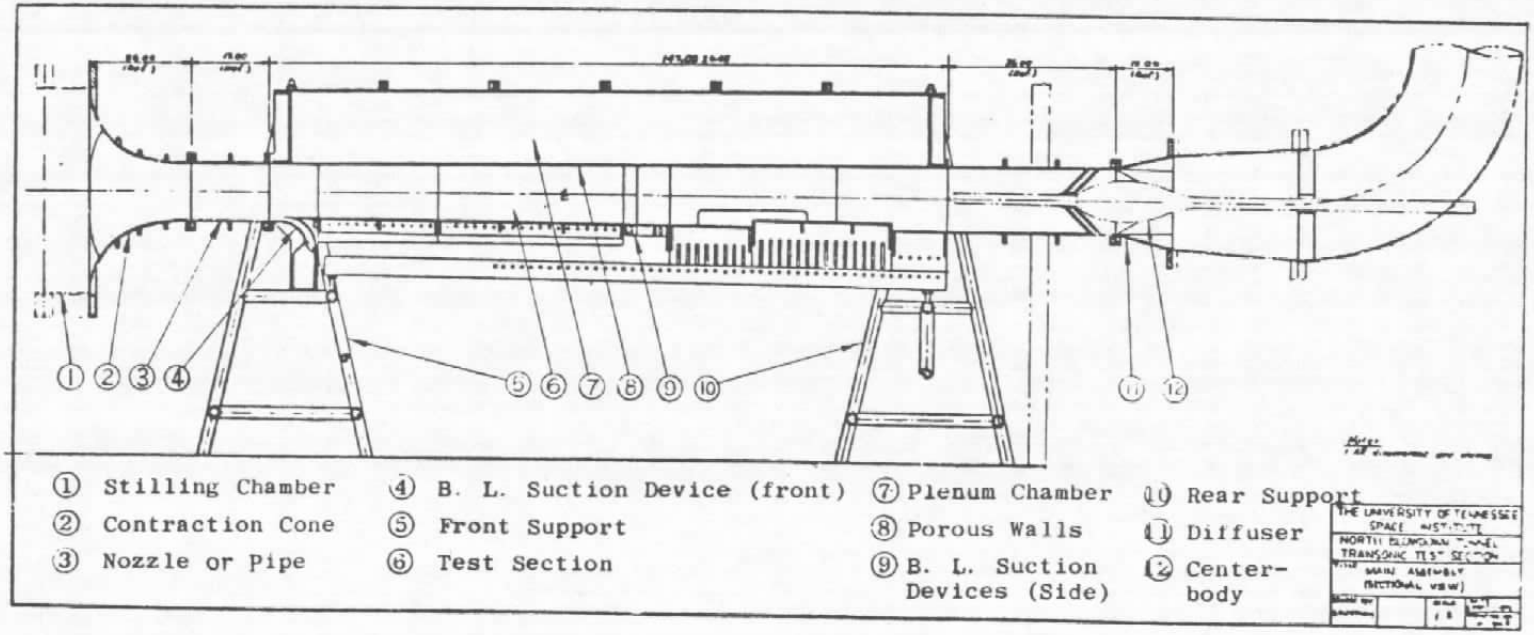

Figure 5. Sectional view of The University of Tennessee Space Institute wind tunnel.

consists of a series of blocks which can be modified or tailored into any desired model within the test section length. The blocks, except the 7 inch piece which forms the leading edge, can be arranged in any sequence and moved up or down into the test section by as much as 3.75 inches, as desired. The floor can be used as either a flat-plate model, or as a forward-facing or a rearward-facing step model of different heights located at different stations. It can also be arranged as a "cavity-like" model with different cavity lengths and depths at various locations. There is enough space underneath the floor for the installation of various sensing instruments. All these wall pieces are movable to facilitate changes in the model and instrumentation arrangement. On top of the test section there is a 16 inch high plenum chamber separated from the test section by a porous ceiling. Ceilings of different porosity can be installed at different locations along the tunnel to minimize the wall interference. At the end of the test section a movable plug is installed in the diffuser for adjusting the subsonic flow Mach number in the test section.

2.2 MODEL CONFIGURATIONS

In the experiments reported herein, a forward-facing step model, five shallow-cavity models and a flat-plate model have been systematically and extensively studied (Figure 6). All these models have a clear-cut leading edge and exhibit two-dimensional flow features. The two-dimensionality of flow was tested by surface oil flow pattern observations, and by lateral static and total pressure measurements. All of these measurements indicated that the flow is in general very close to two-dimensional.

The forward-facing step model was formed by a 1-inch high normal step spanning the 12-inch wide floor of the test section at 74 inches downstream from the leading edge (Figure 6a). The

undisturbed turbulent boundary-layer thickness was about 1-inch at this station. It was tested to show the Reynolds number and the Mach number effects on flow separation.

Shallow-cavity models of equal separation- and recompression-step heights were used to study the phenomenon of wake-separation interaction (Figures 6b-f). These models provide a physical indication of the features of rear separation when the oncoming flow was disturbed by a rearward-facing step. By comparing the results obtained from the "cavity-like" model with that from forward-facing step model, the effect of an upstream disturbance on the downstream separation became clear. All cavities were maintained at a depth of 1 inch and had five different lengths, i.e., 40, 27.5, 23.5, 15.75, and 11 inches, respectively. These different cavity lengths were used to study the effect of upstream disturbance relaxation and its consequence on the downstream separation. The question of whether the separation streamline reattaches or not for the shallow cavity could also be examined from the results for different cavity lengths. A flat-plate model was tested under the same free-stream conditions for a reference of comparison.

Surface pressure taps, 0.042 inch diameter, were distributed longitudinally, 2 inches to the right of the center line of the model surface. Three different spaces between taps, 0.25, 0.5 and 1 inch respectively, were employed (Figure 7). These gave closer measurements in regions where the surface pressure variation was critical.

In order to measure the total pressure variations across the boundary layer (at any desired station on the model) using a traversing pitot-probe, the floor block was slotted along the center line and filled with small blocks of different lengths, as shown in Figure 8. The traversing pitot-probe is screw-mounted such that it can slide freely along this lot.

a. Forward-facing step model

b. 40-inch long shallow-cavity model

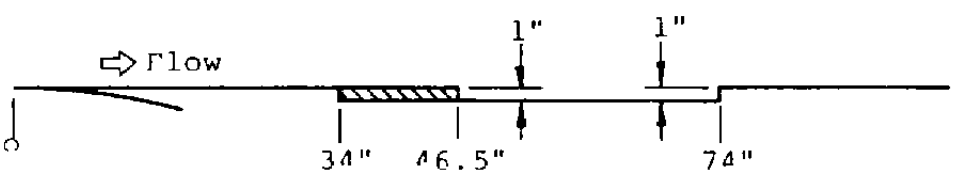

c. 27.5-inch long shallow-cavity model

Figure 6. Schematic diagram of models.

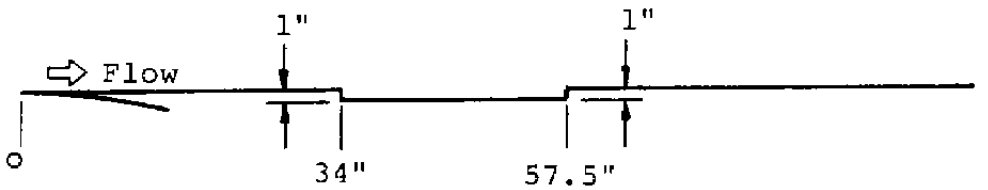

d. 23.5-inch long shallow-cavity model

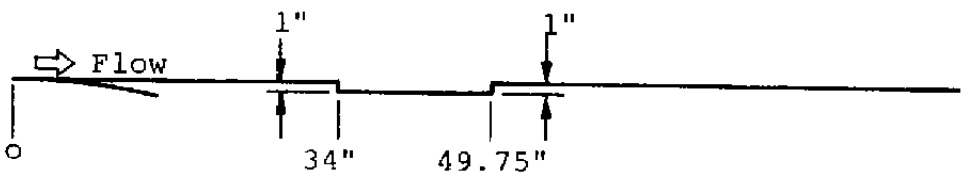

e. 15.75-inch long shallow-cavity model

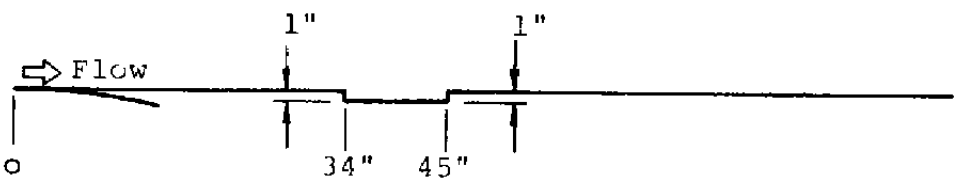

f. 11-inch long shallow-cavity model

Figure 6. Concluded.

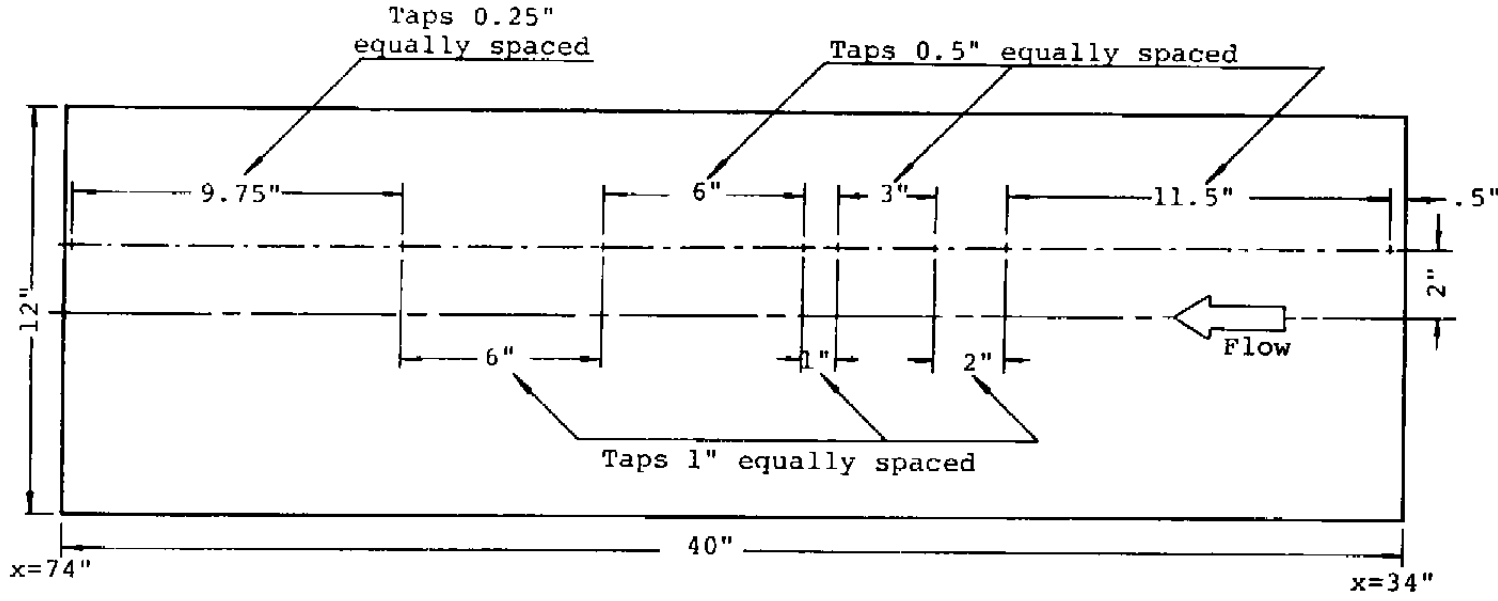

Figure 7. Static pressure tap distributions (Taps have 0.042-inch inside diameter).

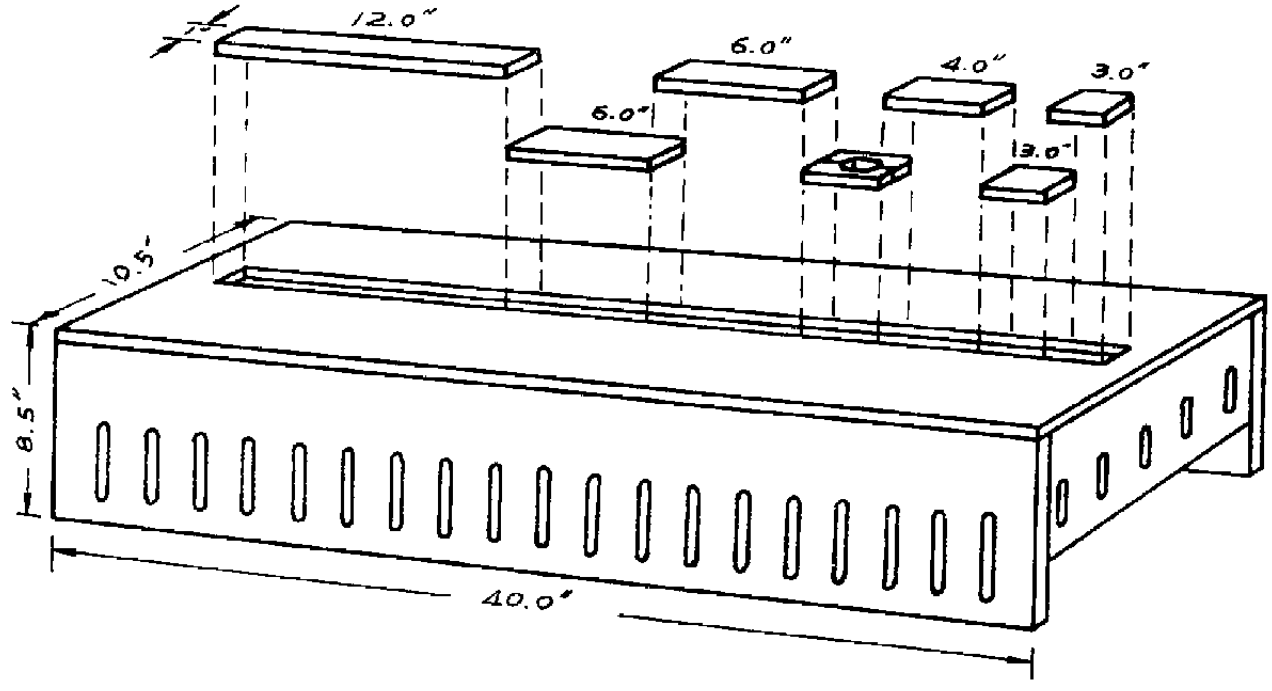

Figure 8. Typical slotted model block.

2.3 INSTRUMENTATION

2.3.1 Traversing Pitot-Probe

A variable speed vertical-traversing pitot-probe was designed to measure continuously the variation of the total pressure across the boundary layer (Figures 9a and b). The traversing mechanism was composed of a Travel Unislide-assembly and a Speed Control, with an approximate motor speed range of 1 to 500 rpm which converted to a linear probe velocity of 0.0007 to 0.45 in./sec. The variable traversing speed permitted a very slow traverse in the inner viscous layer and an adequate speed in outer region, so that better measurements could be performed under an air-saving running condition. A maximum traversing distance of 3.5 inches was possible. The probe was constructed from stainless steel tubing with a squared end and a circular opening. There is an interchangeability between three different tips of 0.04, 0.023, and 0.011 inches outside diameter, and 0.027, 0.0165, and 0.006 inside diameter, respectively, all of which have been used for the measurements (see Ref. 1). However, the major data presented herein is based on 0.023 outside diameter probe. Since the pitot-probe tip opening is circular and its diameter is much less than 4 percent of the boundary-layer thickness, the data acquired is fairly reliable, at least in the buffer and the wake regions, and the displacement effect is also negligible (Refs. 1, 7, and 8).

For the total pressure measurement in the viscous layer, the flow turbulence was believed to be the important source of measuring error, especially in the region very close to the wall surface. In order to minimize the flow turbulence error, the traversing speed of the pitot-probe was limited to 0.35 in./sec. or less through the entire measurements. Besides minimizing the flow turbulence error, the low traversing speed was important in two other aspects. The first is that this speed was approximately one-millionth of the flow speed at a location of 0.05 inches above the model surface when the local external Mach

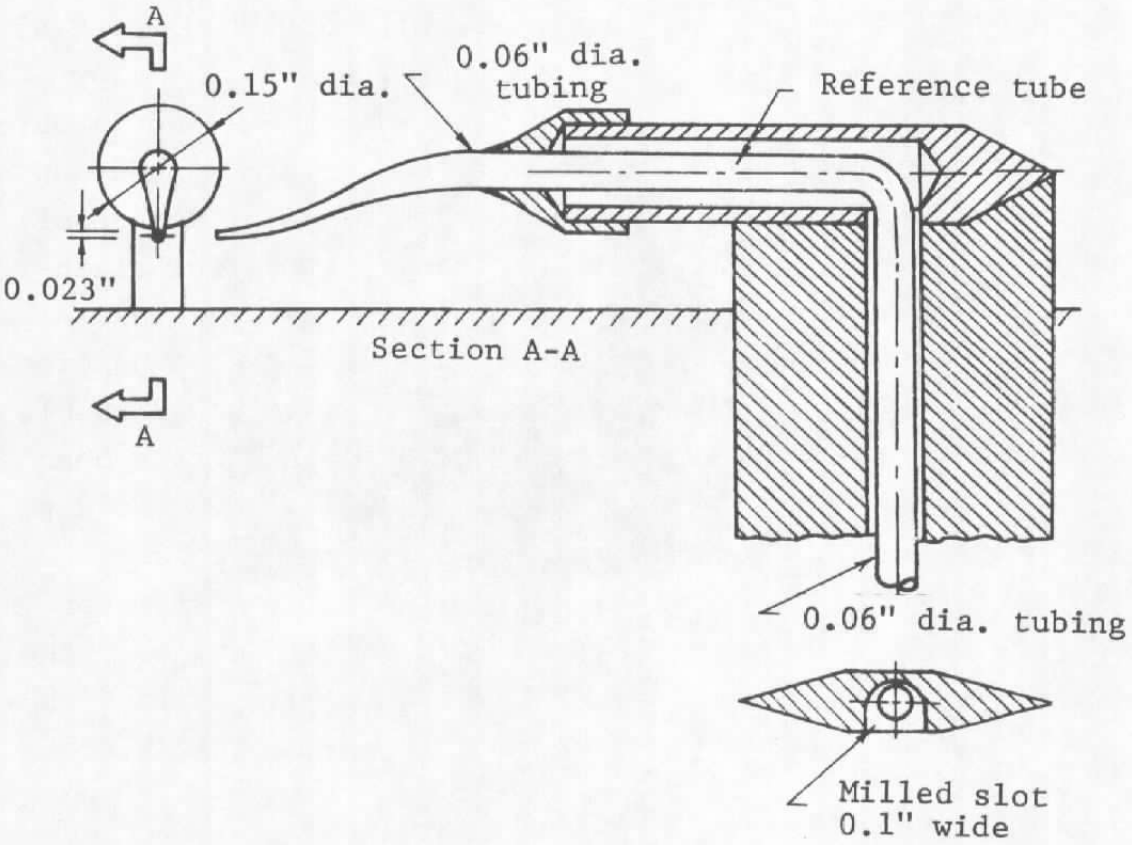

a. Cross-sectional view (schematic)

Figure 9. Traversing pitot probe details.

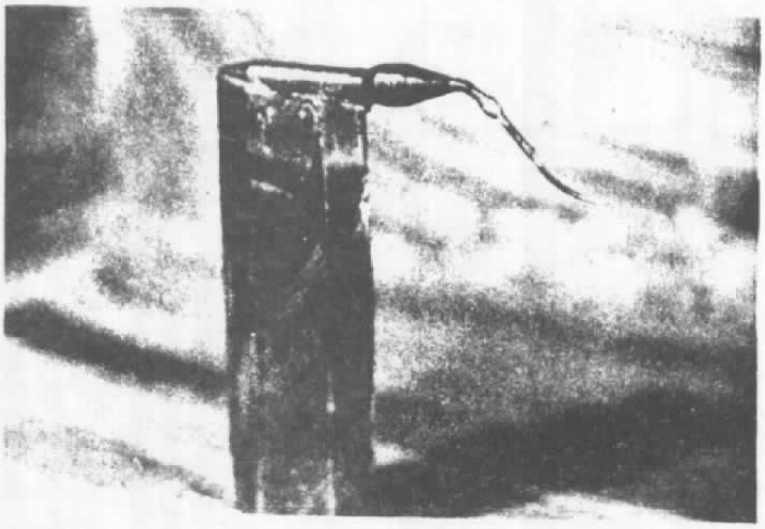

b. Photograph

Figure 9. Concluded.

number was about 0.6 and it was even less than this with increasing Mach number. Hence, the effect of the probe traversing speed on the measured data was negligible. Secondly, the time needed to traverse a 0.5-inch thick boundary layer at this speed was 1.4 seconds. This would render the measurements free from time-lag effects (Ref. 6). Another difficulty in the total pressure measurement arose when the measurement was taken close to the separation or the reattachment points where the streamlines are included to the probe direction. The circular shape of the tip employed was helpful, since the permissible yaw angle of a circular tip can be as high as ±16 degrees or more with a measuring accuracy of 1 percent (Ref. 8). At all locations where the pitot pressure was measured, the inclined angle of the streamlines was less than 16 degrees. Therefore, the error due to the misalignment of the pitot-tube to the flow was also negligible.

2.3.2 Wall Static Pressure Taps

The wall static pressures along the model surface were measured by a set of static pressure taps. The pressure taps were formed by embedding a 0.042-inch inside diameter stainless steel tubing in each of the 0.062-inch diameter holes which were drilled through the model plate. One end of the tubing was flush with the model surface and the other end was extended outside the wind tunnel beneath the floor and connected to either a manometer board or a pressure transducer through a 0.06-inch inside diameter flexible tube.

The tap which was located on the model surface at the same distance from leading edge as the tip of the pitot tube was connected to a Statham pressure transducer (PM-131TC; 0 ~ 12.5 psid). The static pressure obtained by this tap was combined with the pitot pressure to yield the velocity distribution across the boundary layer. All other taps were connected to a vertical manometer board which consisted of five ten-tube racks, two racks

of which were filled with mercury and the others with liquid of specific weight 0.0361 lb_f/in^3. The manometer permitted a reading of 0.01-inch accuracy.

2.3.3 Skin Friction Gauge.

Some measurements of wind tunnel wall skin friction were obtained using a floating element balance which was on loan from the Naval Ordnance Laboratory, White Oak, Maryland. The balance is a null-type instrument because deflections of the floating element due to the wall shear force are reduced to zero by a servomechanism. The shear force causes the balance arm (see Figure 10) to rotate by an amount proportional to the magnitude of the shear stresses on the surface of the element. Movement of the balance arm is sensed by a translational Linear Variable Differential Transformer (LVDT). The LVDT coil is attached to the balance housing while the transformer core is attached to the balance arm. Movement of the balance arm thus produces a differential voltage across the output terminals of the transformer. This voltage is converted into a plus or minus DC voltage which is amplified and fed to the servomotor. Torque is transmitted from the sevomotor and across a gear train to the lead screw. The spring guide moves along the lead screw as it rotates, producing a linear motion of the end of the coil spring. The force of the spring acts to restore the balance arm to a null position. A potentiometer is geared to the servomotor to provide an analogue of the balance arm deflection.

The balance was mounted in the center of the floor of the tunnel. The floating element, of diameter 0.790 inches, was mounted in a hole of diameter 0.800 inches. The hole was contained in a "dummy" block which could be moved to any axial location within the tunnel.

The balance was calibrated by attaching weights to a fiber which was fastened to the floating element and suspended over a

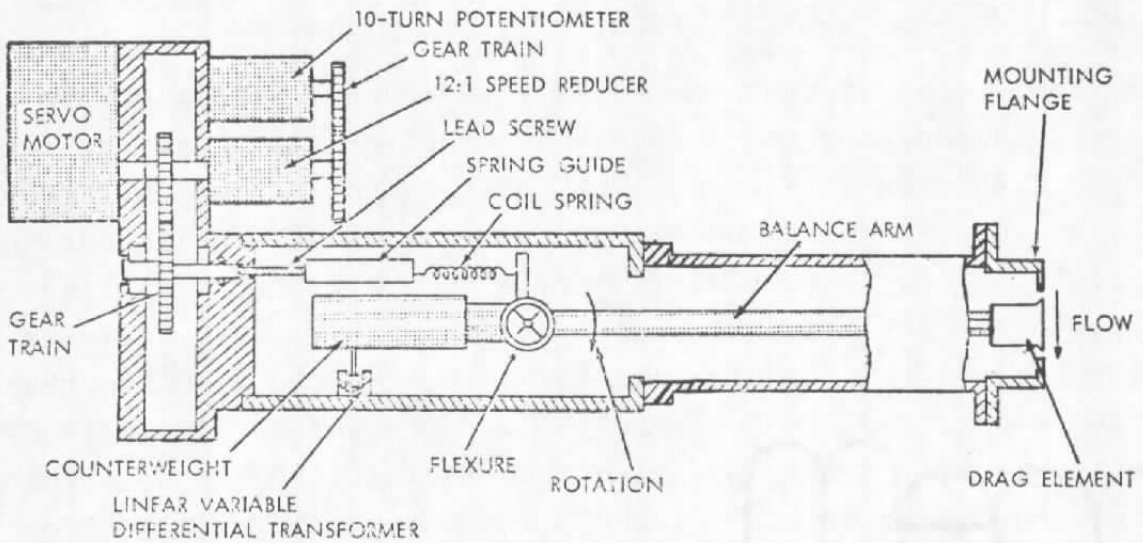

Figure 10. Balance schematic.

pivot with jeweled bearings. The balance can measure forces up to approximately 10 grams and will null in 2 to 3 seconds.

3.0 FLOW MEASUREMENTS

3.1 PITOT PRESSURE MEASUREMENTS

Total pressure profiles were systematically measured along different models at different Mach numbers and Reynolds numbers. The measuring schedule is summarized in Table I.

Table I shows that the total pressure profiles along the forward-facing step model, the 40- and 23.5-inch shallow-cavity models were closely spaced. The data obtained from these models will be used as the foundation for the study of the wake-separation interaction, whereas data from the other cavities will be used to study the effects of cavity length. Data from the flat-plate model were used as reference conditions. The profile at the separation point was not measured since the space between the separation point and the forward-facing step was not long enough to accommodate the probe. Fortunately, the velocity profiles through the shear layer 3 inches ahead of the separation point were considered to be sufficiently downstream to show the representative feature of the flow close to the step. These profiles will be discussed later.

3.2 STATIC PRESSURE MEASUREMENTS

The static pressure distributions along the 11-, 15.75-, 23.5-, 27.5-, 40-inch shallow-cavity models and the forward-facing step model which were used for the wake-separation interaction study were obtained by using the manometer board. The results are shown in Figures 11 to 16. The pressure taps were spaced rather closely (0.25-inch spacing) in the critical regions where the pressure gradients were large or the pressure gradient began to change rapidly. At locations where the total

TABLE I

TOTAL PRESSURE PROFILE MEASUREMENT SCHEDULE

Model	Free Stream Mach Number (M_∞)	Unit Reynolds Number (Re/in.)	Station (inches from leading edge)
Flat Plate	0.4, 0.5 0.6, 0.7 0.8, 0.9	0.29×10^6 to 0.79×10^6	34, 35.5, 49.5 51, 61, 64.5 70
Forward-facing Step	0.6 0.7 0.75 0.9	0.64×10^6 to 0.75×10^6	20, 47, 51, 61 66, 70
40" Cavity	0.6	0.44×10^6	41, 46, 51, 61, 66, 70
27.5" Cavity	0.5	0.39×10^6	54, 61, 70
23.5" Cavity	0.8 0.6	0.97×10^6 0.44×10^6	40.5, 41.5, 42.5, 48.5, 48.5
15.75" Cavity	0.6 0.8	0.44×10^6 0.97×10^6	44.5 44.5
11" Cavity	0.6	0.44×10^6	42.5

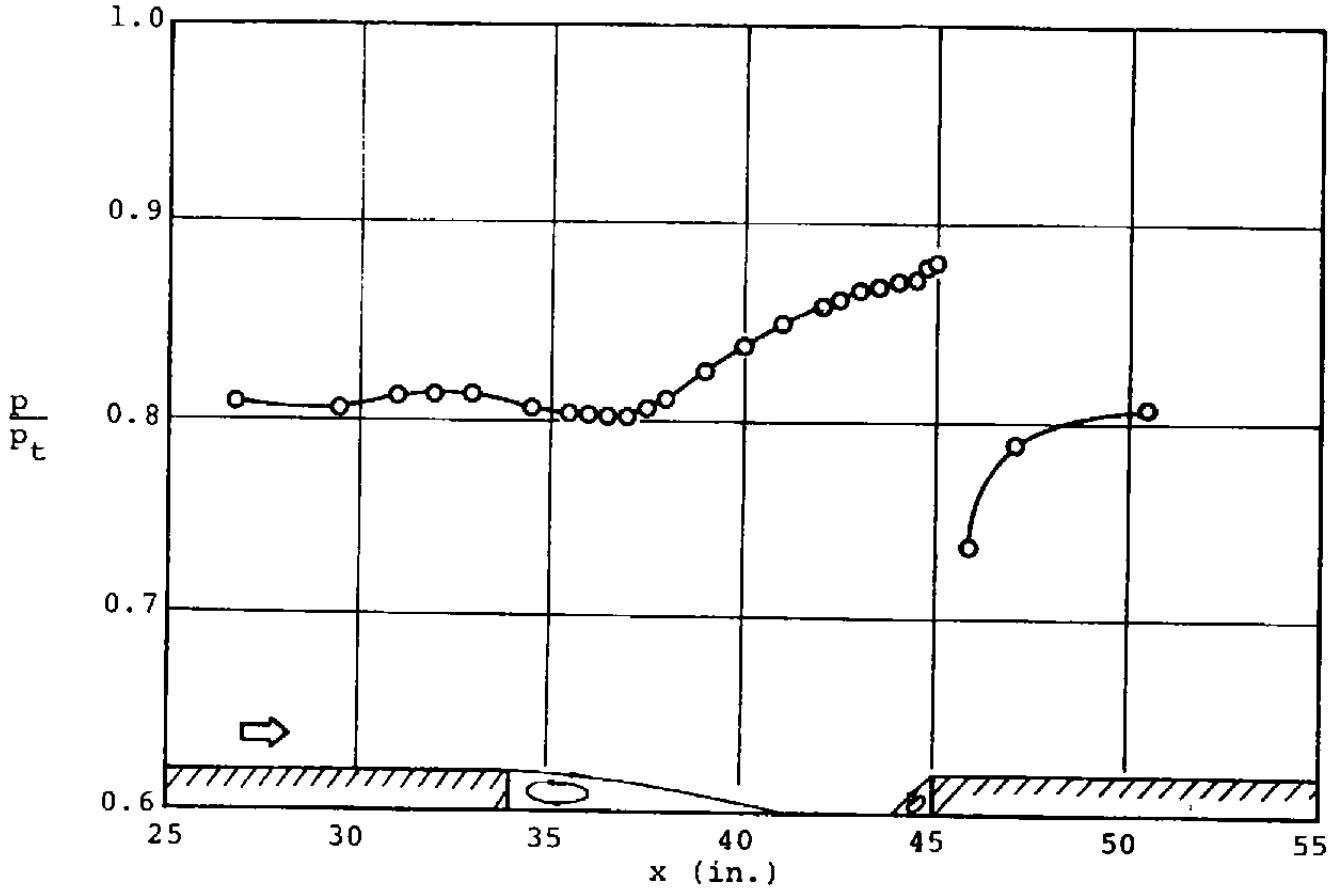

a. $M_\infty = 0.56$, $Re_{L_R} = 14.8 \times 10^6$, h = 1 inch

Figure 11. Surface pressure distribution along 11-inch cavity.

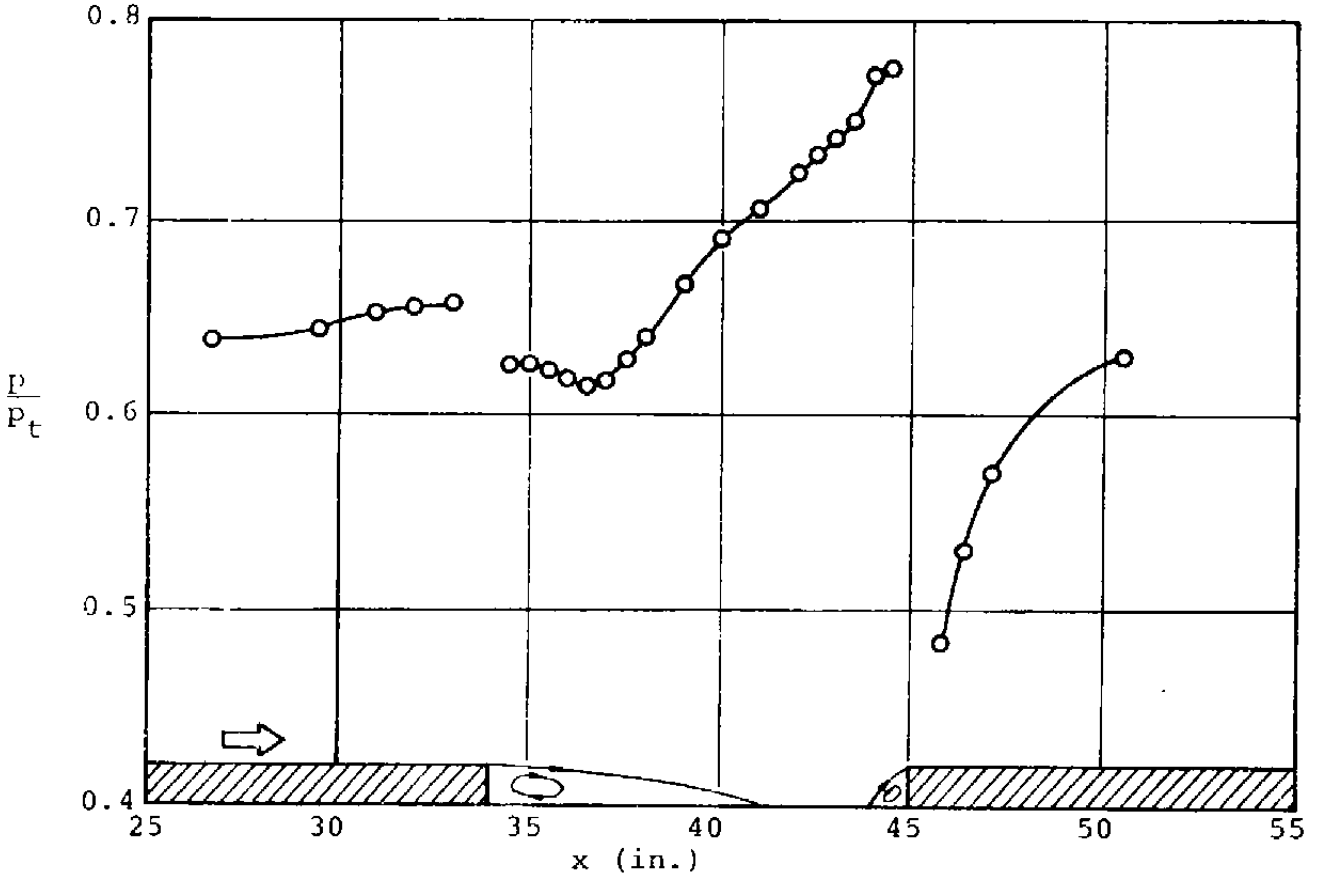

b. $M_\infty = 0.83$, $Re_{L_R} = 34.4 \times 10^6$, h = 1 inch

Figure 11. Concluded.

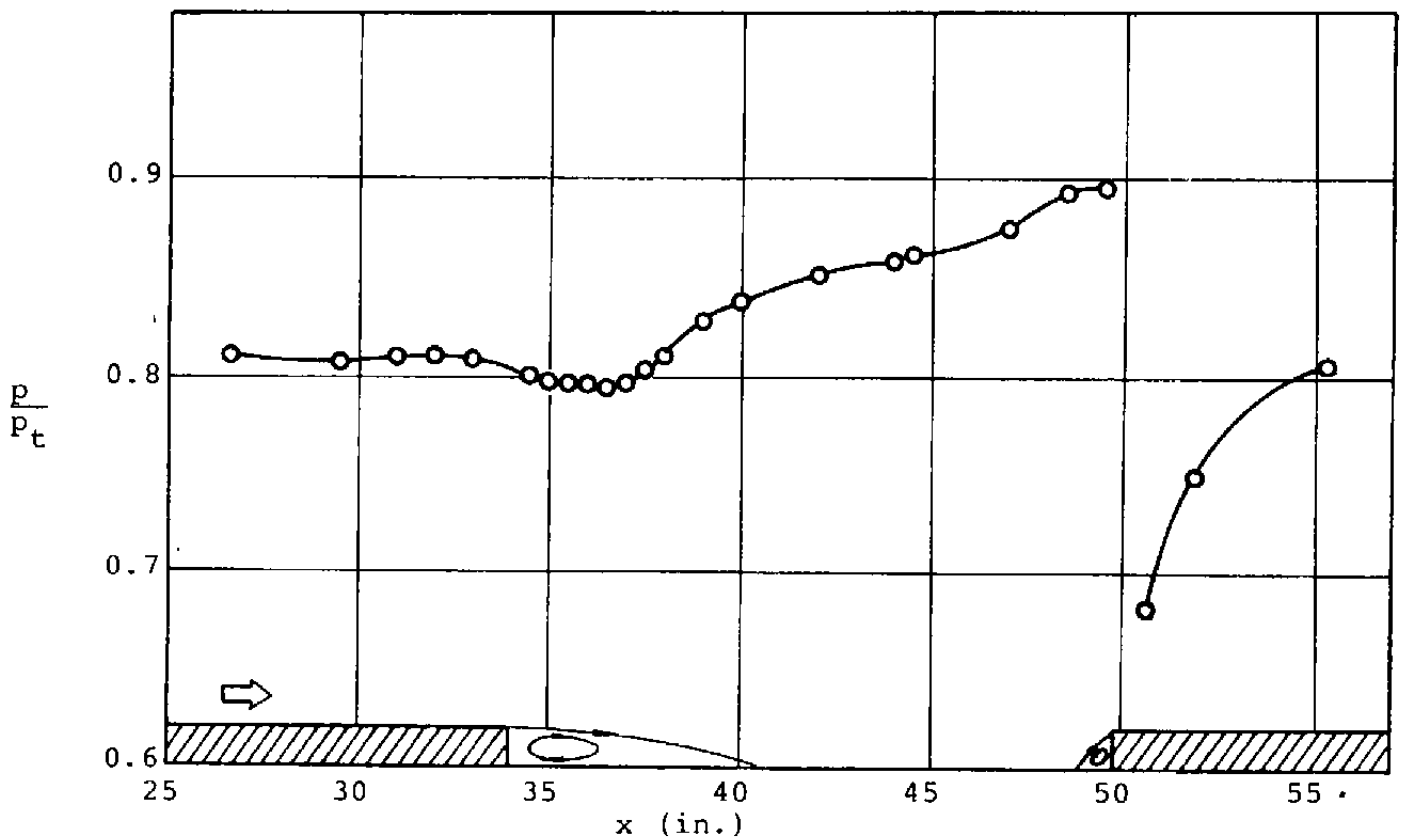

a. $M_\infty = 0.56$, $Re_{L_R} = 14.9 \times 10^6$, h = 1 inch

Figure 12. Surface pressure distribution along 15.75-inch cavity.

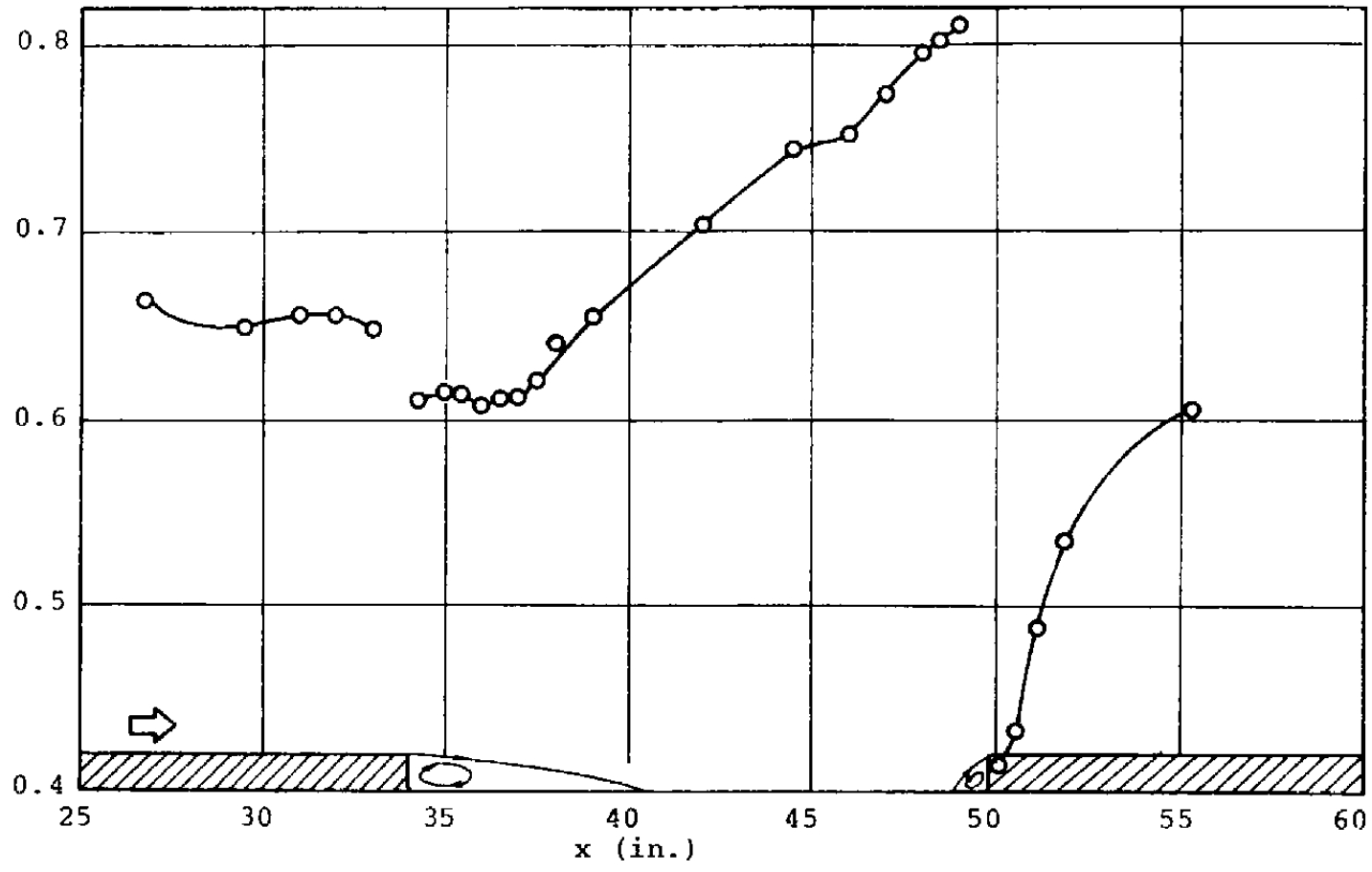

b. $M_\infty = 0.79$, $Re_{L_R} = 29.9 \times 10^6$, h = 1 inch

Figure 12. Concluded.

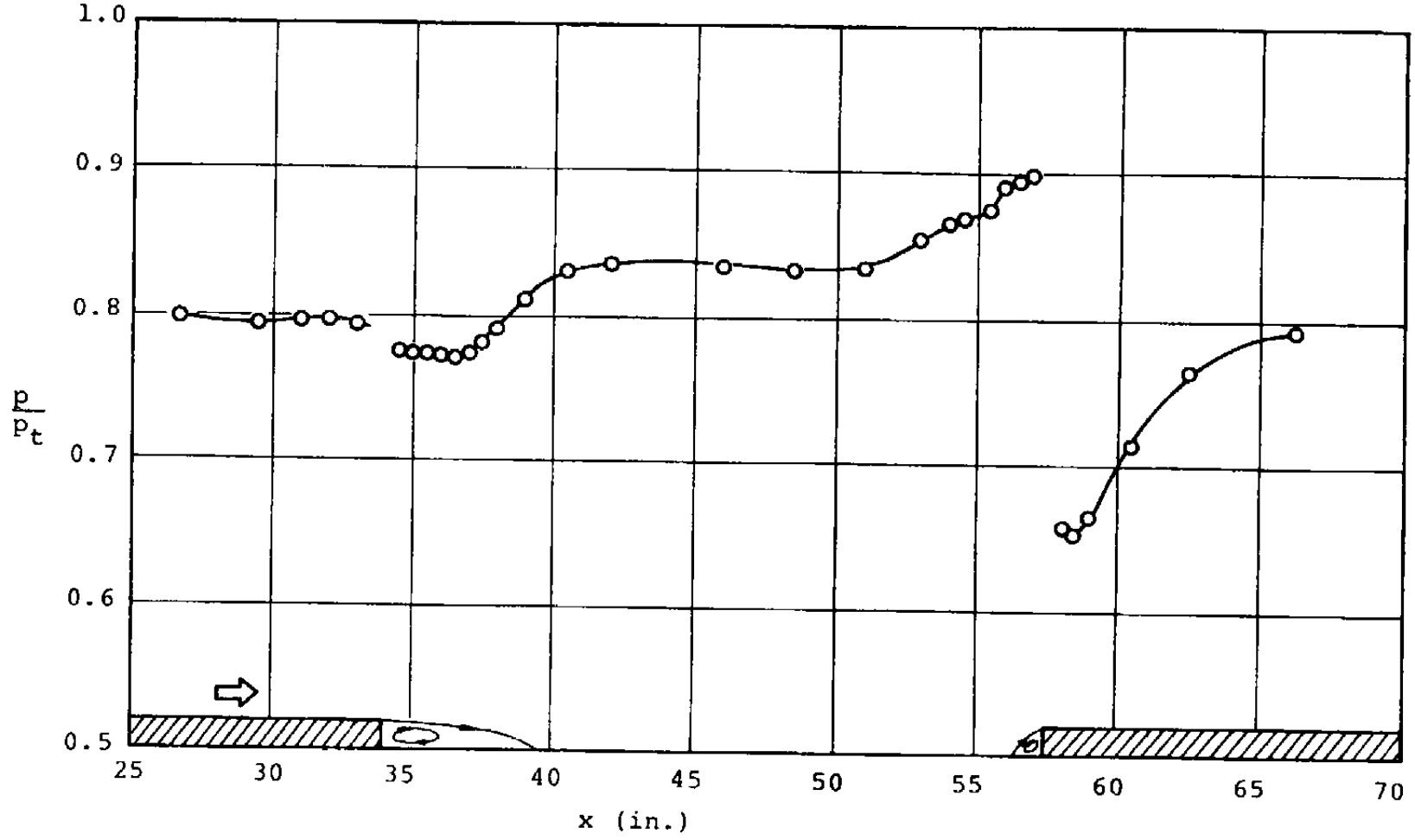

a. $M_\infty = 0.58$, $Re_{L_R} = 15.8 \times 10^6$, h = 1 inch

Figure 13. Surface pressure distribution along 23.5-inch cavity.

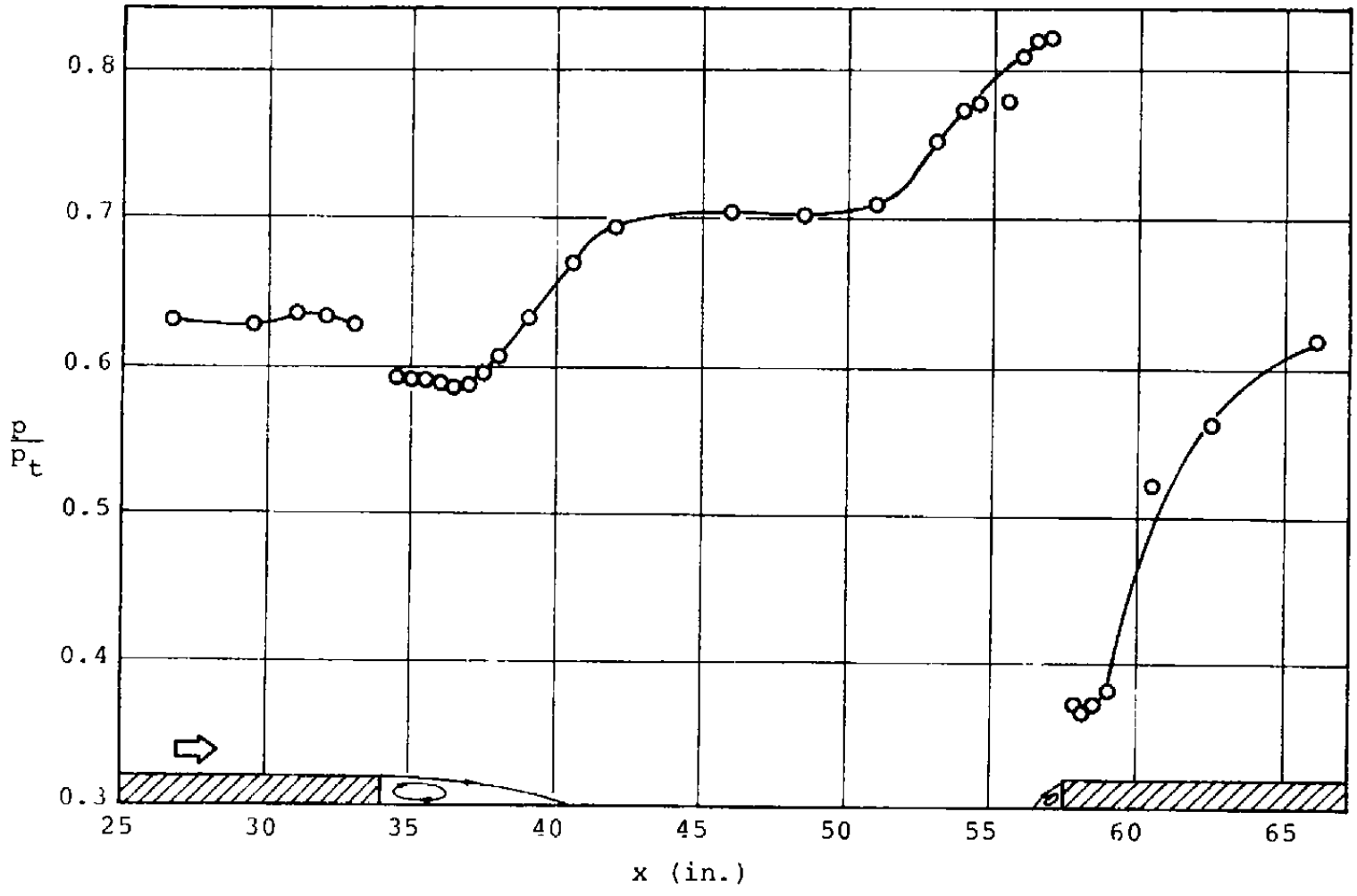

b. $M_\infty = 0.84$, $Re_{L_R} = 32.9 \times 10^6$, h = 1 inch

Figure 13. Continued.

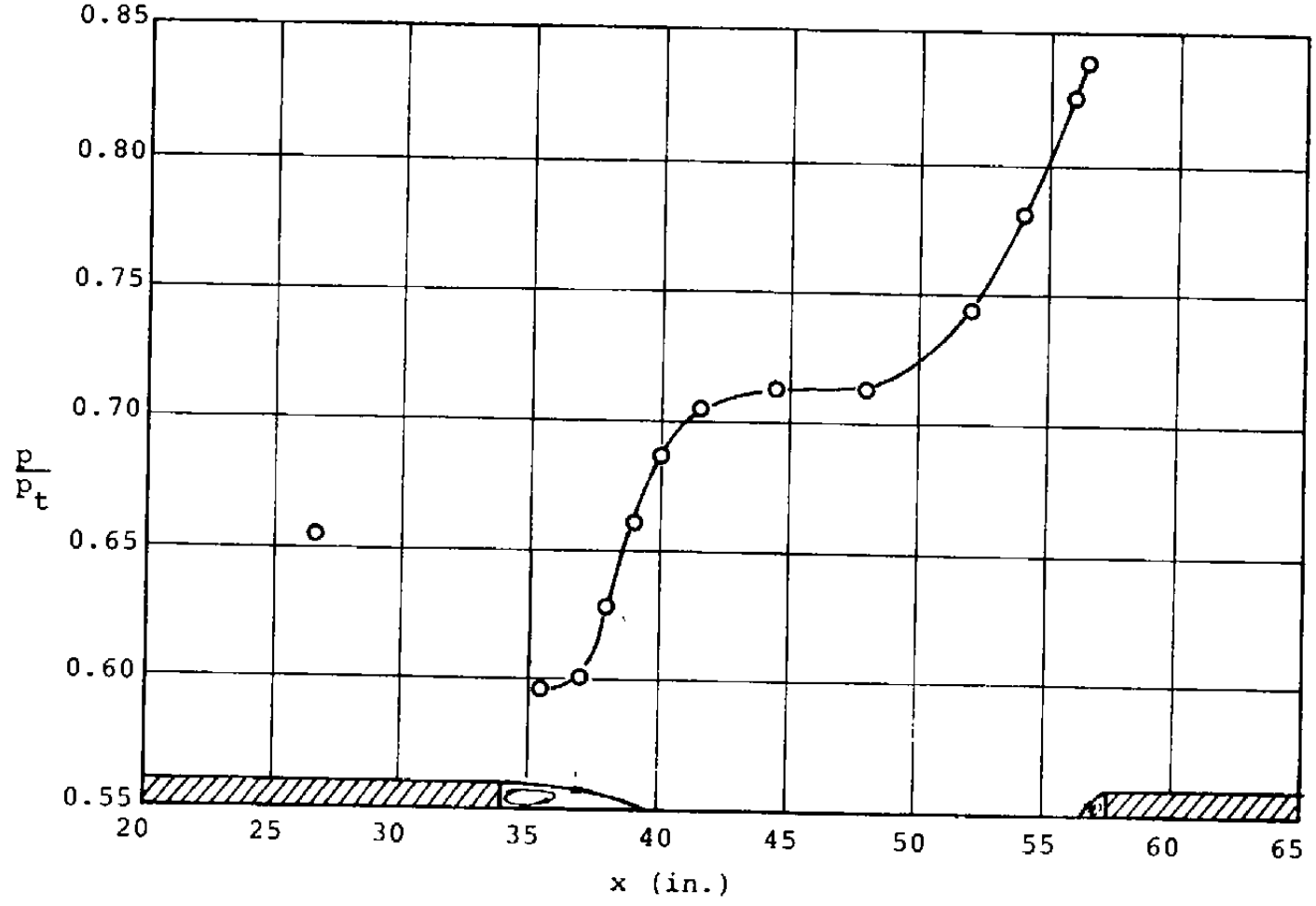

c. $M_\infty = 0.80$, $Re_{L_R} = 28.6 \times 10^6$, h = 1 inch

Figure 13. Continued.

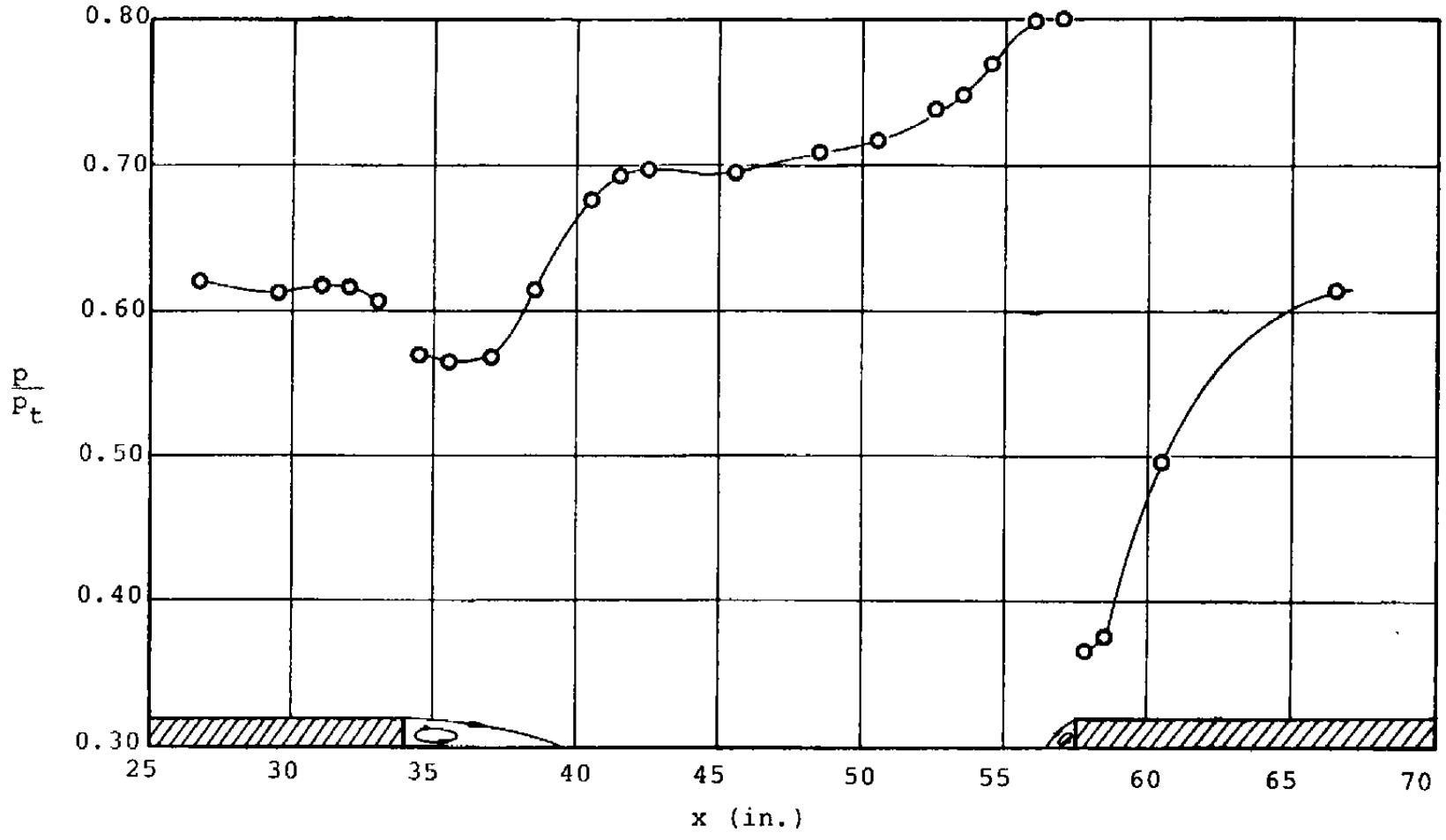

d. $M_\infty = 0.85$, $Re_{L_R} = 37.0 \times 10^6$, h = 1 inch

Figure 13. Continued.

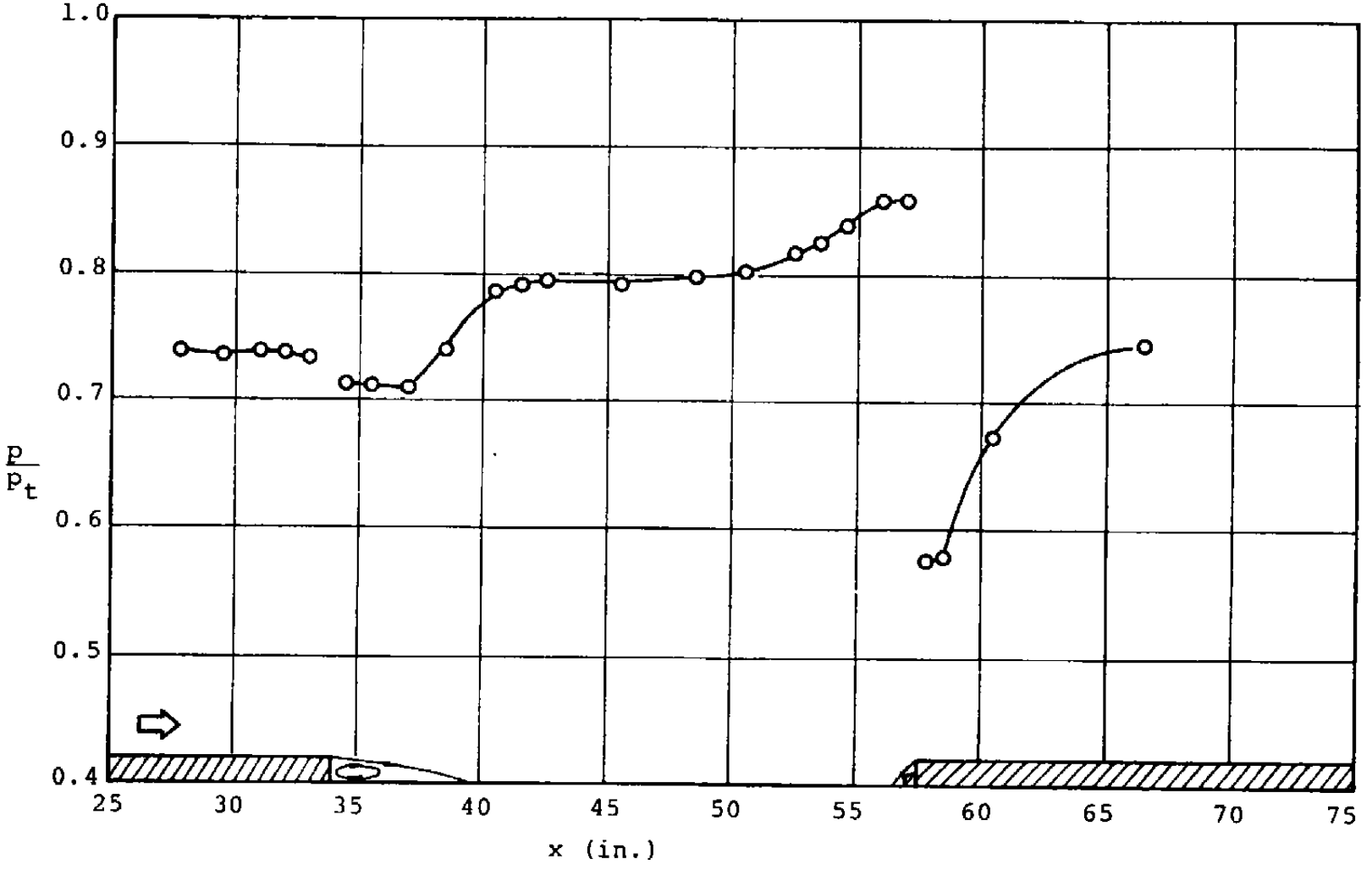

e. M = 0.67, Re_{L_R} = 17.8 x 10^6, h = 1 inch

Figure 13. Continued.

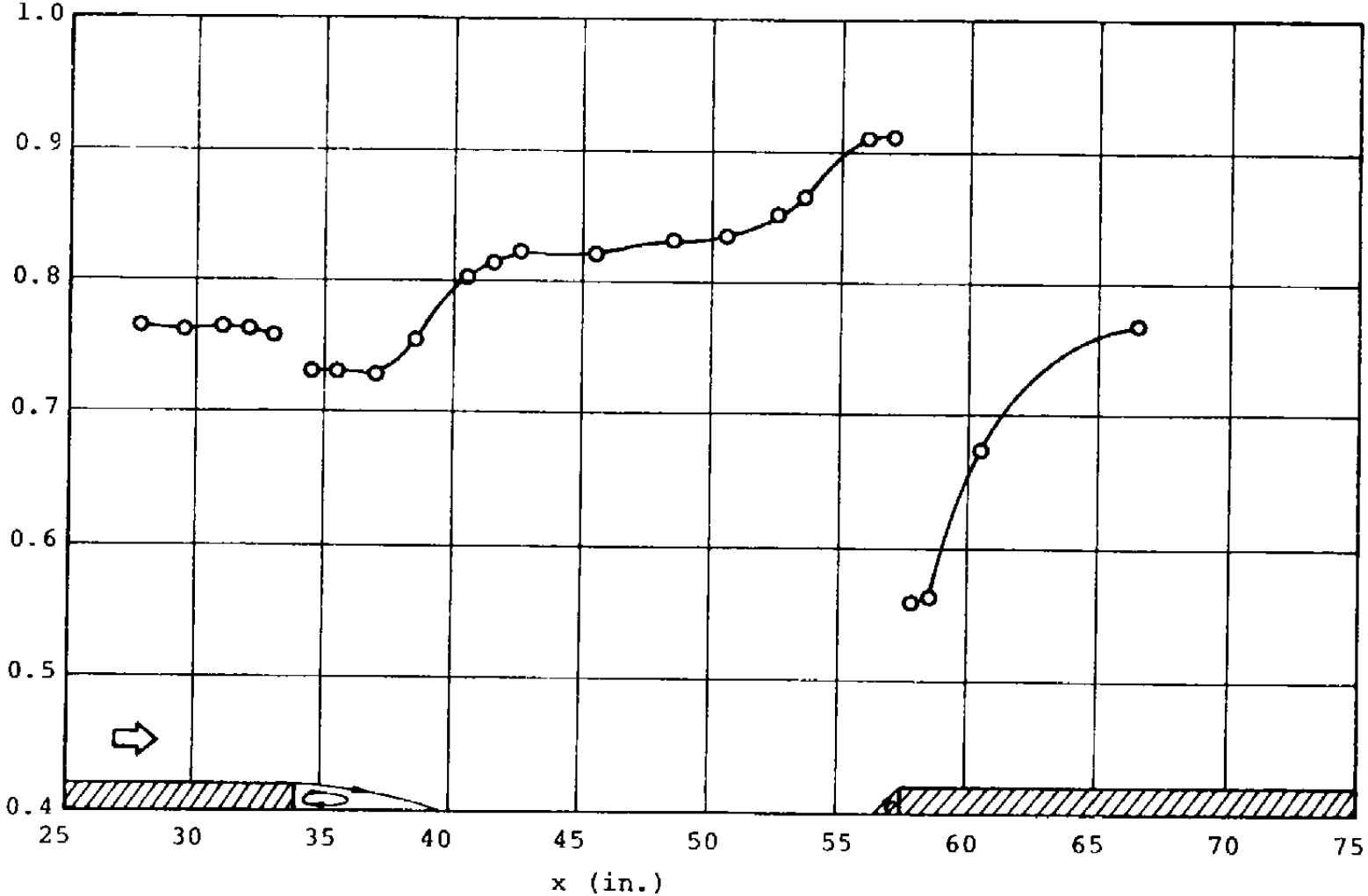

f. $M_\infty = 0.79$, $Re_{L_R} = 22.4 \times 10^6$, h = 1 inch

Figure 13. Continued.

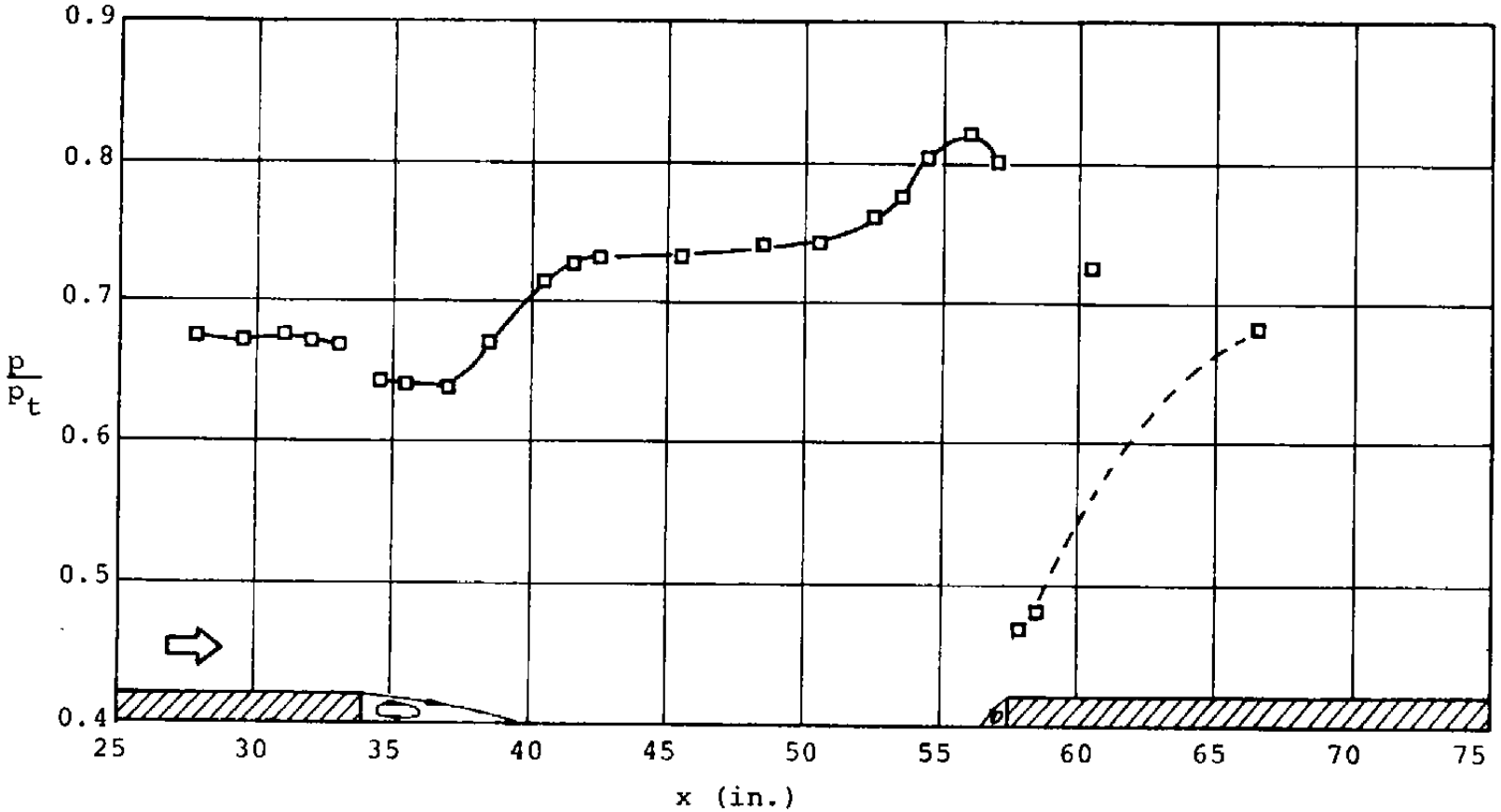

g. $M_\infty = 0.77$, $Re_{L_R} = 21.5 \times 10^6$, h = 1 inch

Figure 13. Continued.

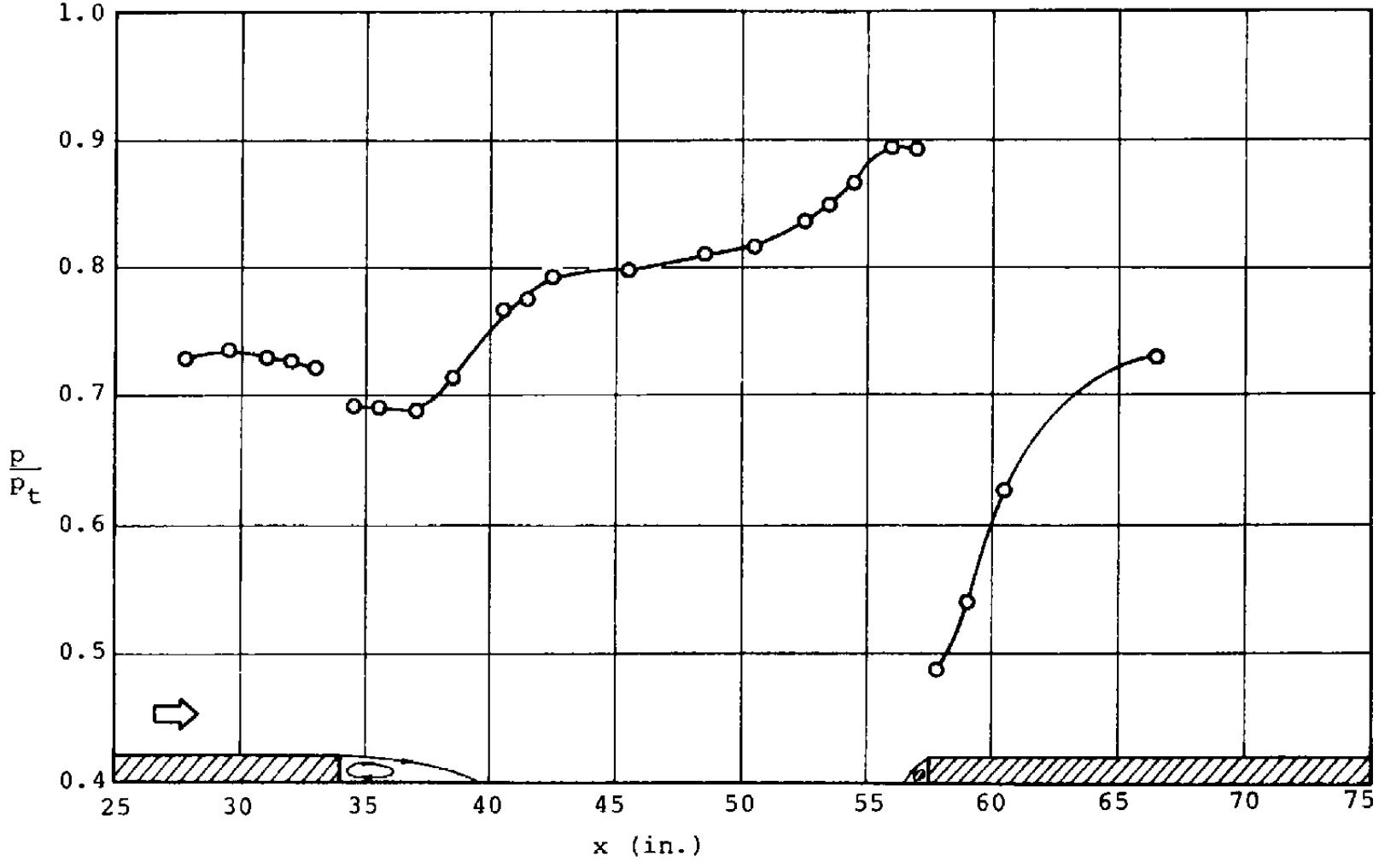

h. $M_\infty = 0.84$, $Re_{L_R} = 24.8 \times 10^6$, h = 1 inch

Figure 13. Continued.

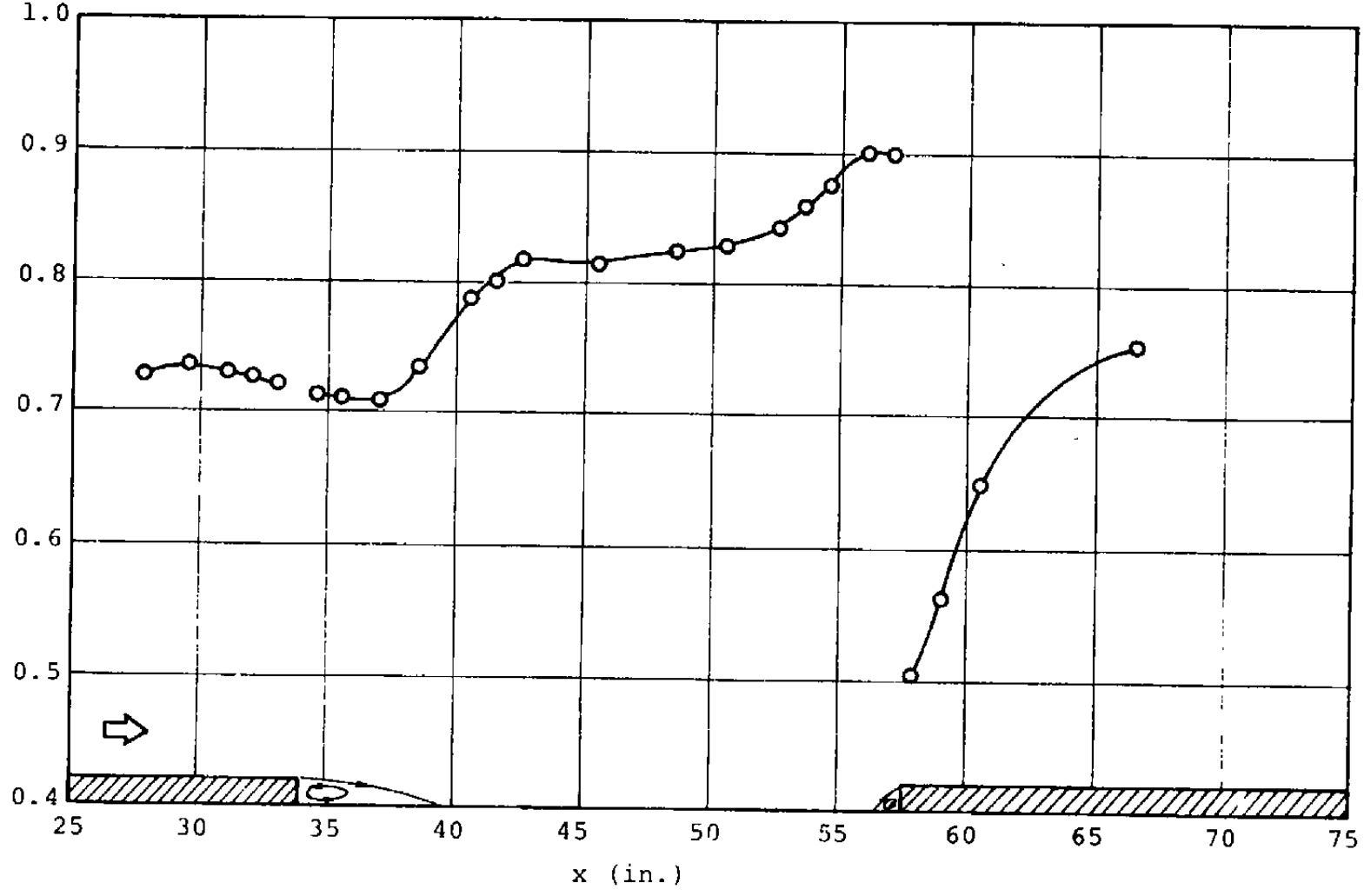

i. $M_\infty = 0.81$, $Re_{L_R} = 23.4 \times 10^6$, h = 1 inch

Figure 13. Concluded.

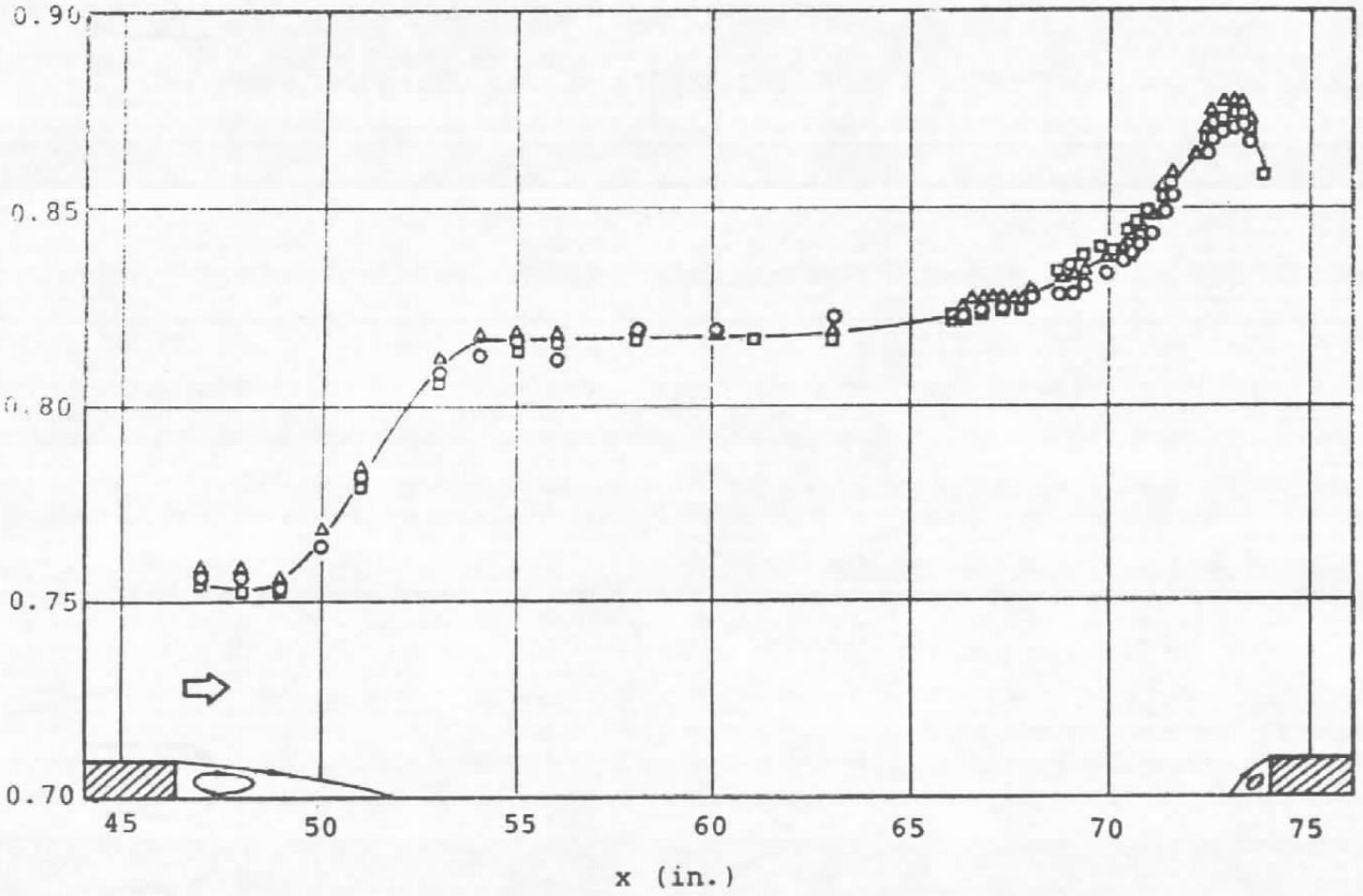

$M_\infty = 0.60$, $Re_{L_R} = 15.5 \times 10^6$, h = 1 inch

Figure 14. Surface pressure distribution along 27.5-inch cavity.

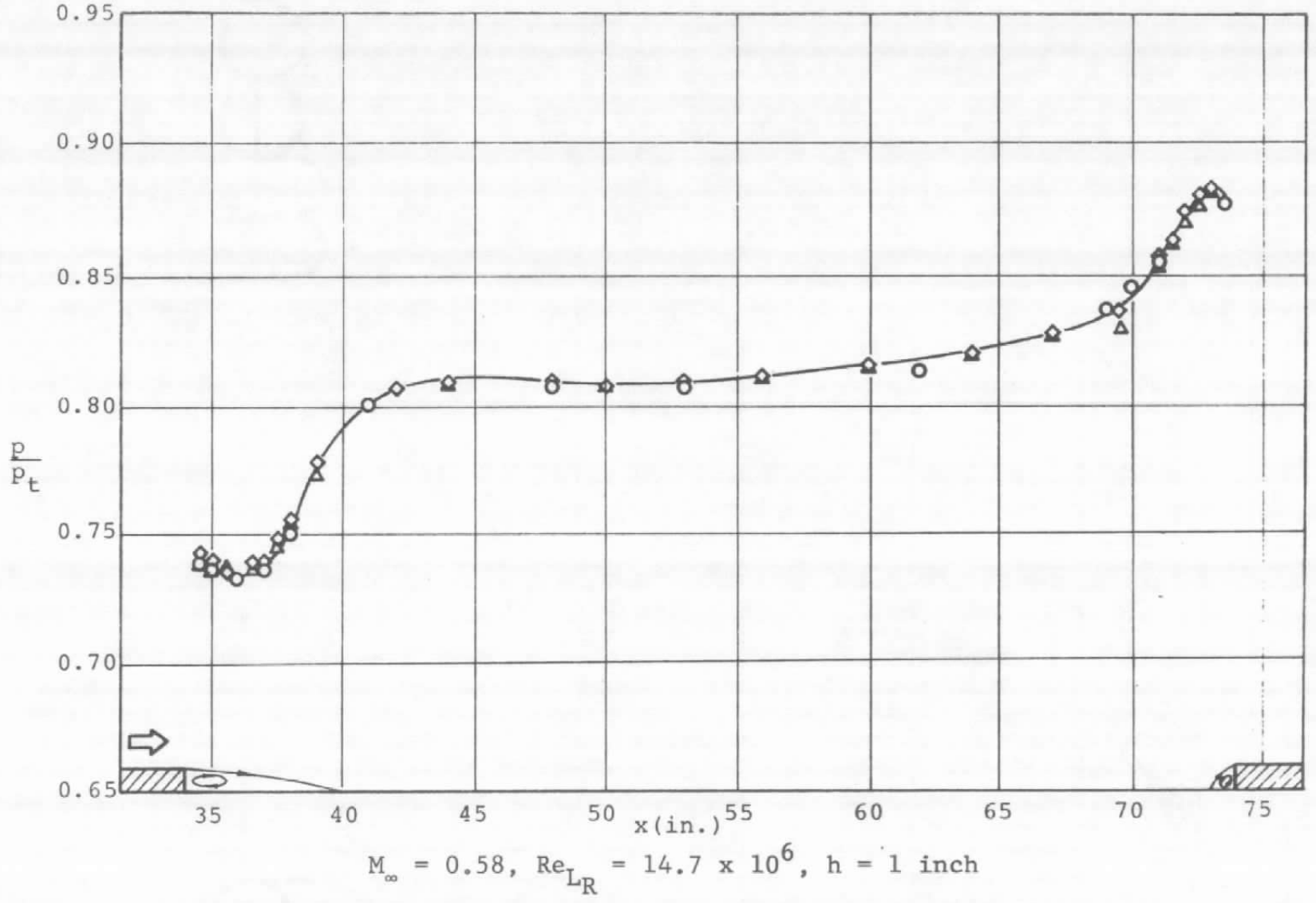

$M_\infty = 0.58$, $Re_{L_R} = 14.7 \times 10^6$, h = 1 inch

Figure 15. Surface pressure distribution along 40-inch cavity.

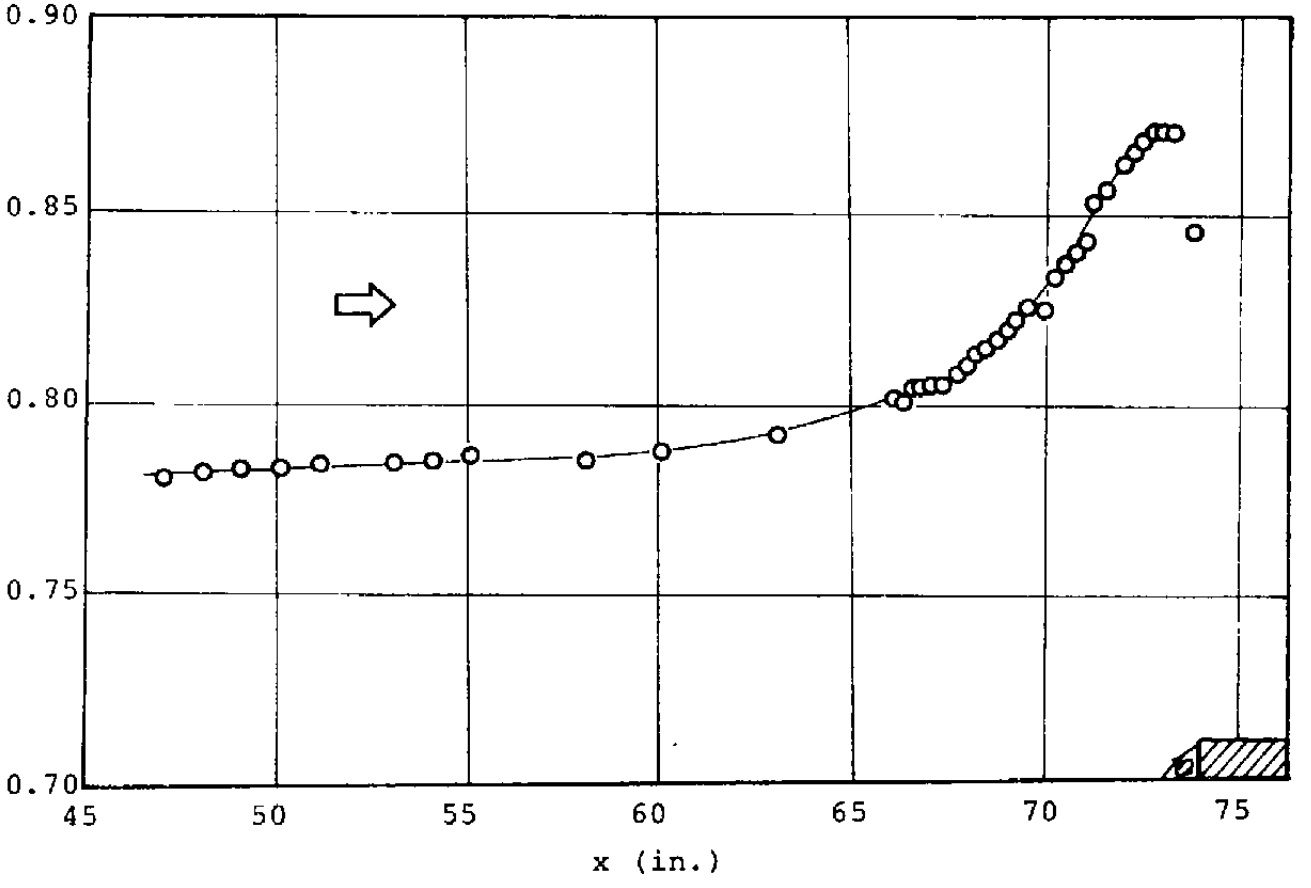

a. M_∞ = 0.61, p_t - 17.9 psia, h = 1 inch, Re_{L_f} = 33.1 x 10^6

Figure 16. Surface pressure distribution along forward-facing step model.

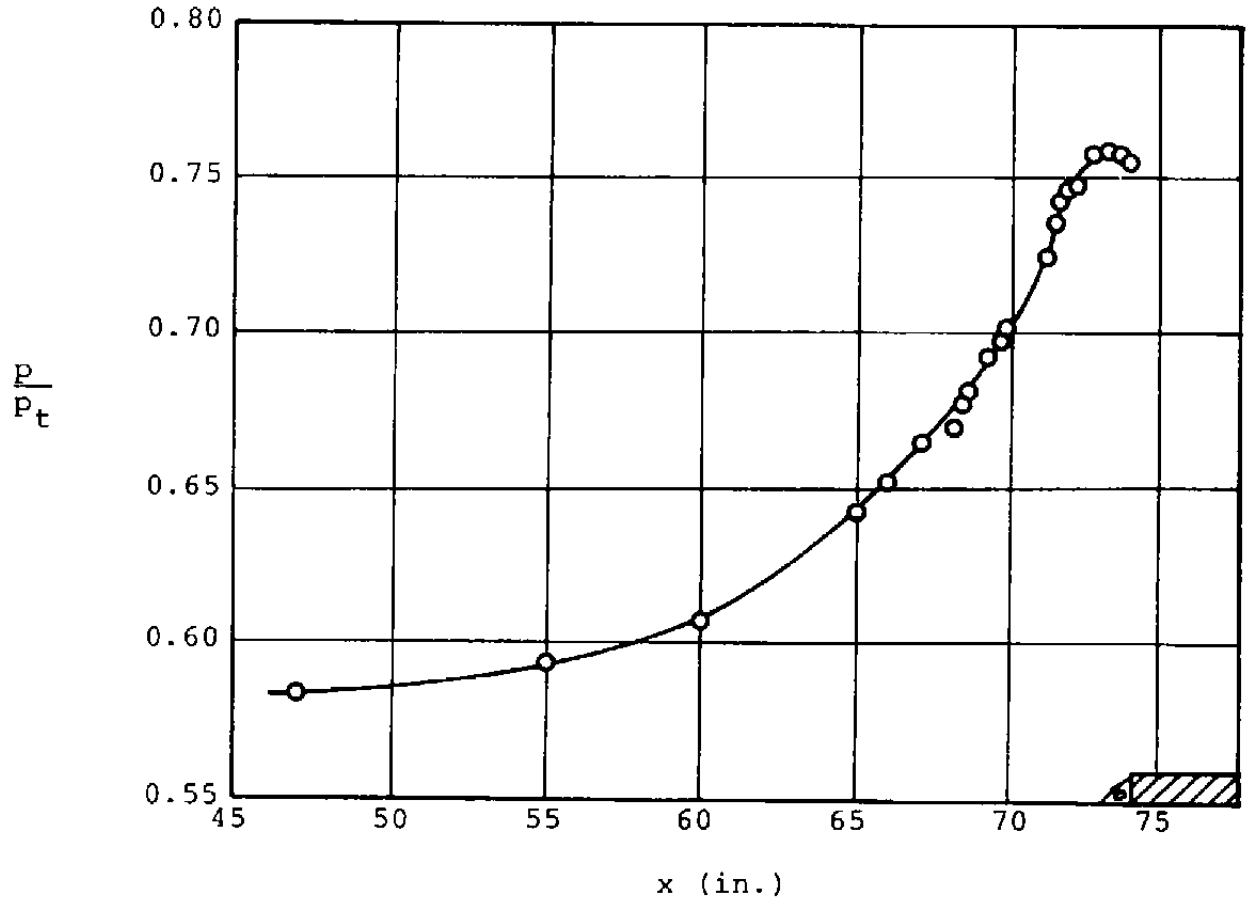

b. $M_\infty = 0.91$, $p_t = 25$ psia, h = 1 inch, $Re_{L_f} = 56.9 \times 10^6$

Figure 16. Concluded.

pressure profiles were measured, the pressure taps were connected to a triple joint. The static pressure at these locations was sensed by a manometer tube and a transducer simultaneously. Data sensed by the transducer was used to calculate the velocity distribution across the shear layer. The difference between the manometer and the transducer data was less than 1 percent as shown in Figure 17. The static pressure distribution on the side wall near the rearward-facing step was also measured (Figure 18).

3.3 SURFACE-OIL FLOW VISUALIZATION

Surface oil flow visualization techniques have been used to extract details of the separation and the reattachment regions. It has also been applied to the side walls in order to obtain a qualitative idea of the three-dimensional structure of the flow. A mixture of titanium dioxide and kerosene oil was used for this purpose.

In order to avoid an excessive oil accumulation near the separation line and to keep the oil from forming U-shaped waves, different proportions of titanium dioxide to kerosene oil were tested and used for the different skin friction regions (Ref. 7). On the side-wall, the viscosity of the applied mixture was high enough so that the patterns were believed to be unaffected by the gravitational force.

A representative surface oil flow photograph for the flow near the forward-facing step in the 27.5-inch cavity (at M_∞ - 0.6 and $Re_{L_f} = 32.5 \times 10^6$) is shown in Figure 19. Data of the separation and reattachment distances on different models at different Mach numbers and Reynolds numbers obtained from the oil flow observations are shown in Table II and Figure 20.

Based on this data, several features of the flow can be discussed as follows. First, for the forward-facing step at the end of the cavity:

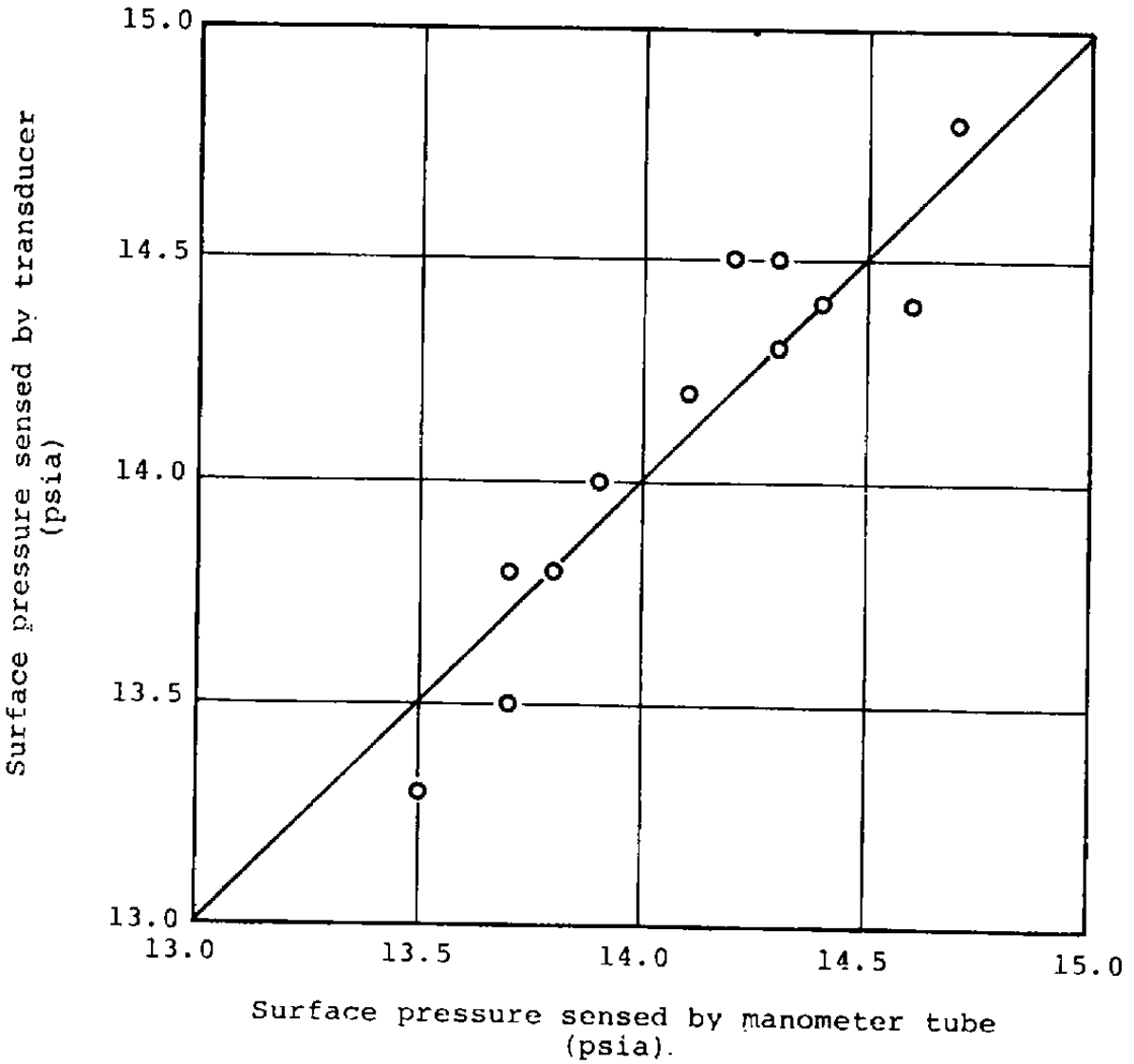

Figure 17. Comparison of pressures sensed by pressure transducer and by manometer tube.

(x_1, y_1) = (47.5, 1.85)
(x_2, y_2) = (47.5, 0.85)
(x_3, y_3) = (48.5, 0.85)
(x_4, y_4) = (49.5, 0.85)

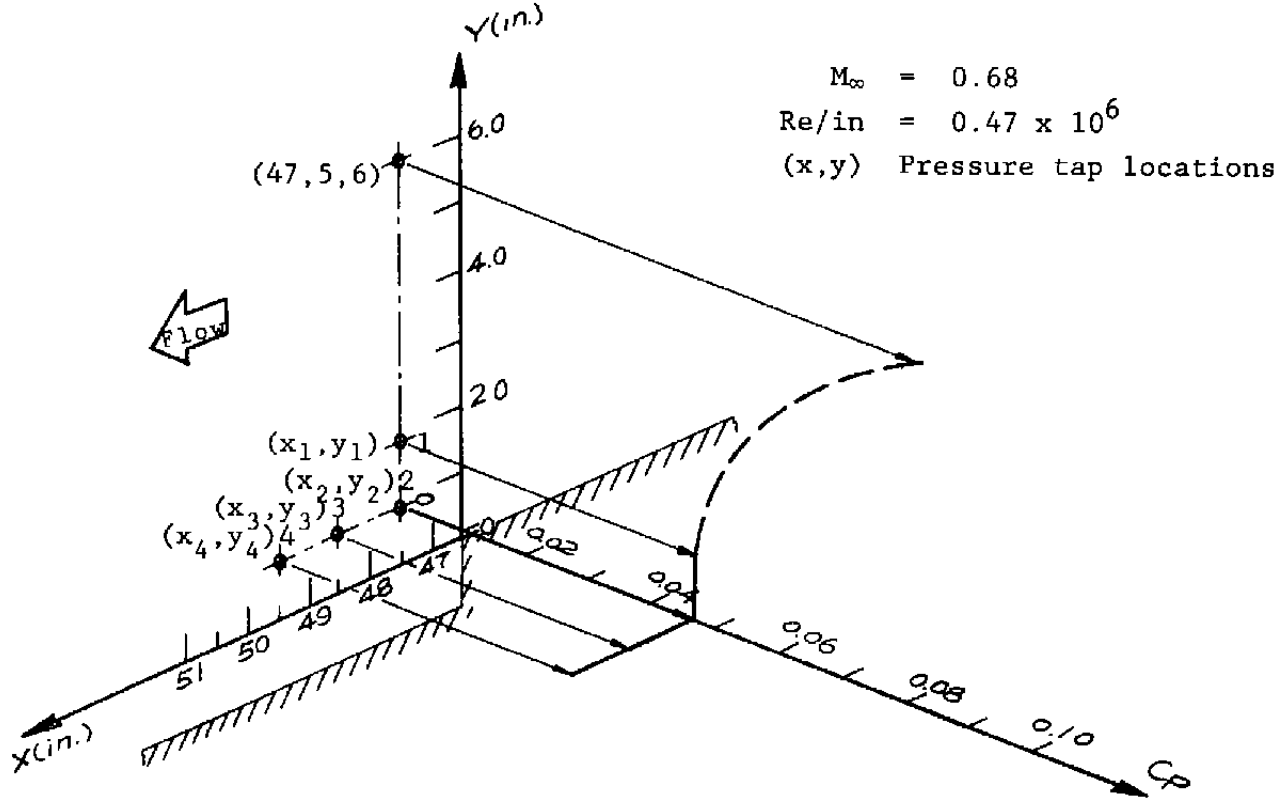

Figure 18. Static pressure distribution on the side wall near the rearward-facing step region.

AEDC-TR-77-103

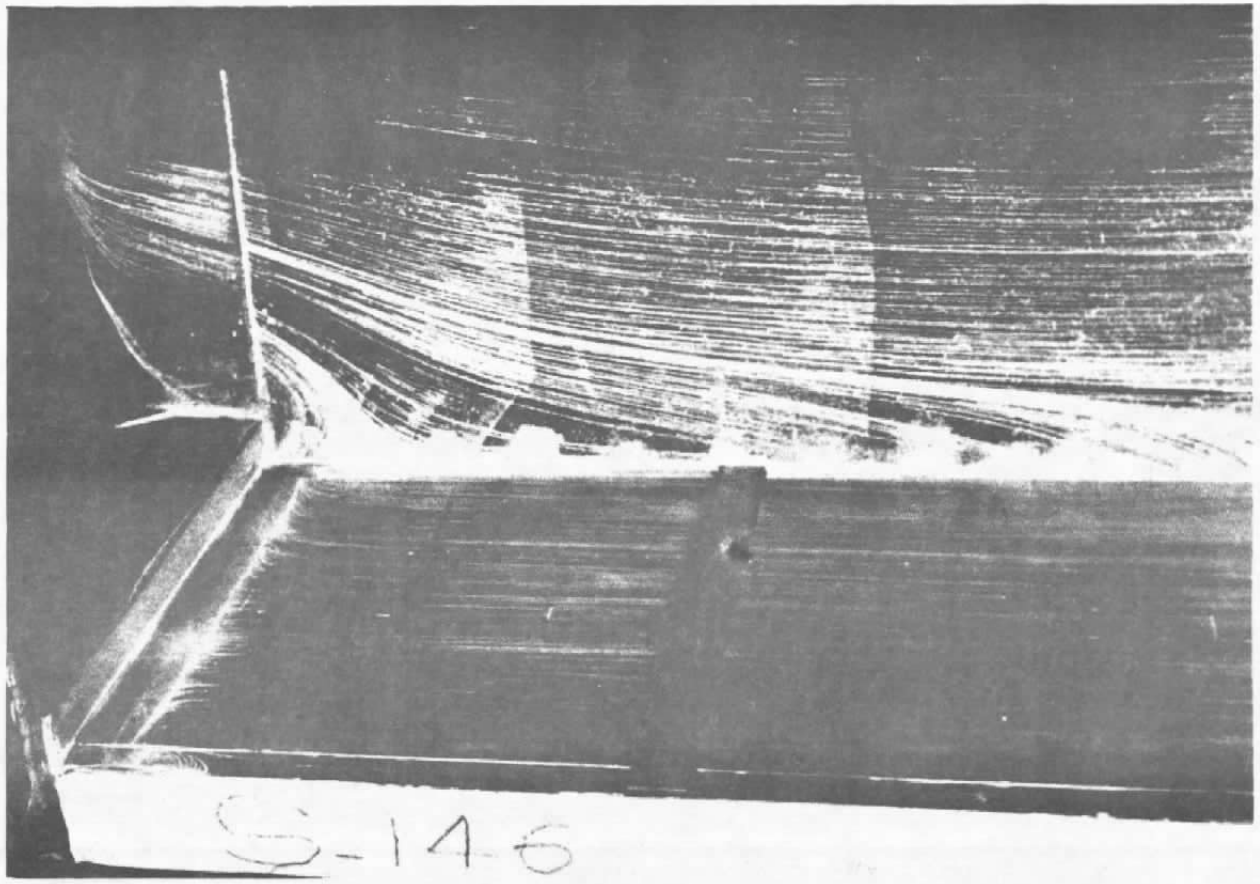

Figure 19. Photograph showing oil flow pattern ahead of the forward-facing step at $M_\infty = 0.6$ and $Re_{L_f} = 32.5 \times 10^6$.

TABLE II

REATTACHMENT AND SEPARATION DISTANCES FOR FLOW OVER CAVITIES

Cavity Length (in.)	M	p_t (psia)	Reattachment Distance, ℓ_r (in.)	Separation Distance, ℓ_s (in.)	Re_{L_R}
11.0	0.83	28.2	7.0	1.0	28.44×10^6
11.0	0.56	18.0	7.0	1.0	14.33×10^6
15.75	0.80	25.2	6.5	0.9	24.99×10^6
15.75	0.66	25.7	6.5	1.0	22.94×10^6
23.5	0.85	29.6	6.0	1.2	39.19×10^6
23.5	0.84	26.6	6.5	0.9	27.09×10^6
23.5	0.58	18.6	5.5	0.9	15.26×10^6
27.5	0.70	17.6	5.2	1.1	22.10×10^6
27.5	0.60	17.5	5.2	1.1	20.00×10^6
27.5	0.60	17.7	5.2	1.1	20.23×10^6
40.0	0.80	17.8	5.9	1.1	17.65×10^6
40.0	0.69	16.9	5.9	1.1	15.37×10^6
40.0	0.67	17.5	5.9	1.1	15.77×10^6

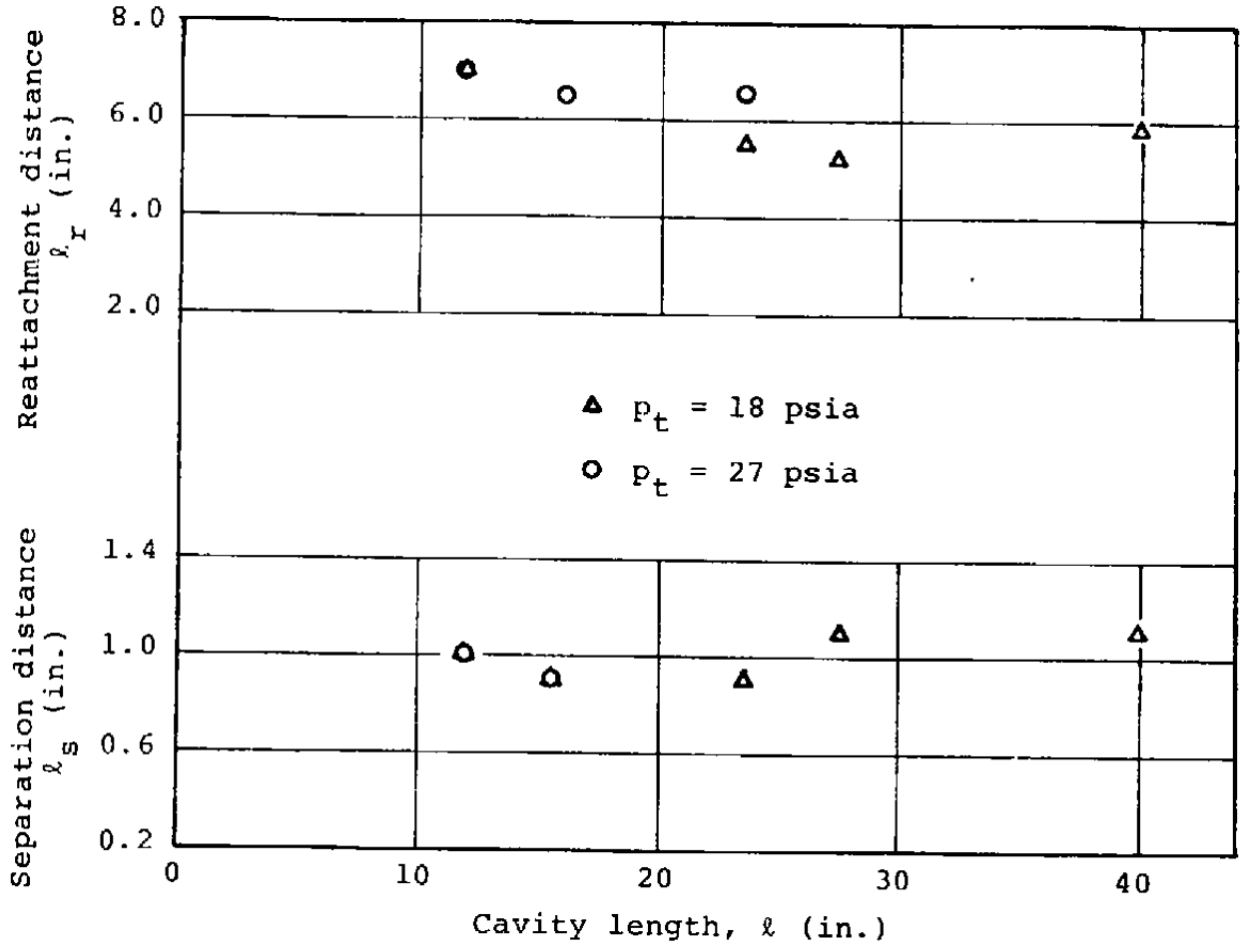

Figure 20. Effect of cavity length on reattachment and separation distance (M = 0.56 to 0.85, Re/ft = 5.04 x 10^6 to 13.8 x 10^6).

1. It was seen that the three-dimensional effects at the corner of the step and the tunnel wall made the flow pattern quite complicated (Figure 19). However, the spanwise influence of this effect was not sufficient to destroy the two-dimensional nature of the flow over the major part of the span.
2. These secondary flows were confined within a region less than two step heights from the side walls.
3. There was a vortex in the flow ahead of the step with its center about 1.8 inches upstream of the step and 0.25 inches from the side wall.
4. The oil flow on top of the step indicated a reattachment line of the separated flow over the step at about 2.4 inches downstream of the step. There was also an accumulation of oil right at the step corner. This would result from the reversed flow in the separation bubble on the top of the step forcing the oil to the foremost portion of the vortex.
5. The separation line on the floor ahead of the forward-facing step was clearly seen. The distance from the separation point to the root of the step (ℓ) was roughly constant (about one step height) in the Mach number range of 0.6 to 0.8. It decreased slightly with increasing cavity length (ℓ) when the cavity length was long enough and reached a minimum (about 0.9 step heights) at a cavity length of about 24 inches, then increased slightly with a further decrease in cavity length.
6. For the rearward-facing step at the beginning of the cavity the following features appeared: the reattachment region behind the rearward-facing step was roughly defined by the oil flow. Several points were clear: the reattachment flow was quite three-dimensional; the

effect of the cavity length on the reattachment distance (ℓ_r) had the same trend as but slightly stronger than that on the separation distance ahead of a forward facing step; the minimum reattachment distance was about 5.2 step-heights occurring at $M_\infty \sim 0.6$ with a cavity length of 27.5 inches and the maximum was about 7.0 step-heights at $M_\infty \sim 0.6$ and 0.8 with a cavity length of 11 inches (Table II, page 45). It appears that the reattachment distance is a function of the cavity length and almost independent of the subsonic free-stream Mach number.

7. Within the recirculating region behind the rearward-facing step, there was an oil line about 1 inch from the step which indicated a separation of the reversed flow and the presence of a secondary vortex.

4.0 DISCUSSION OF EXPERIMENTAL RESULTS

4.1 SURFACE PRESSURE DISTRIBUTIONS

4.1.1 Dimensional Analysis and Reference Parameters

In these experiments, it was assumed that no heat transfer or chemical reactions took place. The non-dimensional parameters that may be pertinent to the analysis of the experimental data can be obtained by applying a dimensional analysis. With the understanding that,

$$p = p \text{ (flow variables and model configurations)}$$
$$= p\ (p_{ref},\ u,\ \mu,\ \rho,\ a,\ x_i,\ g_i)$$

where

p_{ref} = reference pressure, u = flow velocity, a = sound speed,

and

x_i = streamwise characteristic length, such as cavity length, etc.

y_i = characteristic length perpendicular to the model surface such as boundary-layer integral thickness, etc.

It results in:

$$F\left(\frac{p}{p_{ref}}, \frac{\rho u x_i}{\mu}, \frac{u}{a}, \frac{y_i}{x_i}\right) = 0 \qquad (4.1)$$

or

$$\frac{p}{p_{ref}} = f\left(\frac{\rho u x_i}{\mu}, \frac{u}{a}, \frac{y_i}{x_i}\right) = f\left(Re, M, \frac{y_i}{x_i}\right) \qquad (4.2)$$

This relationship indicates the dominating parameters involved in this study.

The significant static pressures concerned in this study could be the base pressure (p_b), the pressure at the reattachment point (p_r), the plateau pressure (p_p), the pressure at the separation point (p_s) or the peak pressure (p_m) (see Figure 4). The most generally used reference pressures are the total pressure (p_t) and the free-stream static pressure (p_∞). In order to understand the trend of the energy consumption by the turbulent mixing and the recovery of the flow along the model surface, some other pressures, such as the base pressure and the plateau pressure, are also worth using as references.

The characteristic length (x_i) considered will be the distance from the leading edge along the streamwise direction (x, L_R or L_f), which indicates the historical effect of the flow turbulence structure. Another streamwise characteristic length will be the cavity length (ℓ) which can partially indicate the strength of the mutual interference effect between the upstream disturbance and the downstream separation. The characteristic length perpendicular to the model surface (y_i) will be the step height (h) and the boundary-layer integral thicknesses (δ, δ^* and θ). The first characteristic y_i, namely h, will relate to

the strength of the upstream disturbance as well as to the downstream separation. The last three will indicate the state of the flow energy in the shear layer. These are all very useful in analyzing the features of the flow.

4.1.2 Surface Pressure Distribution Over the Entire Model

A general description and discussion of the pressure distribution over the entire cavity model is made here (see Figure 21). The detail features of the important pressures such as the base pressure p_b, the reattachment pressure p_r, the cavity plateau pressure p_p, the separation pressure p_s, and the peak pressure p_m and the estimation of the critical cavity length (see p. 65 for definition) based on the features of the pressure distribution over the shallow-cavity model, as well as mutual relationships among the important pressures will be discussed separately in the latter subsections.

4.1.2.1 Flow Over Cavities of Different Length to Depth Ratio

The surface pressure distributions over the cavity-like models of length to depth ratios ℓ/h = 11, 15.75, 23.5, 27.5 and 40 at M_∞ = 0.6 and Re_{L_R} = 15 x 10^6 (based on the length measured from the leading edge to the rearward-facing step station, L_R) has been shown earlier in Figures 11 - 15, as p/p_t versus x (measured in inches from the leading edge), respectively. These distributions are combined together as the pressure coefficient ($C_p \equiv (p - p_\infty)/(\frac{1}{2}\gamma p_\infty M_\infty^2)$) versus the non-dimensional distance, x_R/ℓ in Figure 21. They give a general picture of the cavity length to depth ratio effect at subsonic speeds.

From Figure 21 it is found that the pressure coefficient immediately downstream of the rearward-facing step shows a significant drop which increases as the cavity is shortened. This is a typical behavior of the base pressure problem. The pressure coefficient drop nearly disappers at ℓ/h = 11. The location of the minimum pressure coefficient moves as the cavity length or pressure coefficient drop decreases. The pressure

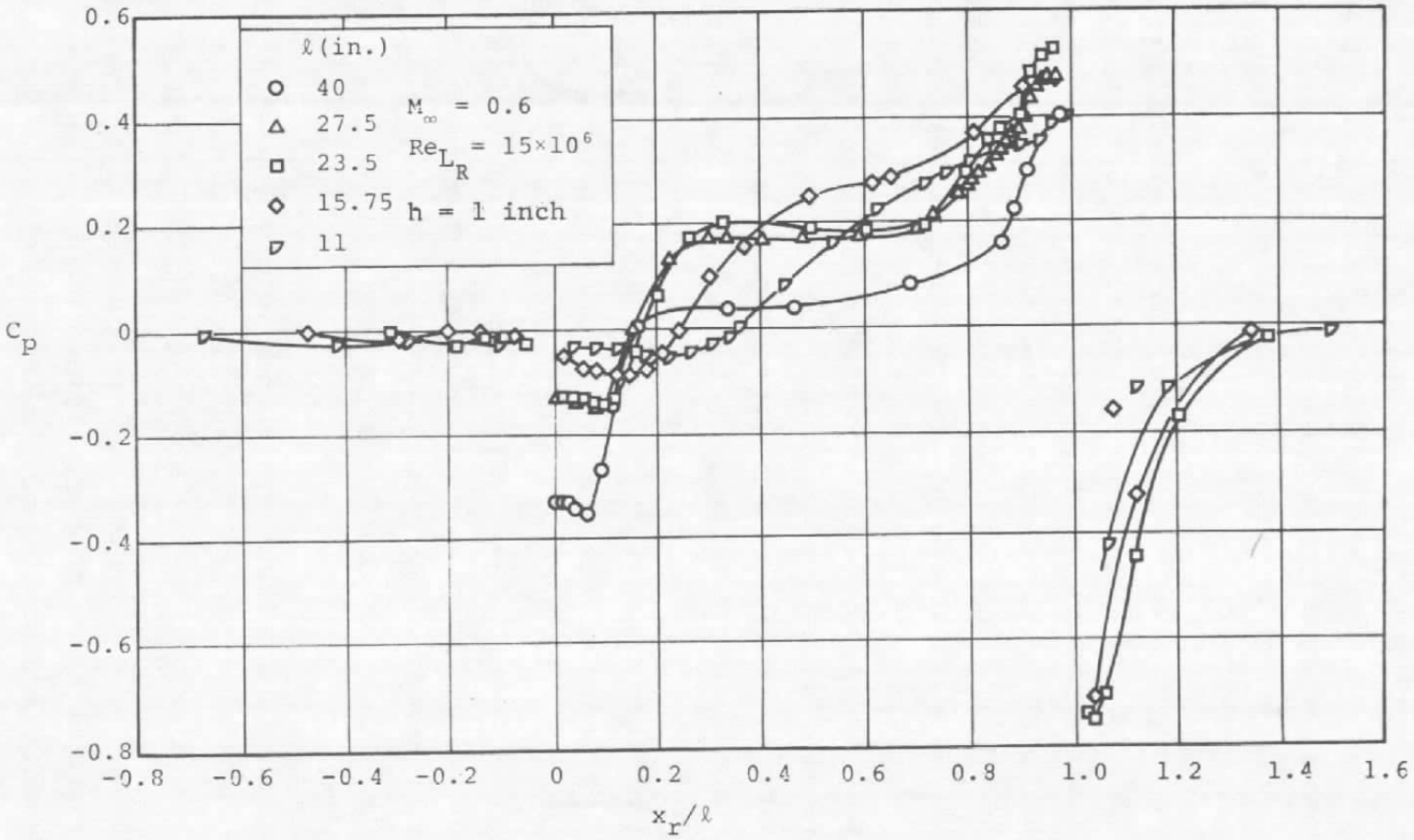

Figure 21. The distribution of pressure coefficient along shallow-cavity models.

coefficient drop is followed by a rapid rise which is steepest for the longer cavity models. The mutual interaction of the rearward and forward facing steps is very strong as evidenced by the great change in the base pressure or the separation pressure even though both steps are up to 30 to 40 boundary layer thickness distance apart.

For the longer cavities ($\ell/h \geq 15.75$), there is a pressure plateau along the center portion of the floor, but the plateau disappears as the cavity shortens, as in the case of $\ell/h = 11$. The starting point of the plateau moves downstream as the cavity length is decreased and eventually coincides with the pressure peak. In the middle portion of the cavities, the pressure coefficient increases at first with shortening cavity, but eventually begins to decrease. In the center portion of the cavity, the pressure coefficient reaches a maximum value of about 0.3 (corresponding to $\ell/h = 15.75$), whereas the maximum peak pressure coefficient ahead of the forward-facing step is about 0.54 (corresponding to $\ell/h = 23.5$). These values are about 50 and 20 percent higher than those for the comparable incompressible flow (Ref. 10). Upstream of the rearward-facing step, i.e., flow ahead of the base, the pressure coefficient shows a sinous feature. Downstream of the forward-facing step there is another pressure coefficient drop which is much stronger than that of a flow over a rearward-facing step and increases with decreasing cavity length. This drop recovers rapidly towards the free-stream condition.

The pressure distribution at transonic speeds along the cavity-like models of length to depth ratios $\ell/h = 15.75$ and 23.5 at $M_\infty \approx 0.8$ and $Re_{L_R} \approx 29 \times 10^6$, shown in Figures 12b and 13c as p/p_t vs. x, are replotted in Figure 22 as C_p versus x_R/ℓ. The general trend of the pressure coefficient distributions for these lower transonic speed flows is similar to that of the subsonic case shown in Figure 21. But there are several special features in the transonic flow cases. These are as follows:

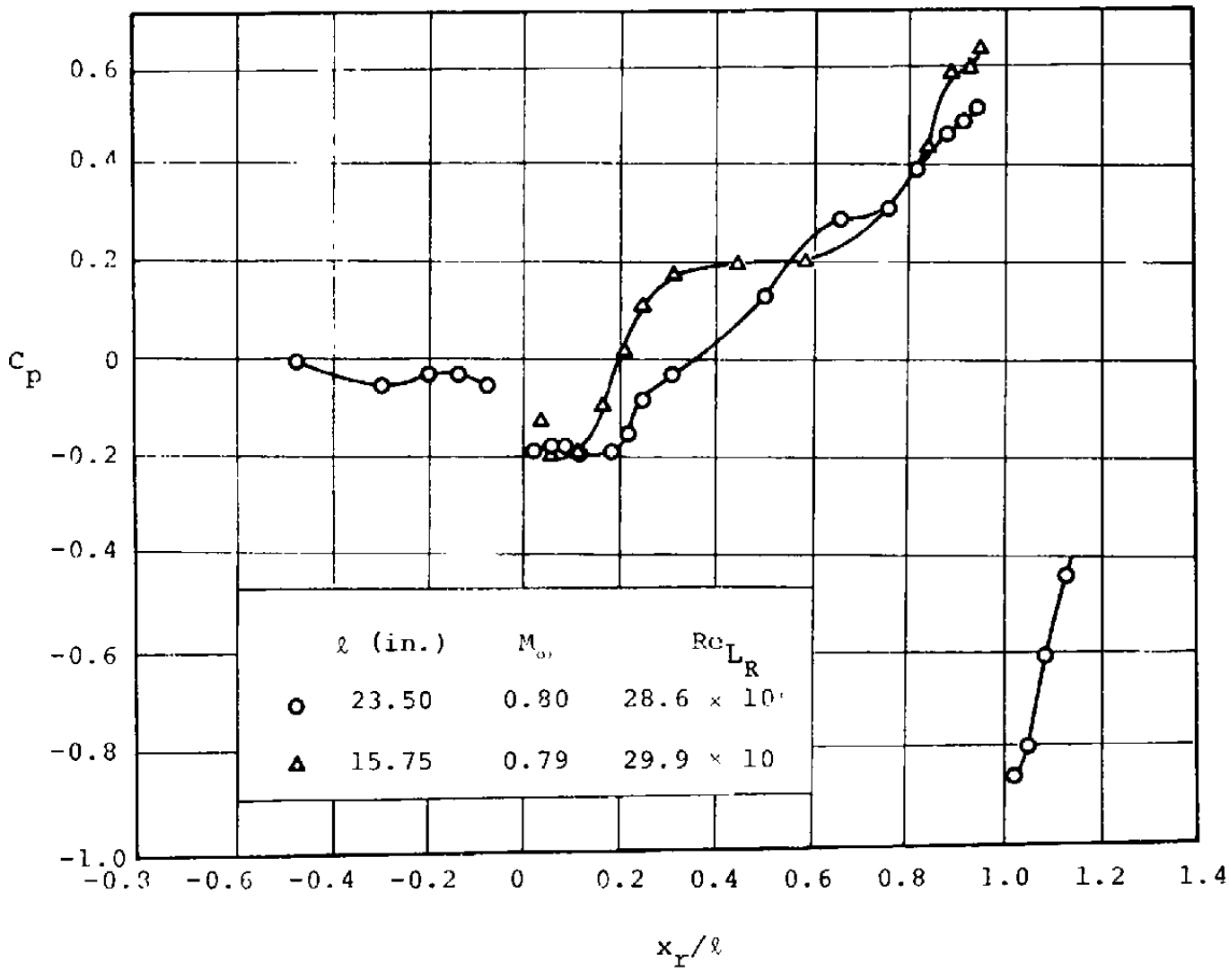

Figure 22. Effect of upstream disturbance.

First, the pressure drop at the base of these two length to depth ratio cavities is nearly the same. Secondly, the peak pressure-coefficient difference between models of $\ell/h = 23.5$ and 15.75 is greater than that of the corresponding subsonic case. Thirdly, variation of the pressure coefficient distribtion upstream of the rearward-facing step is stronger than that in subsonic flow.

It can be pointed out further by observation of Figure 23 that the pressure coefficients along the center portion of model of $\ell/h = 23.5$ are coincident for the higher ($M_\infty = 0.80$ and $Re_{L_R} = 28.6 \times 10^6$) and the lower ($M_\infty = 0.58$ and $Re_{L_R} = 15.8 \times 10^6$). The coincidence seems true for all flows over the model of $\ell/h = 23.5$ at different Mach numbers and Reynolds numbers, which can be verified by the observation of Figures 23, 24, and 25. On the other hand, for a shorter model ($\ell/h = 15.75$), the pressure-coefficient gradient along the center portion of a cavity for a higher inertia energy flow (higher Reynolds number) is much lower than that for a lower inertia energy flow and almost coincides with the pressure-coefficient gradient along the model of $\ell/h = 11.00$ at the lower Reynolds number (Figure 26). The pressure plateau of the higher inertia energy flow disappears at $\ell/h = 15.75$ instead of at $\ell/h = 11$ as in the low inertia energy case (Figures 26 and 21). It seems that the effect of inertia energy upon the pressure coefficient distribution becomes more sensitive when ℓ/h is smaller. And, it can be clarified further in the next subsection that the inertia energy, which will affect the pressure coefficient distribution, is mainly due to the Reynold number change. For longer cavities ($\ell/h \geq 23.5$) the values of the nearly constant pressure over the midsection of the cavity are approximately the mean value of the corresponding maximum and minimum pressures in the cavity. In other words, the magnitude of the pressure drop over the rearward-facing step is approximately equal to the pressure rise induced by a forward-facing step of the same height.

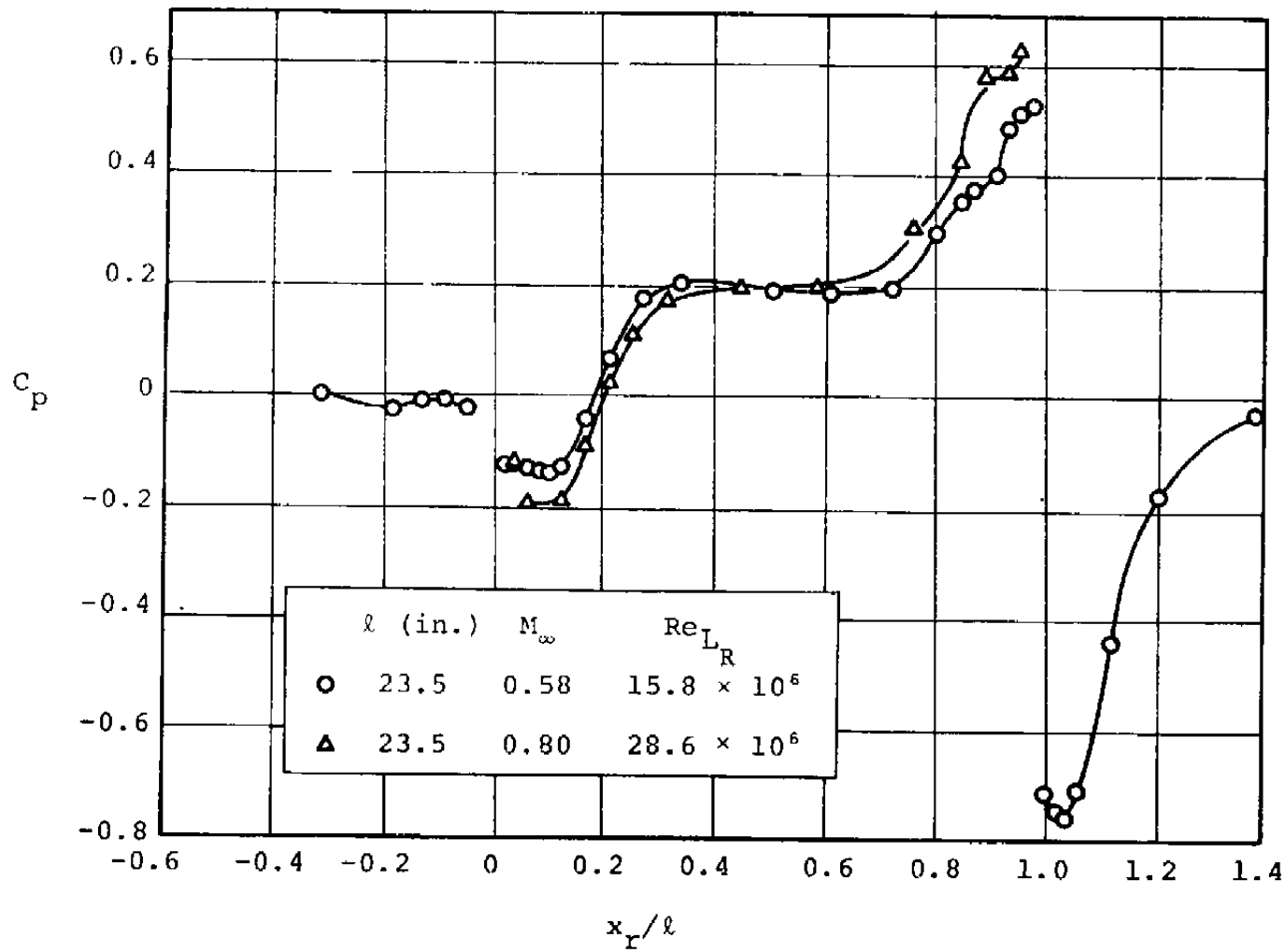

Figure 23. Effect of inertia energy of flow over 23.5-inch cavity.

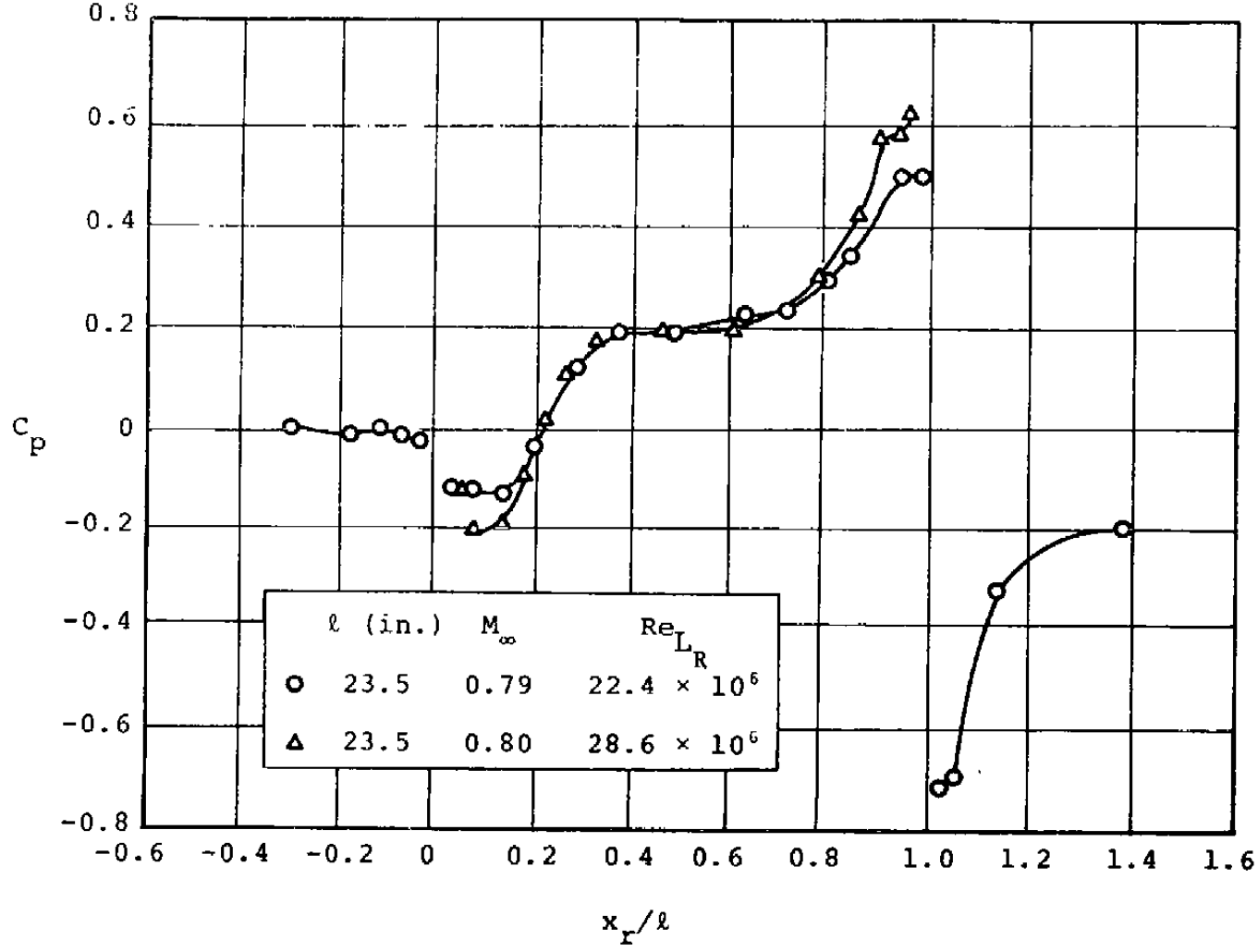

Figure 24. Effect of Reynolds number.

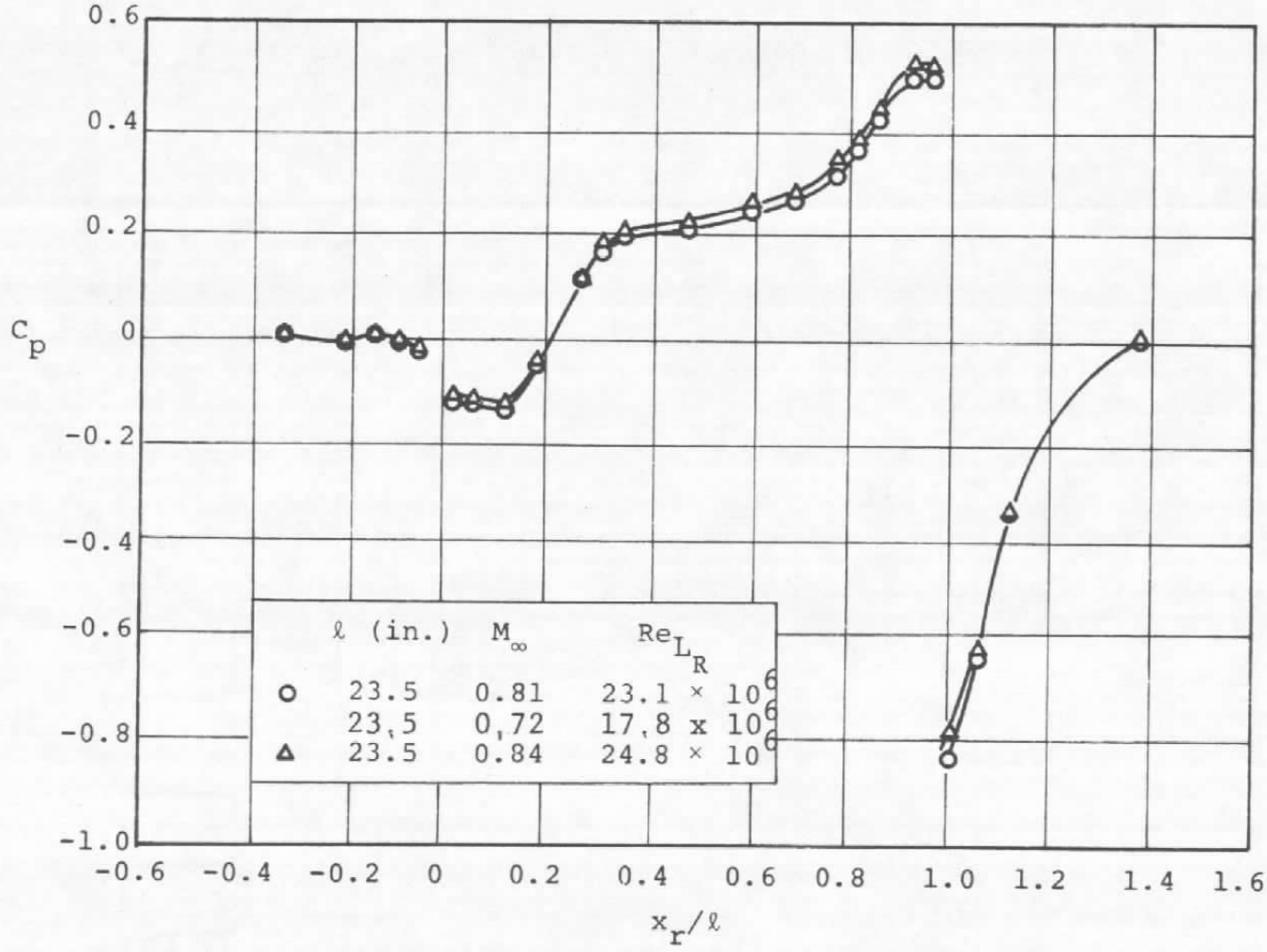

Figure 25. Effect of Mach number.

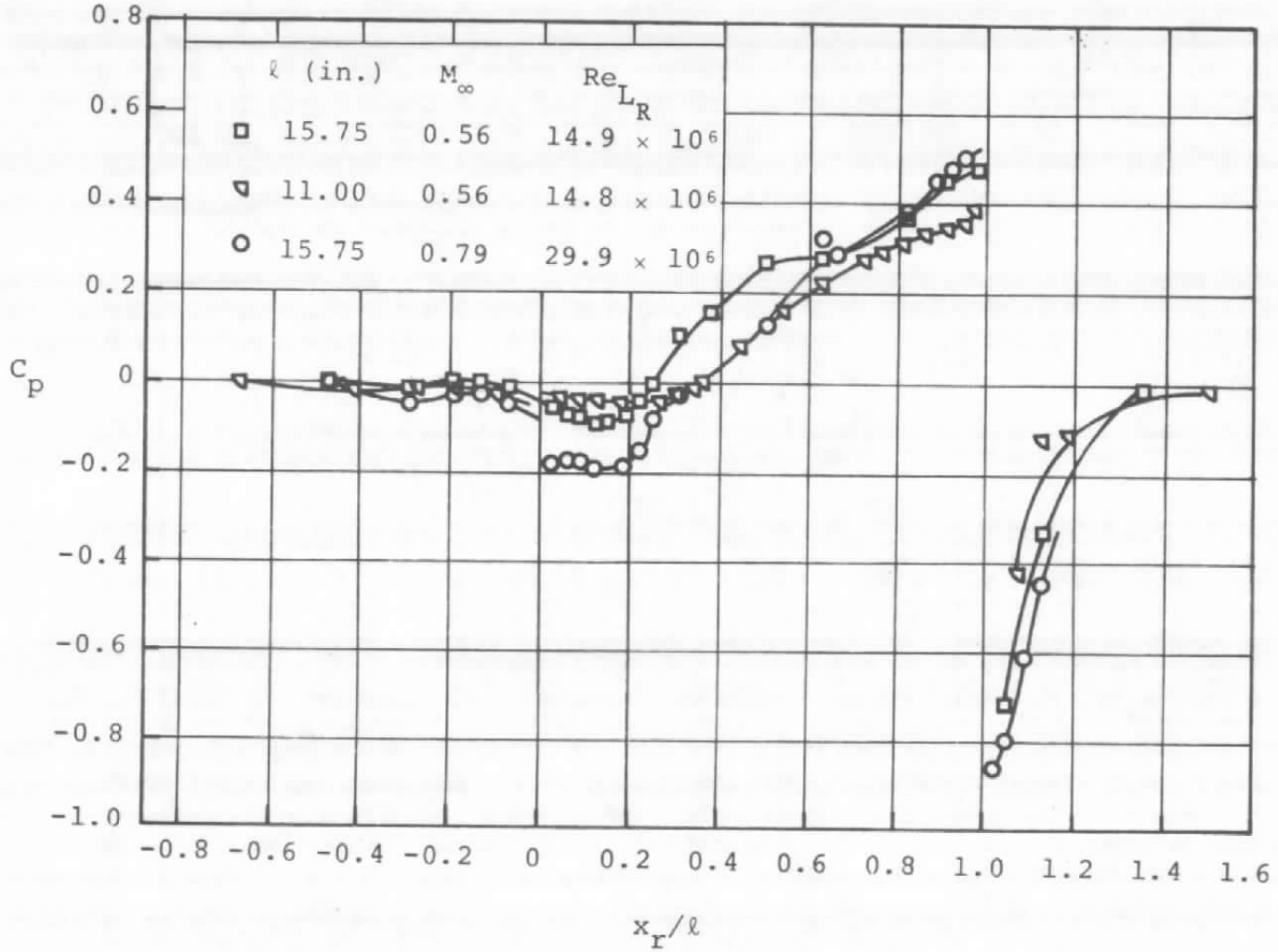

Figure 26. Effect of inertia energy of flow over 15.75-inch cavity.

However, as ℓ/h becomes small ($\ell/h \leq 15.75$), the pressure rise ahead of the forward-facing step becomes less than the pressure drop over the back-step.

From the above description, it is found that the general trend of the surface pressure distribution over the cavity floor of different depth to length ratios is similar to the incompressible flow case. However, it is not possible to predict the pressure coefficient of a compressible flow over a cavity-like model from a corresponding incompressible result by using any existing rules. This is the case even in the region where the separation and reattachment regions are excluded. For instance, consider using the well-known Prandtl-Glauert rule to simulate the flow at $M_\infty = 0.79$ from the measured flow at $M_\infty = 0.19$. The result shows a tremendous error when compared with the measured data. In the center portion of the cavity, the error of the corrected pressure coefficient can be as large as 50 percent (Figure 27).

4.1.2.2 Flow Over Cavity With Different Reynolds Numbers and Mach Numbers.

Figure 24 shows the pressure coefficient distribution for flow over a 23.5 inch cavity-like model at $M_\infty \approx 0.8$ and different Reynolds numbers (22.4×10^6 and 28.6×10^6). It can be seen from this plot that at this transonic speed, the higher Reynolds number flow will cause a lower base pressure and a higher peak pressure, whereas the plateau pressure is relatively insensitive to the Reynolds number change. Figure 25 shows that the pressure coefficient distribution seems insensitive to the variation of Mach number along the entire model.

Figures 23 and 24 give evidence that the flow over a cavity-like model will have a lower base pressure and a higher peak pressure if the inertia energy of the flow is higher. Being aware of the facts described above, it can be further concluded that this phenomenon is mainly attributed to the Reynolds number.

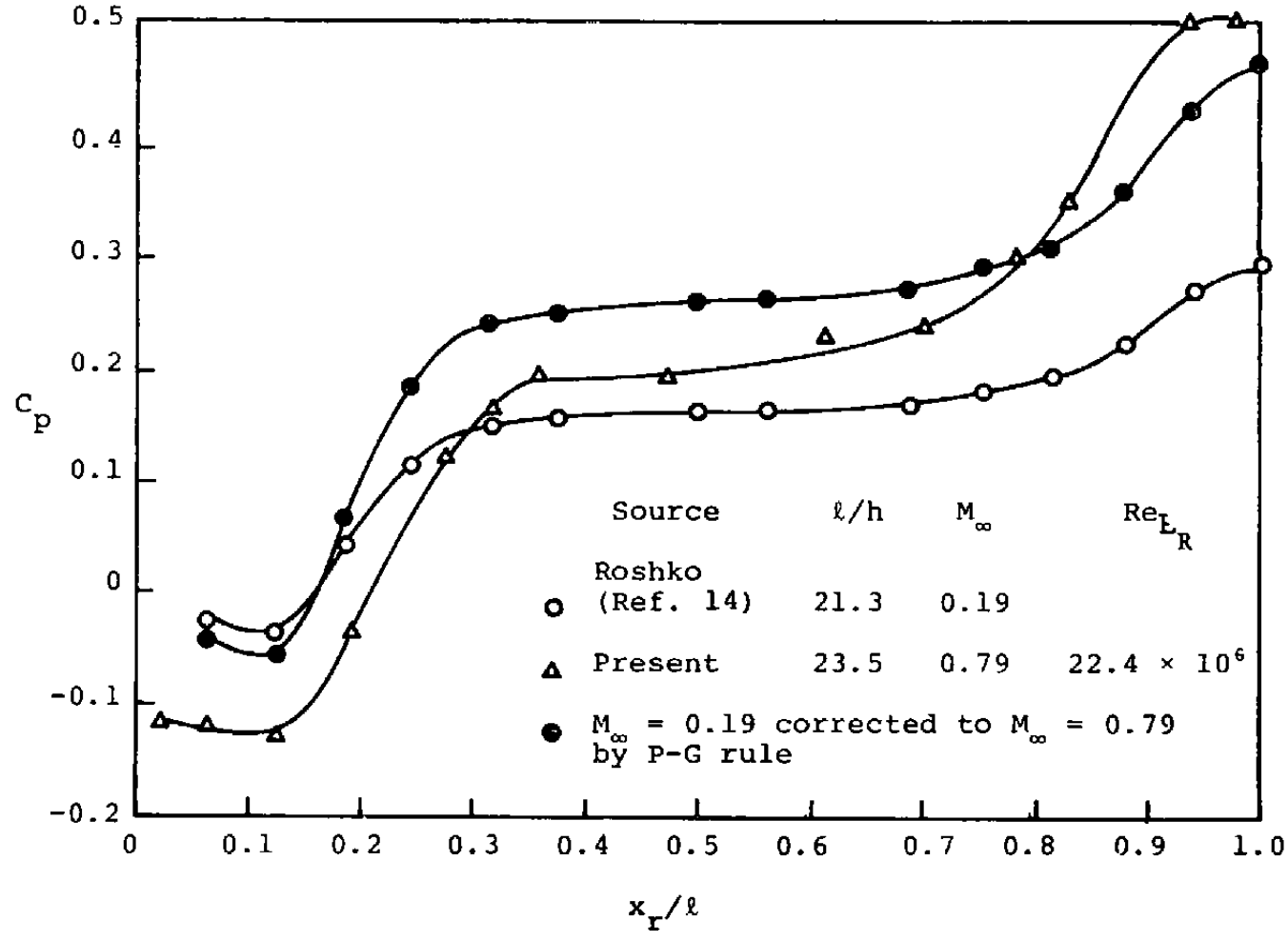

Figure 27. Comparison of measured data and Prandtl-Glauert rule.

4.1.2.3 Pressure Distribution Over Forward-Facing Steps.

The pressure distributions over a forward-facing step model are given in Figures 16a and b, as p/p_t versus x, and, in Figure 28 as p/p_∞ versus x_f/h. A comparison of the pressure distribution for turbulent flow over a forward-facing step model at supersonic, transonic, and subsonic speeds is shown in Figure 29. These figures show that in the lower transonic and subsonic ranges, the pressure distributions over a forward-facing step model have a peak pressure point about one step height upstream of the step, no matter how different the Mach numbers and Reynolds numbers are. The upper transonic and supersonic flows have a pressure plateau in addition to, and ahead of, the pressure peak, and the supersonic flow reaches the highest peak pressure and has the shortest upstream influence distance. In subsonic flows, the pressure rise ahead of the step is simply due to the conversion of the kinetic energy of the flow into pressure energy by the presence of the step. It is natural that the flow having the higher speed will have a higher pressure peak (if the other conditions remain the same). As the flow speed becomes greater than sonic, a shock wave is formed due to the turning of the dividing streamline ahead of the step. This shock and the inviscid flow field result in the so-called plateau pressure regime. As the step is approached, it forms the peak pressure because the flow is required to slow down. By observing the difference in subsonic and supersonic flow separation, it seems that the original separation pressure transfers to the plateau pressure while the separation point suddenly moves in the upstream direction as the approaching Mach number increases from below to over one. This fact is shown in Figure 30. In other words, if the free-stream Mach number decreased from supersonic to subsonic flow, the distinguished plateau and separation pressures merge together to become a subsonic flow separation pressure (Figure 30).

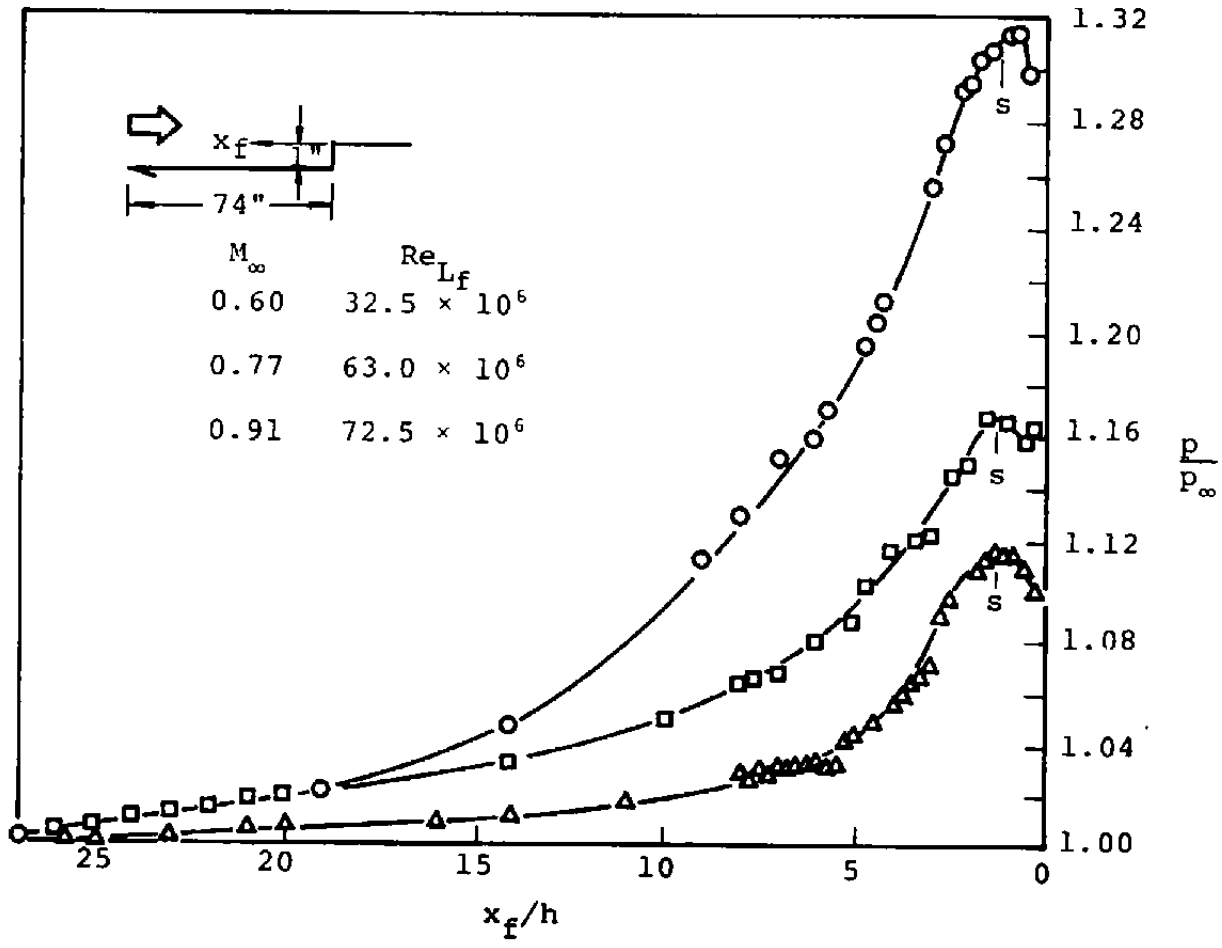

Figure 28. Effect of flow inertia energy on the surface pressure distribution ahead of a forward-facing step.

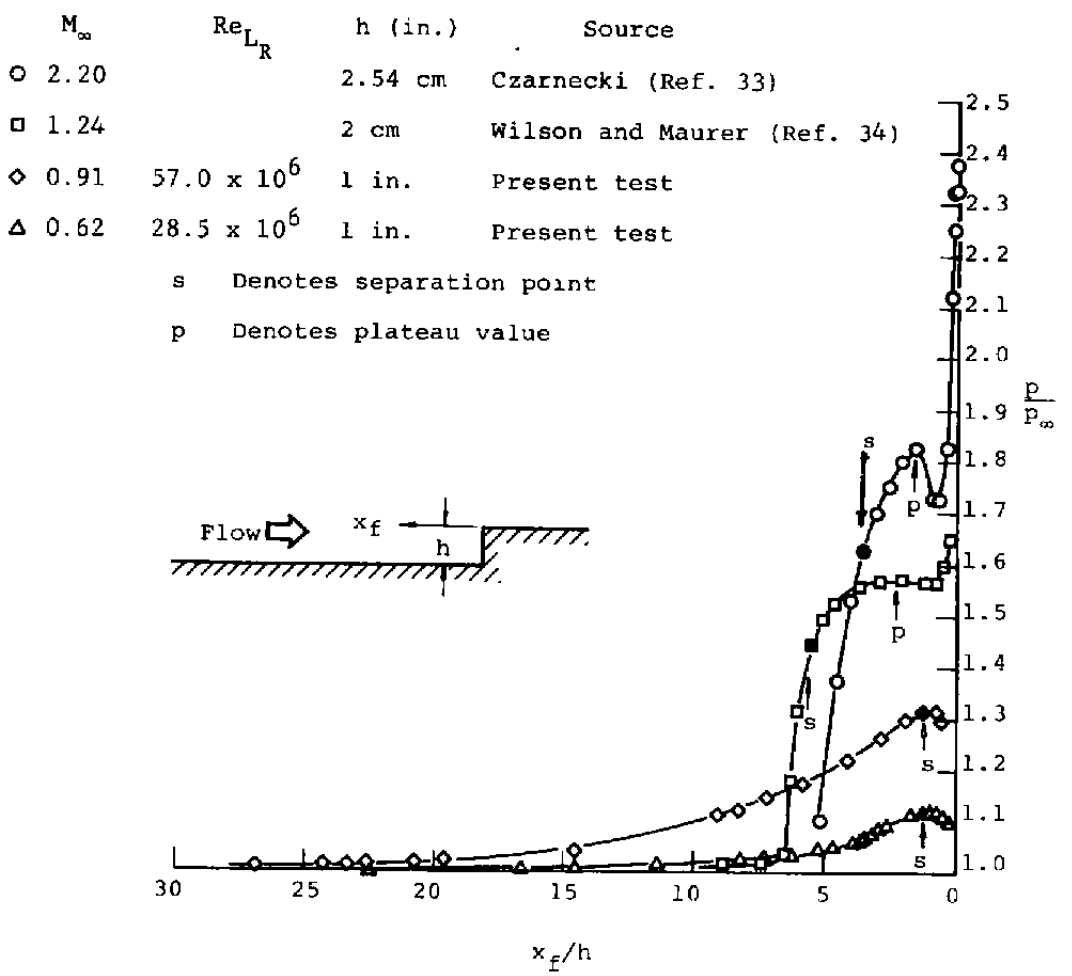

Figure 29. Comparison of pressure distributions for sub-, trans- and supersonic flow ahead of a forward-facing step.

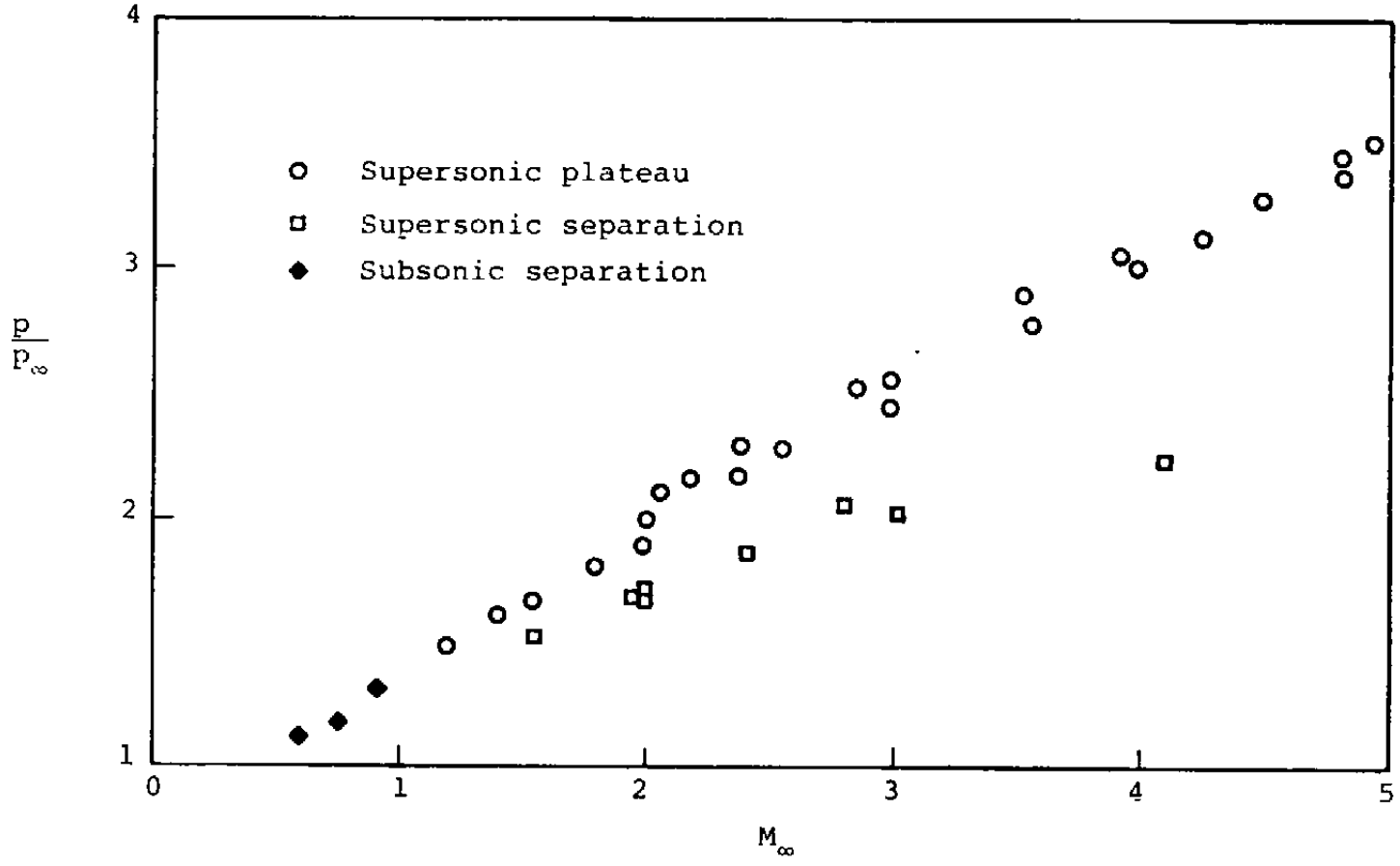

Figure 30. Effect of free-stream Mach number on the separation and plateau pressures.

4.1.2.4 Discussion of Critical Cavity Length Based on Pressure Measurements

When the fluid flows over a cavity, the flow will separate from the corner of the rearward-facing step first, and then reattach to the floor of the cavity if the length to depth ratio of the cavity is large enough. The flow then reseparates as it approaches the forward-facing step. This type of flow is called flow over a "closed" cavity. It is commonly known that two major circulating regions exist in this type of flow, in the reattaching bubble at the rearward-facing step side and in the reseparation bubble at the downstream forward-facing step side, respectively. The distance between the reattachment point and the downstream separation point in the cavity decreases as ℓ/h is decreased. As the length to depth ratio decreases to a certain value, the flow becomes unsteady--the flow will reattach to the cavity floor or jump from the rearward-facing step to the downstream forward-facing step alternately. Further decrease of ℓ/h will cause the flow to jump firmly across the rearward-facing step to the downstream forward-facing step. In such a case no reattachment point can be found on the floor, and the flow becomes steady again. This type of flow is called flow over an "open" cavity because the dividing streamline has jumped across the cavity and never reattaches to the floor.

The pressure distribution in a cavity shows some systematical change corresponding to the variation of the length to depth ratio (Figure 21). This change can be characterized by the pressure measurement at the midpoint on the floor of the cavity ($C_{p\ell/2}$). Figure 31 shows that the pressure at the midpoint of the floor increases with the initial h/ℓ increase. It reaches a maximum value and then decreases. This maximum value corresponds to the envelope value of the C_p distribution in the center portion of cavities with different length to depth ratios (Figure 21). It is found in Figure 31 that $(C_{p\ell/2})_{max}$ for a subsonic flow is

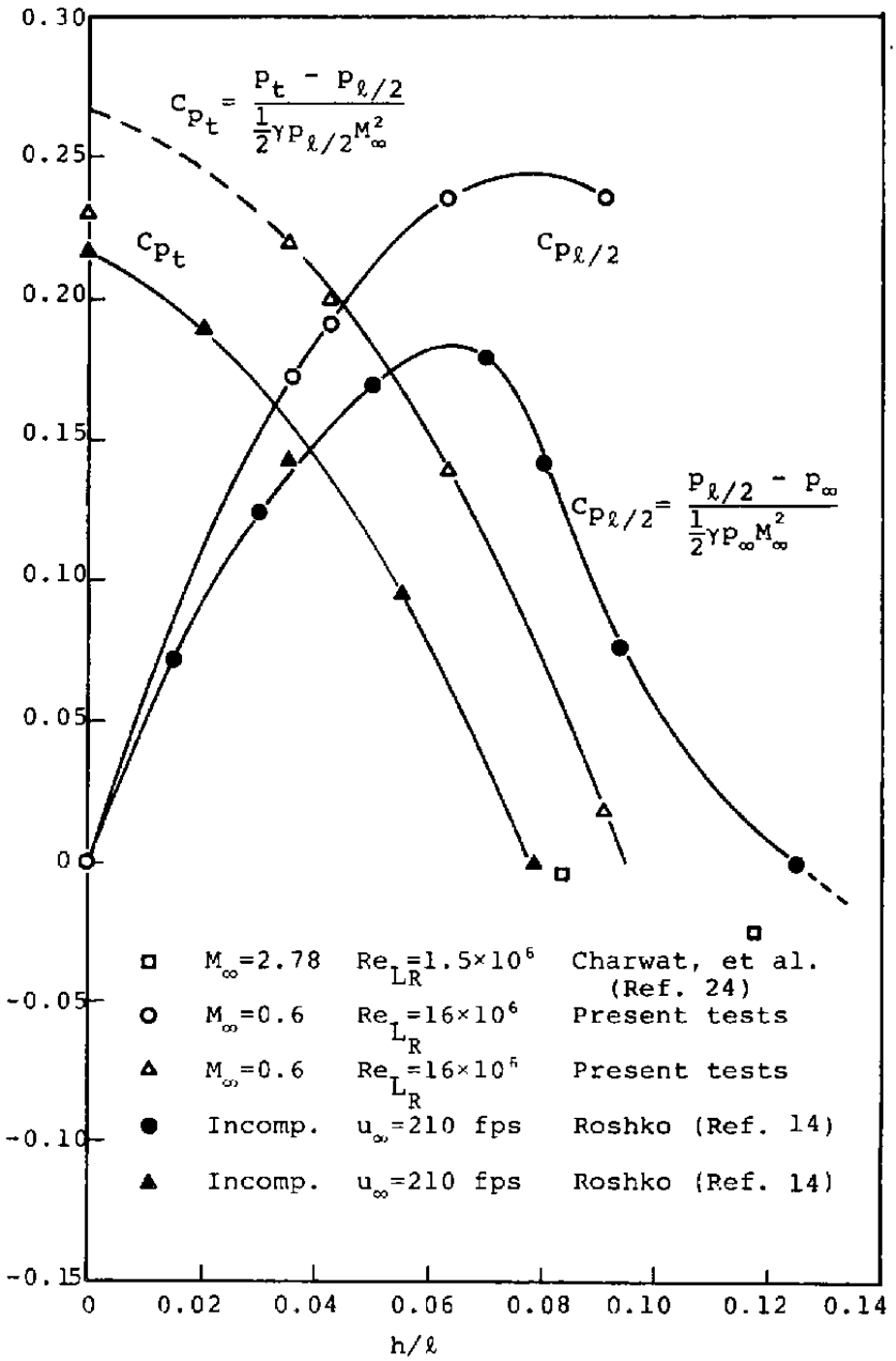

Figure 31. Effect of depth to length ratio on the pressure coefficients at the midpoint of a cavity.

higher than that of the corresponding incompressible flow case. The only $C_{p\ell/2}$ data available at the supersonic speed shows a lower value than that for the incompressible flow. Hence there is no consistent increase in this pressure as the free-stream velocity is increased through subsonic values into the supersonic range. The change of slope of $C_{p\ell/2}$ in Figure 31 from positive to negative with increasing h/ℓ must correspond to some drastic change of the flow structure in the cavity. This point of view can be verified by the total pressure measurements ($C_{p_t} \equiv (P_t - p_{\ell/2})/(\frac{1}{2}\gamma p_{\ell/2} M_\infty^2)$) with a pitot-probe placed on the floor at the midpoint of the cavity. The results show that C_{p_t} decreases with increasing h/ℓ and reaches a zero value at h/ℓ 0.095 ($\ell \approx 10.5$ in.) which is slightly larger than the value corresponding to the maximum $C_{p\ell/2}$. The zero value of C_{p_t} reveals that a separation occurs at the midpoint of the floor, which is evidence of an open cavity. Therefore, it can be concluded that the opening of the cavity will be impending when the cavity is being shortened continuously until the envelope value of the pressure distribution in the center portion of the cavity is reached.

Figure 31 shows that the subsonic flow ($M_\infty = 0.6$, $Re_{L_R} = 15.9 \times 10^6$) has a shorter critical cavity length that the incompressible flow has. Figure 26 shows that a transonic flow ($M_\infty = 0.79$, $Re_{L_R} = 29.9 \times 10^6$) over a cavity of $\ell/h = 15.75$ has the same pressure distribution along the center portion of the cavity as a subsonic flow ($M_\infty = 0.56$, $Re_{L_R} = 15.8 \times 10^6$) over a cavity of $\ell/h = 11$. This phenomenon indicates that at this transonic speed the critical cavity length might be longer than that of the subsonic flow case. But, as Mach number increases further ($M_\infty = 0.83$, $Re_{L_R} = 34.4 \times 10^6$), the critical cavity length decreases again (Figure 32). It seems that the critical cavity length will be a maximum at some particular transonic speed and

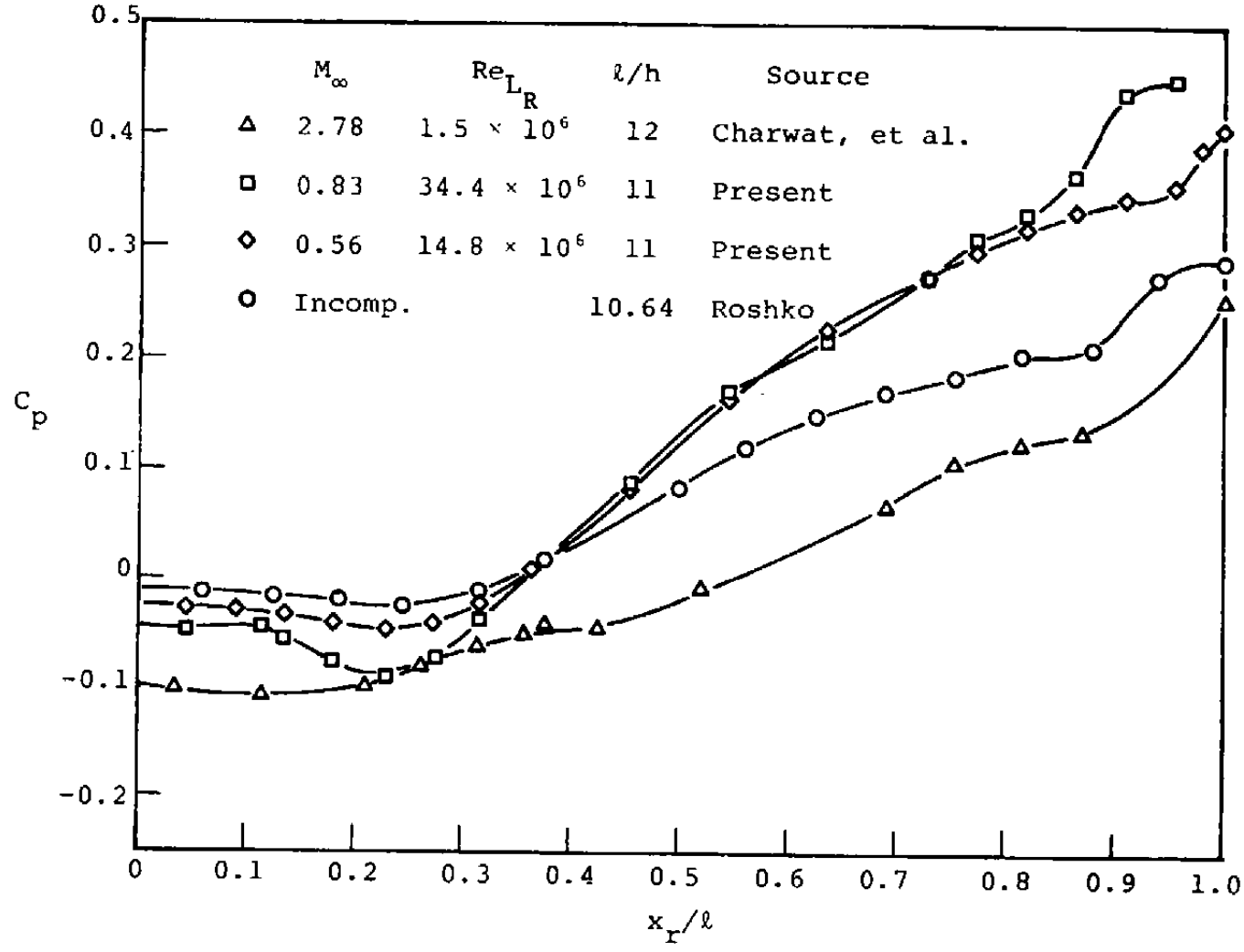

Figure 32. Effect of flow inertia energy on the pressure coefficient distribution over a shallow cavity.

further tests are needed to clarify this point. The flow might be very non-steady when the cavity flow is transferring from the closed to the open mode. Therefore, it is actually impossible to define a single value for the critical cavity length corresponding to a given flow condition. Instead, a range of critical cavity lengths would be estimated for different Mach numbers as shown schematically in Figure 33.

4.1.3 Discussion of Base Pressure

It can be found in Figure 34 that for flow over a rearward-facing step at high subsonic or transonic speeds with a separation bubble at the downstream side, the non-dimensional base pressure (p_b/p_∞) decreases linearly with an increase in the Reynolds number up to $Re_{L_R} = 30 \times 10^6$. At higher Reynolds numbers, the p_b/p_∞ versus Re_{L_R} curve keeps the same slope but shifts to a relatively higher value. Since there are only two data points ($M_\infty = 0.84$ and 0.85 respectively) in the region of $Re_{L_R} > 30 \times 10^6$ and only one data point ($M_\infty = 0.84$) in the region of $Re_{L_R} < 30 \times 10^6$, what will happen for flow speeds of $M_\infty \leq 0.8$ and $M_\infty \geq 0.84$ in the range of $Re_{L_R} > 30 \times 10^6$ and $Re_{L_R} < 30 \times 10^6$, respectively, needs to be clarified by further tests.

The same data which are shown in Figure 34 are replotted as C_{p_b} versus M_∞ in Figure 35. For flow at a Mach number less than 0.8, the pressure coefficient distribution increases slightly with Mach number at a constant total pressure. As the Mach number becomes greater than 0.8, the pressure coefficient changes very peculiarly.

Figures 36 and 37 show the influence of the downstream separation on the upstream disturbance. The non-dimensional base pressure (p_b/p or C_{p_b}) increases with h/ℓ. This means that a separation bubble downstream with a certain given strength

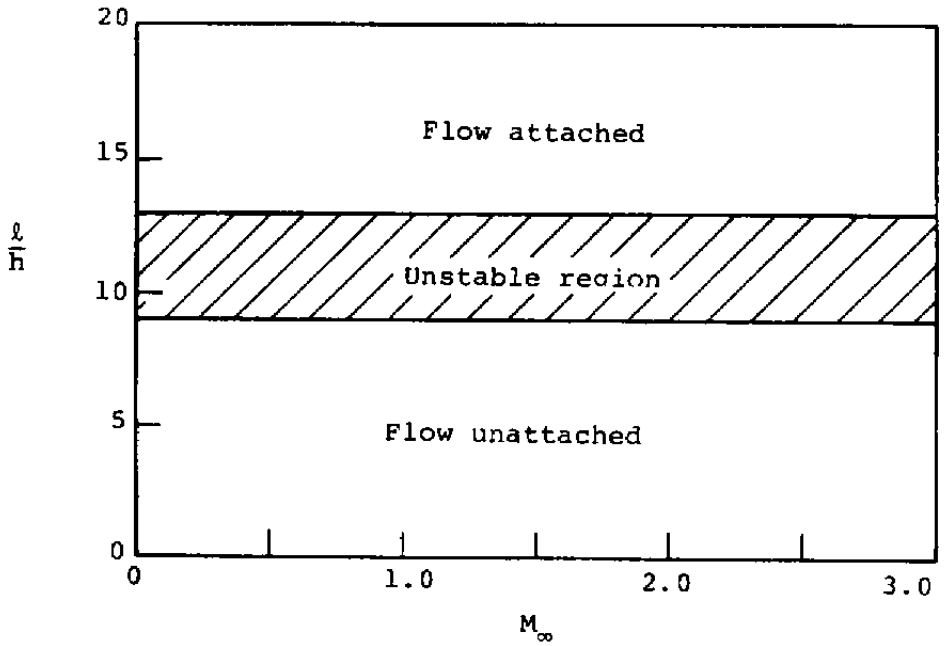

Figure 33. Nondimensional critical cavity length (schematic representation of possible result).

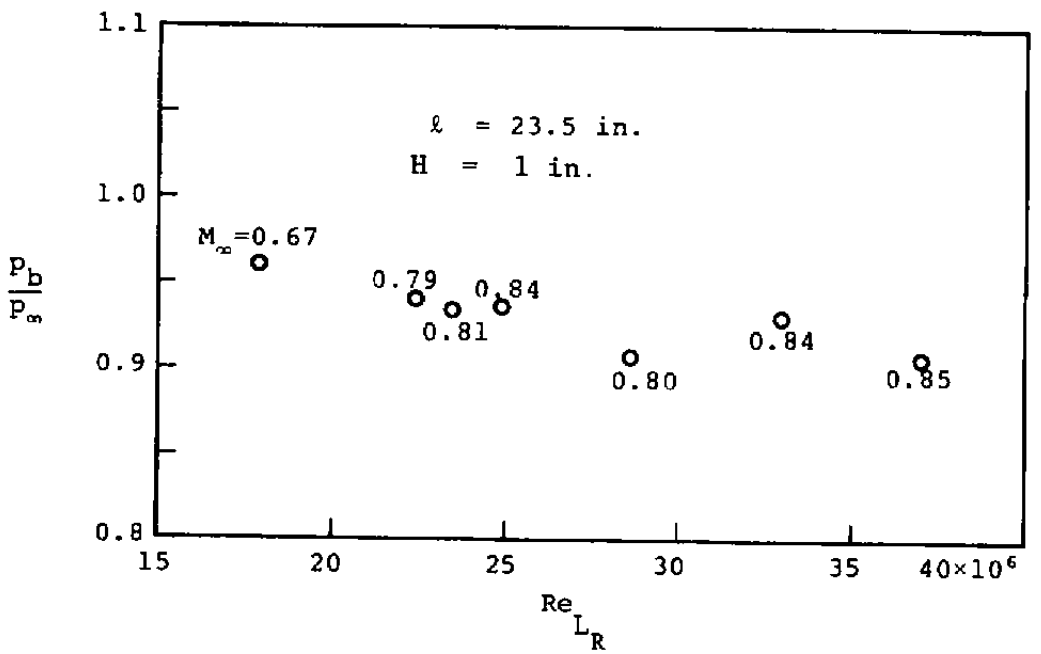

Figure 34. Effect of Reynolds number on the base to free-stream pressure ratio.

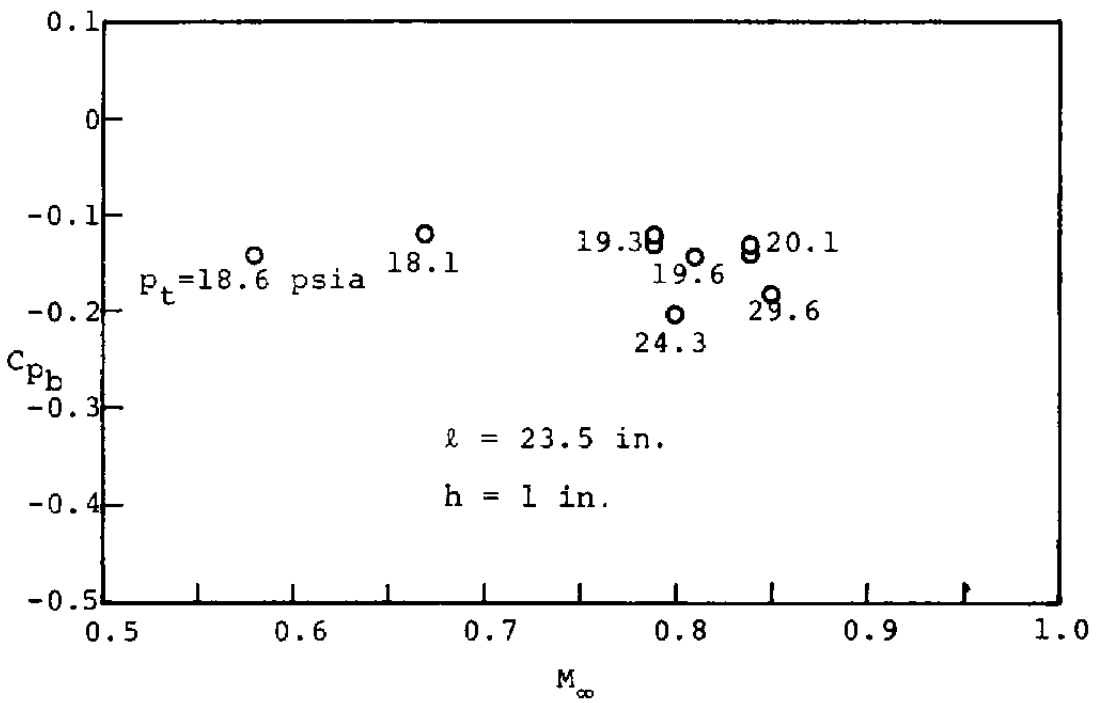

Figure 35. Effect of free-stream Mach number on the base pressure coefficient.

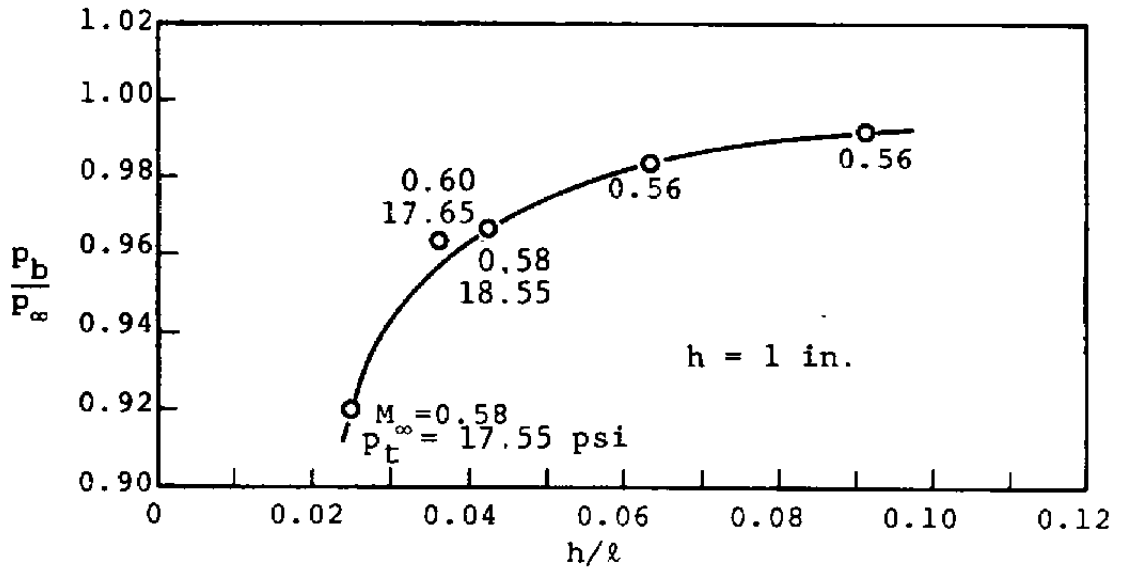

Figure 36. Effect of depth to length ratio on the base to free-stream pressure ratio.

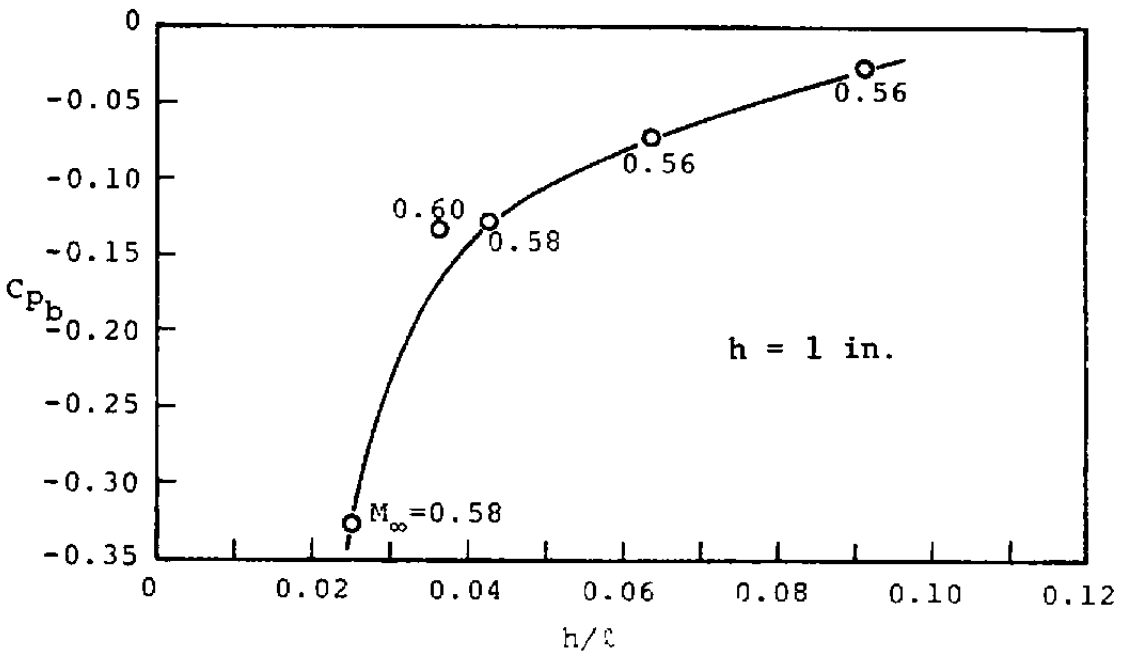

Figure 37. Effect of depth to length ratio on the base pressure coefficient.

(M_∞, Re_{L_R}, ℓ and h) will enhance the base pressure indicated at an upstream location when the separation bubble moves towards the base. As h/ℓ approaches zero, C_{p_b} will reach a negative constant or zero depending upon whether $\ell \to o$ or $h \to \dot{o}$. Whether or not the C_{p_b} verus h/ℓ curve for flow over cavities of different lengths and a fixed step height will coincide with that of different step heights and a fixed cavity length needs to be clarified by further tests.

In the discussion of the base pressure, the approaching boundary-layer thickness (δ_{L_R}) at the top corner of the rearward-facing step is usually a significant parameter. It represents the combined effect of the free-stream Mach number (M_∞), the Reynolds number (Re_{L_R}) and the historical memory of the surface roghness and other aspects of the upstream flow condition. In the present study, δ_{L_R} may also show the effect of different downstream adverse pressure gradients which are more or less severe depending on the depth and the length of the cavity. Therefore, the measurement of δ_{L_R} and a plot of p_b versus δ_{L_R} may be worthwhile in a further study.

4.1.4 Discussion of Reattachment Pressure

In the reattachment zone, the pressure recovers almost immediately in comparison with the long relaxation process of the turbulence and velocity profiles (see Section 4.3). The conditions at the reattachment point are controlled by a mass balance in the so-called dead-air region (but the velocities in this region can be quite high). To accommodate this process, the pressure rise to reattachment must be sufficient to return that quantity of mass entrained by the shear layer back to the dead-air region. The reattachment point is the point where the flow bifurcates and a new viscous sublayer starts downstream. Properties at certain points sufficiently far downstream of the

reattachment point are important for rear separation studies since all historical effects upon the boundary layer hitherto are embedded in the flow properties at this point. These properties form a new upstream boundary-layer condition for the corresponding rear separation. The reattachment pressure is the static pressure at the downstream end of the dividing streamline. The compression process will recover the base pressure to a plateau value higher than the reattachment pressure and equal to or even higher than the corresponding free-stream pressure. At supersonic speeds, the magnitude of the reattachment pressure is roughly the mean value of the corresponding base and plateau pressues, whereas at subsonic or transonic speeds, it is about 2/3 of the base pressure value. Also, as it has already been pointed out, for supersonic speeds the reattachment distance is much shorter than for the subsonic case. From these two pieces of evidence, it can be concluded that the supersonic flow has a greater ability for pressure recovery. By observation of Figure 38, it is found that the reattachment pressure increases linearly with the Reynolds number (Re_{L_R}) at a given Mach number, while at a given Reynolds number, the reattachment pressure decreases linearly with increasing Mach number (Figure 39). Figures 40 and 41 show that C_{p_r} and p_r/p_∞ increase with h/ℓ. It is also found in Figure 40 that for $h/\ell = 0.025$ ($\ell = 40$ in.) the magnitude of reattachment pressure coefficient is less than zero. Theoretically, there are two possibilities as h/ℓ approaches zero: first, if the cavity length is kept constant, the reattachment pressure coefficient will be zero as the cavity depth approaches zero. Second, if cavity depth is a constant, the reattachment pressure coefficient will approach the value corresponding to the flow over a rearward-facing step without a rear separation, where the pressure coefficient is usually less than zero, as the cavity length exceeds a certain value. Data in Figures 40 and 41 were obtained by fixing the step height at h = 1 inch and varying the

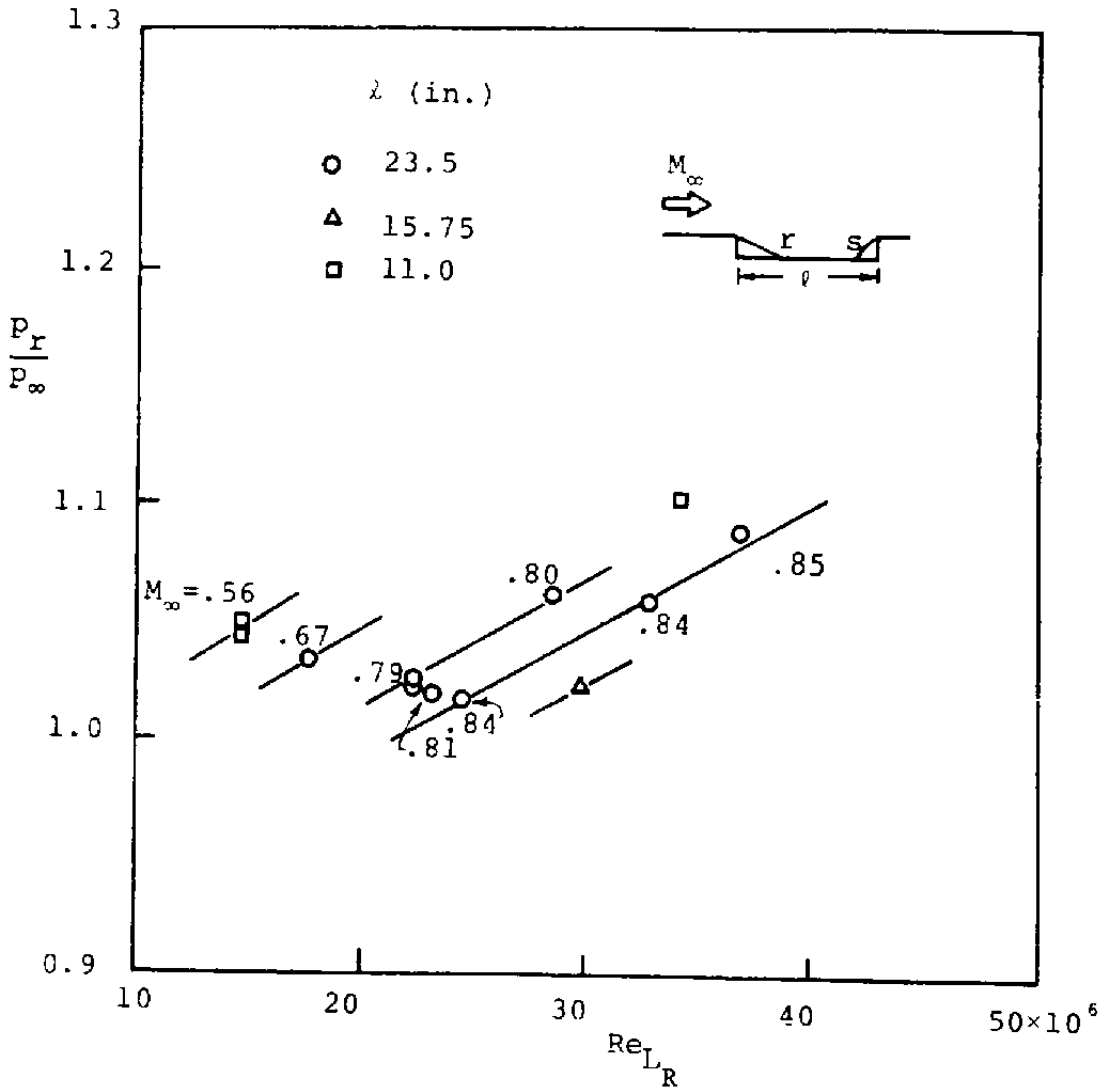

Figure 38. Effect of Reynolds number on the reattachment to free-stream pressure ratio.

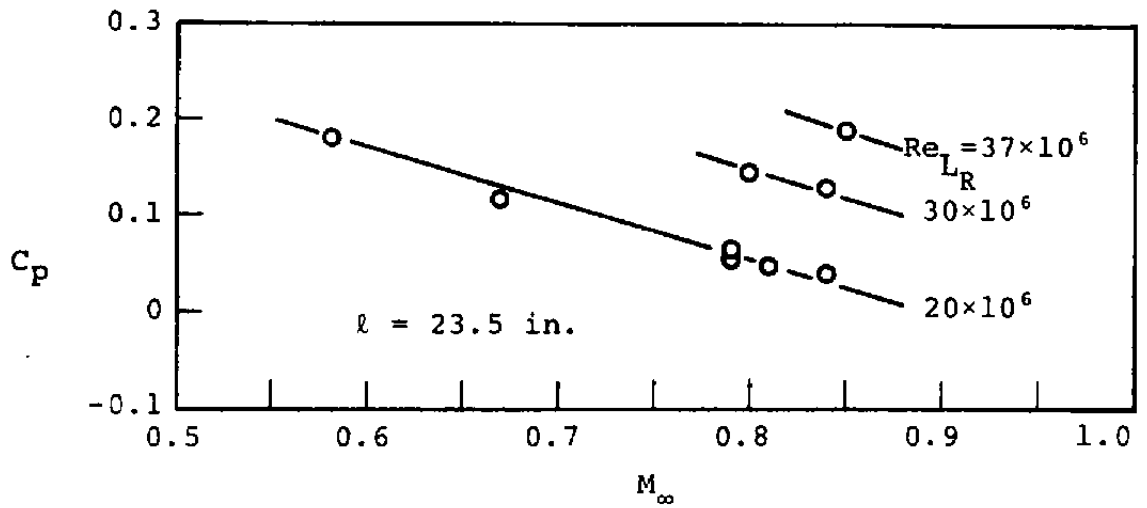

Figure 39. Effect of free-stream Mach number on the reattachment pressure coefficient.

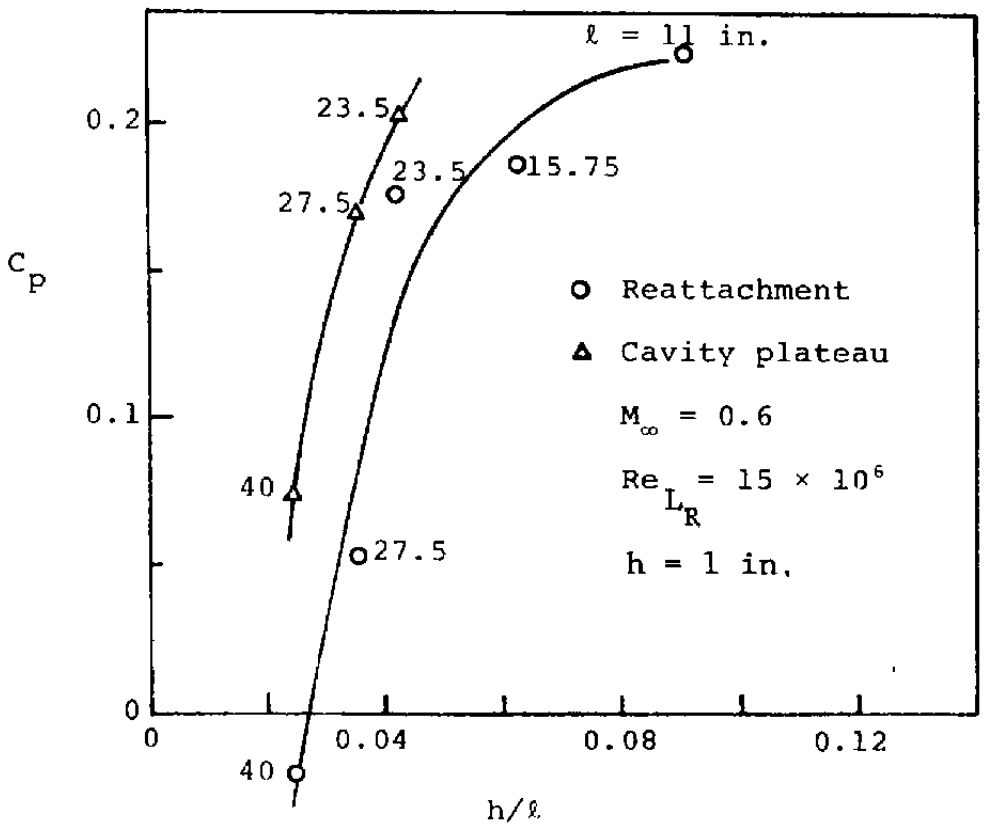

Figure 40. Effect of depth to length ratio on the reattachment and cavity-plateau pressure coefficient.

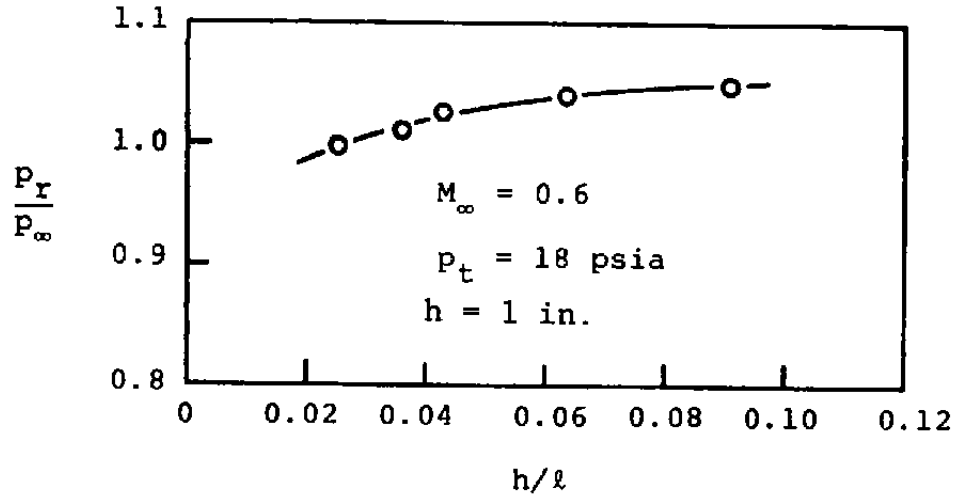

Figure 41. Effect of depth to length ratio on the reattachment to free-stream pressure ratio.

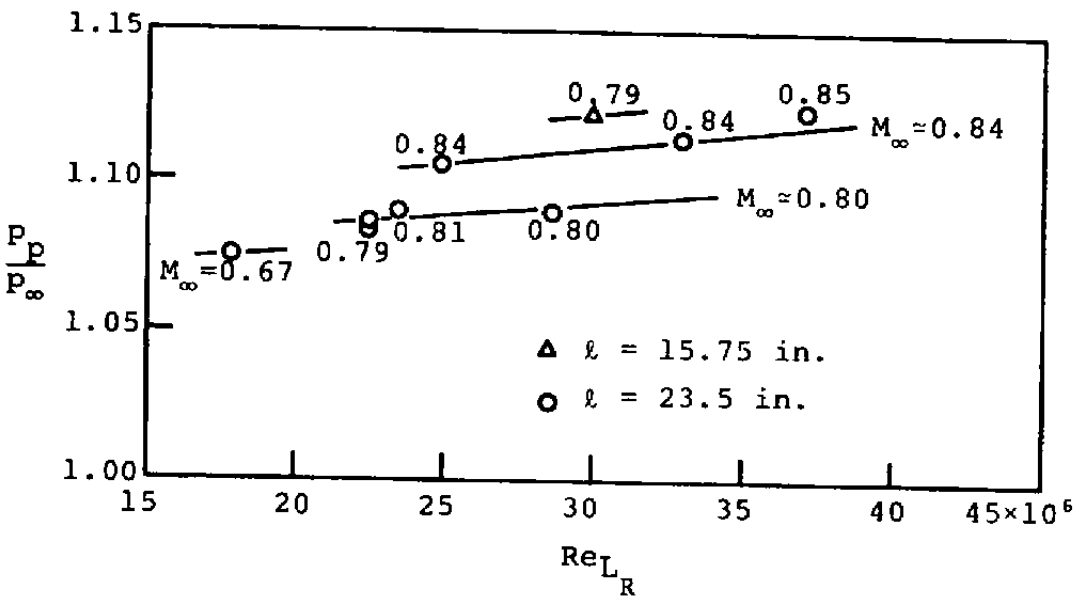

Figure 42. Effect of Reynolds number on the cavity plateau to free-stream pressure ratio.

cavity length from 11 inches to 40 inches. If the test is conducted by fixing the cavity length and varying the step height, different results may be obtained, at least in the range for which h/ℓ approaches zero.

4.1.5 Discussion of the Cavity Plateau Pressure

Cavity plateau pressure is also a function of the Reynolds number but the dependency is weak as compared with the base pressure-Reynolds number relation (Figures 34 and 42). The trend of dependence of the non-dimensional plateau pressure (p_p/p_∞) and the base pressure (p_b/p_∞) on Reynolds number are in the opposite sense. The former shows a slight increasing trend with Reynolds number whereas the latter decreases with increasing Reynolds number. The effect of Mach number upon the non-dimensional plateau pressure p_p/p_∞ is to increase p_b/p_∞ with increasing Mach number (Figure 43). Flow over a rearward-facing step can be recompressed from the base pressure to a higher plateau value by increasing either the Reynolds number (Figure 42) or the free-stream Mach number (Figure 43) or by introducing an adverse pressure gradient downstream (Figure 44). Since the magnitude of the cavity plateau pressure is larger than the free-stream pressure, the rearward-facing step performs somewhat like a vortex generator and acts to suppress the downstream separation. The efficiency of the energizing process will increase with Reynolds number, free-stream Mach number or with the depth to length ratio of the cavity. From the wake-separation interaction point of view, the rear separation will enhance the pressure recovery of the upstream wake and the enhanced cavity plateau pressure will in turn affect the downstream separation as will be explained in detail later. Whether the limiting value of p_b/p_∞ will reach a unique value or not, when either the step height approaches zero or the cavity length approaches infinity, can only be concluded by further tests.

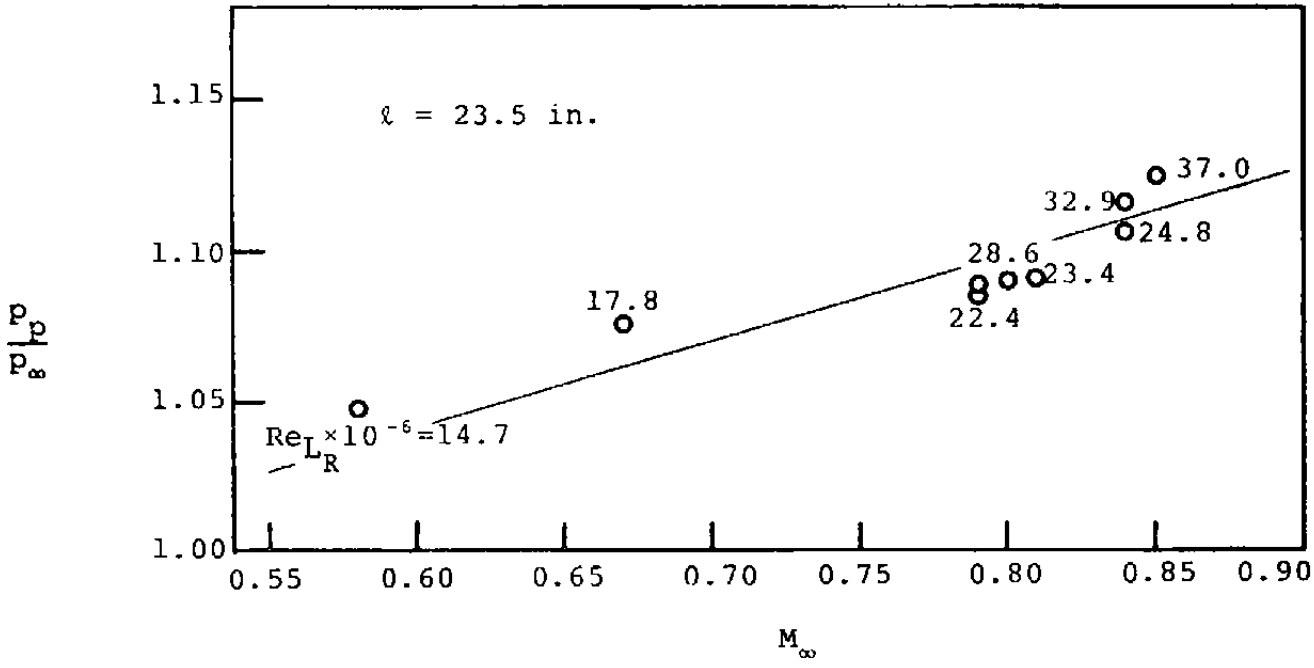

Figure 43. Effect of free-stream Mach number and Reynolds number on the cavity plateau to free-stream pressure ratio.

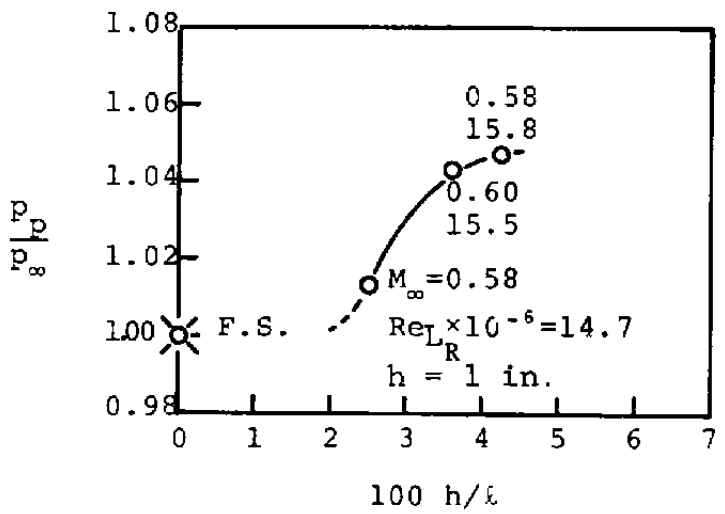

Figure 44. Effect of depth to length ratio on the plateau to free-stream pressure ratio.

4.1.6 Discussion of the Separation Pressure

Through a fairly wide survey of two-dimensional data on the pressure rise to separation in supersonic and high transonic flow, it has been reported that the separation pressure is nearly independent of Reynolds number at sufficiently large Reynolds number (Refs. 11, 12 and 13). In incompressible flow, the separation pressure coefficient was reported to be a function of Reynolds number if this is sufficiently low (Refs. 14 and 15). In the present experiments, it has been found that the non-dimensional separation pressure (p_s/p_∞) has a rather strong dependence on Reynolds number (Figure 45). It should be cautioned however that there are small variations of Mach number which accompany the changes in Reynolds number and thus make it difficult to separate clearly the exact effect of Reynolds number on separation at lower transonic and high subsonic speeds. However, Figure 45 shows clearly a trend of the non-dimensional separation pressure increasing with Reynolds number up to $Re_{L_R} \simeq 30 \times 10^6$ and this is followed by a region of near independency. This tendency is true also for cavities of different depth to length ratios.

The effect of the free-stream Mach number (M_∞) upon the non-dimensional separation pressure ratio is shown in Figure 46. It is found that p_s/p_∞ also increases with M_∞. The dispersion of data points in this figure is probably due to the effect of Reynolds number. Figure 46 also shows that the magnitude of the non-dimensional separation pressure will be higher if the flow experiences an upstream disturbance. This result is equivalent to that of the vortex generator performance of the rearward-facing step case discussed in the last subsection. The increase of the non-dimensional separation pressure ratio with free-stream Mach number for the flow approaching a forward-facing step with a natural oncoming boundary layer will follow the same trend as in supersonic flow. This result has been shown in Figure 30, as discussed previously.

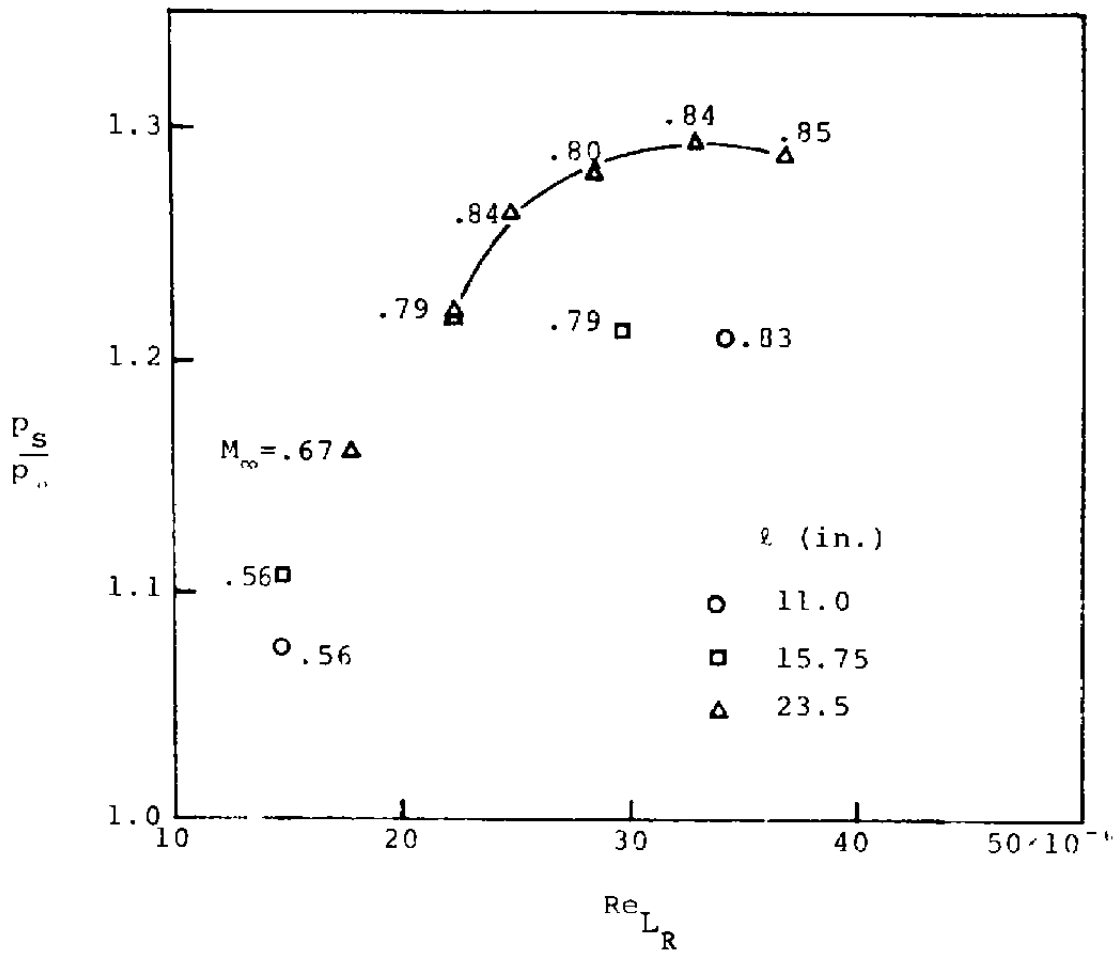

Figure 45. Effect of Reynolds number on the separation to free-stream pressure ratio.

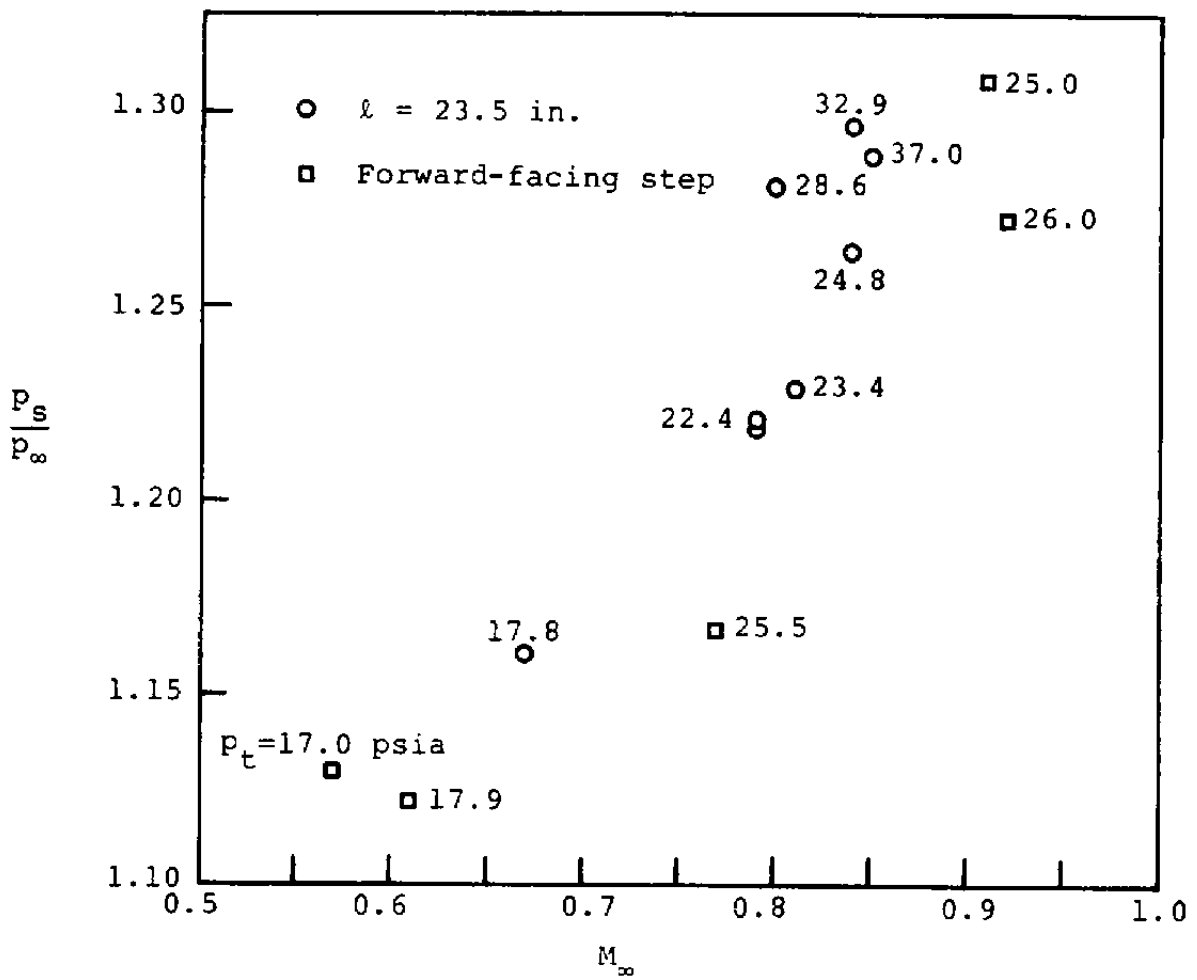

Figure 46. Effect of free-stream Mach number on the separation to free-stream pressure ratio.

Since the upstream disturbance may be initiated by numerous sources, it is sometimes more convenient to use the flow parameters at certain locations downstream of the rearward-facing step as a reference value to predict the phenomenon of the downstream separation. If the flow properties at the starting point of the cavity pressure plateau are used as the reference upstream conditions, then the smaller the magnitude of the separation-plateau pressure ratio (p_s/p_p) the more difficult it becomes for the flow downstream to separate under the same free-stream conditions. This result is shown in Figure 47 where the free-stream pressure is considered as the plateau pressure for the forward-facing step model.

The separation-plateau pressure ratio will increase monotonically with free-stream Mach number (Figure 47), but only up to $Re_{L_R} \approx 30 \times 10^6$ (Figure 48). This means that a continuous increase of free-stream Mach number can continuously enhance the ability of the flow to overcome a downstream separation. But, with respect to the Reynolds number, there exists an optimized value which can suppress the flow separation with the highest efficiency. The effect of different Reynolds numbers upon flow separation will be enhanced as the free-stream Mach number exceeds 0.8 as can be realized from examining Figures 47 and 48. Based on the results of this study, it can be stated that this conclusion holds at least for the range $0.6 < M_\infty < 0.9$ and $16 \times 10^6 < Re_{L_R} < 37 \times 10^6$.

The separation pressure to base pressure ratio (p_s/p_b) characterizes the pressure energy supplied from the external flow by the turbulent mixing process to the viscous layer during the journey of flow along the cavity. Figure 50 shows that increase of Reynolds number can increase the rate of energy supply in the range of $15 \times 10^6 \leqslant Re_{L_R} \leqslant 30 \times 10^6$. In the range of $30 \times 10^6 \leqslant Re_{L_R} \leqslant 35 \times 10^6$, the rate of energy supply is independent of the Reynolds number. That an increase of free-stream Mach

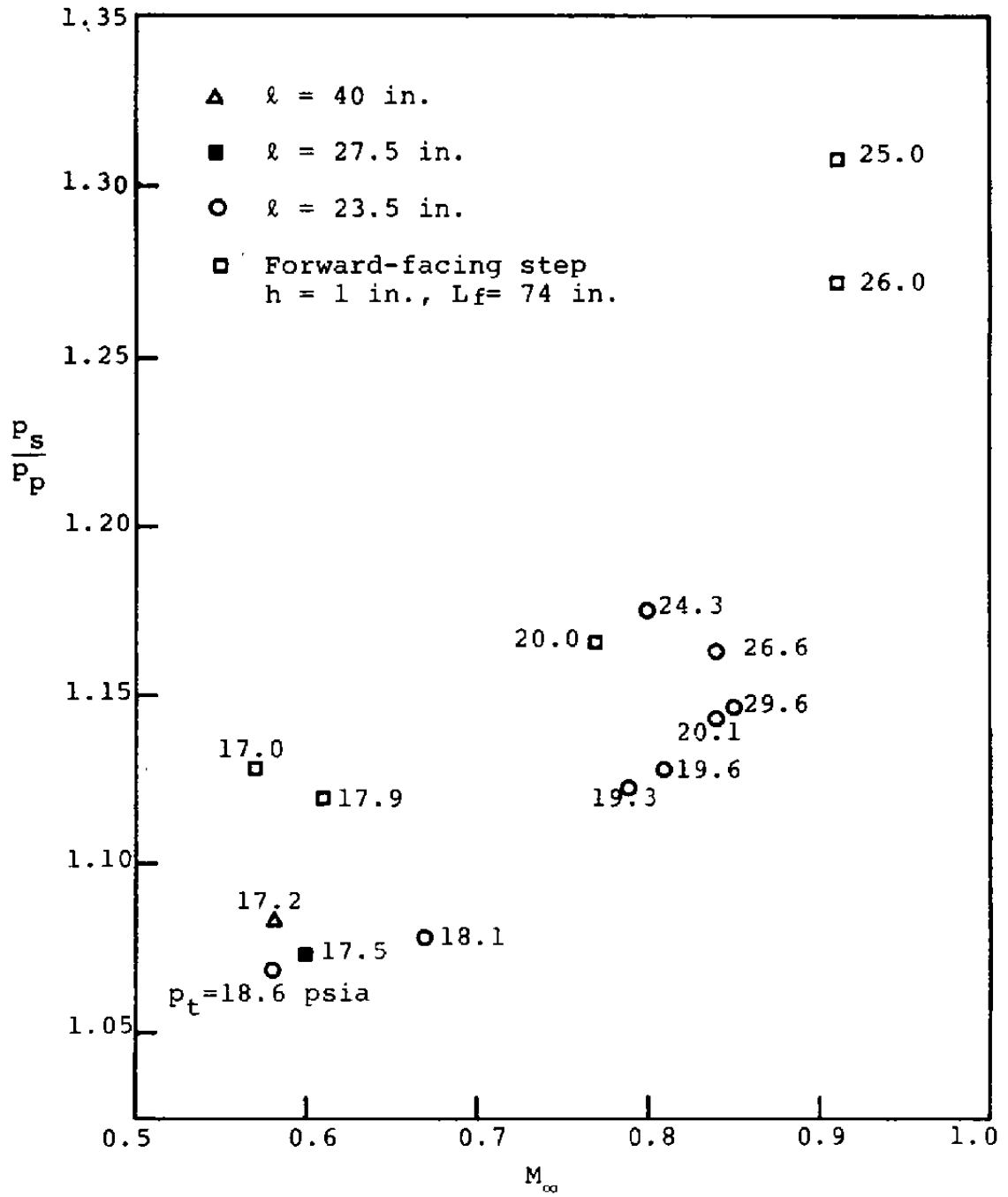

Figure 47. Effect of free-stream Mach number on the separation to plateau pressure ratio.

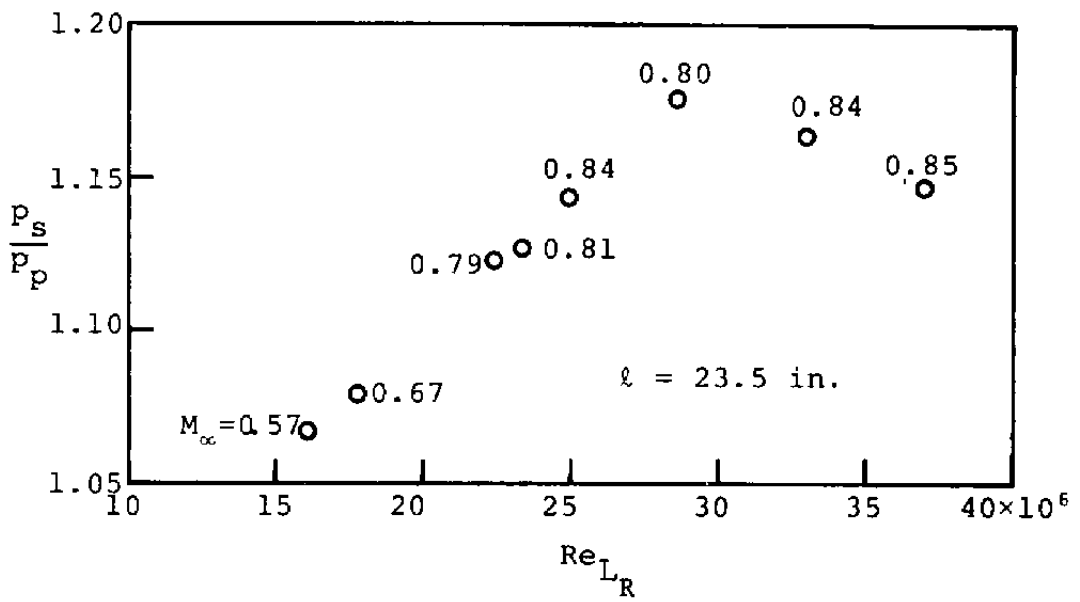

Figure 48. Effect of Reynolds number on the separation to plateau pressure ratio.

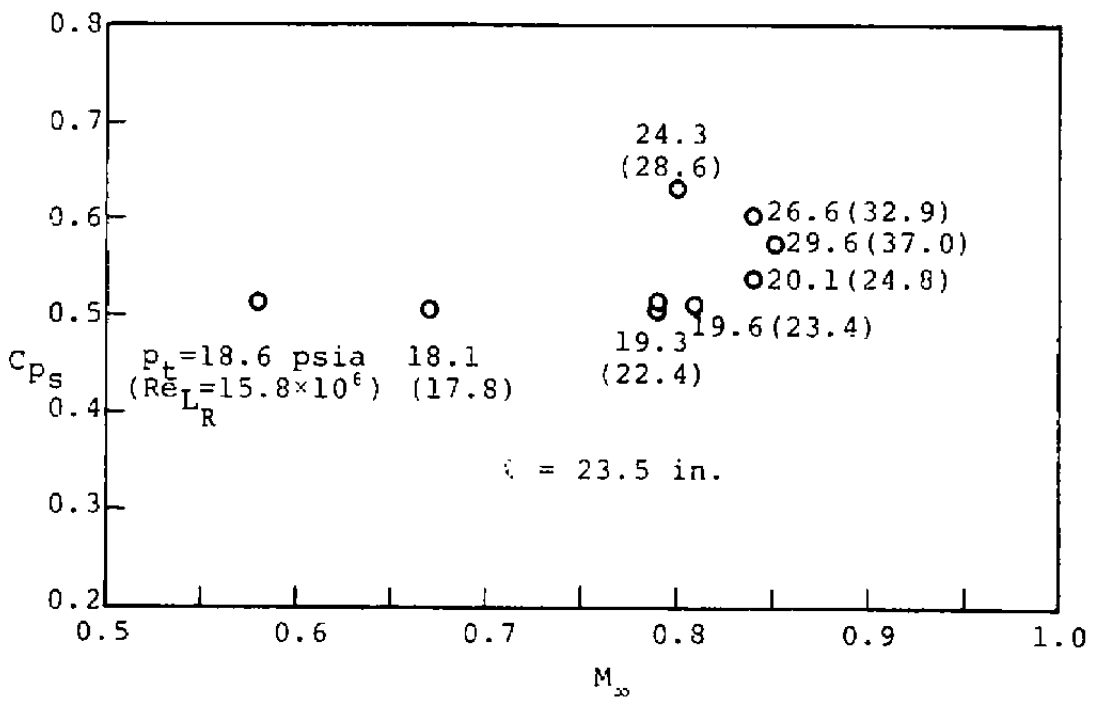

Figure 49. Effect of free-stream Mach number on the separation pressure coefficient.

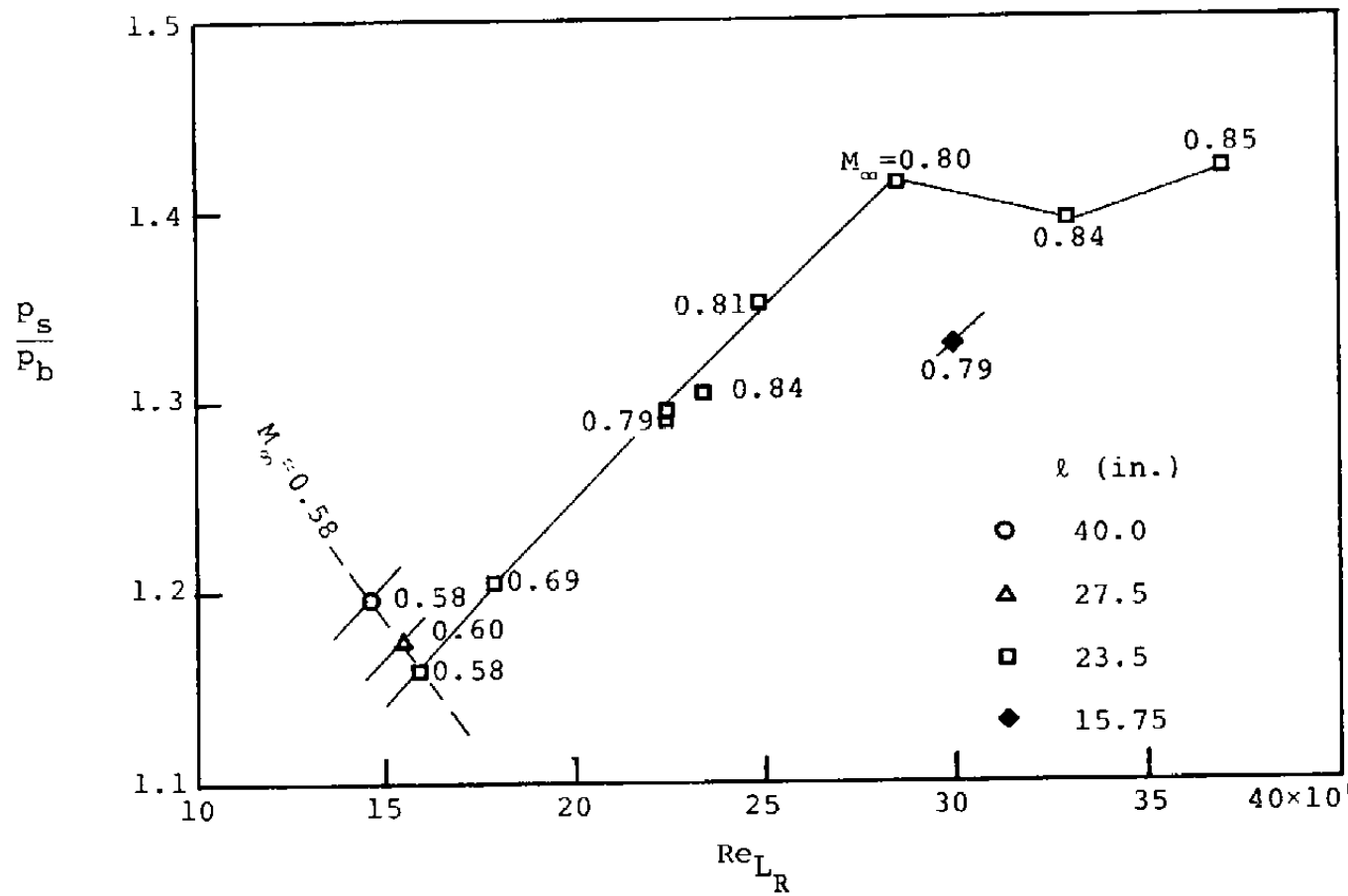

Figure 50. Effect of Reynolds number on the separation to base pressure ratio.

number can increase the rate of energy supply is shown in Figure 51. From this figure, it can be found again that the Reynolds number effect is enhanced as the free-stream Mach number exceeds 0.8.

The depth to length ratio of the cavity is another parameter which will affect the wake-separation process for flow over a cavity-like model. From Figures 52 and 53, it can be realized that, as far as the rear separation is concerned, there exists an optimized depth to length ratio for the flow over a shallow-cavity model at a given Mach number and Reynolds number. Usually, for flow over a discontinuity on the boundary, there will be some energy loss which may reduce the peak pressure ahead of the downstream step to a degree lower than that of the flow approaching a forward-facing step without the upstream disturbance. But an upstream disturbance, if located at some proper distance ahead of the rear separation, can act as a vortex generator to energize the viscous layer. With this in mind, it can be understood how the rear separation can occur at a higher pressure condition (Figure 53). For the flow at a Mach number of 0.6 and a Reynolds number at 15×10^6, the optimized depth to length ratio (h/ℓ) is about 0.025 (corresponding to ℓ = 23.5 in.). It has been pointed out earlier that the flow will become unsteady and the cavity is ready to open if the depth to length ratio is less than 0.0634 (ℓ = 15.75 in.). Therefore, in this case the optimized depth to length ratio of the cavity is one-third larger than the critical depth to length ratio under the same free-stream conditions. That a disturbed flow can sometimes have a peak pressure higher than the undisturbed flow can be explained as follows: as it turns over the rearward-facing step, the flow speed increases drastically and this is accompanied by a large pressure drop and the flow becomes highly turbulent. Due to this high turbulent mixing phenomenon, the energy of the external flow is pumped into the boundary layer at a very high rate. The surface pressure in the reattachment region then recovers from the base

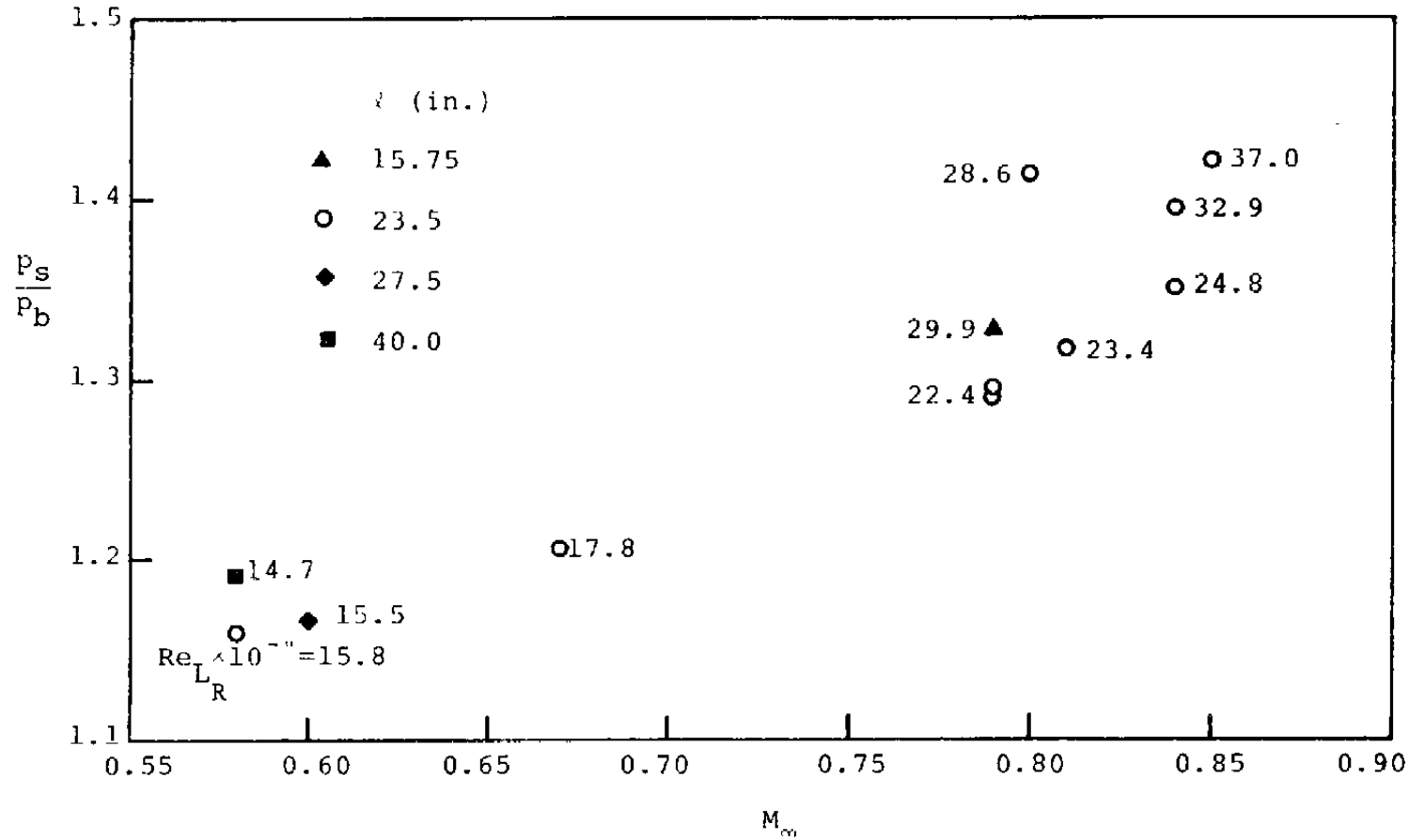

Figure 51. Effect of free-stream Mach number on the separation to base pressure ratio.

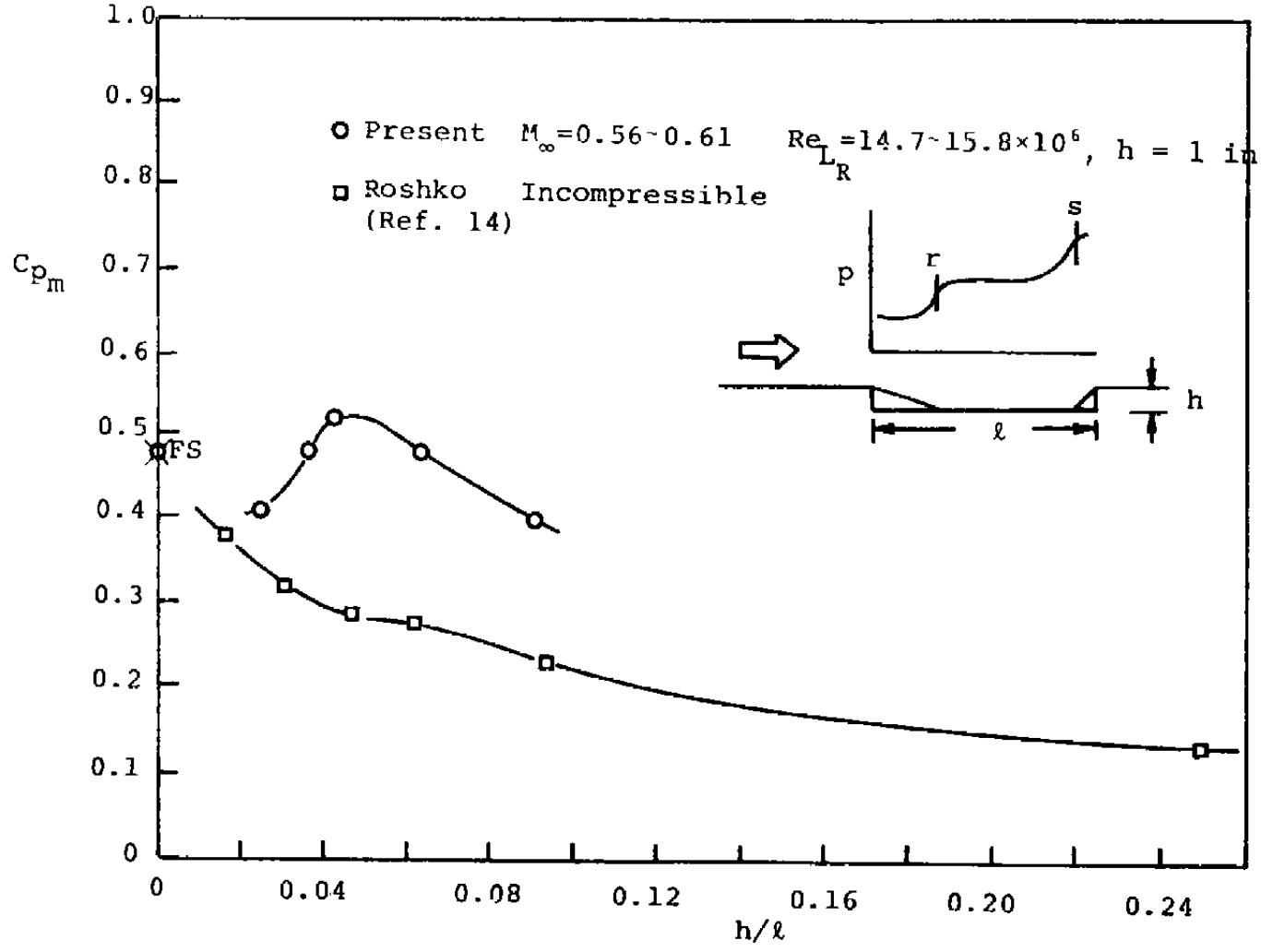

Figure 52. Effect of depth to length ratio on the peak pressure coefficient.

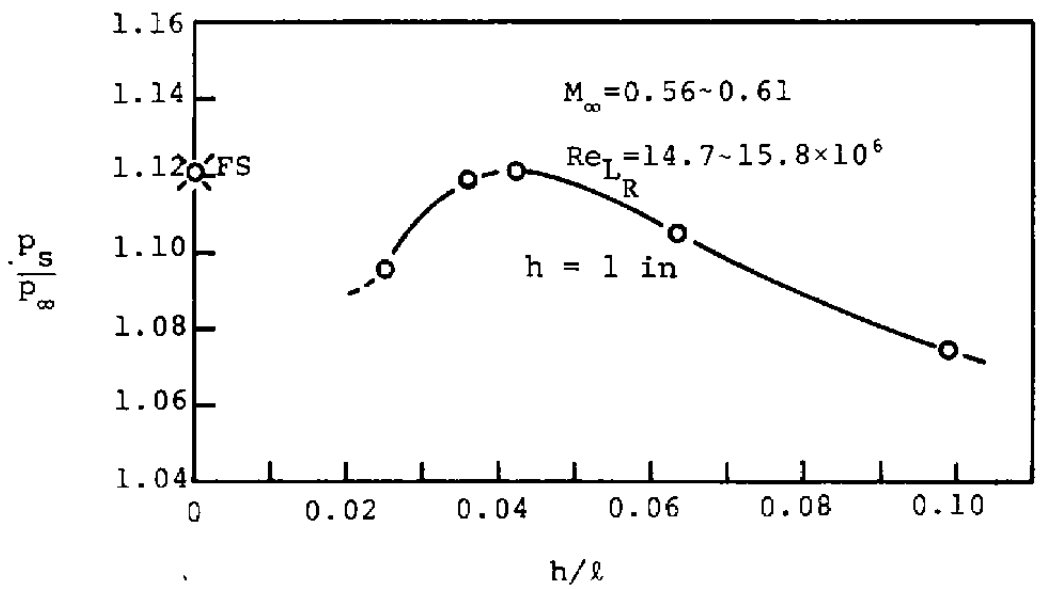

Figure 53. Effect of depth to length ratio on the separation to free-stream pressure ratio.

pressure to the plateau pressure with a very steep gradient. The plateau pressure always attains a level higher than that of the free-stream pressure. In addition to this high pressure level, there is a continuous inflow of high energy fluid from the external region at a rate higher than that of an equilibrium flow. This results in the total energy of the boundary layer in the region slightly downstream from the start of the cavity pressure plateau being higher than that of the corresponding flow approaching the downstream step in the absence of the upstream disturbance. Therefore, the disturbed flow can overcome the downstream separation easier than the undisturbed flow, if the forward-facing step is located immediately downstream of this region. Downstream from this region, the rate of energy inflow slows down due to the decrease of the turbulence level. The shear layer velocity profile recovers continuously by absorbing the energy from the inflow of fluid, but the loss due to viscous dissipation remains. Therefore, the net inflow of energy which can benefit the surface pressure becomes negative. As the flow moves further downstream to a certain distance, the magnitude of the surface pressure may be lower than that for a flow without the upstream disturbance. Therefore, for a cavity of that length or longer, the peak pressure ahead of the downstream step will be lower than that of the undisturbed flow approaching a forward-facing step. On the other hand, if the cavity is too short, the quantity of the incoming energy from the external region will not be enough to raise the energy in the viscous layer to a level higher than that of the flow without an upstream disturbance during the limited journey of the flow in the cavity. So, the peak pressure ahead of the downstream step will also be smaller than that for a flow without the upstream disturbance. Only when the depth to length ratio is within a proper range does the boundary-layer flow have more ability to overcome the downstream separation than does the flow approaching

a forward-facing step with an undisturbed natural boundary layer upstream.

4.2 CORRELATION OF THE SEPARATION PRESSURE

A purely empirical equation for the prediction of the separation pressure ahead of a forward-facing step with an upstream disturbance has been established as follows:

$$\left(\frac{Re_{L_R} \times 10^{-6}}{M_\infty}\right)^{1/4} \frac{p_s}{p_t} = 2 \qquad (4.3)$$

This equation is plotted in Figure 54. It shows good agreement with the experimental results. The maximum error is about 2.5 percent and occurred at the depth to length ratio $h/\ell = 0.0425$ ($\ell = 23.5$ in.). This is the ratio which results in the maximum separation pressure for a given flow condition (see Figure 53). By fixing attention on the data points of flow at $M_\infty \approx 0.6$ and $Re_{L_R} \approx 15 \times 10^6$, it can be found that the trace of deviation of the data points from the empirical equation has the same trend as that shown in Figures 52 and 53. Therefore, it can be reasonably concluded that the error of this equation is mostly due to the neglect of the depth to length ratio which is another parameter that can affect the separation pressure as pointed out in the last subsection.

4.3 TURBULENT MEAN-VELOCITY MEASUREMENTS

4.3.1 Mean Velocity Profiles

The total pressure distribution across the shear layer and the corresponding static pressure were used to yield the Mach number and the velocity distribution at different stations along models. The following equations were used,

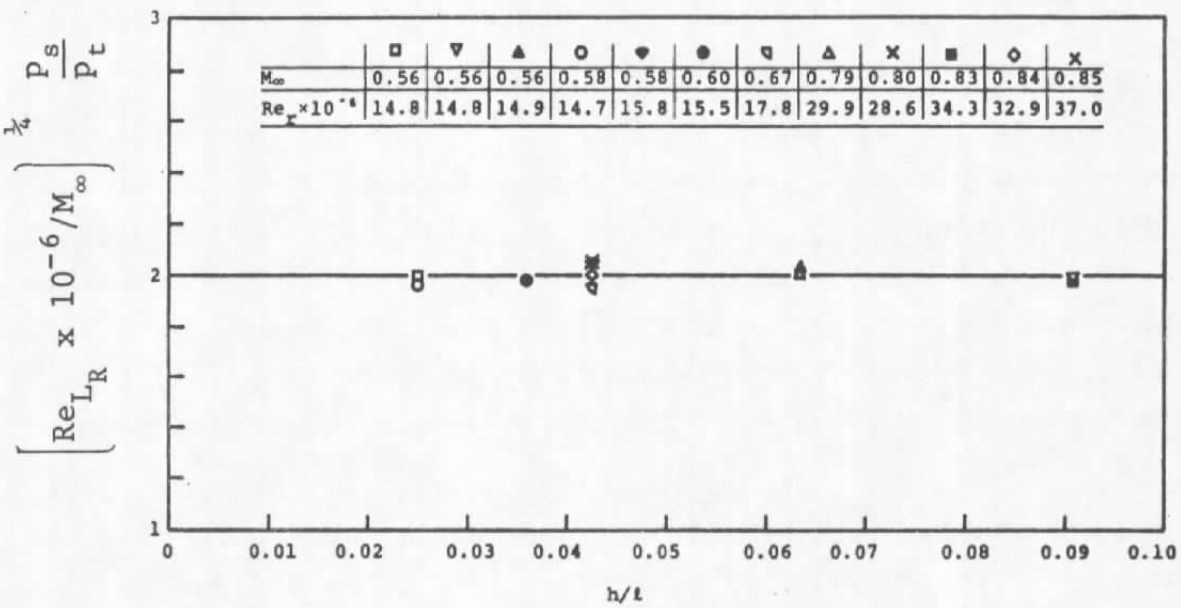

Figure 54. Separation pressure correlation.

$$M = \left\{ \frac{5}{3} \left[\left(\frac{p}{p_t} \right)^{-2/7} - 1 \right] \right\}^{1/2} \tag{4.4}$$

and,

$$\frac{u}{u_\infty} = \frac{M}{M_\infty} \left(\frac{1 + 0.2\ r\ M_\infty^2}{1 + 0.2\ r\ M^2} \right)^{1/2} \tag{4.5}$$

where r is the recovery factor which was assumed to be related to the Prandtl number by the relation

$$r = (Pr)^{1/3}$$

In this experiment emphasis was placed on the study of the wake-separation interaction phenomenon instead of the vortex-mechanics, as was done in most of the published literature. After extensive testing on different depth to length ratio cavities, it was found that cavities which have a depth to length ratio of 0.0425 to 0.0250 (corresponding to ℓ = 23.5 and 50 inches for h = 1 inch) are the most suitable geometries for the present study. These cavities revealed the most information on the wake-separation interaction phenomenon. They are long enough to avoid the dividing streamline jumping across the entire upstream wake and the downstream separation. Therefore, in this second phase of the study, cavities of 40-, 27.5- and 23.5-inches long with a 1-inch depth were used as the principal models. The stations for the velocity profile measurement were closely spaced along these models. Two shorter cavities (h/ℓ = 0.0909 and 0.0634, correspondong to ℓ = 11 and 15.75 inches) were also used to study the feature of cavity flow under the situation when the dividing streaming was about to jump across the cavity. Only at one or two stations were velocity profiles measured for these short cavities.

Mach number versus a vertical distance y is plotted in Figures 55 through 61. The continuous variation of Mach number along the flat plate, the forward-facing step, the 40-, 27.5- and 23.5-inch long cavity models is shown in Figures 62 through 66, respectively. At the reattachment points, velocity profile was about three inches upstream of the separation point. At this station $(\partial M/\partial y)_w \neq 0$ was expected. A special feature of the velocity profile, near the step-induced separation point, needs attention. The profile is slightly different from that of a natural separation by a uniform adverse pressure gradient (in the flow direction). The velocity profile, close to a step-induced separation point, shows an abnormally thin portion (velocity defect) roughly at one step height from the wall surface. This is due to the non-uniformity in traverse static pressure variation. For incompressible and supersonic flow, the static pressure distribution ahead of the step increases upward from the wall and reaches a maximum at roughly $y/h \approx 1$ (Refs. 16 and 17). In transonic and subsonic flow, this phenomenon is also expected. Along the middle portion of the cavity, the velocity profile continuously becomes fuller downstream from the reattachment point and starts to thin again (u/u_∞ decreases for a given y/δ) when it is near the downstream separation point. The recovery and the decay of these velocity profile changes are rather gradual as compared with the pressure variation along the model surface.

The dimensionless velocity profiles (u/u_∞), at the middle station between the reattachment point and the separation point, for flow over different cavity models with depth to length ratios $h/\ell = 0.0909$, 0.0634, 0.0425 and 0.0360 (i.e., ℓ = 11, 15.75, 23.5 and 27.75 inches) are plotted against y/δ in Figure 67. The velocity profile for flow over a flat plate at the station 61 (indicating the distance measured from the leading edge in inches) is also shown in Figure 67 for comparison. Data for a cavity of $h/\ell = 0.0909$ (ℓ = 11 in.) have shown some dispersion

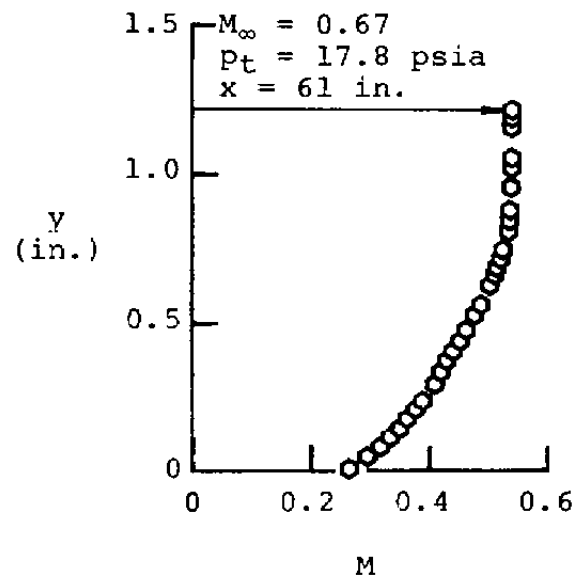

Figure 55. Velocity profile on the flat-plate model.

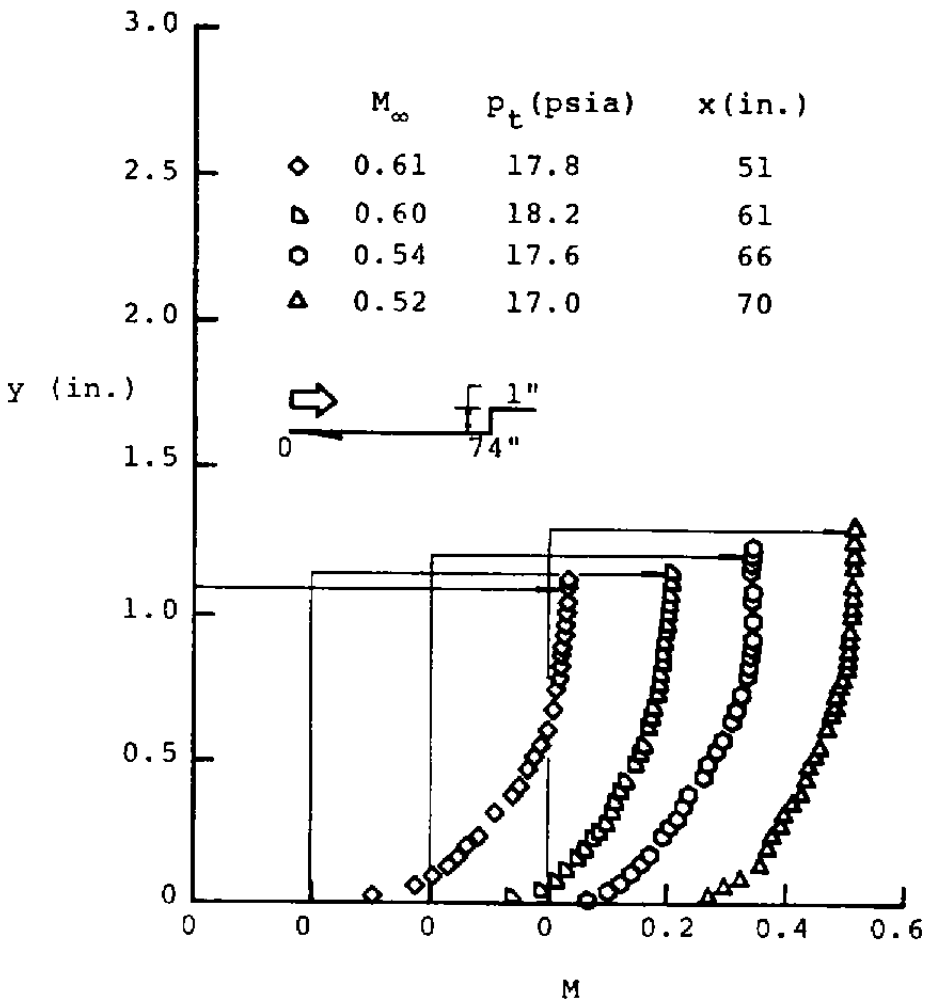

Figure 56. Velocity profiles on the forward-facing step model.

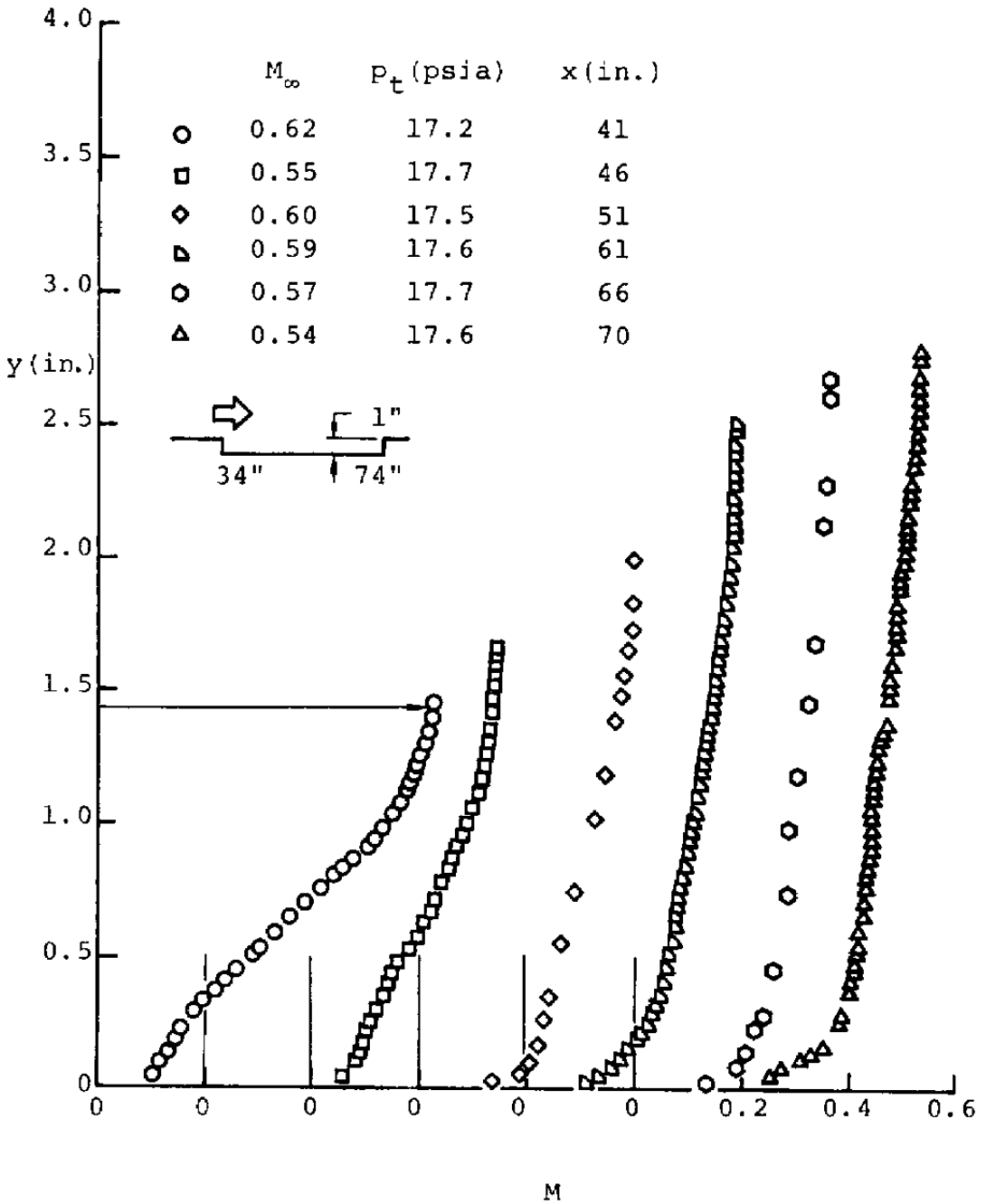

Figure 57. Velocity profiles on the 40-inch shallow-cavity model.

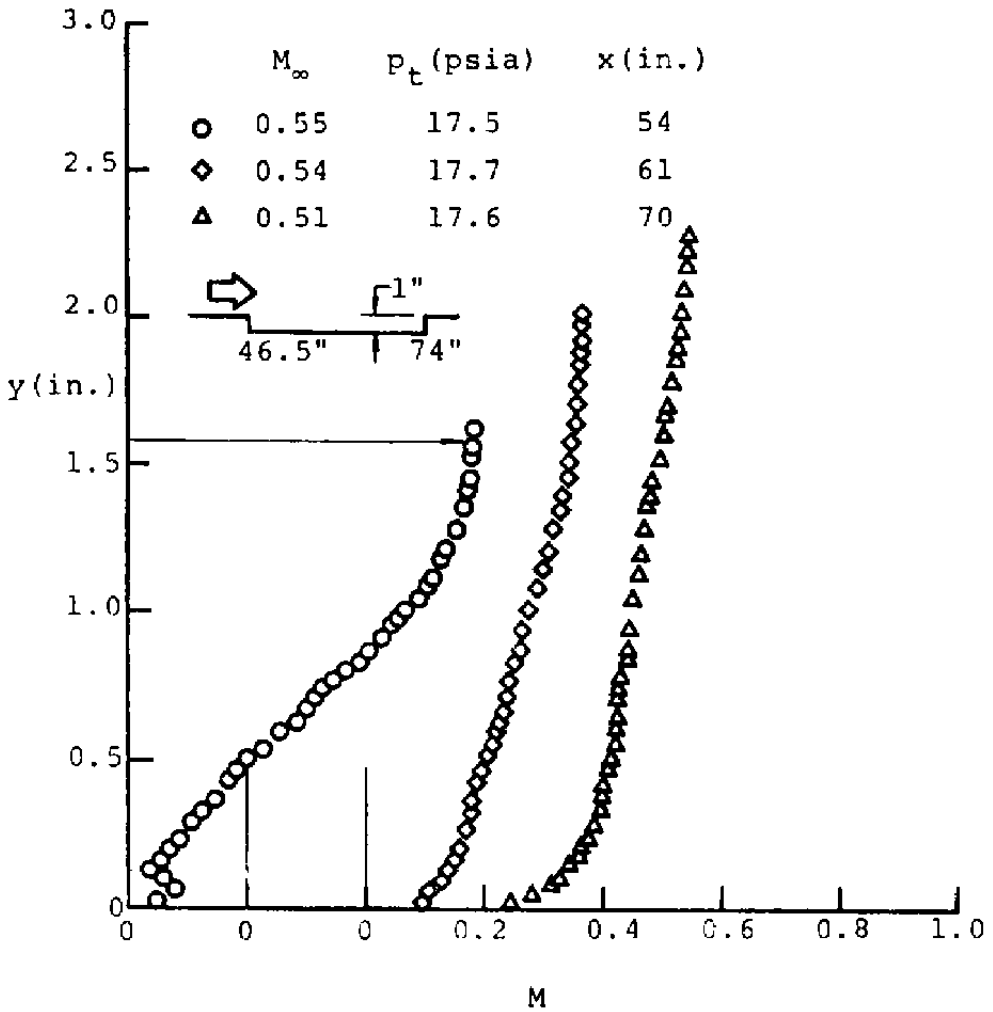

Figure 58. Velocity profiles on the 27.5-inch shallow-cavity model.

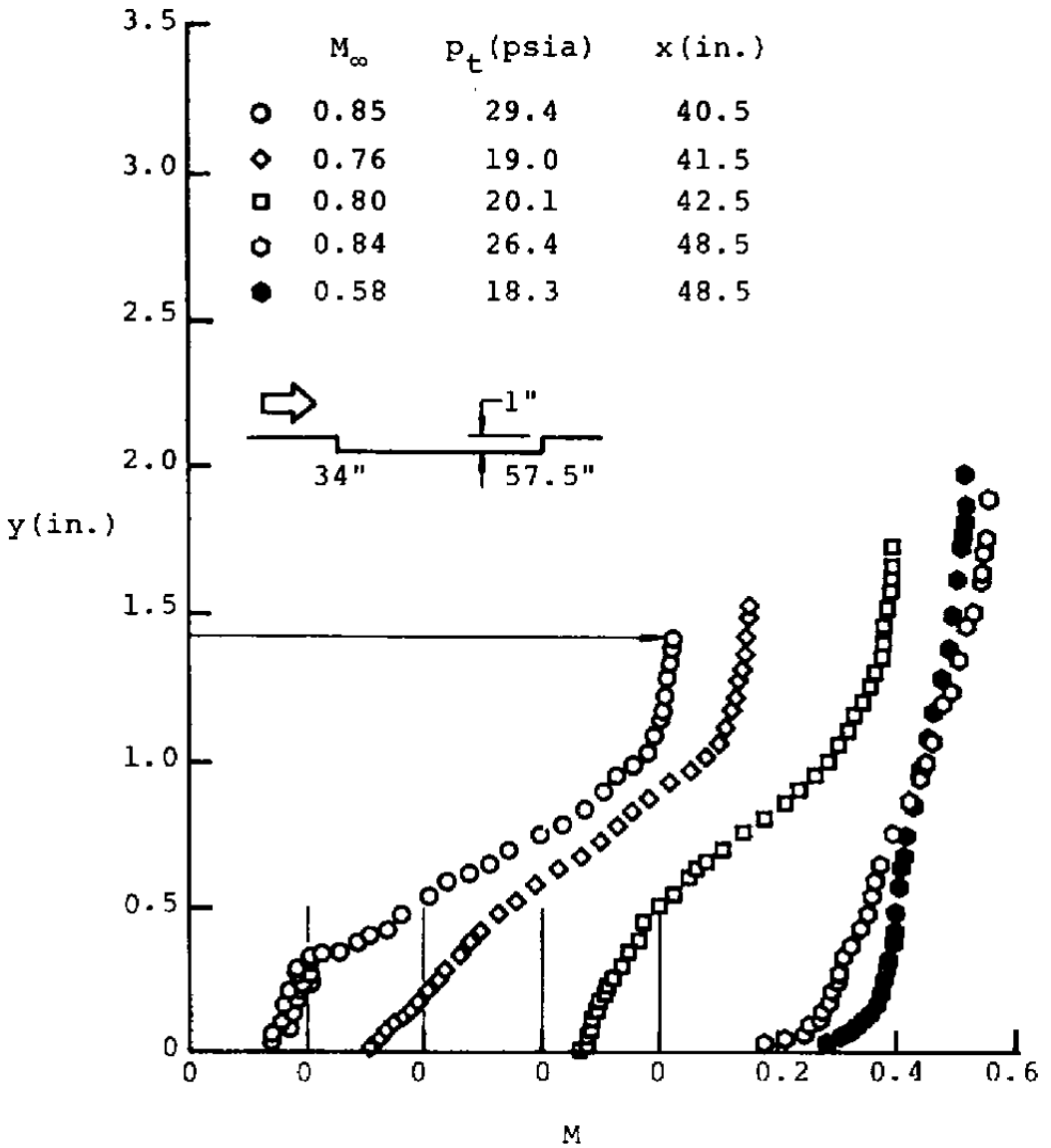

Figure 59. Velocity profiles on the 23.5-inch shallow-cavity model.

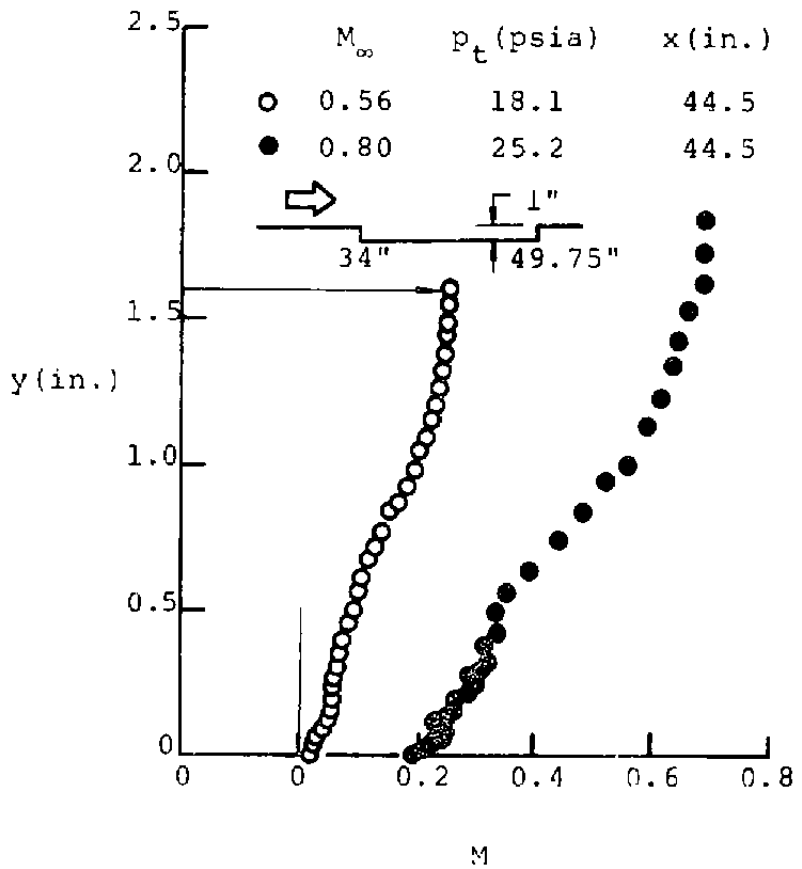

Figure 60. Velocity profile on the 15.75-inch shallow-cavity model.

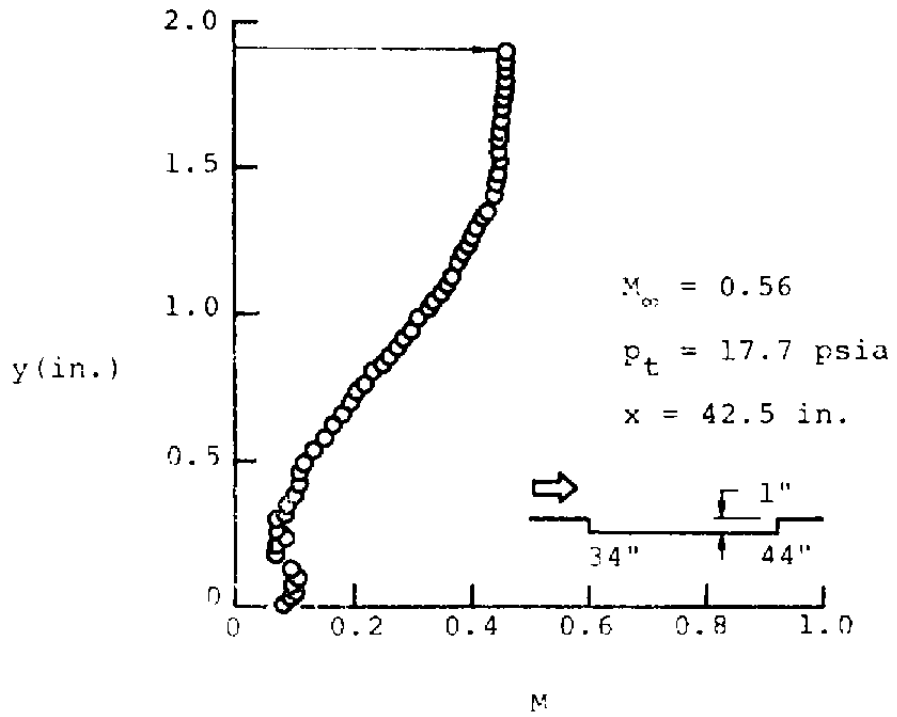

Figure 61. Velocity profile on the 11-inch shallow-cavity model.

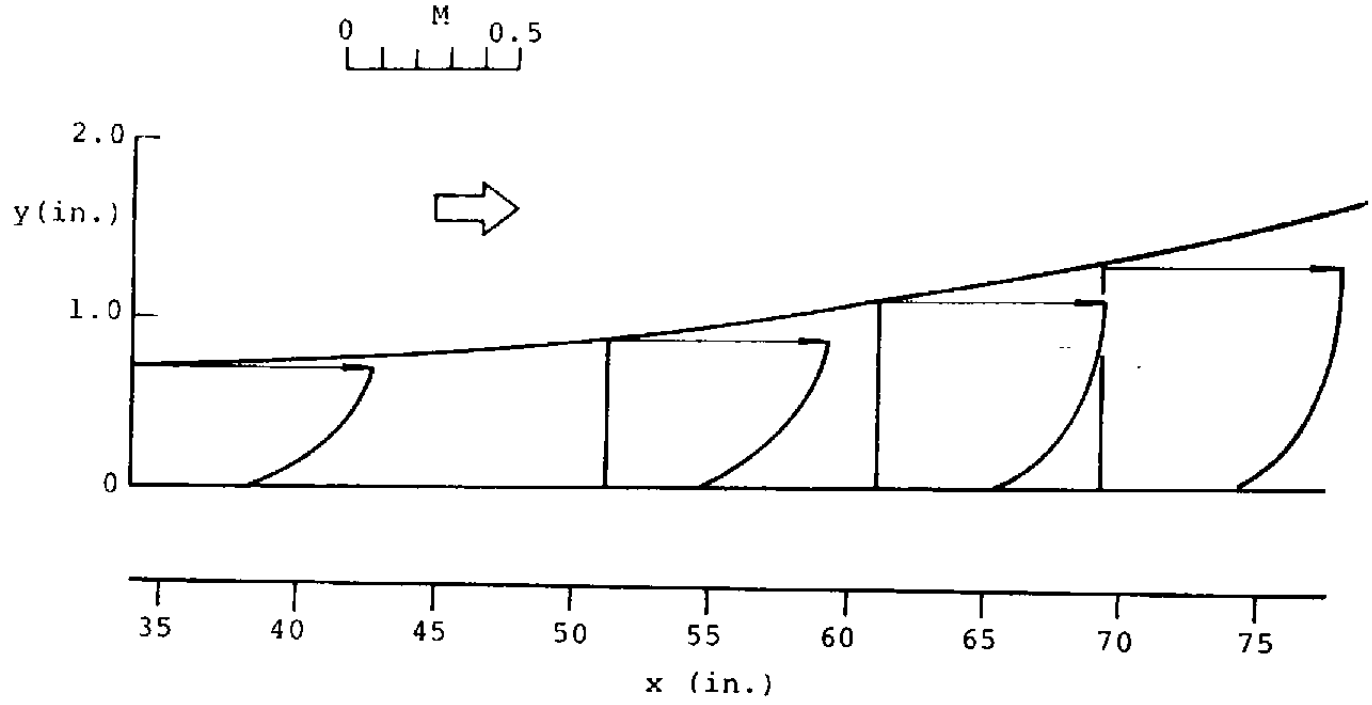

$M_\infty = 0.6$, $Re_{L_f} = 32.5 \times 10^6$

Figure 62. Flow variation along the flat-plate model (The Reynolds number is calculated for the distance to the forward-facing step in Figure 63; from AEDC-TR-75-95).

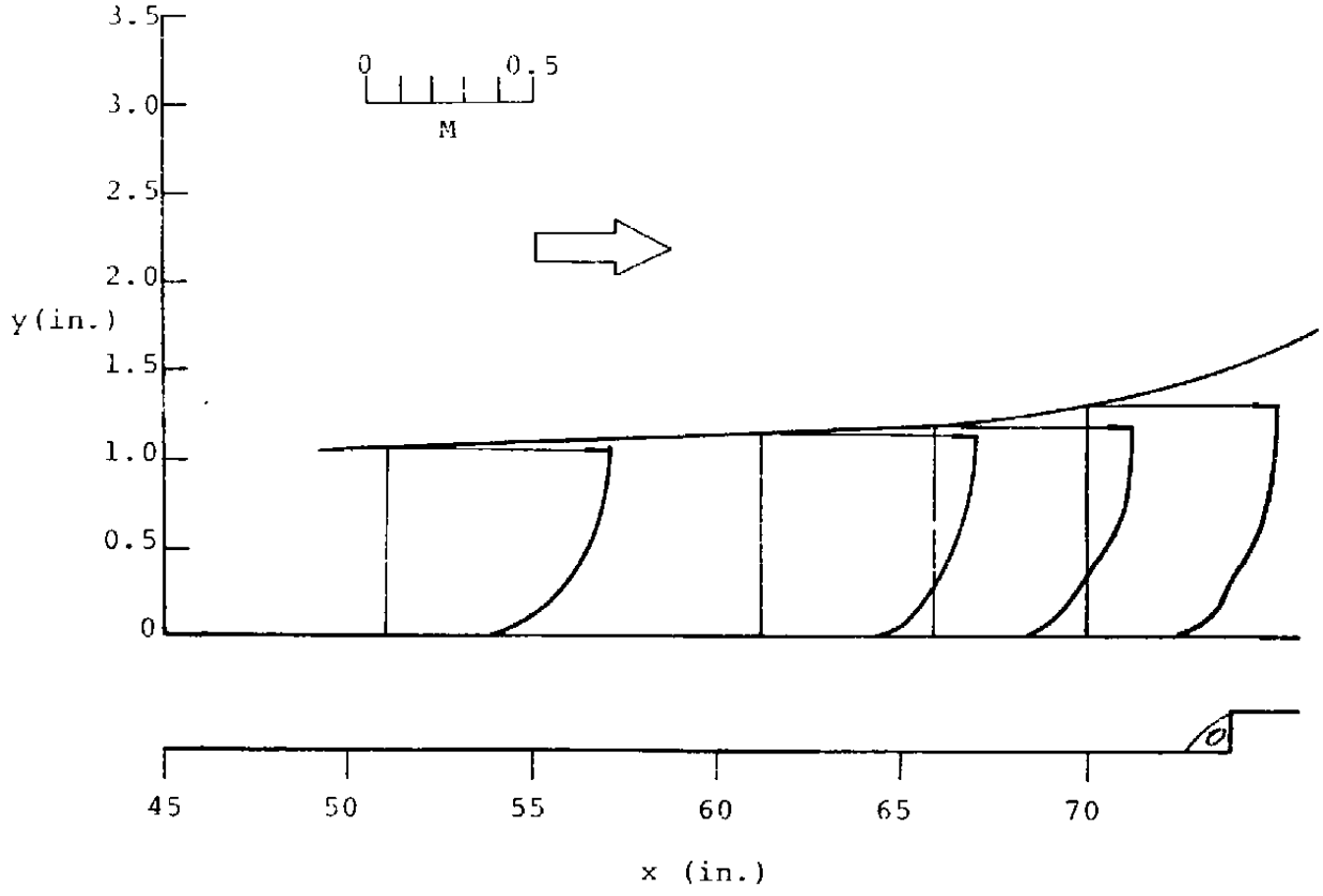

$M_e = 0.6$, $Re_{L_f} = 32.5 \times 10^6$

Figure 63. Flow variation along the forward-facing step model (from AEDC-TR-75-95).

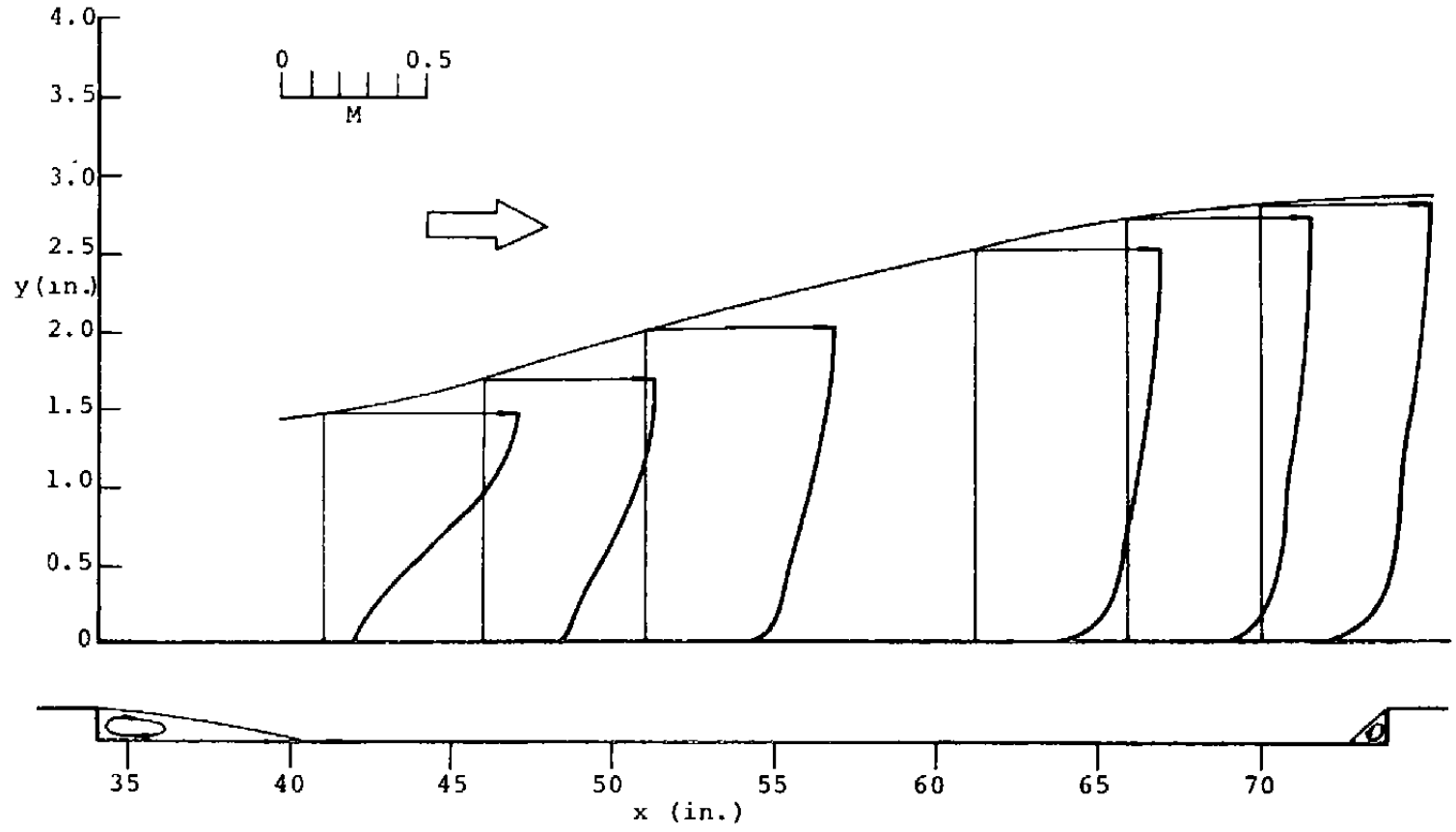

$M_\infty = 0.6$, $Re_{L_R} = 15 \times 10^6$

Figure 64. Flow variation along the 40-inch cavity model.

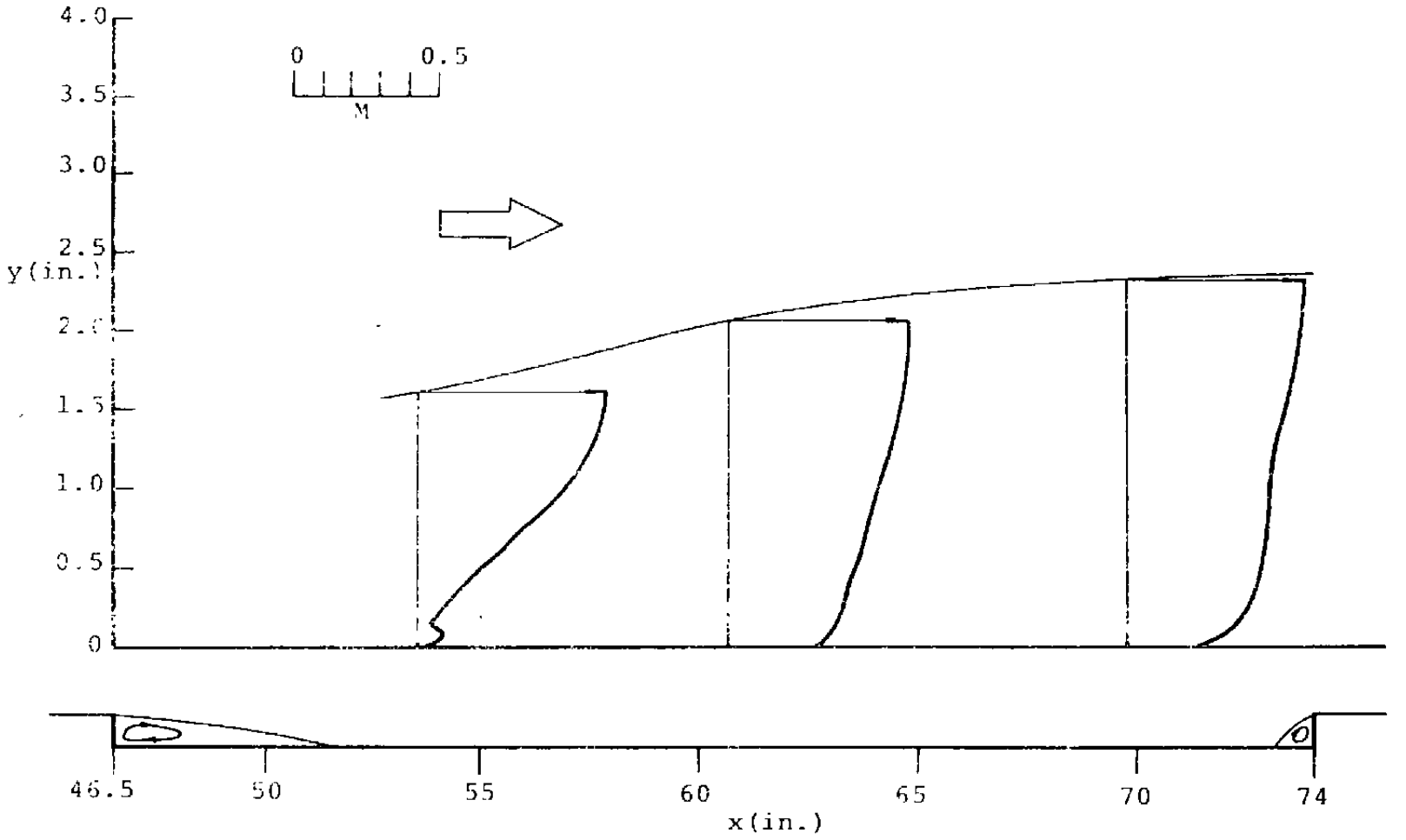

$M_\infty = 0.6$, $Re_{L_R} = 20 \times 10^6$

Figure 65. Flow variation along the 27.5-inch cavity model.

AEDC-TR-77-103

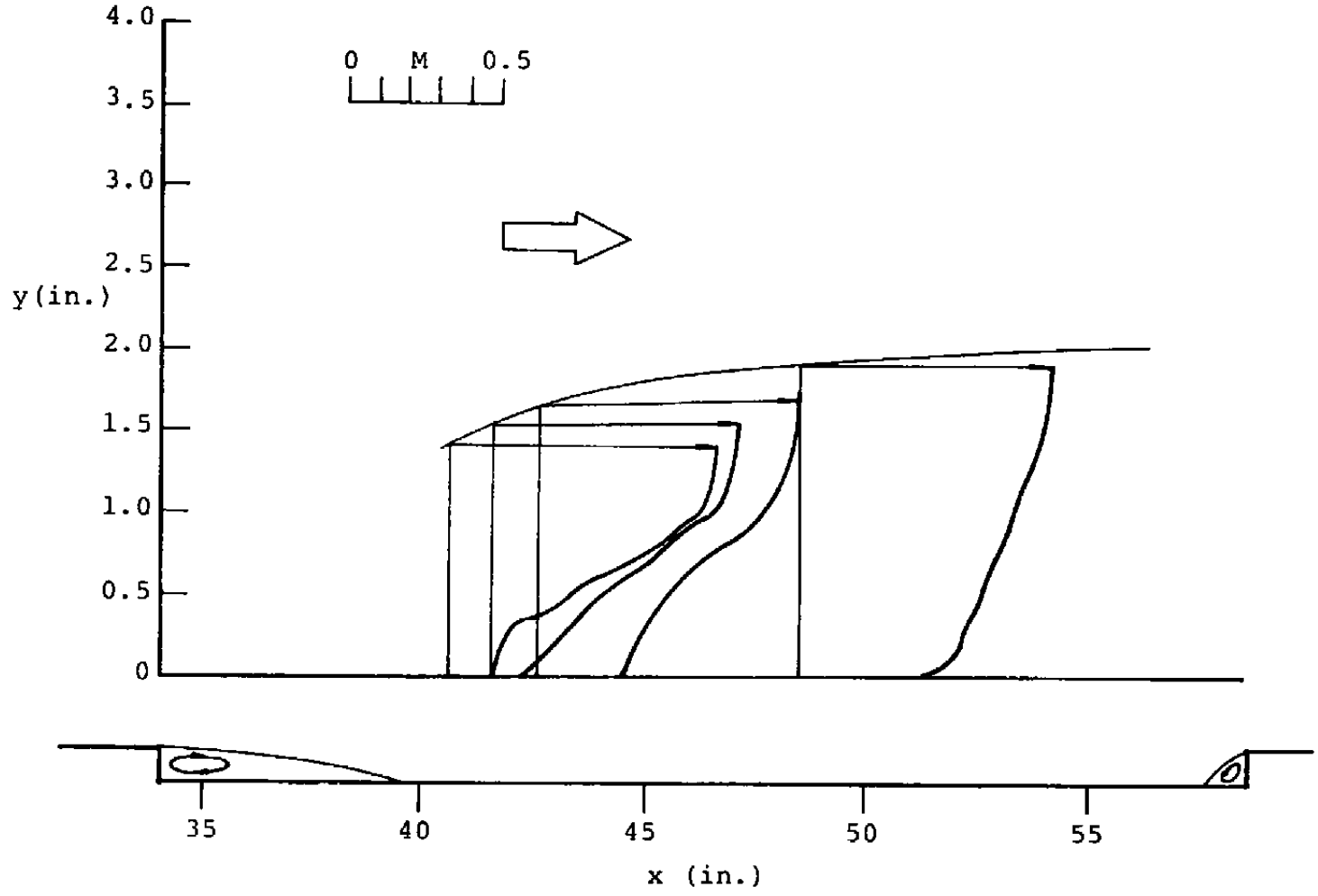

Figure 66. Flow variation along the 23.5-inch cavity model.

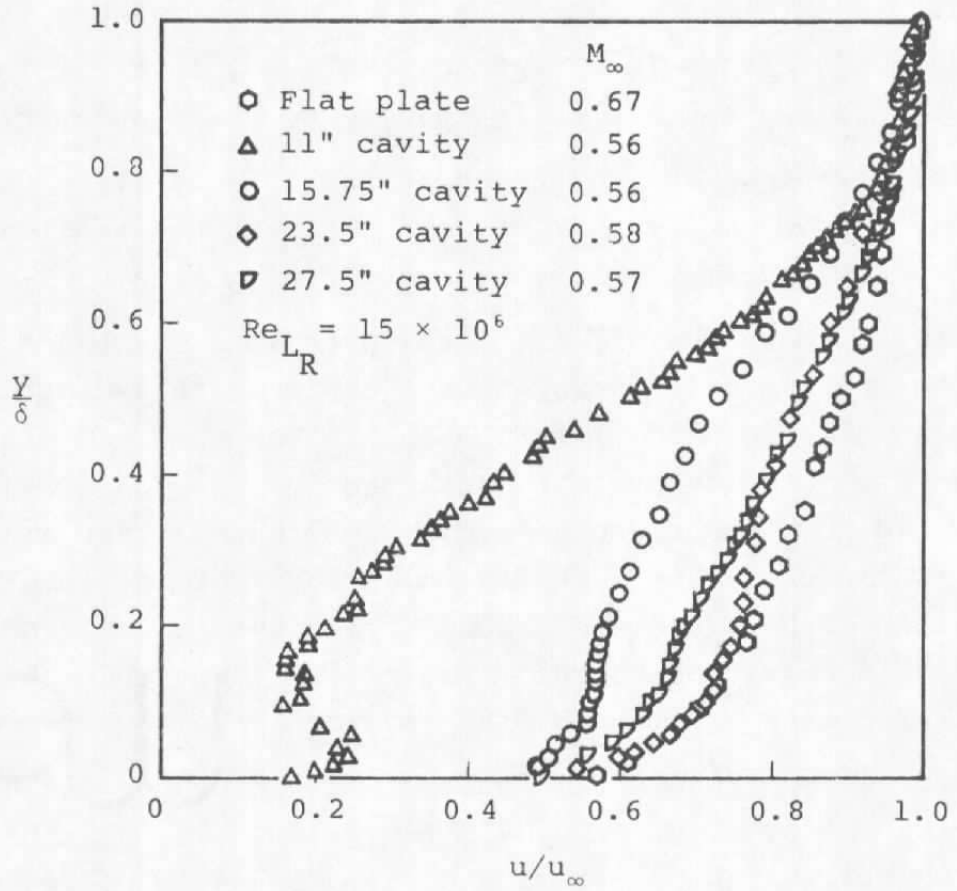

Figure 67. Effect of cavity length on the non-dimensional velocity profile at the middle point between the reattachment and separation points.

at $y/\delta < 1.5$, which is due to the unsteadiness of the flow as the cavity flow becomes nearly open, i.e., the dividing streamline is about to leave the floor.

The velocity profile in Figure 67 gets fuller with decreasing depth to length ratio until $h/\ell = 0.0425$ ($\ell = 23.5$ in.) and then becomes thinner again. As mentioned in the last section, the rearward-facing step of a cavity of $h/\ell = 0.0425$ ($\ell = 23.5$ in.) has the best efficiency in energizing the shear layer of the flow at $M_\infty \approx 0.6$ and $Re_{L_R} \approx 15 \times 10^6$. Therefore, the flow over this cavity will have a higher energy and a fuller velocity profile than the same flow over the 27.5-inch cavity at the station 14.5 inches downstream from the rearward-facing step.

Figure 68 shows the effect of an upstream disturbance induced by the rearward-facing step of a cavity with a depth to length ratio $h/\ell = 0.0425$ ($\ell = 23.5$ in.). The upstream disturbance makes the velocity profile in the region of $y/\delta \leq 0.4$ fuller than it would be without the upstream disturbance. For a depth to length ratio of 0.036 ($\ell = 27.5$ in.), the profile almost coincides with the upstream disturbance free case--corresponding to a naturally developed boundary-layer flow approaching a forward-facing step. For $M_\infty = 0.84$ and $Re_{L_R} = 24.8 \times 10^6$, the rate of decrease of the kinetic energy, in the region close to the floor of the cavity of $h/\ell = 0.0425$ ($\ell = 23.5$ in.), is higher than that for the flow at $M = 0.56$ and $Re_{L_R} = 15.8 \times 10^6$ (Figure 69).

The results shown in Figures 67, 68, and 69 imply that the recovery of boundary layer properties after any upstream disturbance, such as change of free-stream Mach number and approach Reynolds number, or a discontinuity in the boundary, etc., all start in the shear-layer adjacent to the wall surface and spread upward as the flow moves downstream.

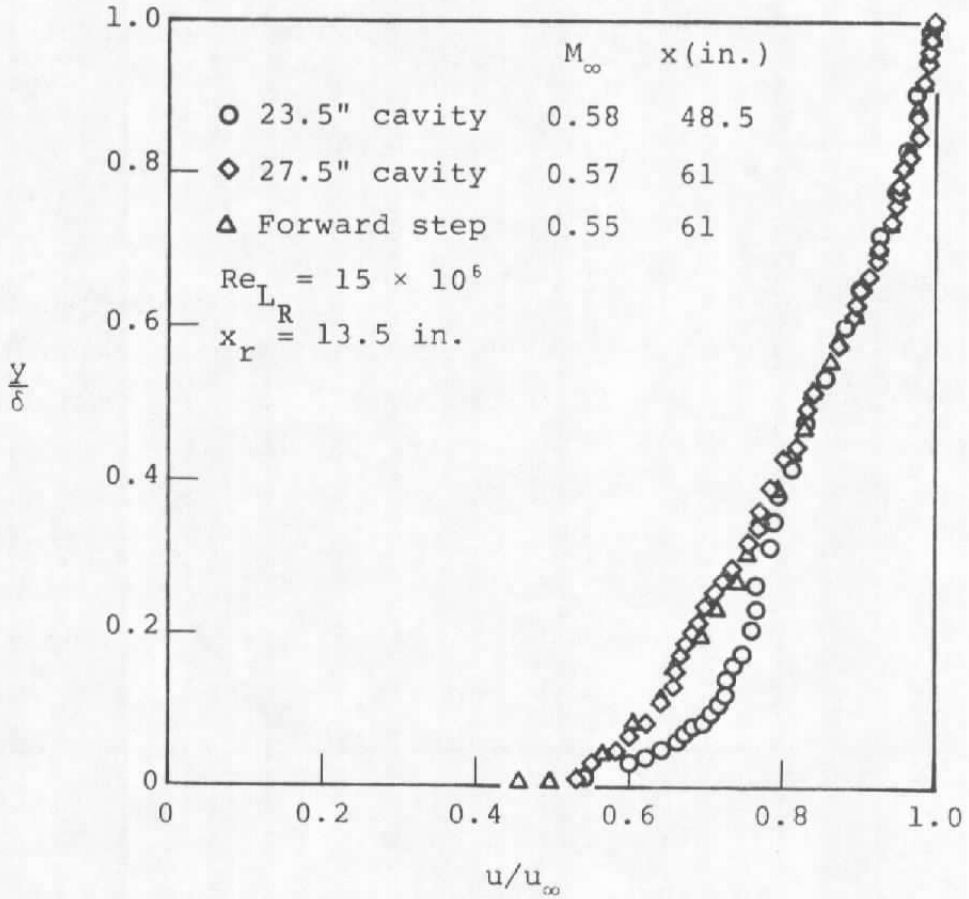

Figure 68. Effect of upstream disturbance on the non-dimensional velocity profile.

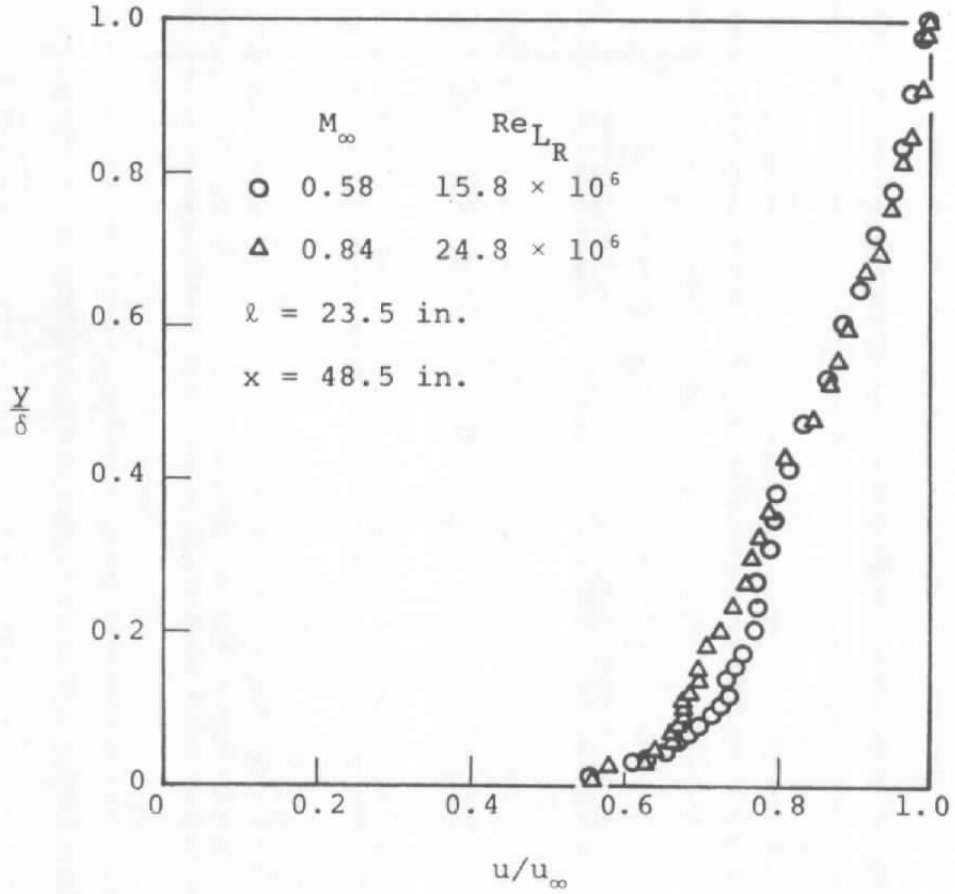

Figure 69. Effect of inertia energy on the non-dimensional velocity profile.

4.3.2 Law of the Wall and Law of the Wake

Very near the wall surface the pitot-probe measurements become difficult and the results are doubtful due to the combined effects of wall interference and local flow turbulence. Therefore, in the present study, the wall and wake law in the form

$$\frac{u}{u_\tau} = \frac{1}{\kappa} \ln \left(\frac{u_\tau y}{\nu} \right) + B + \frac{\Pi}{\kappa} \omega \left(\frac{y}{\delta} \right) \tag{4.6}$$

was fitted by using the outer region data, with κ and B taken as 0.41 and 5.0 respectively. The law of the wake was represented by,

$$\omega \left(\frac{y}{\delta} \right) = 1 - \cos \left(\pi \frac{y}{\delta} \right) \tag{4.7}$$

The compressibility effect was taken into account by use of Van Driest's generalized velocity u* as a substitute for u (Ref. 18), i.e.,

$$u^* = \frac{u_e}{a} \sin^{-1} \left(a \frac{u}{u_e} \right) \tag{4.8}$$

where

$$a = \left(\frac{r(\gamma - 1)M_e^2}{2 + r(\gamma - 1)M_e^2} \right)^{1/2} \tag{4.9}$$

and r is the recovery factor, u_e and M_e denote local condition at the external edge of the boundary layer.

Making these substitutions, Equation 4.6 becomes

$$\frac{u^*}{u_\tau} = \frac{1}{0.041} \ln \left(\frac{u_\tau y}{\nu} \right) + 5.0 + \frac{\pi}{0.041} \left[1 - \cos \left(\pi \frac{y}{\delta} \right) \right] \tag{4.10}$$

The displacement thickness can be expressed as

$$\frac{\delta^*}{\delta}\frac{u_\infty}{u_\tau} = \int_o^\infty \left(\frac{u_\infty - u}{u_\tau}\right) d\left(\frac{y}{\delta}\right) \tag{4.11}$$

By combining this with Equation (4.6) yields the result,

$$\kappa \frac{\delta^*}{\delta}\frac{u_\infty}{u_\tau} = 0.41 \frac{\delta^* u}{\delta u_\tau} = 1 + \bar{\pi} \tag{4.12}$$

To use this equation the displacement thickness δ^* was found by a graphical method from a plot of the corresponding velocity profile and u_τ and $\bar{\pi}$ were determined through an iteration process. The slope of the wall and wake law at the outer edge of the boundary layer is,

$$\left[\frac{du}{dy}\right]_{y=\delta} = \frac{u_\tau}{\kappa}\left[\frac{1}{y} + \bar{\pi}\frac{\pi}{\delta}\sin\left(\bar{\pi}\frac{y}{\delta}\right)\right]_{y=\delta} = \frac{u_\tau}{\kappa\delta} \tag{4.13}$$

and is different from the actual flow condition. In order to fit the curve with the experimental data, the value of δ was determined by a method of trial and error. The fitting region is usually limited to $(y/\delta) < 0.9$ for flow with a strong wake or even $(y/\delta) < 0.75$ with a weak wake.

A typical plot of the wall and wake law for flow over a flat plate is shown in Figure 70. The data points near the wall show a value which is too high. This is probably due to the deflection of the streamlines inducted by the trailing vortex system which is generated by the circular tip of the pitot-probe. The calculated wake-strength parameter $\bar{\pi}$ is 0.72 which is slightly greater than the value, $\bar{\pi} = 0.55$, predicted by Coles (Ref. 19) based on Wieghardt and Tillmann's incompressible flow data (Ref. 20). The higher magnitude of $\bar{\pi}$ of the present study

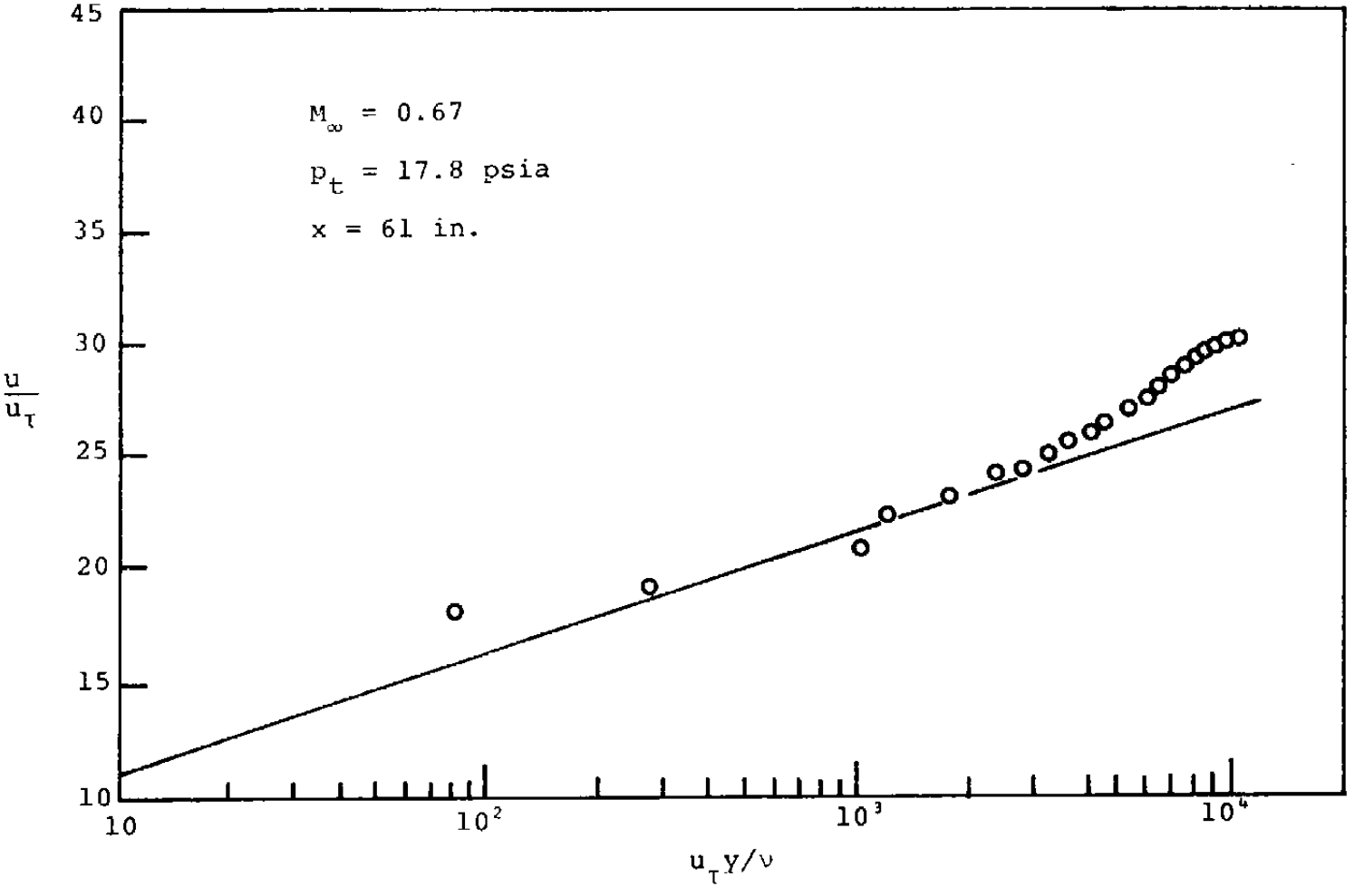

Figure 70. Wall and wake law plot for flow over the flat-plate model.

is probably due to the effects of the higher surface roughness of the model used here as compared with the waxed-plywood plate used in Wieghardt and Tillman's test (Ref. 20). The slight discontinuity of the joints between the floor blocks and between the filling blocks may also result in an increase of $\bar{\pi}$. However, the tests of all the different models in the present study are carried out under the same roughness condition. Therefore, the results of this flat-plate model are still adequate for use as a standard for the discussion of the influence of wake and/or separation on the velocity distribution in both the transverse and streamwise directions.

The wall and wake law plots for flow over a forward-facing step model are shown in Figure 71. By comparing the results for the flow over a flat plate and a forward-facing step model (Figure 72), it is found that at station 61 the two profiles nearly coincide. Only around the portion where $3000 < (u_\tau y/\nu) < 5000$ does the latter show a very small hump. This hump will become more obvious as the profile is taken closer to the step (Figure 71). It is certainly due to the upstream effect of the downstream separation. Another comment will be mentioned here, namely, that the Mach number at the outer edge of the boundary layer for the forward-facing step is slightly smaller than that of the flat plate. However, the free-stream Mach number of the flow over the forward-facing step model should be slightly higher than that of the corresponding downstream Mach number at the external edge of the boundary layer. Therefore, it is believed that the free-stream Mach number for these two profiles is nearly equal.

For flow over the 40- and 27.5-inch cavities, the plots of the wall and wake law are shown in Figures 73 and 74, respectively. After examining these figures, several points can be made as follows:

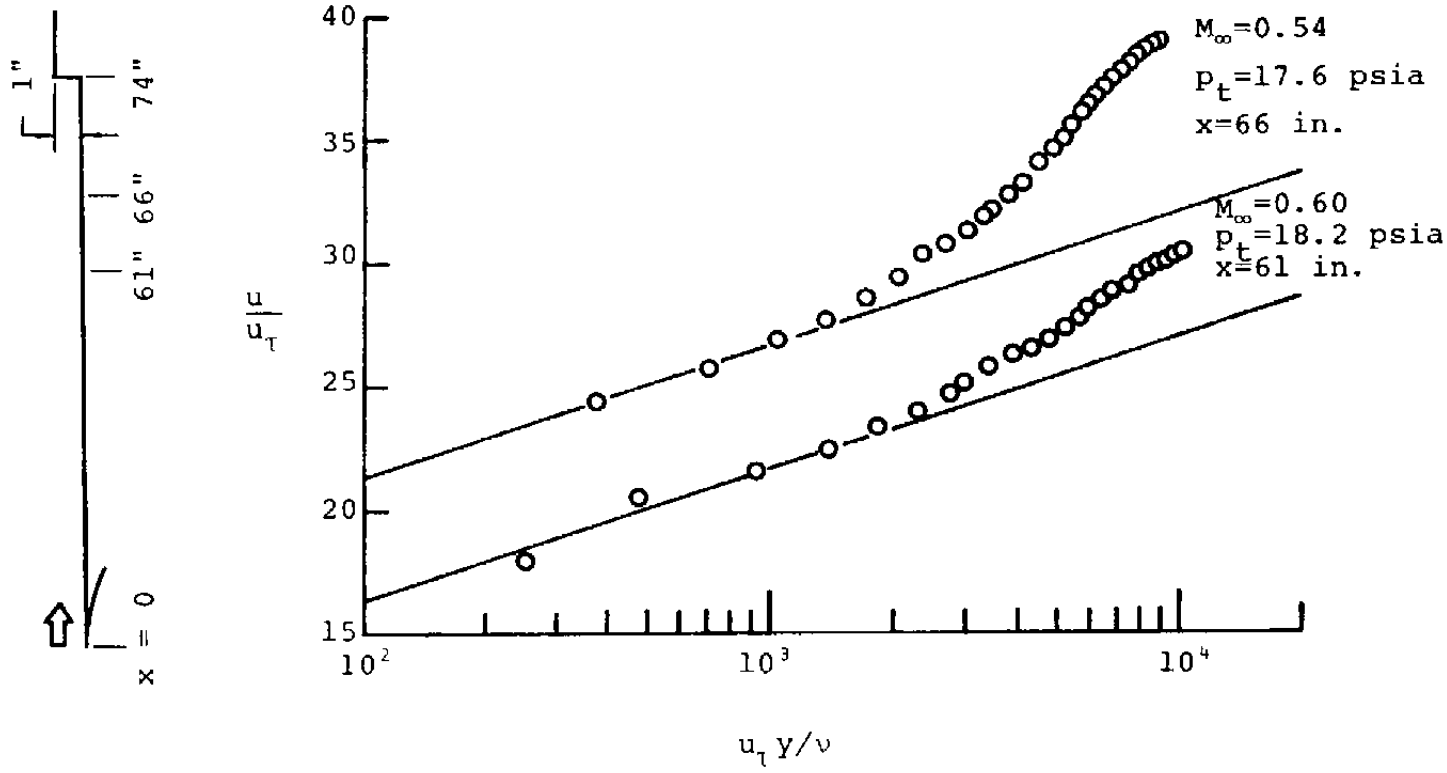

Figure 71. Wall and wake law plots for flow over the forward-facing step model.

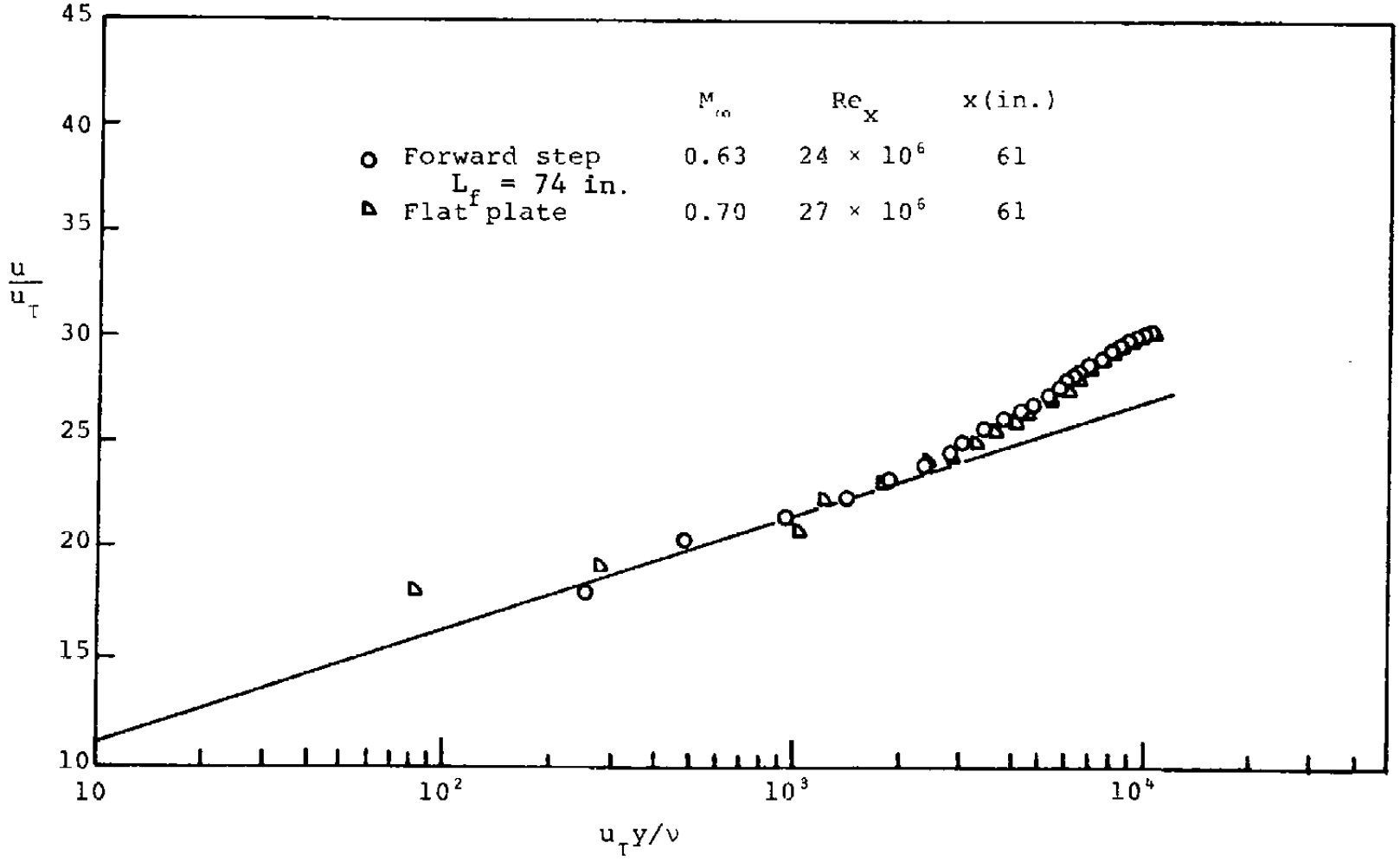

Figure 72. Comparison of wall and wake law plots for flow over the forward-facing step and the flat-plate models.

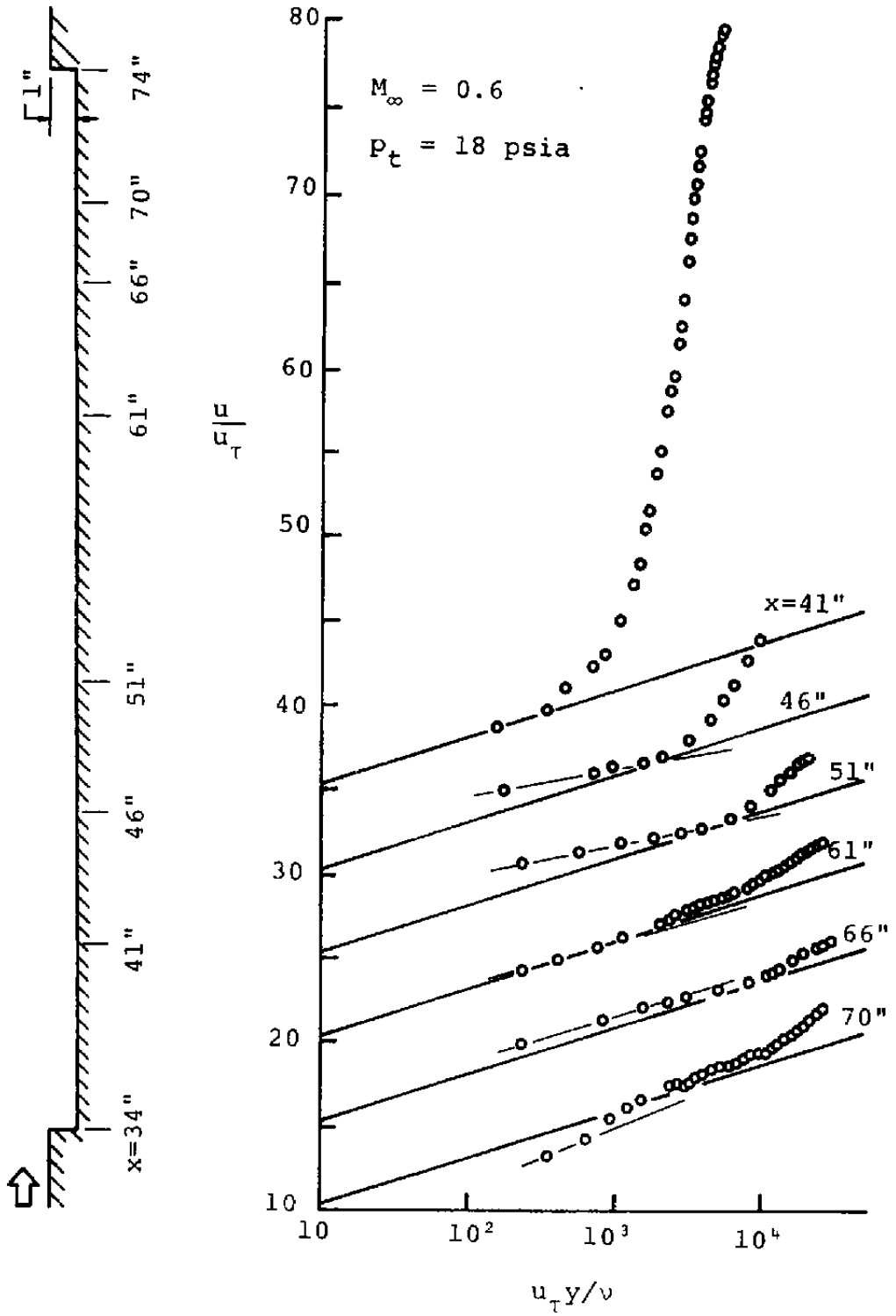

Figure 73. Wall and wake law plots for flow over the 40-inch cavity model.

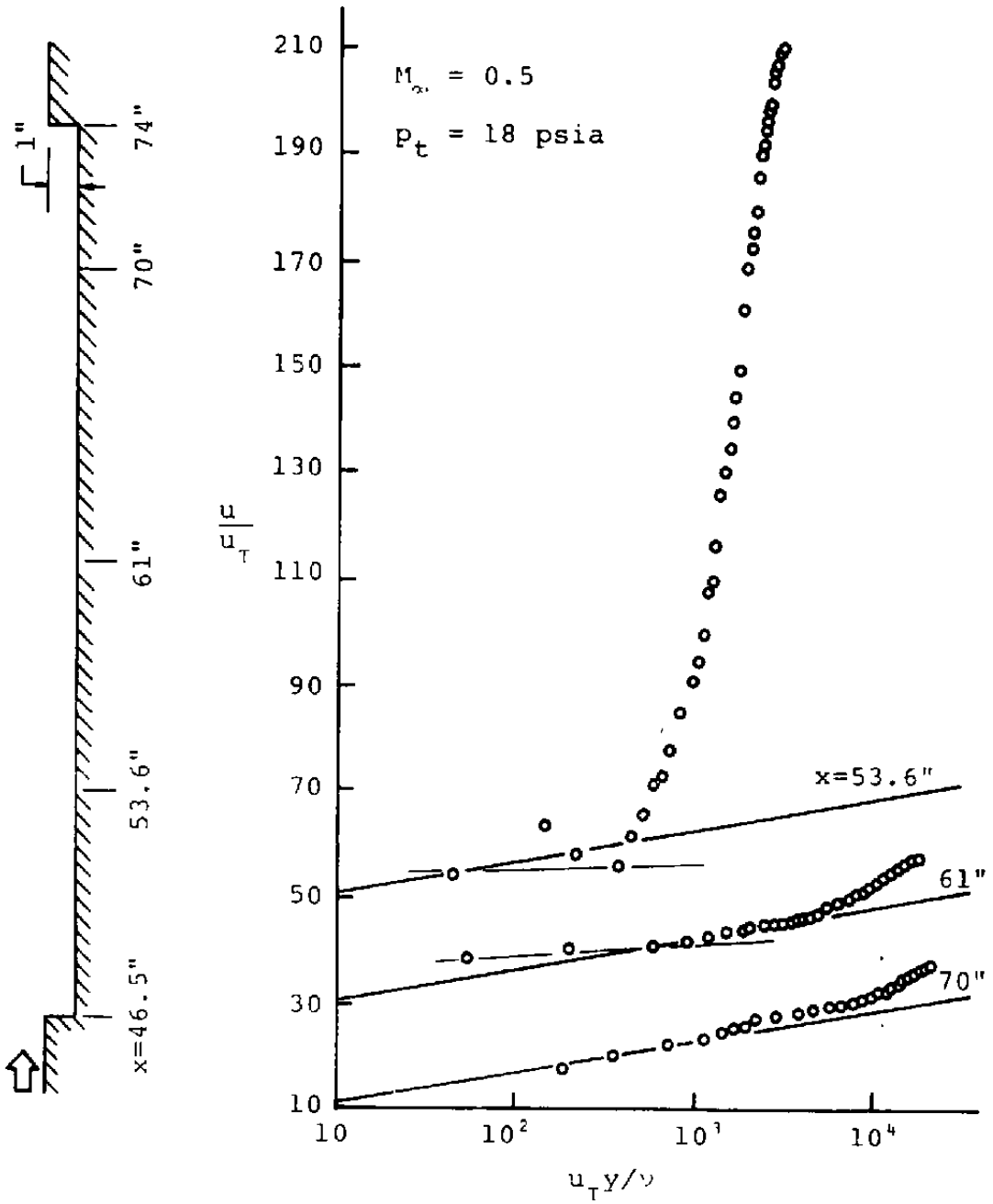

Figure 74. Wall and wake law plots for flow over the 27.5-inch cavity model.

(a) The velocity profiles recover continuously from the effects of the rearward-facing step after passing the reattachment point in the 40-inch cavity case. The upstream effect of the downstream separation will overwhelm the relaxing process after the flow has reached the station 70 (Figure 73). For flow over the 27.5-inch cavity, the velocity profiles at fewer stations were measured; hence no such conclusion can be made.

(b) At the location 21 inches downstream from the reattachment point (station 61), in the 40-inch cavity, the outermost portion of the wall- and wake-law profile coincides closely with that of the upstream-disturbance-free case, as is clearly illustrated in Figure 75. In the region $0.07 < (y/\delta) < 0.3$ the forward-facing step profile has a substantial hump. Since the external flow velocity of the two flows is equal and the frictional felocity (u_τ) of the cavity flow is 18.8 ft/sec while it is 20.6 ft/sec for the forward-facing step, it is concluded that this hump denotes the kinetic energy of the cavity flow near the floor must be smaller. Furthermore, the surface pressure is 14.6 psia for the cavity flow and is 15.2 psia for the forward-facing step. Therefore, the total energy of the cavity is smaller and this results in a lower peak pressure ahead of the downstream step as was pointed out in Section 4.1.0.

(c) At stations near either the reattachment or the separation point, the agreement with the law of the wall is fairly poor. Vasanta, Ram and Wauschkuhn (Ref. 21) assumed that at different stations downstream from the reattachment point the law of the wall should be fitted by different slopes. Schofield (Ref. 22) thought that this change of slope is attributed to this "non-equilibrium of the wall turbulence." Coles (Ref. 23) said that near the wall data could be wrong but the formula is correct. The present experiments show a tendency for the slope of the law of the wall at the reattachment point to be smaller than that of the flat plate. The slope increases as the flow moves downstream and finally becomes greater than the flat plate case as the flow

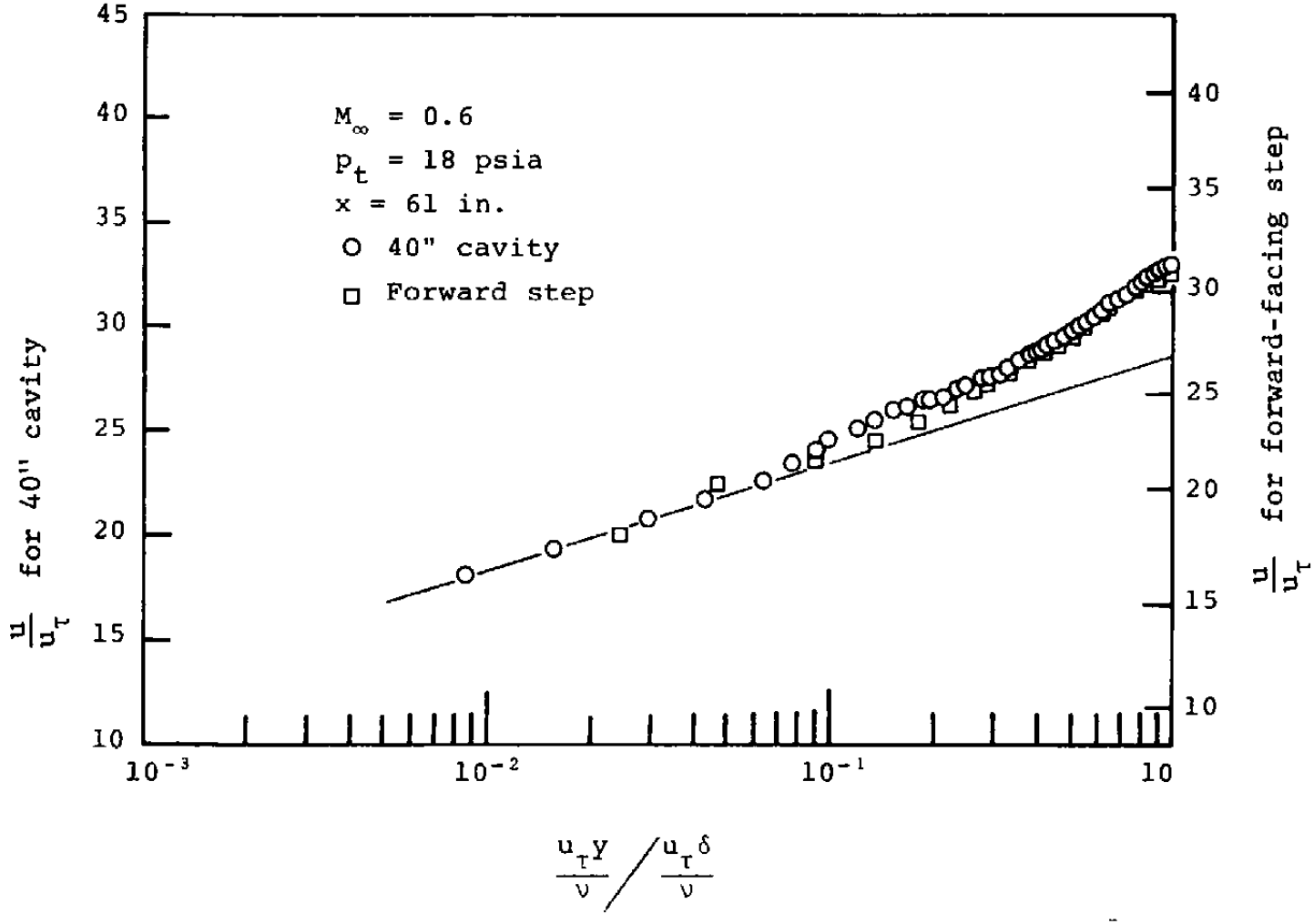

Figure 75. Effect of upstream disturbance on the wall and wake law plots.

approaches the separation point (Figures 73 and 74). The data points in the wall region more nearly fall along a straight line than along a sinuous shape as was asserted by Schofield (Ref. 22) based on Bradshaw and Wong's experiments (Ref. 24). However, the flow measurement using an impact probe near the wall with a high turbulence usually resulted in a higher degree of wall interference and thus yielded data of relatively low reliability. Unfortunately, all existing experiments rely on such a measuring technique; hence all the different explanations concerning the agreements with the law of the wall are plausible, but open to question. Before the data can be obtained by an interference-free type of measurement, no definite conclusion can be suggested here.

(d) The law of the wake profile shows a hump at station 61 in the 40-inch cavity as mentioned in (b) above. It disappears at the station 66, and shows up again, more strongly, at station 70. In the 27.5-inch cavity flow, there is also a significant hump on the wake profile at the station 70. Since it has been found that the static pressure ahead of the downstream step increases transversely from the floor and reaches a maximum at one step height as in a supersonic or an incompressible flow passing a shallow cavity, the transverse pressure gradient becomes larger at the stations closer to the forward-facing step (Ref. 16). Although there has been no measured information about this for subsonic and transonic flow, it is expected that the tendency must be the same. This transverse static pressure gradient will produce a change in the velocity profile. The result is that the velocity profiles near the downstream step show an unusual velocity defect which occurs between a height of one step height to the layer near the floor. This unusual defect region forms the hump on the wake-law plot.

4.3.3 The Wake Strength Parameter $\bar{\pi}$ and the Velocity Profile Defect Parameter G

The law of the wake is characterized by a universal function ω (y/δ) for all two-dimensional turbulent boundary layers and a wake strength parameter $\bar{\pi}$ which specifies different strengths of the wake component. Coles found that $\bar{\pi}$ is very nearly 0.55 for flow at constant pressure (Ref. 19) but is different under different non-equilibrium flow conditions (Ref. 23). $\bar{\pi}$ increases for the flow over an adverse pressure gradient field and decreases with a favorable pressure gradient. Its magnitude can be either positive or negative. At the separation or reattachment point, $\bar{\pi}$ approaches infinity. The results for $\bar{\pi}$ from the present experiments are plotted in Figure 76.

For flow over a flat plate, Prandtl derived an equation for the estimation of the skin friction (Ref. 25), i.e.,

$$C_f = 0.074\ (Re_x)^{-1/5};\ 5 \times 10^5 < Re_x < 10^7,\ Re_\delta < 10^5 \quad (4.14)$$

By substitution and rearrangement from the above equation, and by assuming that $(\delta^*/\delta) = (1/8)$ and that $\kappa = 0.41$, the expression for $\bar{\pi}$ becomes,

$$\bar{\pi} = \kappa \frac{\delta^*}{\delta} \frac{u_\infty}{u_\tau} - 1 = 0.3\ (Re_x)^{0.1} - 1 \quad (4.15)$$

This equation shows that $\bar{\pi}$ for the flow over a flat plate is a function of Reynolds number only. Intuitively, $\bar{\pi}$ should depend also on the surface roughness which will show up as a component of skin friction. By observation of the above two equations, it is understood that the roughness effect is embedded in the Reynolds number. The Reynolds numbers based on length (Re_x) and the boundary layer thickness (Re_δ) for the present experiments are about 32.5×10^6 and 6×10^5, respectively, for flow at $M_\infty \approx 0.6$. These values are slightly higher than the

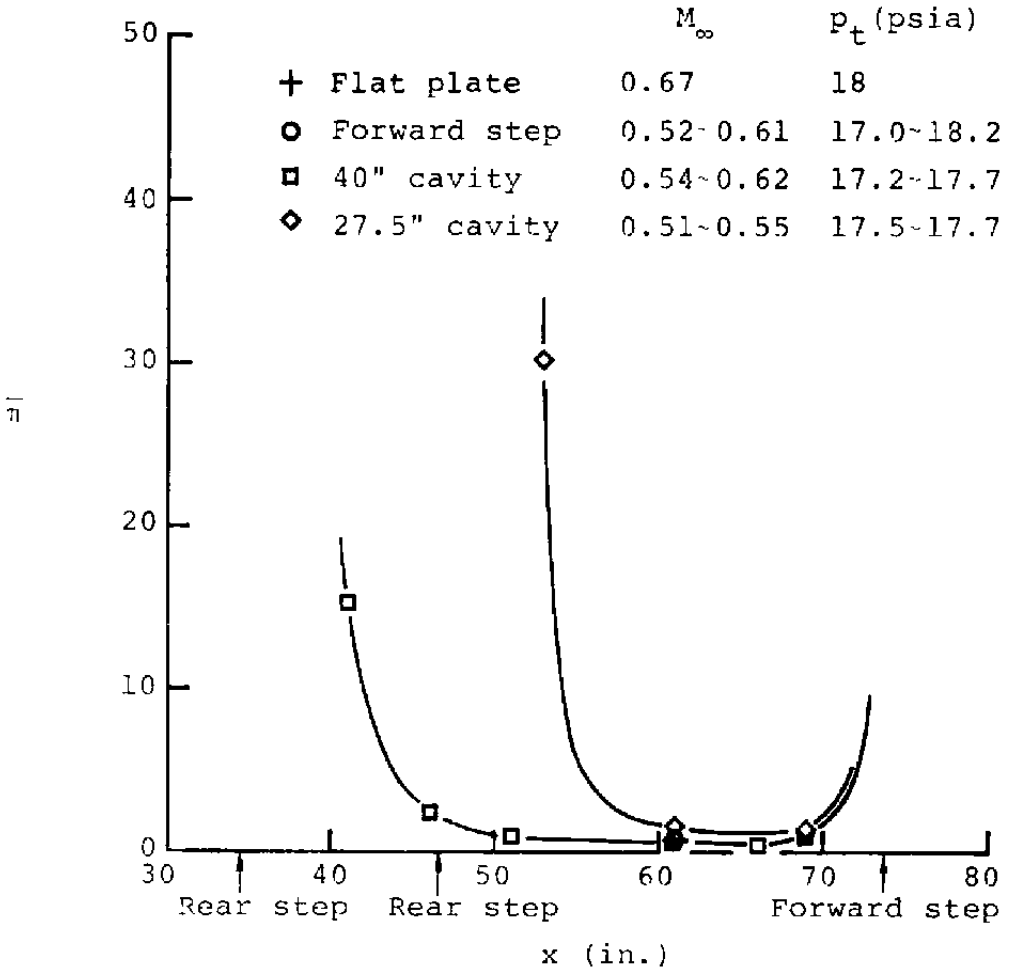

Figure 76. Variation of $\bar{\pi}$ along various models.

magnitudes specified in the above equation. However, the magnitude of the wake strength parameter, $\bar{\pi} = 0.69$, determined by the equation, is still very close to the measured data of 0.72. This result is much better than that obtained from the Schultz-Grunow skin friction formula (Ref. 26), i.e.,

$$C_f = 0.427 \ (\log Re_x - 0.407)^{-2.64} \tag{4.16}$$

$$\bar{\pi} = 0.11 \ (\log Re_x - 0.407)^{1.32} - 1$$

which gives a rather low value of $\bar{\pi}$ (0.46).

Clauser (Ref. 27) introduced a universal thickness parameter,

$$\Delta \equiv \int_0^\infty \frac{u_\infty - u}{u_\tau} \, dy \tag{4.17}$$

for turbulent boundary-layer data analysis, which will make the velocity defect plot, $(u - u_\infty)/u_\tau$ versus (y/Δ), independent of Reynolds number and the surface roughness. By substitution of u_e for u_∞ in the above equation and by the application of the wall and wake law with the boundary condition $u = u_e$ as $y \to \delta$, yields,

$$\bar{\pi} = \kappa \frac{\Delta}{\delta} - 1 \tag{4.18}$$

This equation shows that $\bar{\pi}$ is linearly related to (Δ/δ), where δ contains the mixed response of Reynolds number, surface roughness and any other existing upstream disturbances. The plot of $\bar{\pi}$ versus (Δ/δ) is shown in Figure 77.

In addition to Δ, Clauser introduced a velocity profile defect parameter G to characterize the various members of the

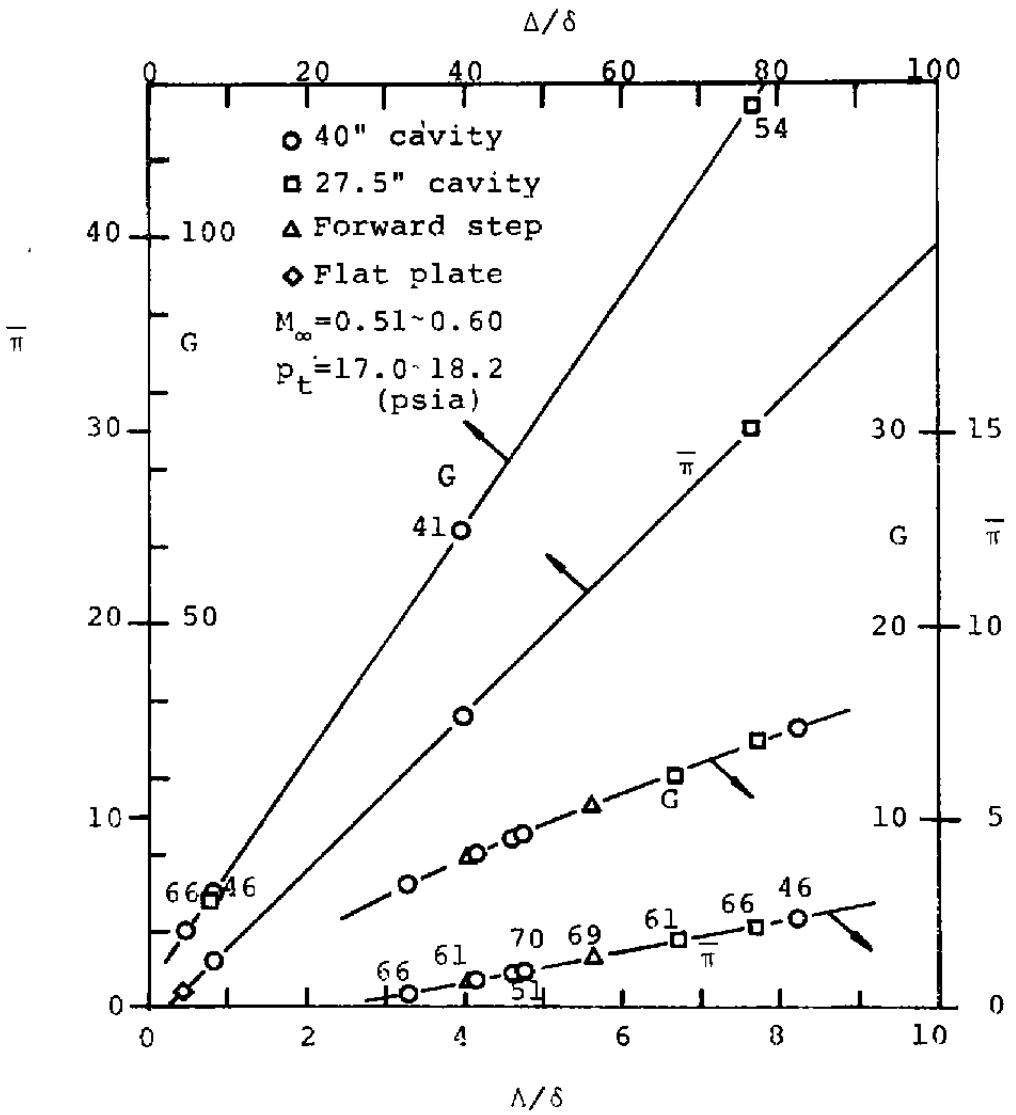

Figure 77. Coles' parameter $\bar{\pi}$ and Clauser's parameter G.

universal family of turbulent boundary-layer velocity profiles in the following fashion, i.e.,

$$G \equiv \int_0^\infty \left(\frac{u_\infty - u}{u_\tau} \right)^2 dy \Big/ \int_0^\infty \left(\frac{u_\infty - u}{u_\tau} \right) dy \qquad (4.19)$$

$$= \int_0^\infty \left(\frac{u_\infty - u}{u_\tau} \right)^2 d\left(\frac{y}{\Delta}\right)$$

Similarly, G can be expressed as

$$G = \frac{\delta}{\Delta} \int_0^\infty \frac{1}{\kappa} \ln\left(\frac{y}{\delta}\right) \frac{\bar{\pi}}{\kappa} \cdot \left[1 + \cos \pi\left(\frac{y}{\delta}\right) \right]^2 d\left(\frac{y}{\delta}\right) \qquad (4.20)$$

After integration (Refs. 28 and 29), the last equation yields,

$$G = \frac{\delta}{\Delta} \left(11.89 + 24.85\ \bar{\pi} + 8.92\ \bar{\pi}^{\,2}\right) \qquad (4.21)$$

The plot of G versus (Δ/δ) is also shown in Figure 77. This equation gives G = 7.47 corresponding to $\bar{\pi}$ = 0.55 as compared to G = 6.1 obtained by Clauser (Ref. 27).

4.3.4 The Velocity Defect Law

In the preceding subsection, it was shown that the law of the wall and the law of the wake can yield,

$$\frac{u - u_e}{u_\tau} = \frac{1}{\kappa} \ln\left(\frac{y}{\delta}\right) - \frac{\bar{\pi}}{\kappa} \left[1 + \cos\left(\pi \frac{y}{\delta}\right) \right] \qquad (4.22)$$

$$= f\left(\bar{\pi}, \frac{y}{\delta}\right)$$

This equation is known as the velocity defect law. The plot of the defect law for the flow over the 40-inch cavity is shown in Figure 78. It reveals the same trends as those exhibited by the

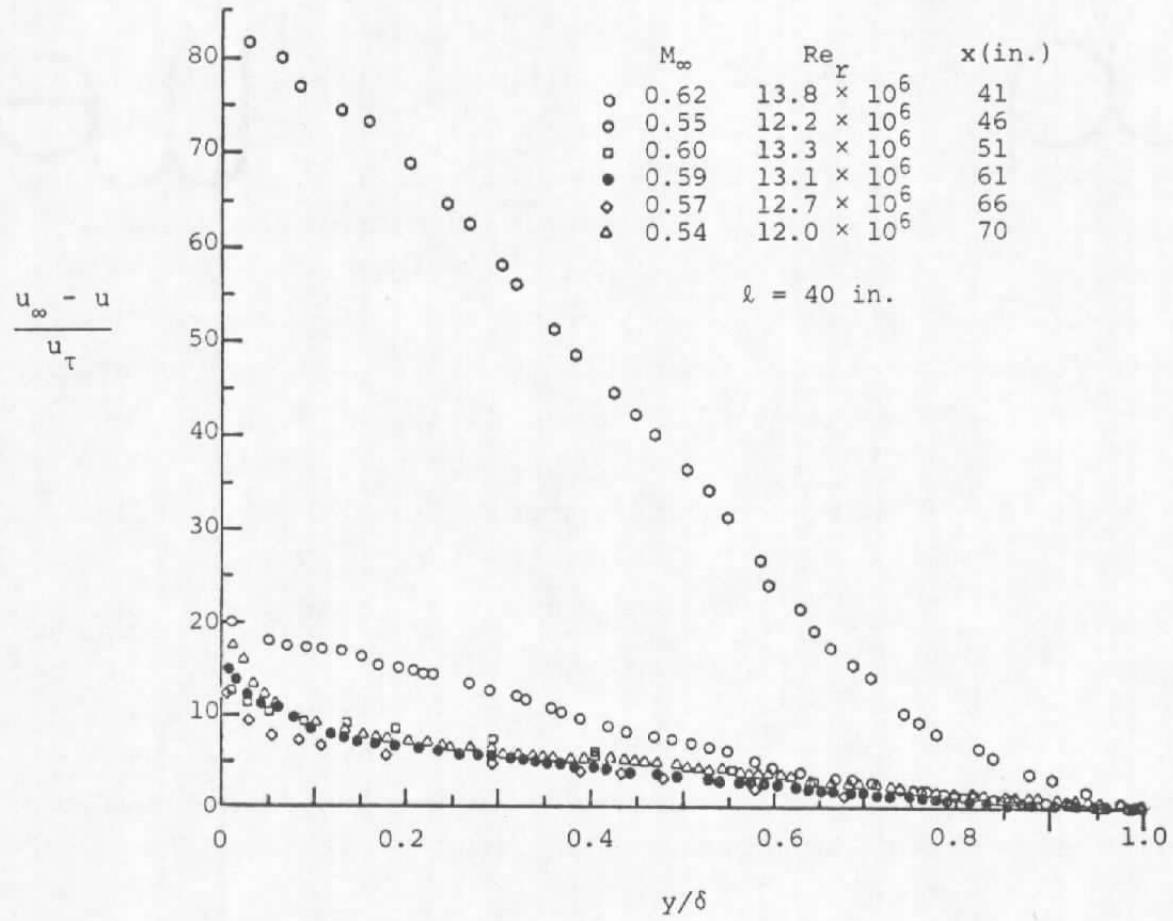

Figure 78. Velocity defect plot for flow over the 40-inch cavity model.

wall and wake law, namely, that the upstream effect of the downstream separation does not overwhelm the relaxation process until station 70. Figure 79 is a velocity defect plot at the station 70 for the flow over different models--the 40- and 27.5-inch cavities, the forward-facing step and the flat plate. It shows the phenomena of the downstream effect on the upstream disturbance and the upstream effect on the downstream separation. The inner portion of the velocity defect profile for the flow over a forward-facing step model is slightly fuller than that of the flow over the 27.5-inch cavity model but thinner than that for the flow over a 40-inch cavity model. Unlike the relaxation of the base pressure which will slightly overshoot almost immediately downstream of the reattachment point and then decreases slightly as the flow moves further downstream, the velocity profile will relax at a slower rate. At a station about 18 inches downstream from the reattachment point (i.e., station 70 in the 27.5-inch shallow cavity), the inner portion of the velocity profile has recovered to the state of the upstream disturbance-free case (i.e., flow over a forward-facing step model). While at the same station, but with a disturbance at about 30 inches upstream (i.e., flow over 40-inch shallow cavity), the inner portion of the profile becomes even fuller than that without an upstream disturbance and almost coincides with the profile for the flow over a flat plate. This is perhaps due to the turbulent mixing process which can transport energy from the external flow into the inner shear region.

It would be of interest to determine, when the cavity length is further increased, whether or not the turbulent mixing process can cause the velocity profile at certain downstream stations to become fuller than the flat plate case followed by a subsequent thinning. As far as the outer portion of the viscous layer is concerned, the velocity defect profile coincides with that of the flow over a flat plate if there is no upstream disturbance. The closer the upstream disturbance is, the thinner will be the outer portion of the velocity defect profile.

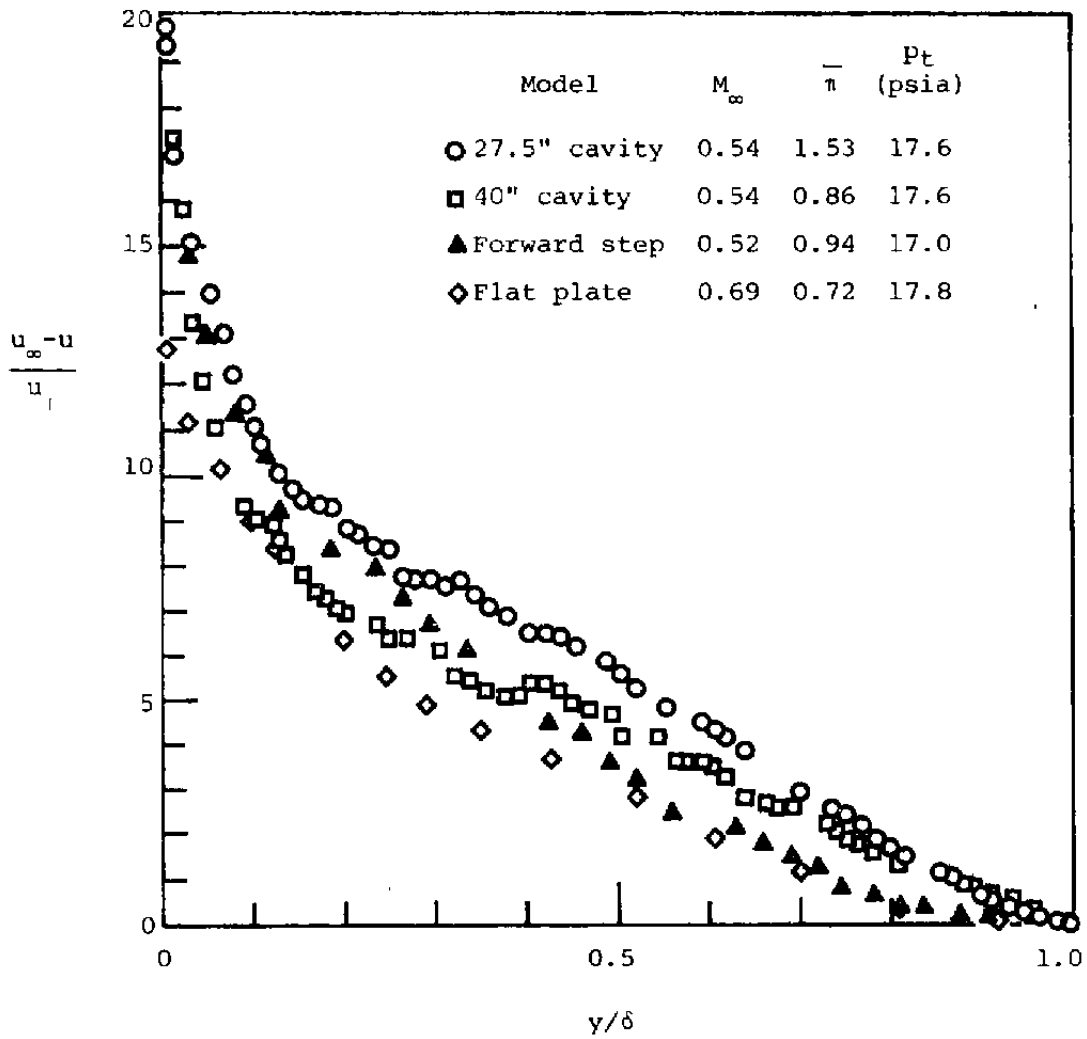

Figure 79. Velocity defect plot at the 70-inch station.

4.4 BOUNDARY-LAYER THICKNESS PARAMETER

The boundary-layer thickness (δ) development along different models (flat plate, forward-facing step, 27.5- and 40-inch cavities) for flow at a free-stream Mach number $M_\infty = 0.6$ and unit Reynolds number $(u_\infty/\nu) = 4.5 \times 10^6$ are shown in Figure 80. These values were determined by the rule $u = 0.99\ u_e$ at $y = \delta$. The boundary-layer thickness defined by the law of the wall and the law of the wake, known as the Coles boundary-layer thickness (δ_c), are also shown in this figure. When the wake component is small, the difference between δ and δ_c is significant.

The displacement thickness (δ^*) was determined by a graphical method from the plot of the corresponding velocity profile according to the definition

$$\delta^* = \int_0^\infty \left[1 - \frac{u}{u_e}\right] dy$$

The displacement thickness based on Coles boundary layer thickness (δ_c^*) was also determined. The results obtained for δ^* are shown in Figure 81.

The momentum thickness is calculated as follows.

$$\theta = \int_0^\infty \frac{u}{u_e}\left[1 - \frac{u}{u_e}\right] dy$$

$$= \int_0^\infty 1 - \left[\frac{u_e - u}{u_e}\right]\left[\frac{u_e - u}{u_e}\right] dy$$

$$= \Delta \int_0^\infty \left[\frac{u_\tau}{u_e}\right]\left[\frac{u_e - u}{u_\tau}\right] d\left[\frac{y}{\Delta}\right]$$

$$-\Delta \left[\frac{u_\tau}{u_e}\right]^2 \int_0^\infty \left[\frac{u_e - u}{u_\tau}\right]^2 d\left[\frac{y}{\Delta}\right]$$

$$= \sqrt{C_f/2}\ (1 - G\sqrt{C_f/2})\ \Delta$$

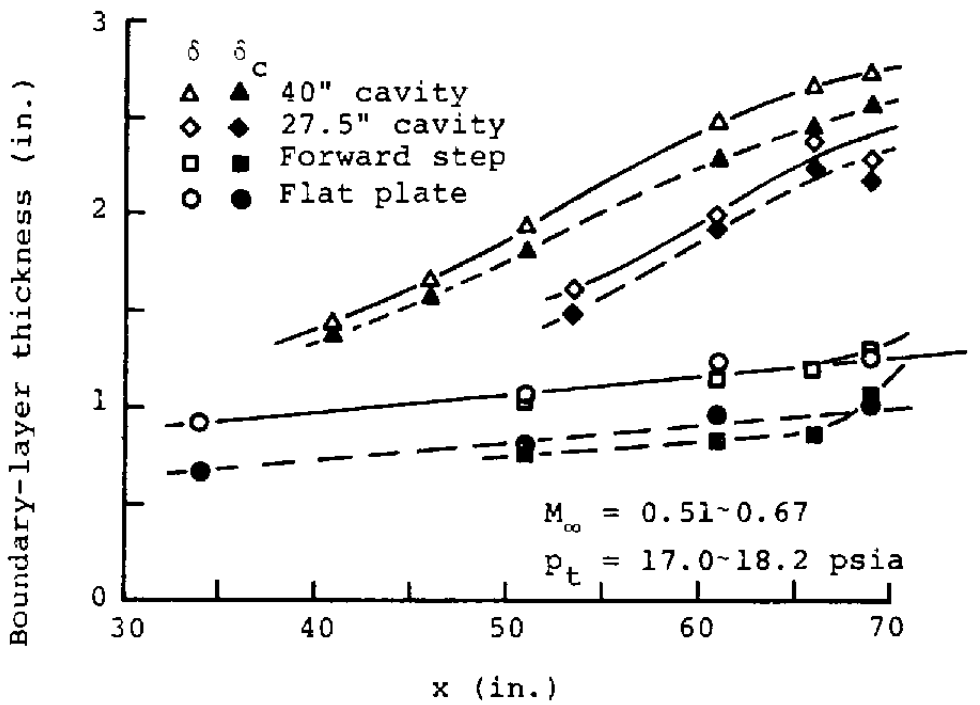

Figure 80. Development of the boundary-layer thickness along different models.

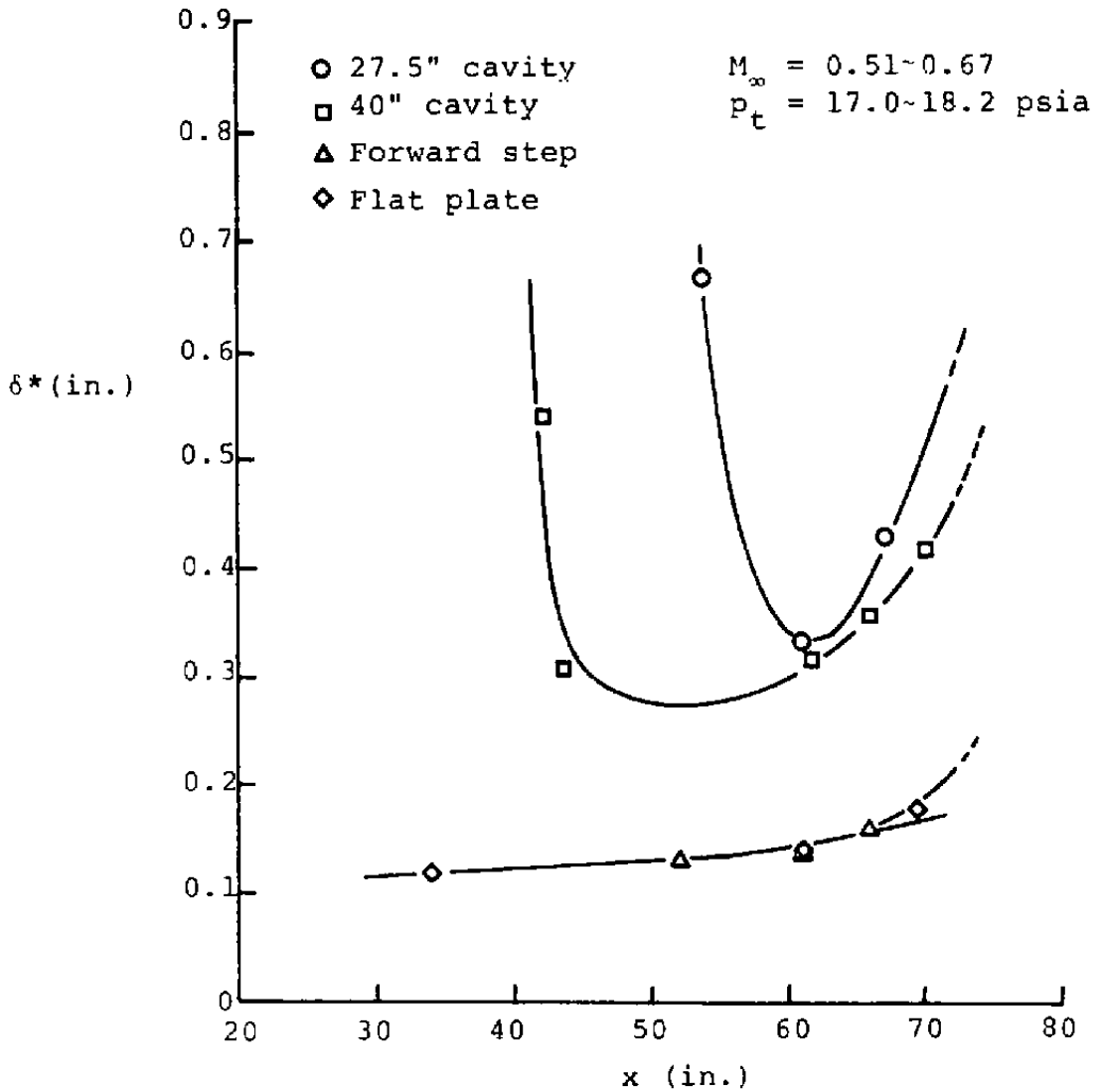

Figure 81. Development of the displacement thickness along different models.

where C_f is determined by the law of the wall and the law of the wake. The momentum thickness determined by this equation should be called Coles momentum thickness (θ_c). The results determined for Coles momentum thickness are shown in Figure 82.

4.5 WALL SHEAR STRESS DISTRIBUTION

The skin friction coefficient (C_f) was determined from the result of the law of the wall and the law of the wake. The direct measurement of the skin friction coefficient was just beginning at this reporting time. Therefore, the comparison was done through the wall and wake law. The skin friction variation along the model surface is shown in Figure 83. In the region of $60 < x < 70$ inches, the skin friction coefficient for the flow over the 40-inch cavity model nearly coincides with that for the flow over the flat plate model and this corresponds to the equilibrium condition. In contrast, the plot of the skin friction coefficient for the flow over the 27.5-inch cavity always shows a lower value than that for the corresponding equilibrium flow.

The plot of skin friction coefficient versus Reynolds number based on Coles displacement thickness (δ_c^*)is shown in Figure 84. The empirical relations are formulated as follows:

For the flat plate,

$$C_f = 0.0189 \, (Re_{\delta_c^*})^{-0.174}$$

For the forward-facing step,

$$C_f = 2.38 \, (Re_{\delta_c^*})^{-0.667}$$

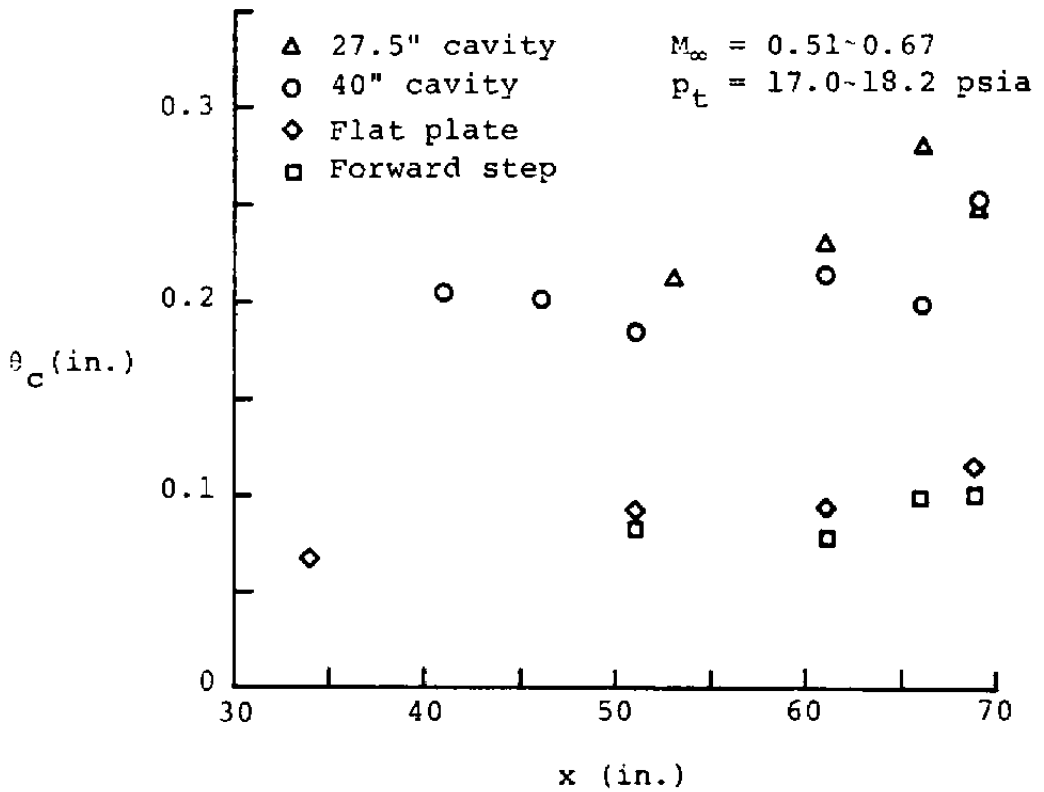

Figure 82. Development of Coles' momentum thickness along different models.

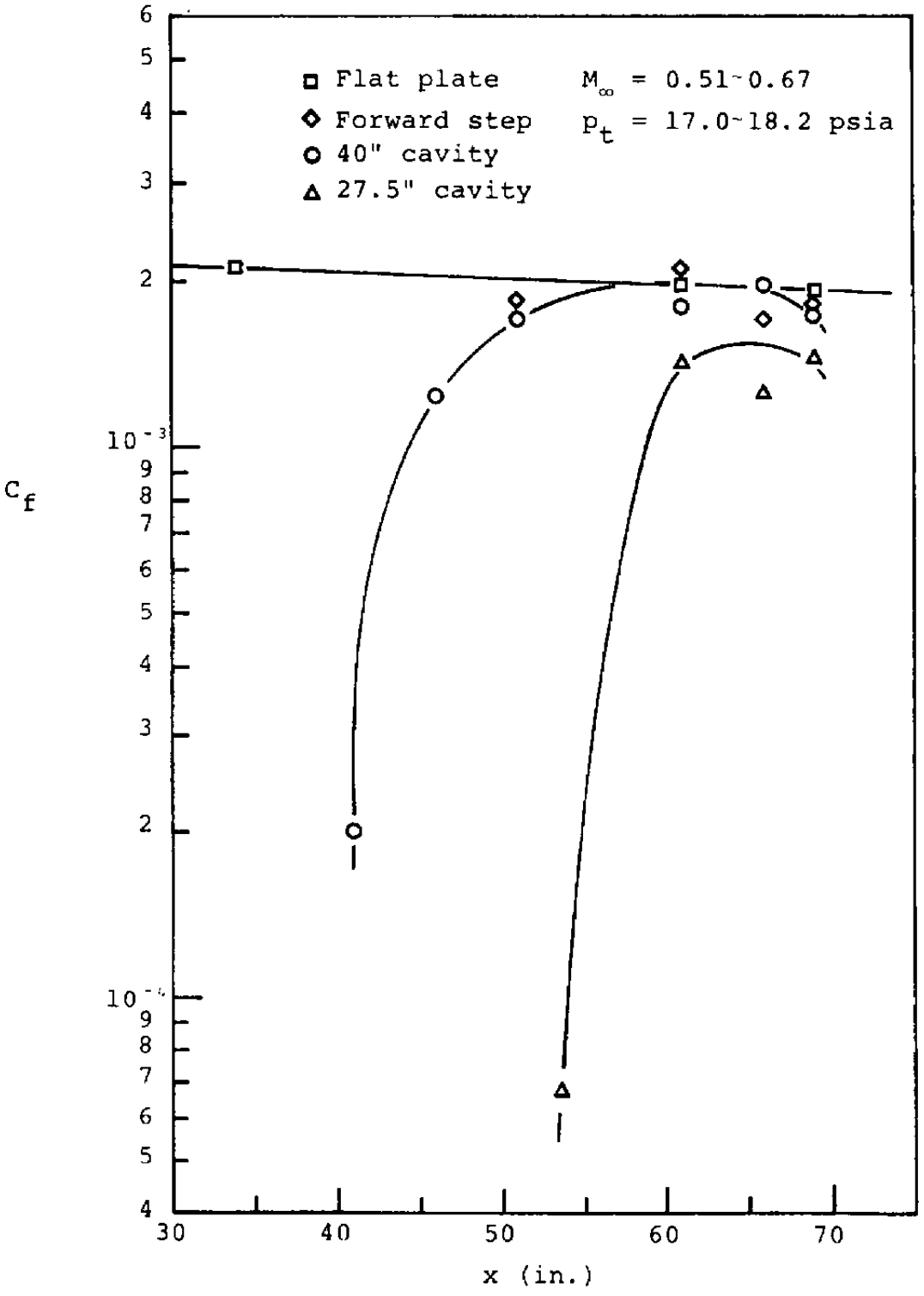

Figure 83. Distribution of skin friction coefficient along different models.

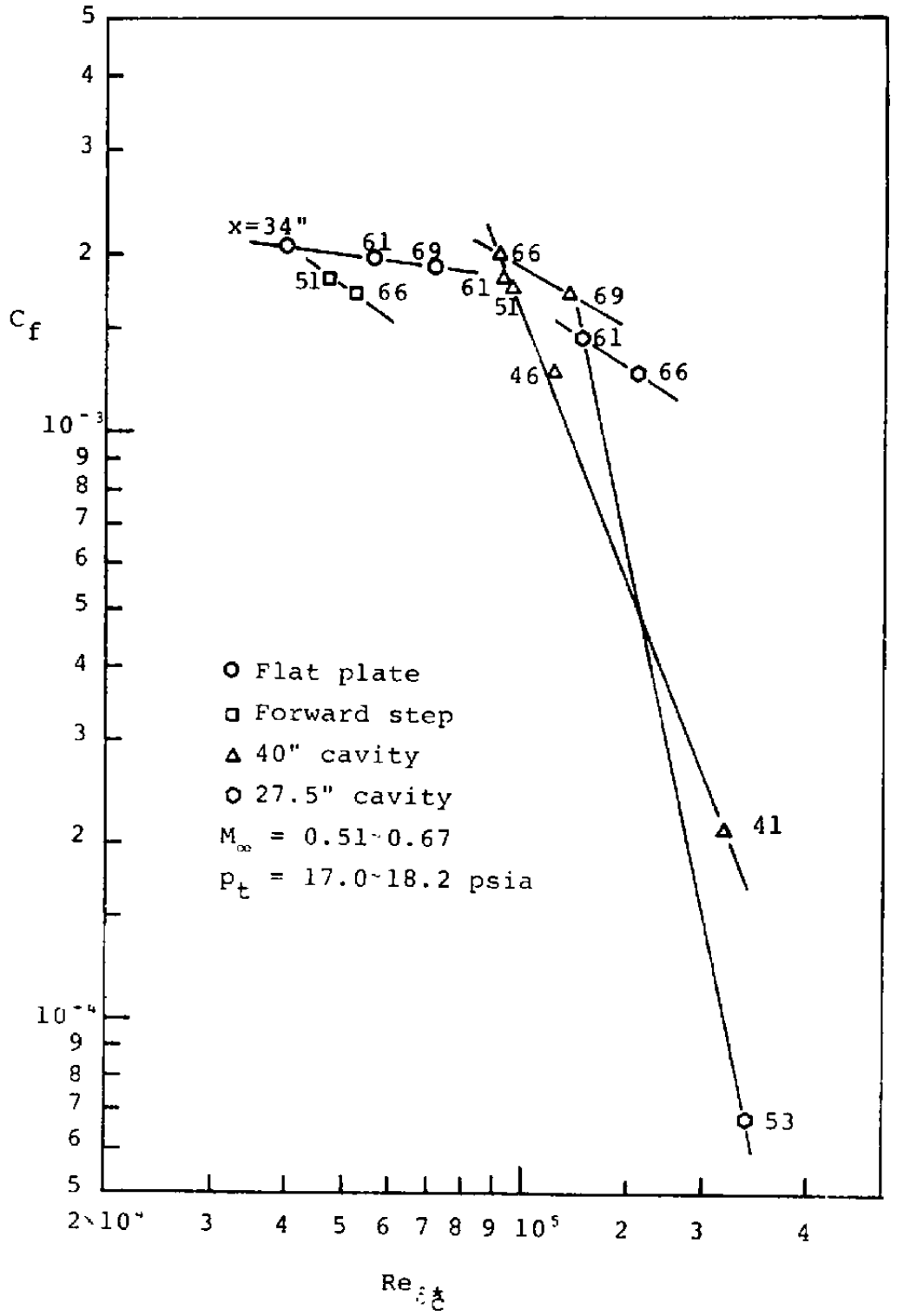

Figure 84. Variation of skin friction coefficient with a Reynolds number based on Coles' displacement thickness.

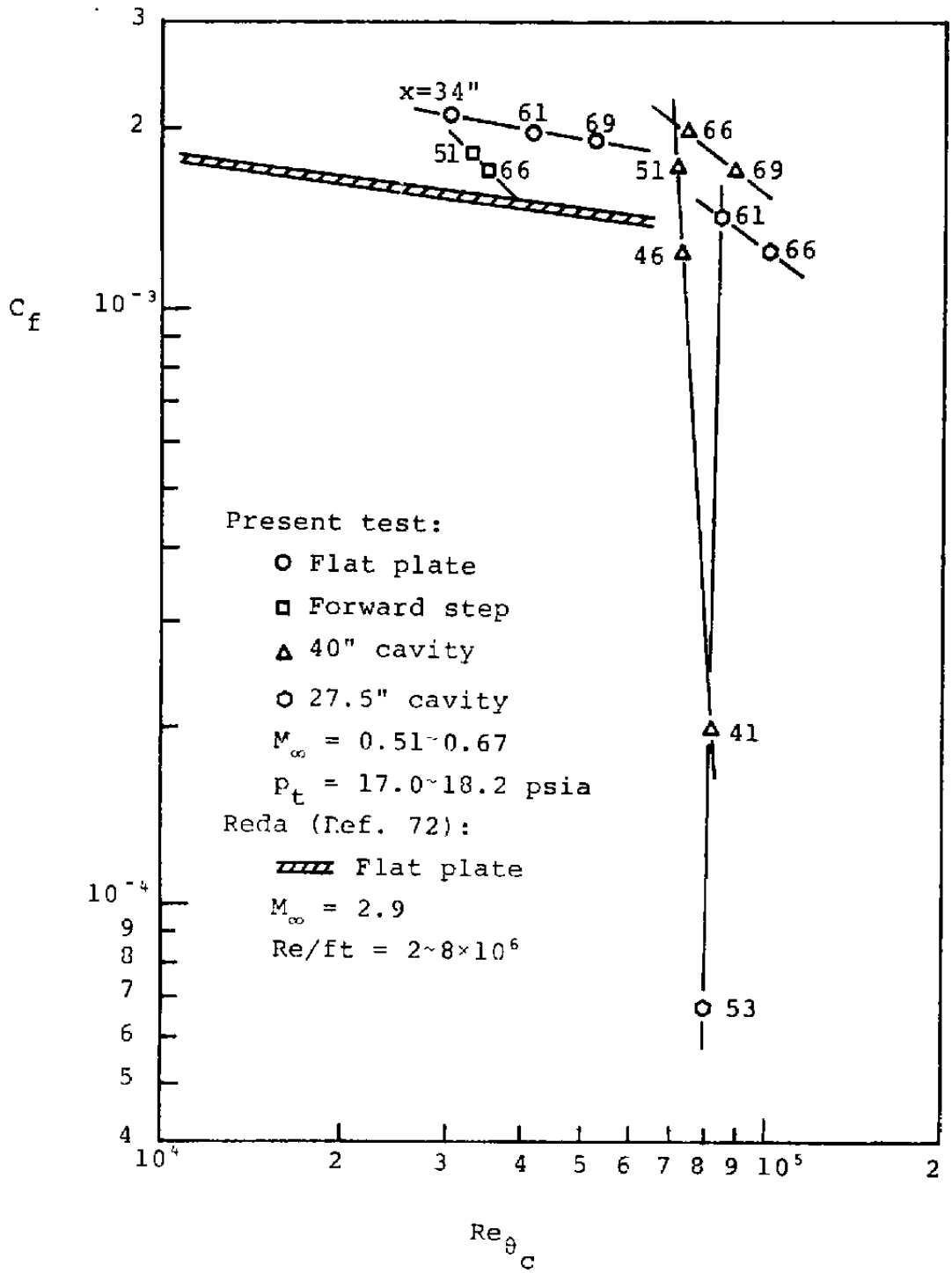

Figure 85. Variation of skin friction coefficient with a Reynolds number based on Coles' momentum thickness.

TABLE III

DIMENSIONS OF SKIN FRICTION BALANCE
(See Figure 86 for Notation)

Area of Circular Floating Element	0.490 in^2
Width of Gap	0.005 in
Length L	9.25 in
Length L_1	3.475 in
Length 6	0.625 in

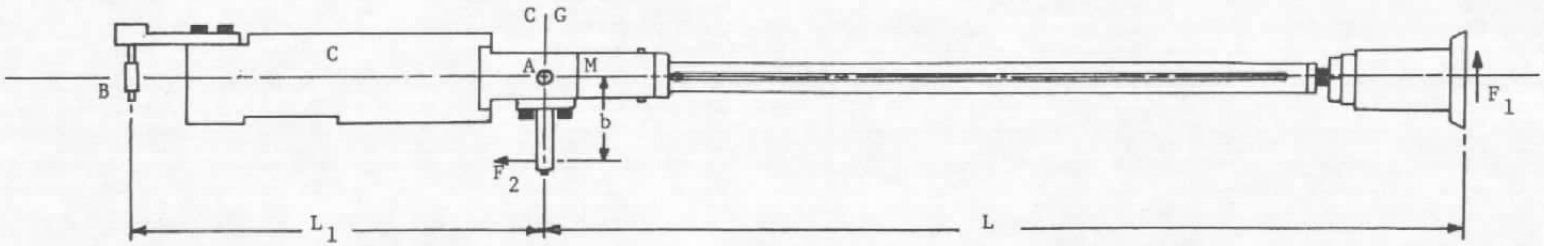

Figure 86. Schematic of balance arm for UTSI balance.

For the 40-inch shallow cavity,

$$C_f = 4.83 \times 10^{10} \left(Re_{\delta_c}^*\right)^{-2.693}, \quad 41 < x < 61 \text{ inches}$$

$$C_f = 1.13 \left(Re_{\delta_c}^*\right)^{-0.555}, \quad 41 < x < 66 \text{ inches}$$

For the 27.5-inch shallow cavity,

$$C_f = 4.76 \times 10^{20} \left(Re_{\delta_c}^*\right)^{-4.61}, \quad 41 < x < 61 \text{ inches}$$

$$C_f = 1.12 \left(Re_{\delta_c}^*\right)^{-0.567}, \quad 61 < x < 66 \text{ inches}$$

Since some of these formulas were determined by only two data points, the reliability is somewhat doubtful. This will be checked against our own direct force measurements soon.

Figure 85 shows the relation between the skin friction coefficient and the Reynolds number based on Coles momentum thickness. Reda's (Ref. 30) direct measurement of the surface shear for flow over a smooth flat plate is included for comparison. The present measurement is about 20 percent higher than Reda's result. This may be mainly due to different degrees in the surface roughness of the models used.

Skin friction coefficient measurements were just beginning at the end of this reporting period. Therefore, no results can be presented. However, a complete description of the operation of the skin friction balance will be given.

The operation of the skin friction balance is explained in detail in Figure 86. Important dimensions are given in Table III. The skin friction acting on the area of the floating element causes the support rod to rotate about point A. This motion is sensed by the motion of the LVDT core, at point B, with respect

to the LVDT coil. A pair of flexures, Figure 87, are provided at the pivot point. The flexures, made from a single piece of stainless steel, consist of a center axle and four ribs which radiate from the axle to an outer rim. The rim is held stationary in the balance housing while the axle is firmly attached to the floating element arm. When the arm is rotating the flexure ribs deform giving rotational stiffness and provide a frictional pivot. The torque provided by the flexures is indicated by M in Figure 86. Damping is also provided in the flexure to lessen the effects of vibrations (see Figure 87).

A counterweight C (Figure 86) is provided to place the center of gravity of the balance arm at the pivot point A. This also has the effect of lessening the sensitivity of the balance measurement to tunnel vibrations.

Upon the application of a skin friction force, F_1, the balance arm will rotate about A, displacing the LVDT core B. The LVDT signal will rotate the motor causing a linear extension of the coil spring. The elongated spring will create a force F_2 which will increase until the moment of the skin friction force (F_1 L) will equal the moment of the spring force (F_2b). The total rotation of the motor shaft, as measured by the potentiometer, is then proportional to the force F_1.

The electronics which control the sevomechanism are shown in Figure 88. The LVDT coil is electrically excited by a 20 kHz signal from a Schaevitz CAS-200 signal conditioner. Movement of the LVDT core from the null position results in a coil output signal of the same frequency but different phase from the excitation signal. The signal conditioner produces a signed-DC output proportional to the AC input from the coil. The sign of the output (plus or minus) depends upon the phase of the coil output with respect to the excitation signal, one sign for each of the directions of motion of the core from the null position.

The DC signal from the Schaevitz signal conditioner is fed to the DC motor controller. The motor controller consists of

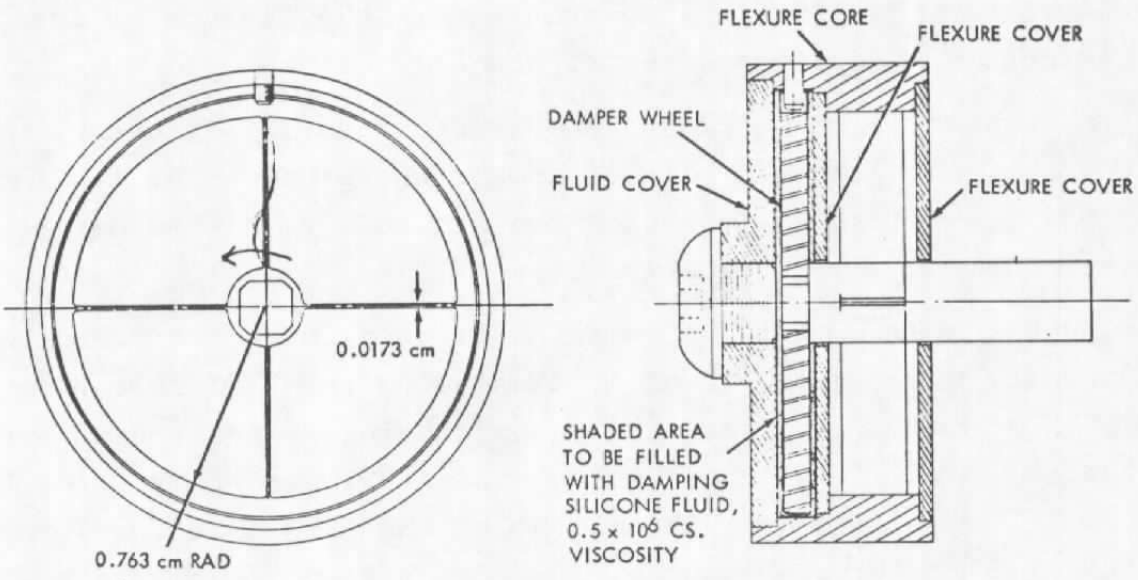

Figure 87. Flexure used in UTSI balance (Ref. 4).

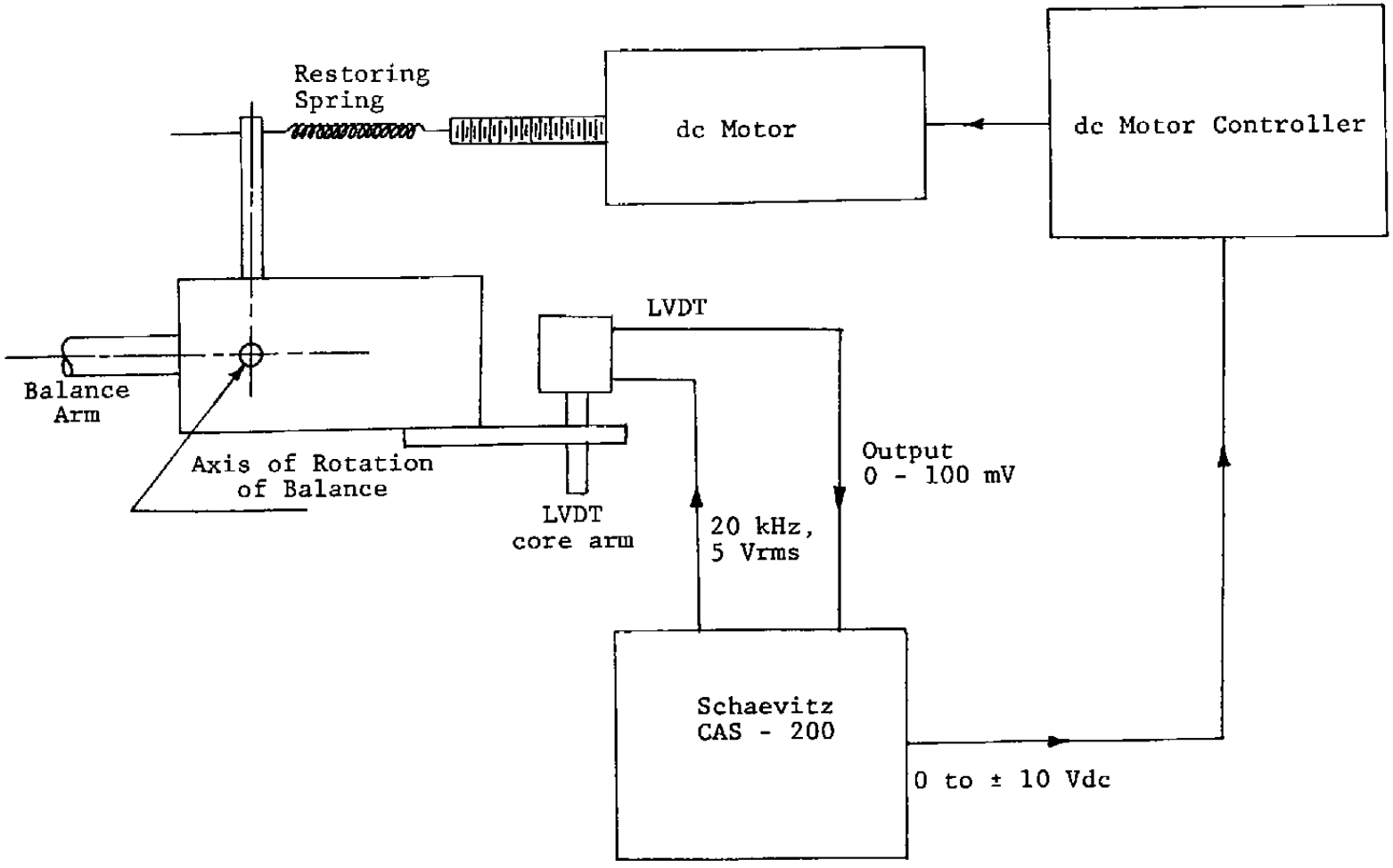

Figure 88. Skin friction balance electronics.

a high current operational amplifier (1 amp) (Figure 89). The amplified DC signal then operates the DC motor (155 rpm, 60 in oz maximum torque). The speed of the motor is controlled by the magnitude of the input voltage, which, in turn, depends upon the distance of the LVDT core from null. As the core approaches the null position, the motor will slow and come to a stop, if enough damping has been provided in the system to prevent overshoot.

The skin friction balance was calibrated by hanging small weights from a flexible filament which was attached to the floating element by tape and suspended over a pivot which has jeweled bearings (Figure 90). The pivot was attached to the end of the "dummy" block which contains the floating element; the adjacent floor block was removed to facilitate this operation. Typical calibration curves are shown in Figure 91.

A number of modifications were made to the balance before it would operate in the UTSI Transonic Wind Tunnel. In addition to modifying the housing to attack the balance to the UTSI tunnel, modifications also were made to the mechanical and electrical parts of the feed-back loop.

Two aspects of the operating environment in the UTSI tunnel were different from those which exist in the NOL tunnel, namely, the magnitude of the skin friction force to be measured and the vibrational environment. The balance was originally designed to measure skin friction forces in the range 0.03 to 1 gm while the forces expected in the UTSI tunnel are 1 to 15 gm. The average UTSI tunnel acceleration is 4 g's, rms. Therefore, a stiffer restoring spring and additional damping were required. After replacing a broken flexure and the damping fluid satisfactory performance was obtained with a very stiff restoring spring.

Two motor control systems were examined. The first motor controller used, manufactured by AST Servo Systems, Inc., would not operate in a stable manner and was replaced by a high current operational amplifier (Figure 89). Electronic RC damping circuits were not required to stabilize the servo circuit.

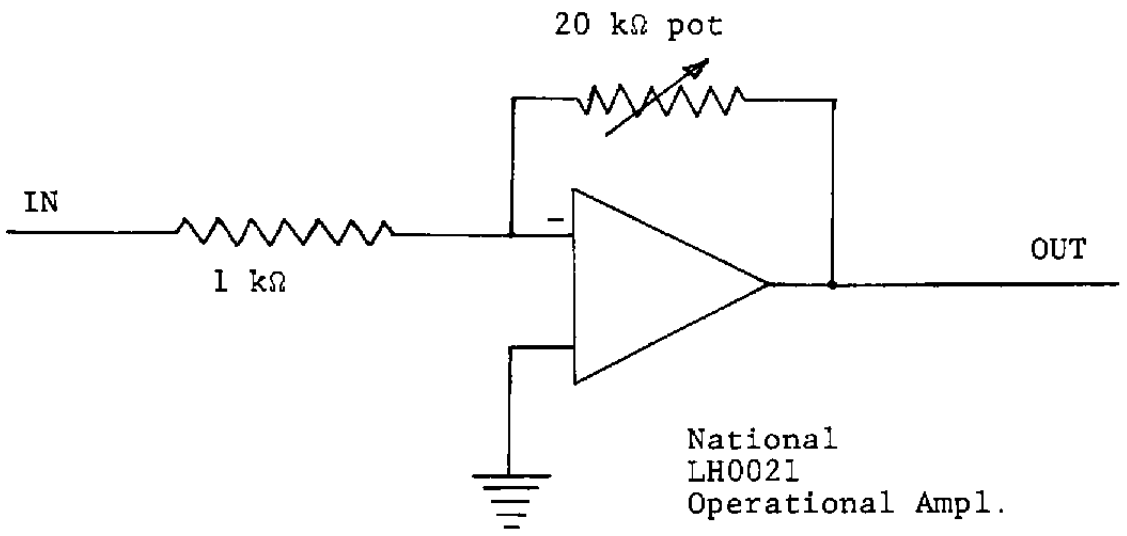

Figure 89. Motor controller.

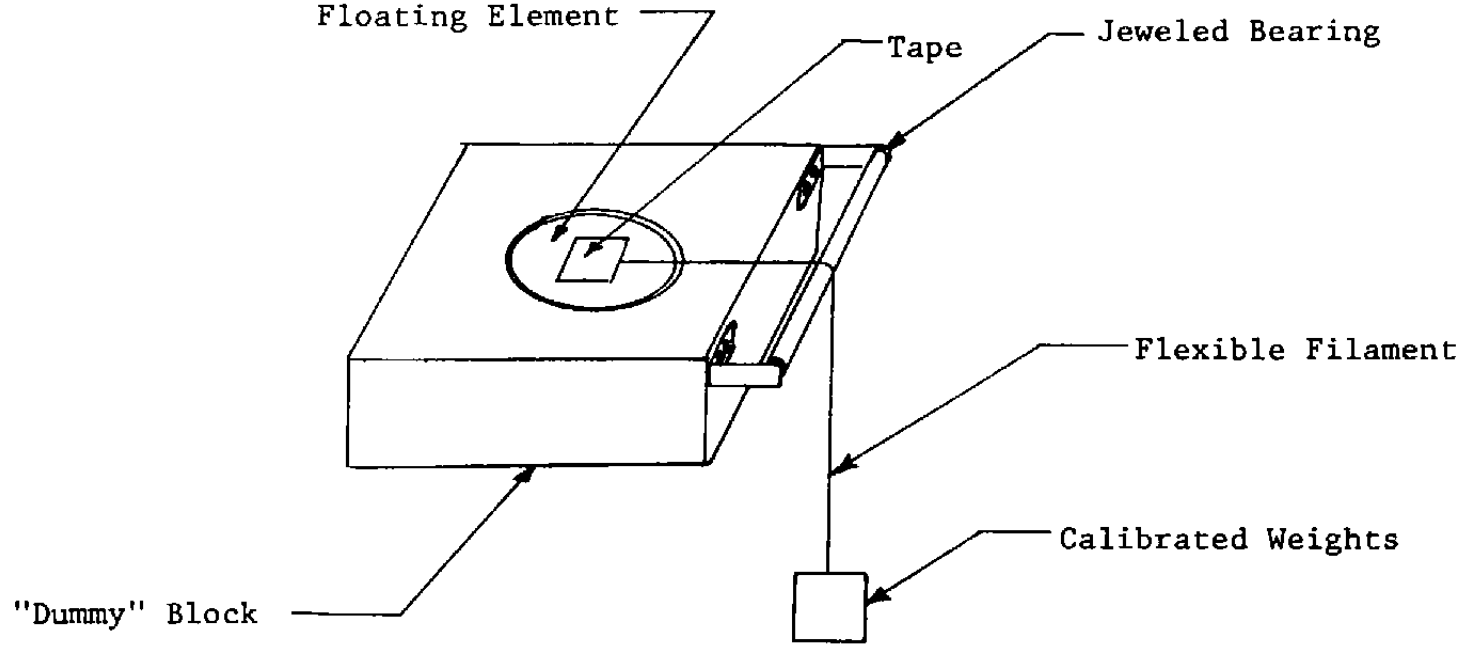

Figure 90. Calibration technique.

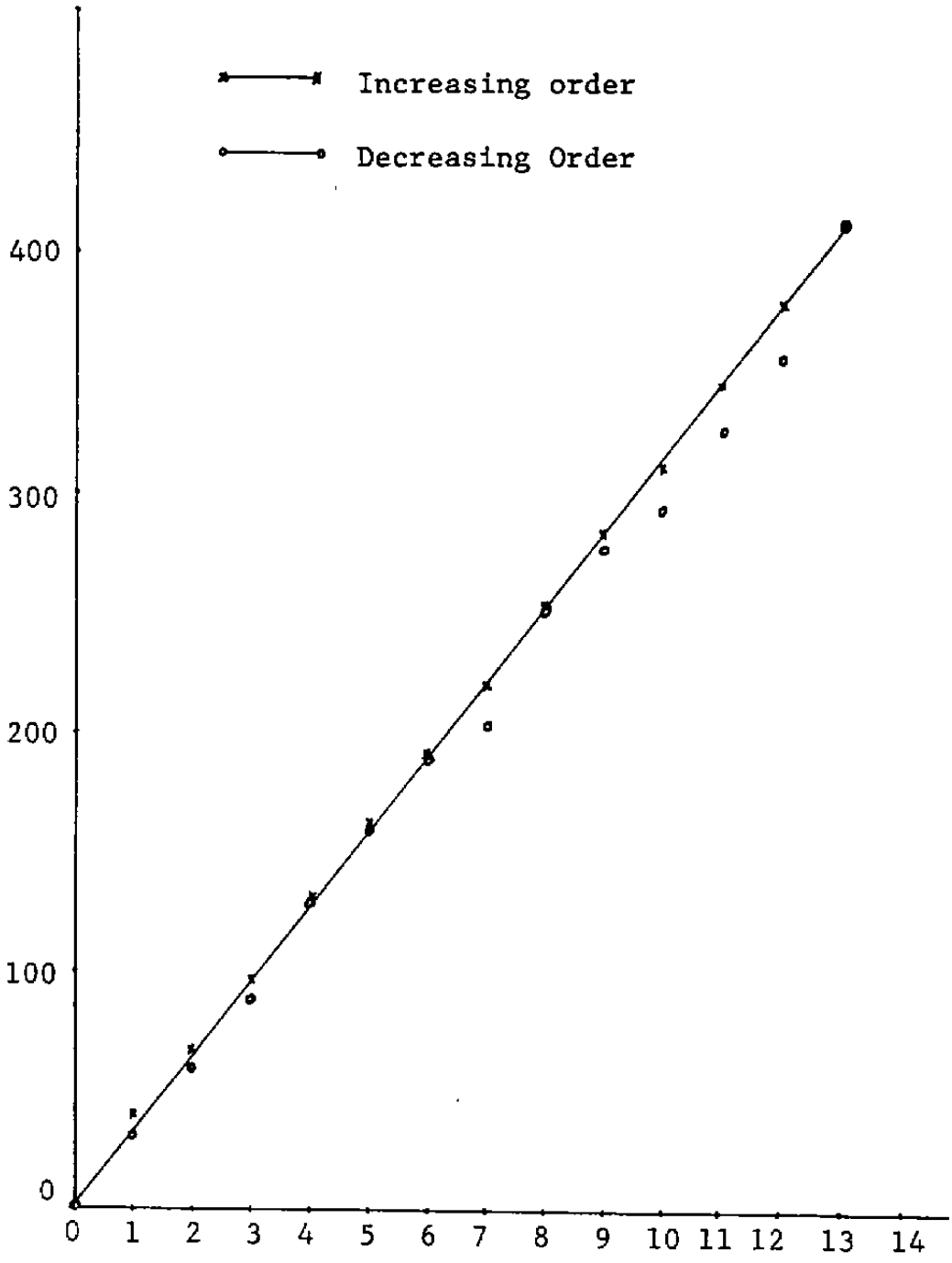

Figure 91a. Calibration curve of skin friction meter mounted in UTSI Transonic Wind Tunnel.

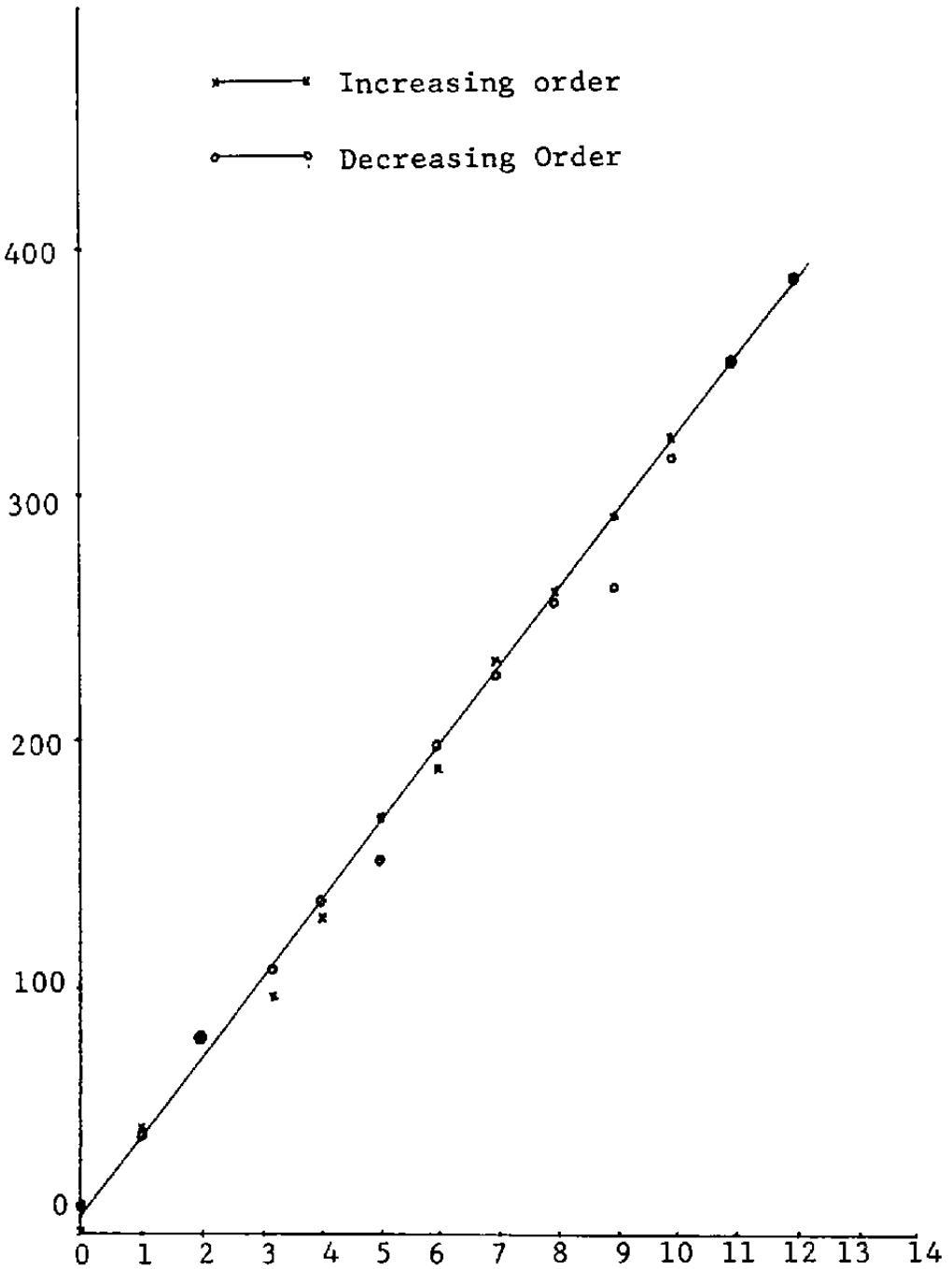

Figure 91b. Calibration curve of skin friction meter mounted in UTSI Transonic Wind Tunnel.

The signal from the potentiometer which was geared to the servomotor (Figure 10) was amplified and recorded on an oscillograph.

5.0 THEORETICAL CONSIDERATIONS

In order to correlate the experimentally measured pressure data for flows past cavities at different Mach numbers, the following theoretical method has been developed.

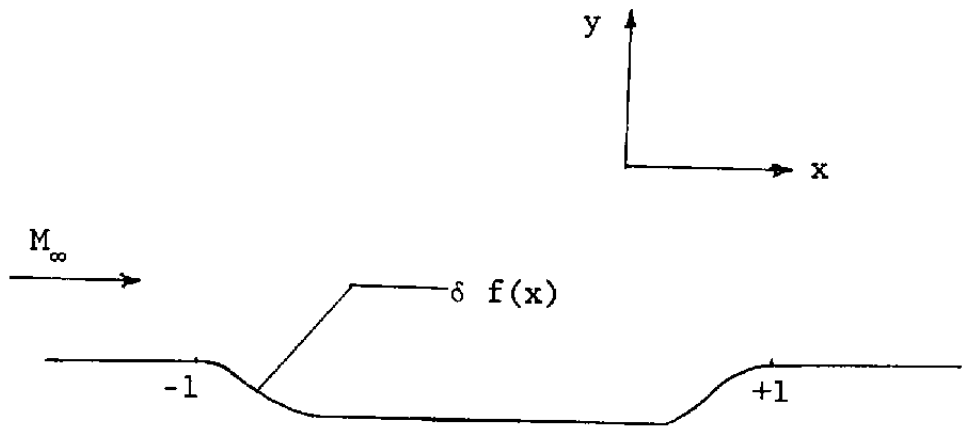

Sketch of Flow Field

In a purely subsonic flow, the pressure coefficient, $C_p(x)$, for flow past a cavity as shown in the sketch above, based on subsonic small disturbance theory, can be written as

$$C_p(x) = \frac{2\delta}{\pi\sqrt{1-M_\infty^2}} \oint_{-1}^{1} \frac{f'(\xi)}{\xi - x}\, d\xi$$

We have developed a method (Ref. 1) by which the inverse solution for the above equation can be obtained, that is, we can obtain an expression for the shape of an inviscid stream line on the cavity, the flow past which will produce an experimentally measured C_p - distribution based on inviscid subsonic small disturbance theory. Such an expression can be written as

$$5 \quad f(x) = -\frac{(1-M_\infty^2)^{\frac{1}{2}}}{2\pi} \oint_{-1}^{1} \ln \left| \frac{r(\eta) + r(x)}{r(\eta) - r(x)} \right| C_p(\eta) d\eta$$

where $r(x) = \{ (1 - x)/(1 + x) \}^{\frac{1}{2}}$

This expression ought to give a reasonably good approximation for the outer inviscid flow stream line under the assumption that the normal pressure gradient in the viscous layer is negligible. Figure 92 represents a typical inviscid stream line shape along the cavity wall which corresponds to a measured $C_p(x)$.

Based on a conjecture that the thin viscous layer thickness may not change appreciably when we increase the Mach number from a pure subsonic level to a transonic level (with $M_\infty < 1$, still), we have used the outer inviscid stream line computed as indicated earlier for a pure subsonic flow, to compute $C_p(x)$ at a higher Mach number using inviscid transonic small disturbance equation. The small disturbance potential ϕ in transonic flow is governed by

$$(K - \phi_x)\, \phi_{xx} + \phi_{\tilde{y}\tilde{y}} = 0 \quad , \quad \tilde{y} = 5^{\frac{1}{3}} y$$

$$K = (1 - M_\infty^2)/5^{\frac{2}{3}}$$

We have modified and adapted a computer program developed by Murman and Krupp for solving such an equation by a mixed finite difference scheme for airfoil flows, to solve the flow past a cavity.

An experimental C_p distribution for $M_\infty = 0.58$ and cavity length 23.5" has been utilized to compute the inviscid stream line along the cavity by the inverse method for pure subsonic flows outlined earlier. Using this inviscid stream line, a transonic inviscid flow computation has been carried out for

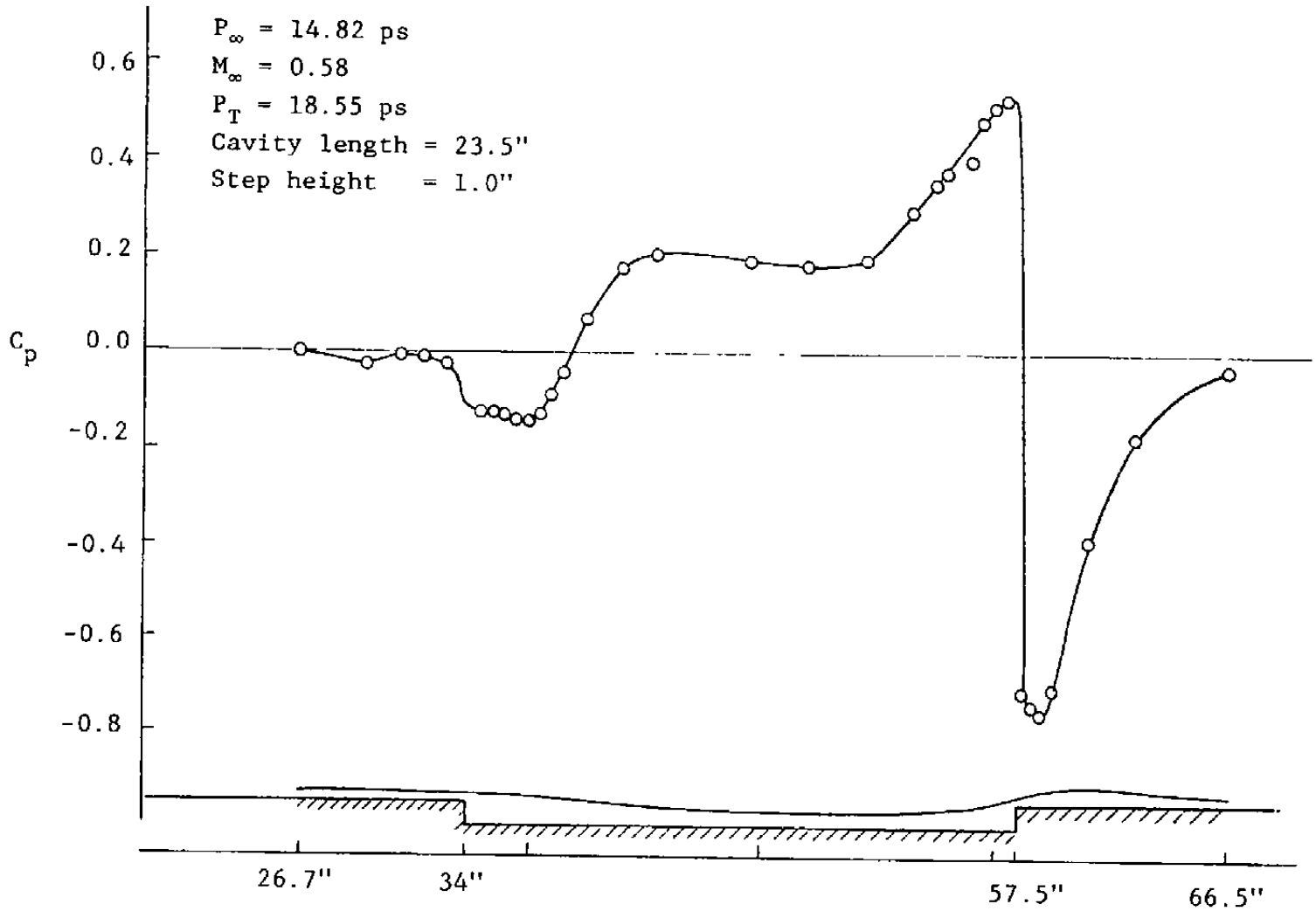

Figure 92. Computed inviscid streamline corresponding to the experimentally measured C_p distribution at M_∞ = 0.58.

$M_\infty = 0.84$. The computed C_p distribution agrees rather well with the measured C_p - distribution at $M_\infty = 0.84$ (Fig. 93). This shows that the viscous flow is limited to the same region at both Mach numbers, thus the inviscid stream line outside the boundary layer does not seem to change much for Mach numbers from 0.58 to 0.84.

It is well known (Ref. 31) that the inviscid transonic equation and Rankine-Hugoniot conditions lead to inconsistencies in the region where the shock terminating an embedded supersonic pocket touched the curved surface of an airfoil, and the computed surface pressure jump is more than what is observed experimentally. The viscous-transonic equation, which includes the effects of compressive viscosity on the structure and thus location of the shock, seeks to overcome these shortcomings. It is a small disturbance approximation to the Navier-Stokes equations and includes the effects of compressive viscosity on non-Rankine-Hugoniot regions, but does not include the boundary layer effects. It can be written as

$$K_v \varphi_{xxx} + (K_i - \varphi_x)\varphi_{xx} + \varphi_{yy} = 0$$

where

$$K_i = \frac{1 - M_\infty^2}{\delta^{\frac{2}{\tau}} M_\infty^{4/3} (\gamma + 1)^{\frac{2}{\tau}}}$$ - Inviscid transonic similarity parameter

$$K_v = \frac{(1 + \gamma - 1)}{Pr} \frac{}{Re\, \delta^{\frac{2}{\tau}} (\gamma + 1)^{\frac{2}{\tau}} M_\infty^{4/3}}$$

- viscous transonic similarity parameter

This equation is parabolic everywhere, unlike the inviscid transonic equation which is mixed elliptic-hyperbolic, but it is not an initial value problem in any one direction. The boundary conditions are prescribed all around the boundary like

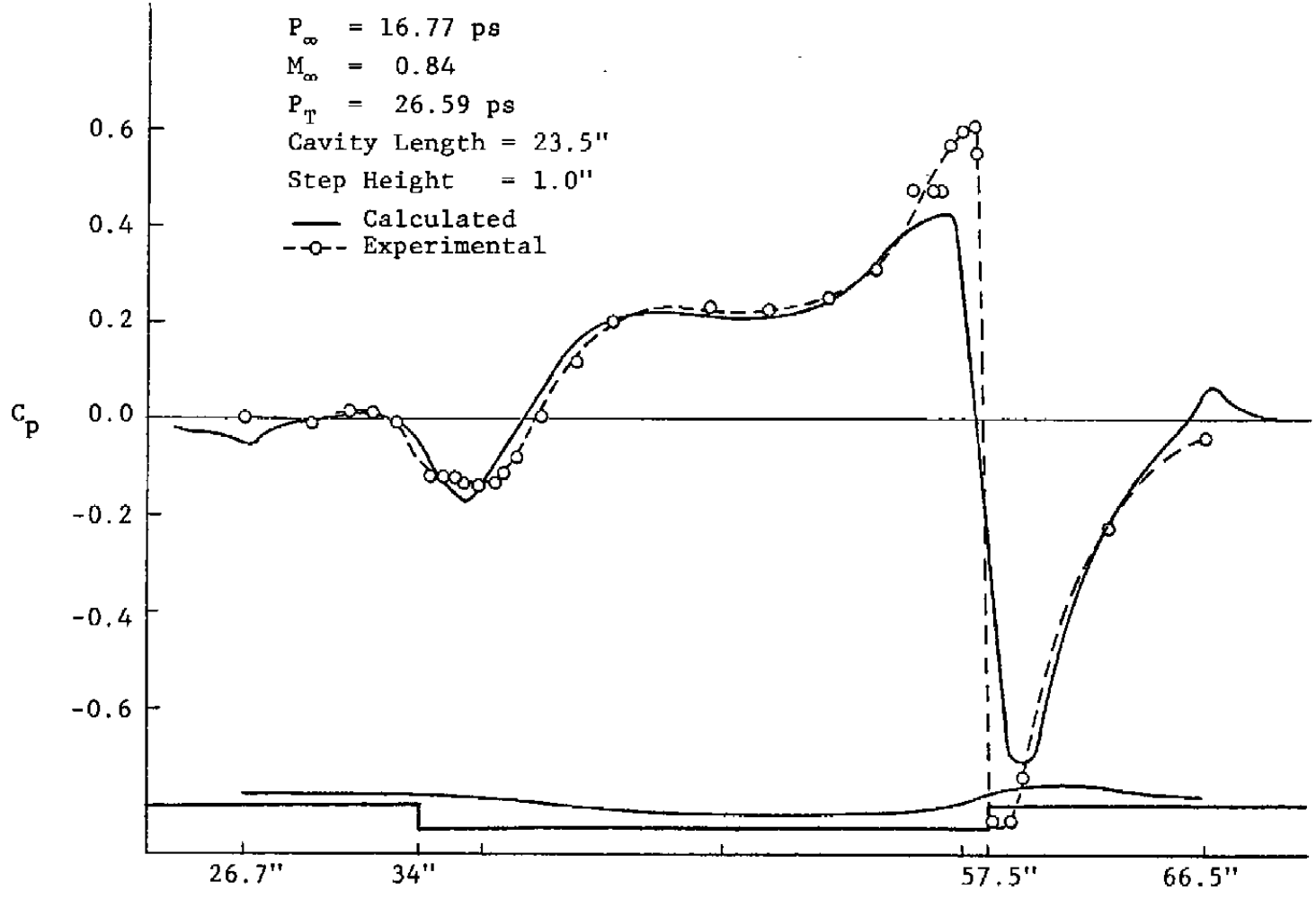

Figure 93. Experimental and calculated C_p - distributions at M_∞ = 0.84.

an elliptic problem. We have adopted a finite difference scheme which is similar to the "box scheme" developed by Keller (Ref. 32). The non-linear algebraic equations are solved iteratively by a horizontal line relaxation technique. The results are very promising. The details of the method of solution are outlined in the Appendix.

We have performed test calculations for a thin parabolic symmetric airfoil. For $K_v = 0.01$ and $K_i = 0.725$, starting with zero initial conditions, Figure 94 shows the development of the C_p distribution on the airfoil surface at 100 sweep intervals in the relaxation method. Figure 95 shows the converged C_p after 1600 sweeps. Several runs have been made to analyze the influence of the viscous transonic similarity parameters as it is reduced to smaller and smaller values. It is expected theoretically that the results ought to approach those of the inviscid flow computations. It has been found that when the viscous similarity parameter K_v is reduced from 0.01 to 0.005 and to 0.001 for a subcritical case with $K_i = 1.67$, the C_p -distribution is essentially unchanged and it agrees with known computational and experimental results (Figs. 96 and 97). For a super-critical case with $K_i = 1.0$, the C_p - distribution has been shown to undergo little change as K_v is reduced from 0.01 to 0.005 except in the region of flow re-expansion behind the shock (Figs. 98 and 99). The method has also been extended to compute the flow with a separation wake just behind the shock terminating the sonic rocket. With $K_v = 0.01$ and $K_i = 1.00$, Figures 100, 101 and 102 show the C_p - distribution with or without separation wakes. Figure 102 indicates the forward movement of the shock because of the separation and the significant influence on the flow field way ahead of the shock.

The feasibility of the use of viscous transonic equation for computing invisid transonic flows is established. The method of solution has some advantages over the method of mixed difference schemes for inviscid transonic equation. Further applications of

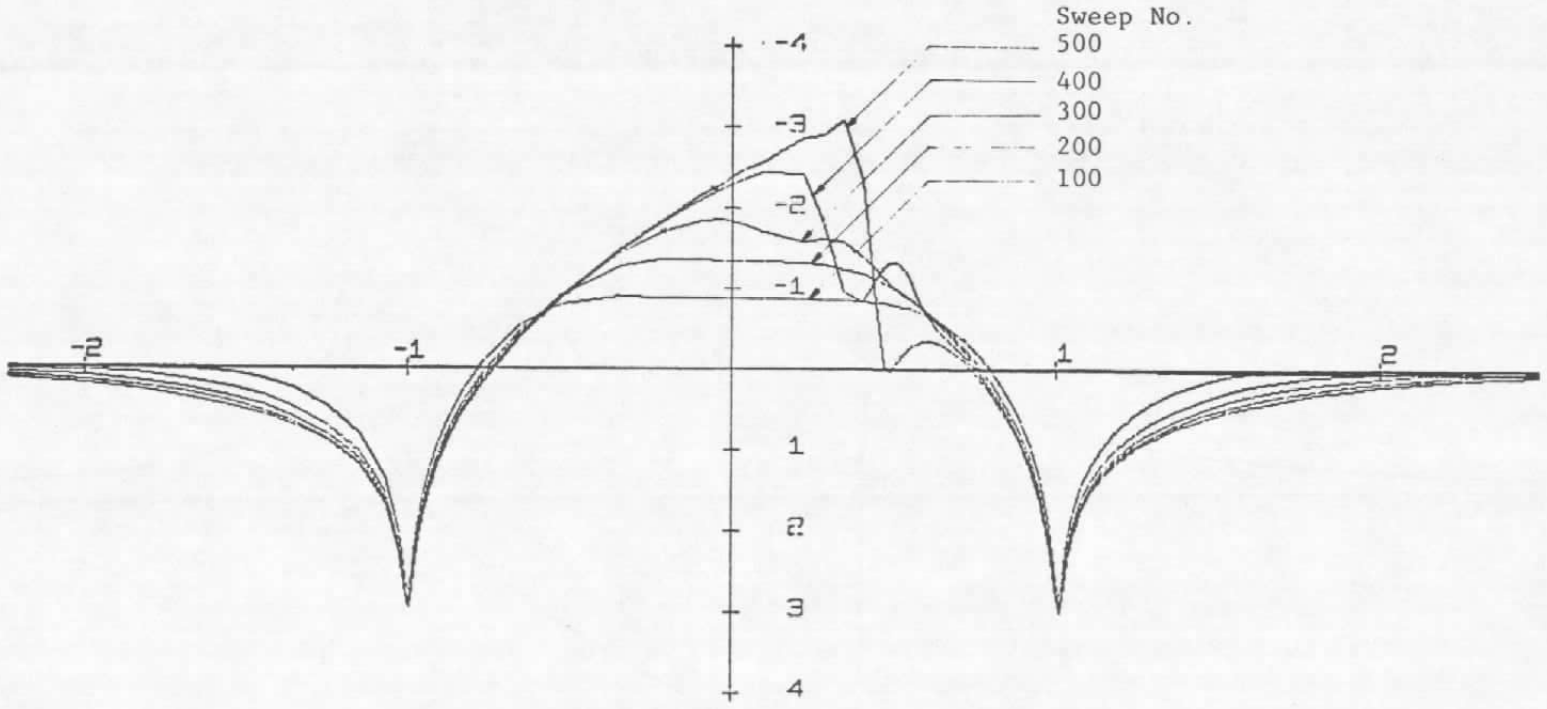

Figure 94. Development of C_p distribution.

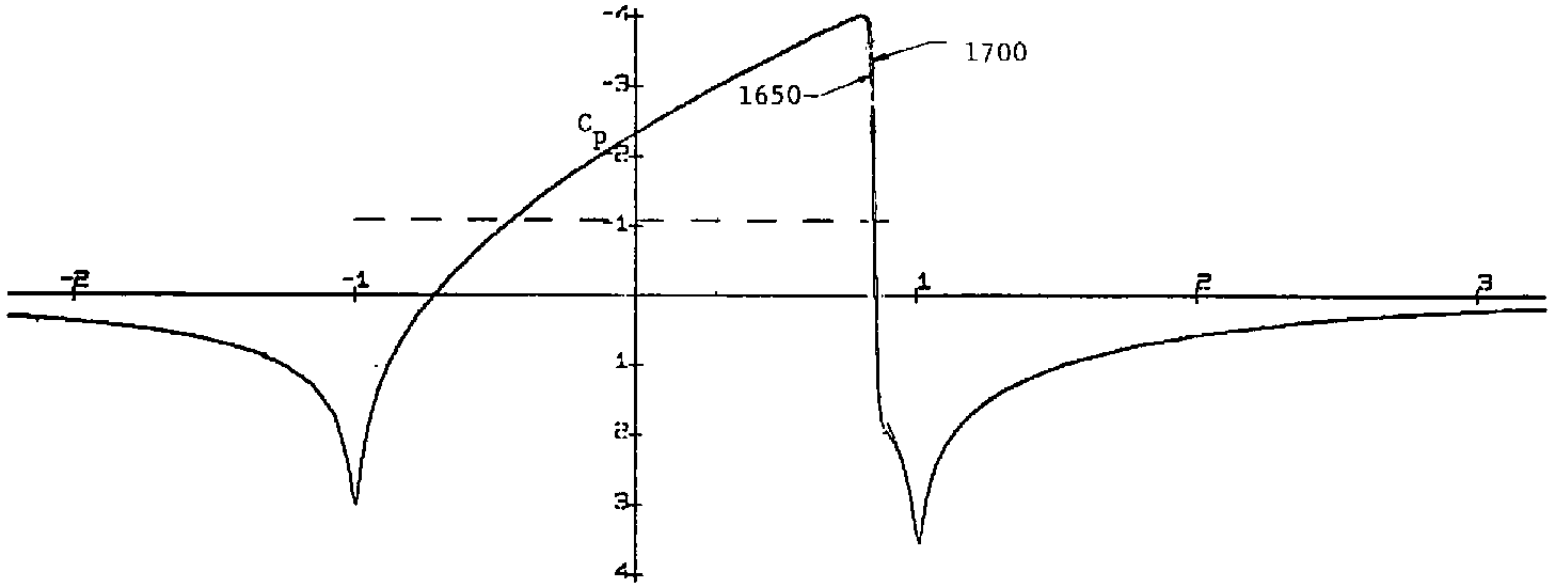

Figure 95. C_p - distribution on the surface of a parabolic airfoil - supercritical case - K_v = 0.01, K_i = 0.725, sweeps 1650 and 1700.

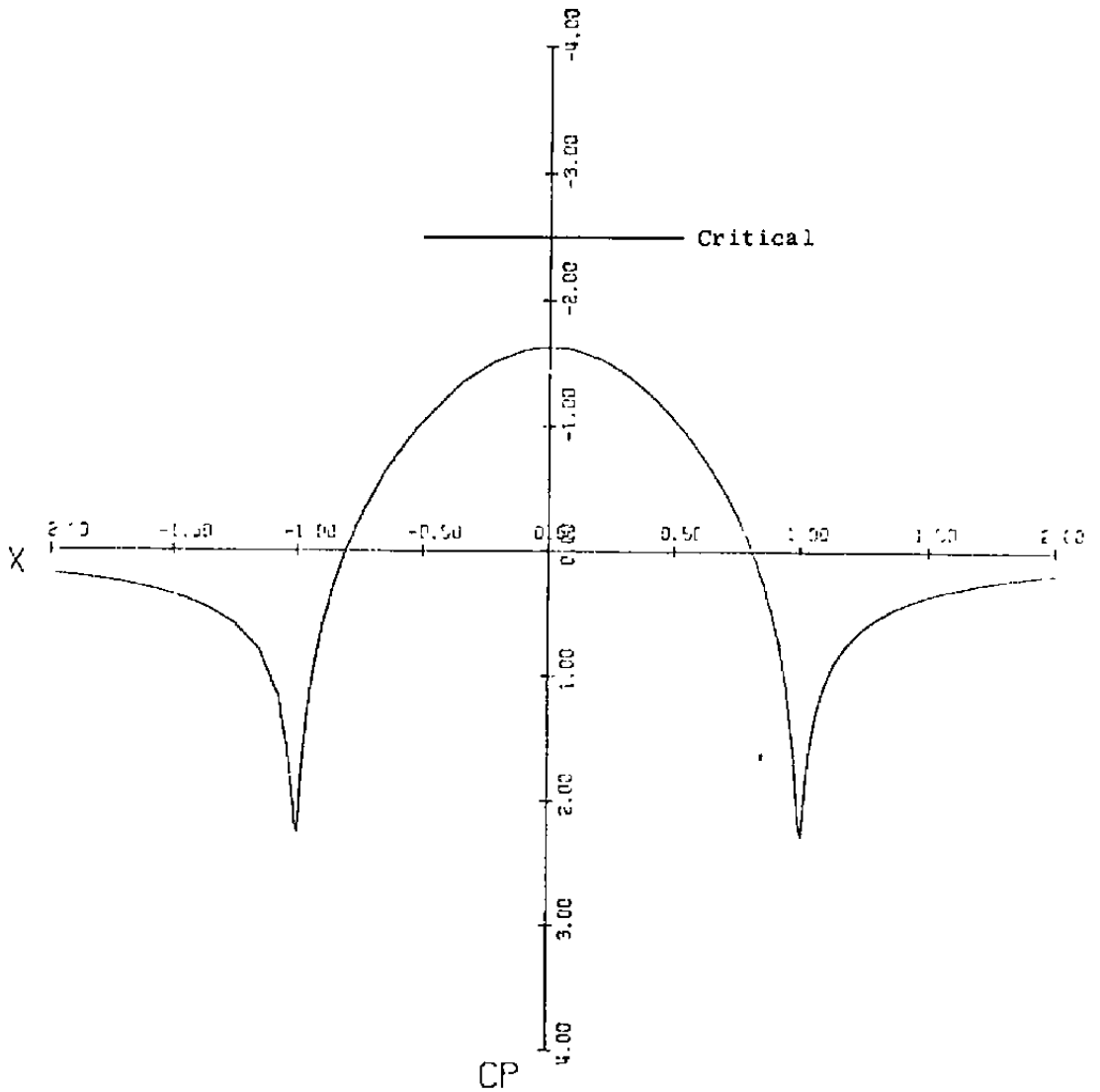

Figure 96. C_p - distribution on the surface of a parabolic airfoil - sub-critical case - K_v = 0.005, K_i = 1.67.

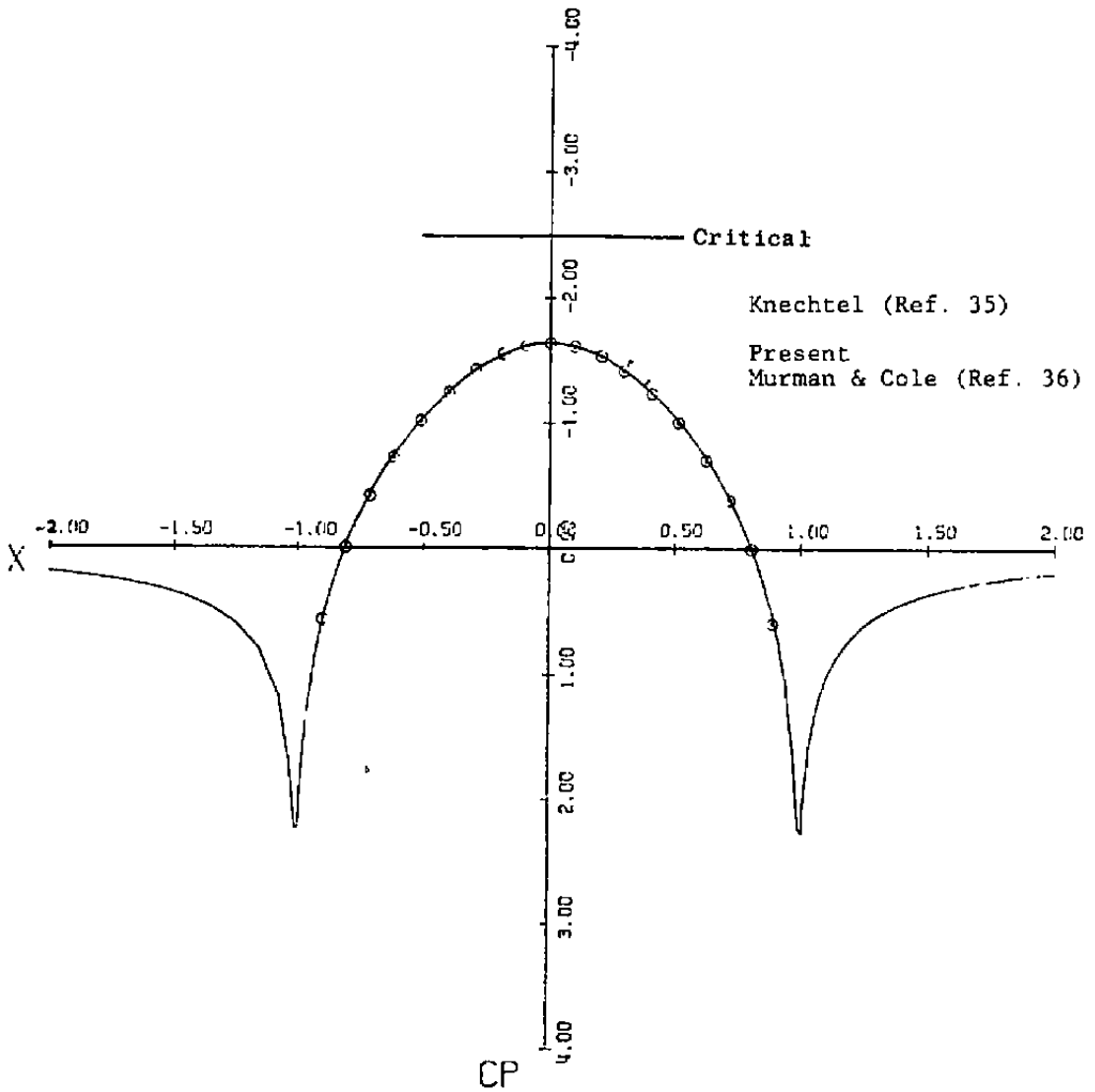

Figure 97. C_p - distribution on the surface of a parabolic airfoil - sub-critical case - K_v = 0.001, K_i = 1.67.

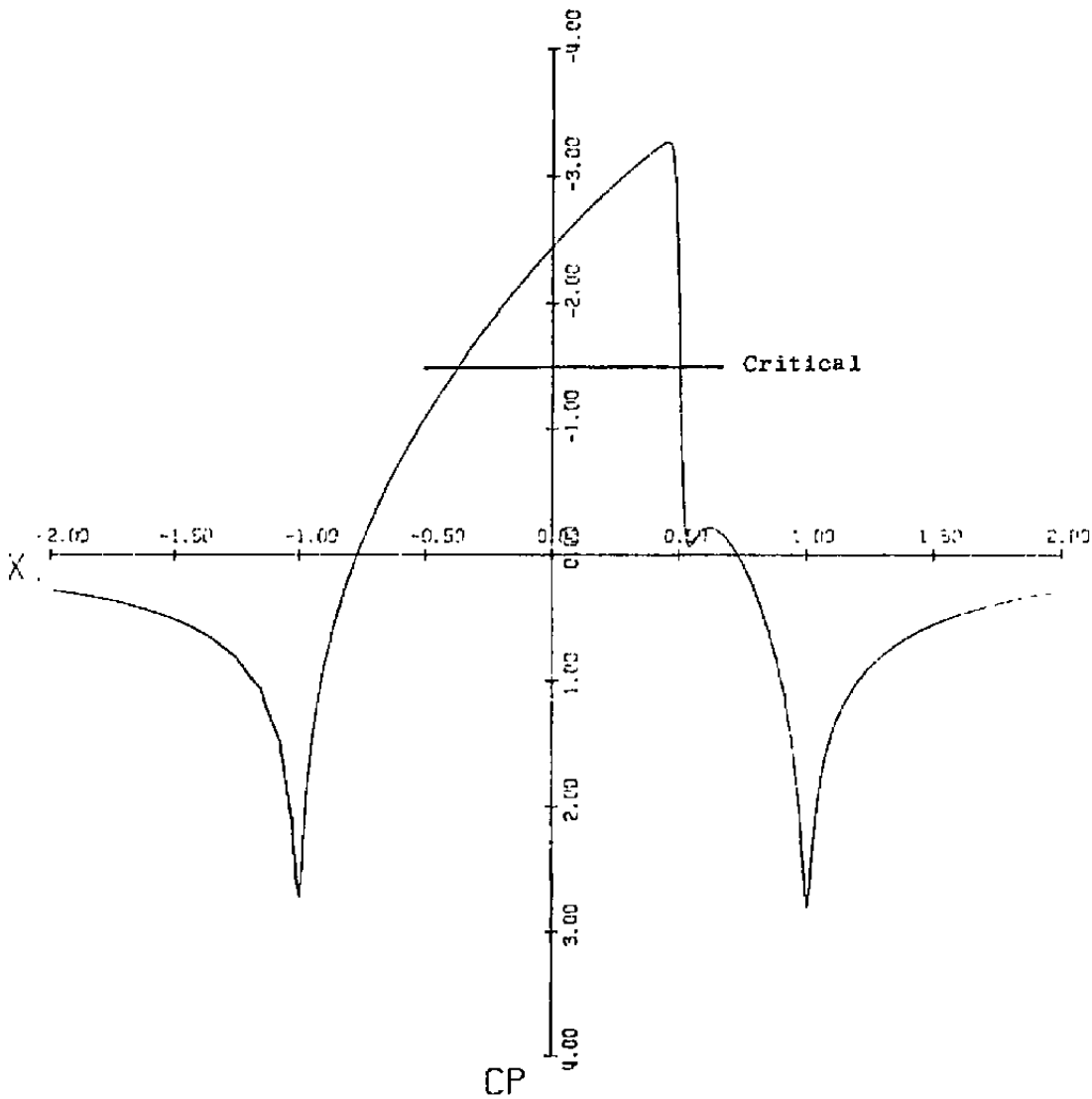

Figure 98. C_p - distribution on the surface of a parabolic airfoil - super-critical case, K_v = 0.01, K_i = 1.0.

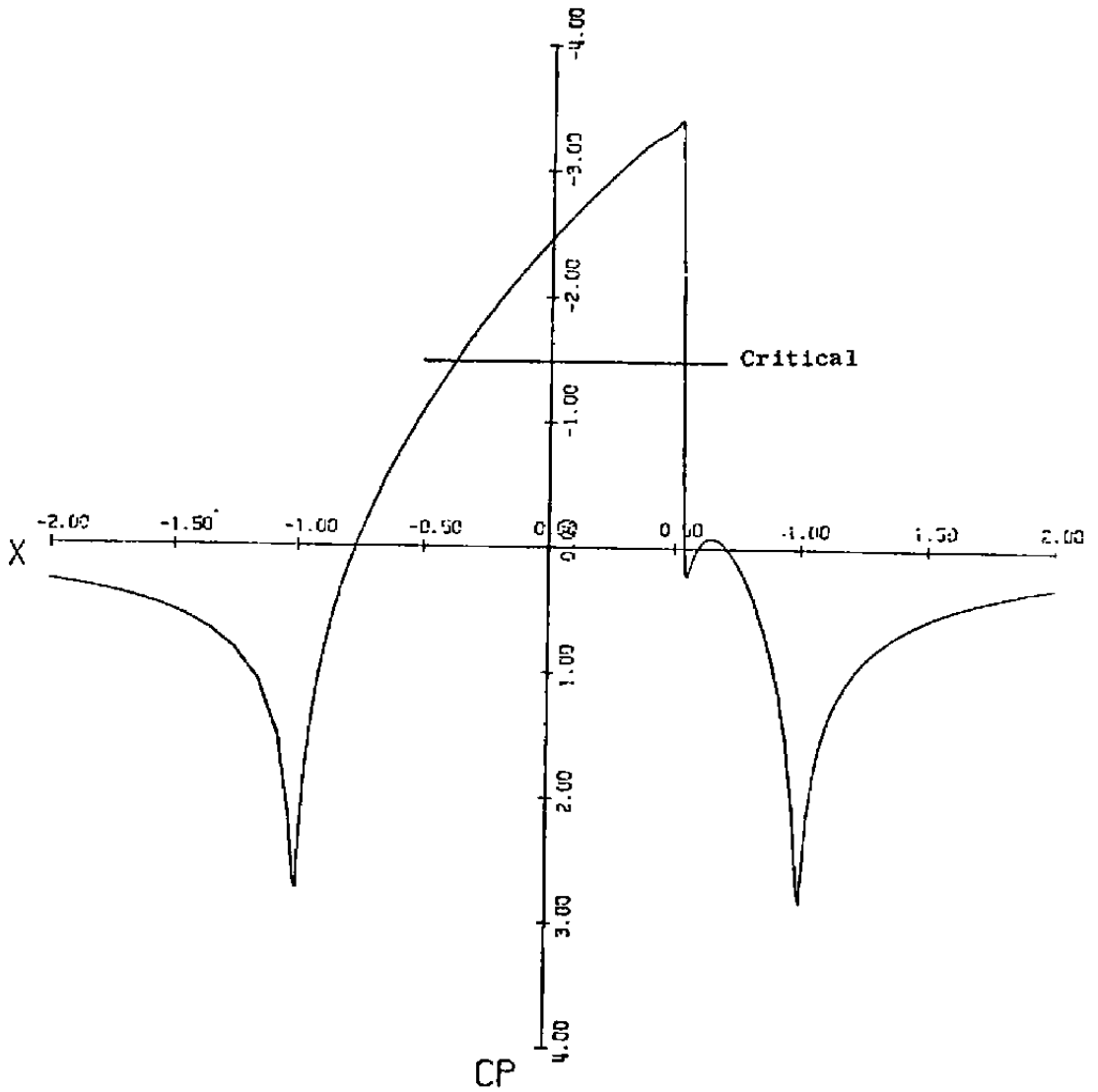

Figure 99. C_p - distribution on the surface of a parabolic airfoil - super-critical case - $K_v = 0.005$, $K_i = 1.0$.

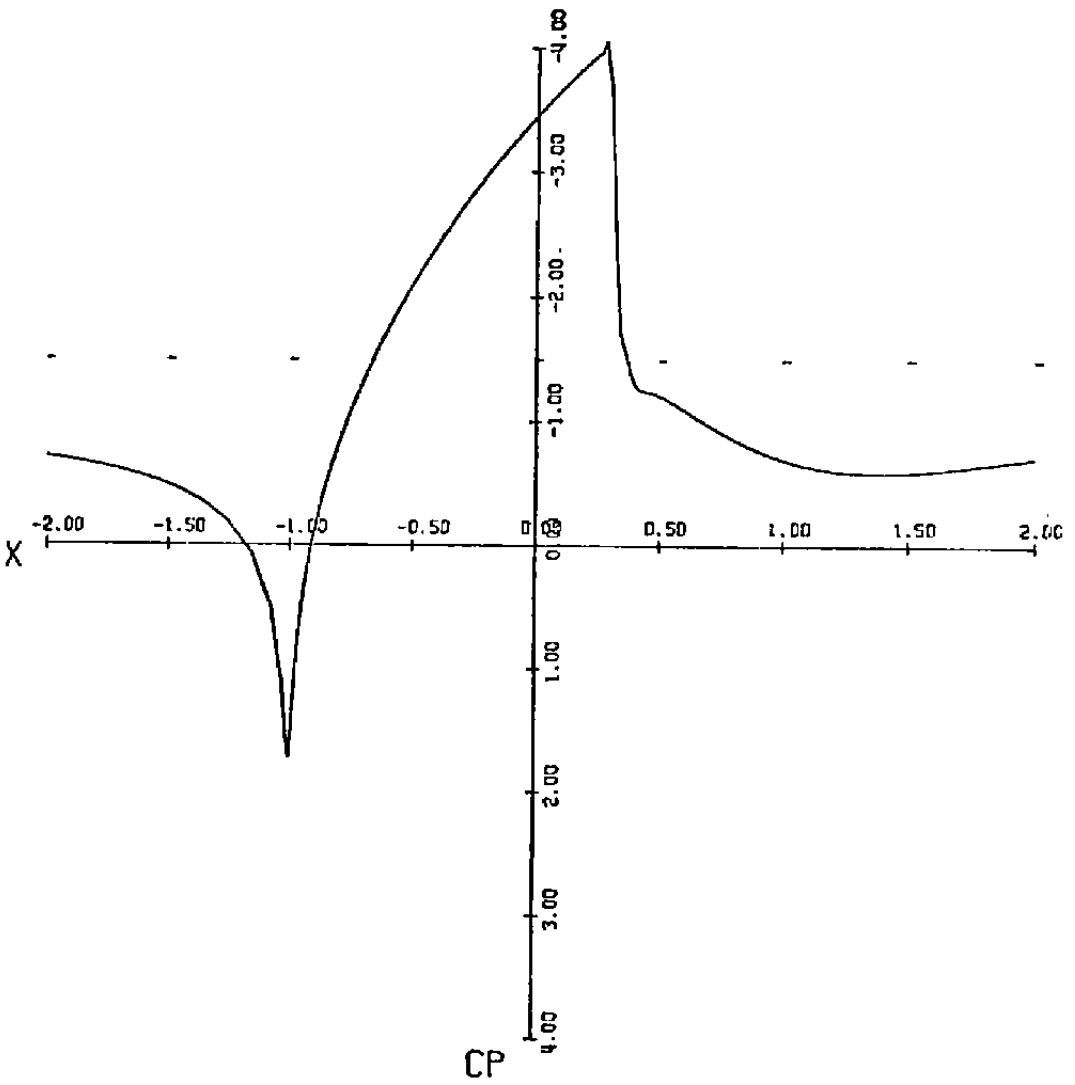

Figure 100. Intermediate C_p - distribution after 100 iterations with a separate wake.

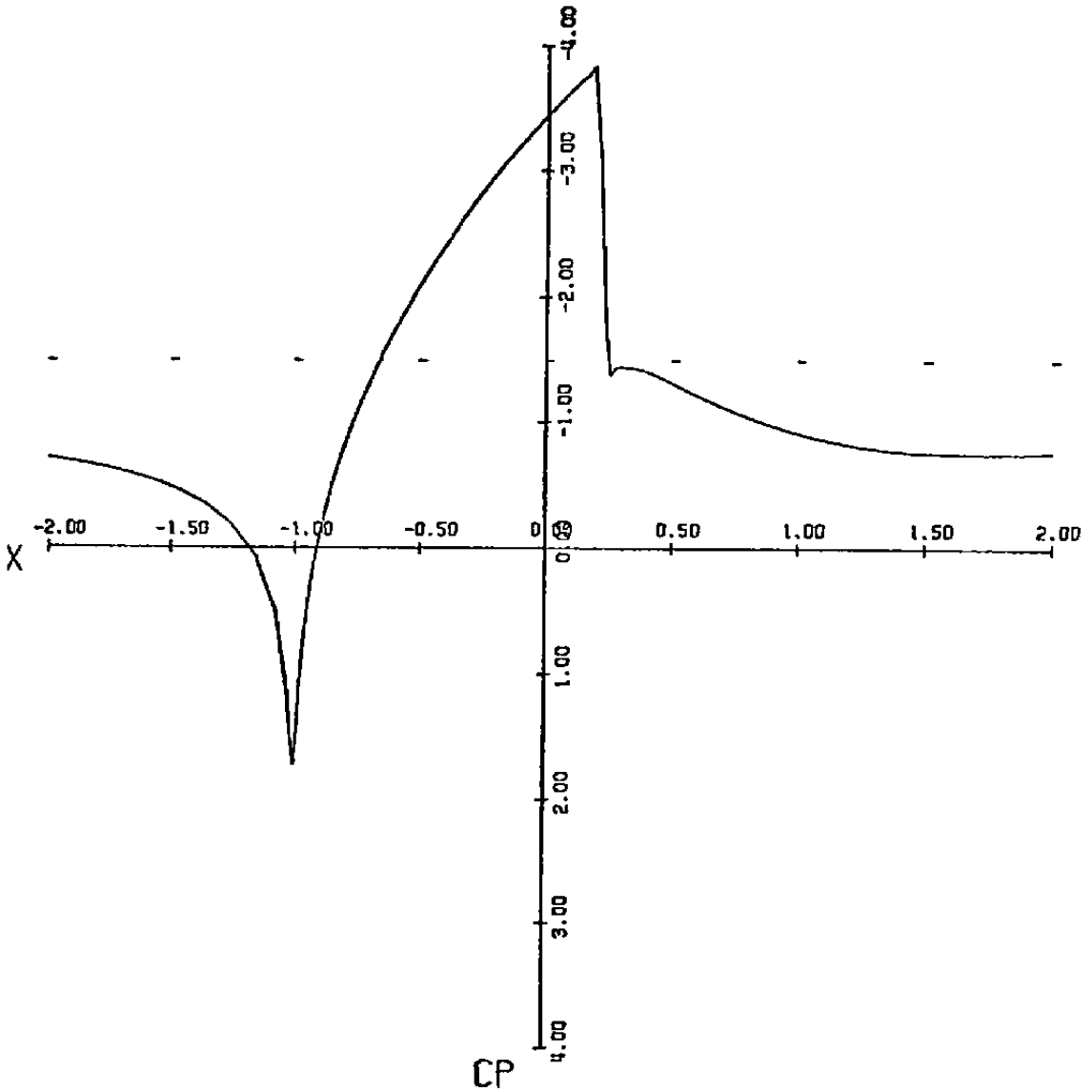

Figure 101. Intermediate C_p - distribution after 200 iterations with a separation wake.

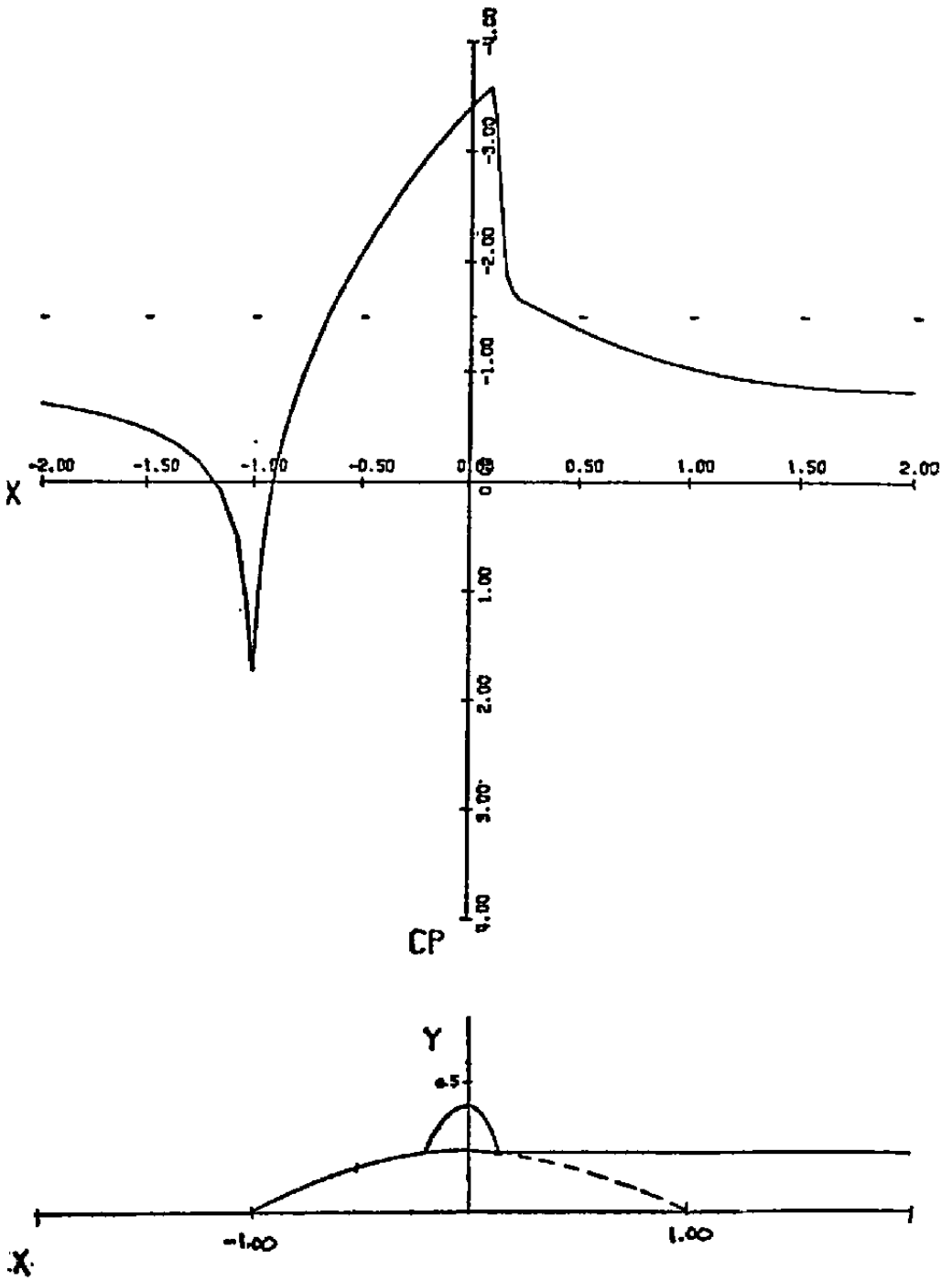

Figure 102. C_p - distribution as a parabolic airfoil with separation wake behind the shock and the sonic pocket - K_v = 0.01, K_i = 1.0 (14% airfoil at M = 0.9).

the method and more refinements of the method itself are possible and will be pursued.

6.0 CONCLUSION

The second phase of a program to study the wake/separation interaction flow field by employing several shallow-cavity models has been accomplished. The entire program is intended to shed some light on the upstream disturbance effect on transonic flow suffering a significant adverse pressure gradient downstream. Both experimental and theoretical work has been incorporated in the study. It is hoped that through this program, the scaling effect as well as the mechanism by which the flow is rehabilitated and re-energized can be better understood.

The present experiments were carried out with a natural boundary layer developed from the model leading edge. The extraordinarily long model results in a range of high Reynolds number which can cover that of actual flight conditions. The upstream disturbance was simulated by a rearward-facing step. The strength of the upstream disturbance was controlled by varying the free-stream Mach number and Reynolds number, as well as the location of the steps.

It was found that the upstream disturbance can either suppress or enhance the downstream separation depending on the magnitude of the disturbance, the distance between them and the Reynolds number and the Mach number of the oncoming flow. The variations in the base pressure, the reattachment pressure, the plateau pressure, the re-separation pressure, as well as the peak (i.e., maximum) pressure within the shallow-cavity flow by varying various parameters have been obtained. Among these parameters, it was found that the flow responded more acutely to the depth/length ratio and the Reynolds number.

Based on the present experiments, it was found that the Reynolds number influences the flow pattern strongly initially, however, it then leveled off at a certain Reynolds number. For an optimized cavity length for the pressure variation case, this Reynolds number is in the neighborhood of 30×10^8.

It was found that the rate of pressure recovery is different from the rate of velocity profile recovery. The pressure recovers faster (that is with less relaxation distance) than does the velocity profile. The reason for these differences is that the surface pressure is mainly determined by the immediate external flow field while the change in the velocity profile depends on the mass entrainment from the external flow. The mass entrainment through mixing during the rehabilitation process requires a longer relaxation distance. At an optimized cavity length for the pressure recovery, it was found that the final peak pressure as well as the reseparation pressure were higher than those for the no upstream disturbance flow case. At an optimized cavity length for the velocity profile recovery, it was found that the skin friction can be higher than that for the case with no upstream disturbance.

By observing the measured velocity profile development during the rehabilitation phase, it was found that the recovery (the pressure as well as the velocity) starts from the wall and spreads outward. The inner portion of the outer boundary layer (i.e., the wake-component) has a longer memory of the upstream disturbance than does the outer layer (i.e., the wall-component). These points are even more clearly demonstrated by analyzing the velocity defect and the law of wall and wake.

It was found that the value used for the law of the wall in the flow over a flat plate does not agree with the condition where a large pressure gradient is presented. Therefore, the slope on Coles' plot deviates from the universally accepted value near the reattachment and the reseparation points.

A method of computing the shape of the inviscid streamlines has been developed for subsonic flows past cavities using the experimentally measured data. Using such inviscid streamlines, inviscid transonic flow computation for flows past cavities at transonic speeds yields pressure distribution on the cavities which agrees with the experimentally measured pressure distributions at transonic speeds. This indicates that the extent of the viscous region does not change much as the Mach number is increased from subsonic to transonic level.

A new finite difference technique for solving the viscous-transonic equations has also been developed which includes the effects of compressive viscosity in the regions of shocks. The method has been applied for solving flows past symmetric airfoils and it has been established that the results agree with those obtained by other methods and the present technique has certain computational advantages. Using this method, pressure distributions on circular airfoils with a pre-assigned separation wake either just behind the point where the shock touches the airfoil or at a point further downstream have been computed.

This work has gone some way towards developing an understanding of transonic strong interaction flows but significant additional work is still required for a complete knowledge of the problem.

REFERENCES

1. Wu, J. M., et al "Fundamental Studies of Subsonic and Transonic Flow Separation, Part I - First Phase Summary Report" AEDC-TR-75-95, Arnold Engineering Development Center, Tullahoma, Tennessee, September, 1975.

2. Pearcy, H. H., Osborne, J., and Haines, A. B., "The Interaction between Local Effects at the Shock and Rear Separation--a Source of Significant Scale Effects in Wind Tunnel Tests on Aerofoils and Wings." AGARD CP 35 on Transonic Aerodynamics. Paper presented at the Fluid Dynamics Panel Specialists' Meeting, Paris, France, September, 1968.

3. Yoshihara, H., and Zonnars, D., "The Many Facets of 3D Transonic Shock-Induced Separation." Paper 42, AGARD Conference on Flow Separation, Gottingen, Germany, May, 1975.

4. Whitcomb, R. I., "Review of NASA Supercritical Airfoils." The Ninth Congress of the International Council of the Aeronautical Sciences." Paper No. 74-10, Haifa, Israel, Aug. 25, 1974 and Transonic Flow Short Course Notes, The Univ. of Tenn. Space Institute, Tullahoma, Tenn., October, 1975.

5. Shen, L., "On Transonic Wind Tunnel Design Consideration." M. S. Thesis, The University of Tennessee Space Institute, Tullahoma, Tennessee, 1974.

6. Chen, C. H., "Study of Subsonic and Transonic Flow Separation - With and Without Upstream Disturbance." Ph.D Dissertation, The University of Tennessee Space Institute, Tullahoma, Tenn, March, 1975.

7. Gray, J. D., "A Compendium of Flow Measurement Methods and Techniques." Short Course on Flow Separation at the University of Tennessee Space Institute, Tullahoma, Tenn., November 26-30, 1973.

8. Dudziniski, T. J., and Krause, L. N., "Effects of Inlet Geometry on Flow-Angle Characteristics of Miniature Total-Pressure Tubes." National Aeronautics and Space Administration TND-6406, Washington, D.C., July, 1971.

9. Brederode, V. de, and Bradshaw, P., "Three-Dimensional Flow in Nominally Two-Dimensional Separation Bubbles, I. Flow Behind a Rearward-Facing Step," Imperial College Report, 72-19, London, England, August, 1972.

10. Roshko, A., "Some Measurements of Flow in a Rectangular Cutout." National Advisory Committee for Aeronautics TN-3488, Washington, D.C., August, 1955.

11. Bogdonoff, S. M., and Kepler, C.E., "Separation of a Supersonic Turbulent Boundary Layer," Journal of Aeronautical Sciences, 22:414-430, June, 1955.

12. Zukoski, E. E., "Turbulent Boundary-Layer Separation in Front of a Forward-Facing Step." AIAA Journal 5:1746-1753, October, 1967.

13. Love, E. S., "On the Effect of Reynolds Number upon the Peak Pressure-Rise Coefficient Associated with the Separation of a Turbulent Boundary Layer in Supersonic Flow." Journal of the Aeronautical Sciences, 22:345, May, 1955.

14. Robertson, J. M., and Taulbee, D. B., "Turbulent Boundary Layer and Separation Flow Ahead of a Step." Developments in Mechanics, H. J. Weiss, D. F. Young, W. F. Riley, and T. R. Rogge, editors. Vol. 5. Ames, Iowa: Iowa State University Press, 1969, pp 171-183.

15. Taulbee, D. B., and Robertson, J. M., "Turbulent Separation Analysis Ahead of a Step." American Society of Mechanical Engineers Paper No. 71-WA/FE-32, presented at ASME Winter Annual Meeting, Washington, D.C., November, 1971.

16. Bradshaw, P., and Galea, P. V., "Step-Induces Separation of a Turbulent Boundary Layer in Incompressible Flow." Journal of Fluid Mechanics, 27:111-130, January, 1967.

17. Charwat, A. F., Roos, J. N., Dewey, F. C. and Hits, J. A., "An Investigation of Separated Flows--Part I: The Pressure Field." Journal of the Aerospace Sciences, 28:457-470, June, 1961.

18. Van Driest, E. R., "Turbulent Boundary Layer in Compressible Fluids," Journal of the Aeronautical Sciences, 18:145-160, March, 1951.

19. Coles, D. E., "The Law of theWake in the Turbulent Boundary Layer." Journal of Fluid Mechanics, 1:191-226, July, 1956.

20. Wieghardt, K., and Tillmann, W., "On the Turbulent Friction Layer for Rising Pressure." National Advisory Committee for Aeronautics TM-1314, Washington, D.C., October, 1951.

21. Ram, V. Vasanta, and Wauschkuhn, P., "Die Turbulente Grenzschicht hinter einem Ablösungsgebiet." Ruhr-Universität Bochum, Lehrstuhl für Strömungslehre, Bericht Nr. 32, 1974.

22. Schofield, W. H., "The Effect of Sudden Discontinuities on Turbulent Boundary Layer Development." Aeronautical Research Laboratories Mechanical Engineering Report No. 139, Australian Defense Scientific Service, Melbourne, Australia, March, 1973.

23. Coles, D. E., and Hirst, E. A. (eds.). Proceedings Computation of Turbulent Boundary Layers--1968 AFOSR-IFP-Stanford Conference. Vol. 2. California: The Department of Mechanical Engineering, Stanford University, August, 1968.

24. Bradshaw, P., and Wong, F. V. F. "The Reattachment and Relaxation of a Turbulent Shear Layer," Journal of Fluid Mechanics, 52:113-135, March, 1972.

25. Schlichting, H., Boundary-Layer Theory. Sixth edition. New York: McGraw-Hill Book Company, Inc., 1966.

26. Schultz-Grunow, F., "New Frictional Law for Smooth Plates." National Advisory Committee for Aeronautics TM-986, Washington, D.C., September, 1941.

27. Clauser, F. H., "Turbulent Boundary Layers in Adverse Pressure Gradients," Journal of the Aeronautical Sciences, 21:91-108, February, 1954.

28. Gradshteyn, I. S., and Ryzhik, I. M., Table of Integrals, Series, and Products. English translation edited by Alan Jeffrey. New York: Academic Press, Inc., 1965.

29. Selby, S. M. (ed). Standard Mathematical Tables. Fourteenth edition. Cleveland, Ohio: The Chemical Rubber Co., 1965.

30. Reda, D. C., "Compressible Turbulent Skin Friction on Rough and Rough/Wavy Walls in Adiabatic Flow," Naval Ordnance Laboratory TR-74-34, White Oak, Silver Spring, Maryland, February, 1974.

31. Murman, E. M., "Analysis of Embedded Shock Waves Calculated by Relaxation Methods," AIAA J., Vol. 13, p. 626, 1974.

32. H. B. Keller, "A New Difference Scheme for Parabolic Problems," Numerical Solution of Partial Differential Equations - II, (ed. B. Hubbard), Academic Press, New York, p. 327-350, 1970.

33. Czarnecki, K. R., and M. W. Jacson. "Turbulent Boundary Layer Separation Due to a Forward-Facing Step." American Institute of Aeronautics and Astronautics Paper No. 74-581, presented at AIAA 7th Fluid and Plasma Dynamics Conference Palo A to, California, June, 1974.

34. Wilson, R. E. and F. Maurer. "Turbulent Boundary-Layer Separation at Low Supersonic Mach Numbers," AIAA Journal, 9:189-190, January; 1971.

35. Knechtel, E. D., "Experimental Investigation at Transonic Speeds of Pressure Distributions over Wedge and Circular Arc Airfoil Sections and Evaluation of Perforated-Wall Interference", TN D-15, 1959, NASA.

36. Murman, E. M., and Cole, J. D., "Calculation of Plane Steady Transonic Flows", AIAA Journal, Vol. 9, No. 1. p. 114-121, 1971.

APPENDIX

NUMERICAL SOLUTION OF VISCOUS-TRANSONIC EQUATION

The small disturbance equations for the disturbance velocity potential for inviscid transonic flow past an airfoil with effects of compressive viscosity included are

$$K_v \phi_{xxx} + (K_i - \phi_x)\phi_{xx} + \phi_{yy} = 0 \tag{1}$$

where K_i is the inviscid transonic similarity parameter and K_v the viscous transonic similarity parameter defined by

$$K_i = \frac{1 - M_\infty^2}{\delta^{2/3} M_\infty^{4/3} (\gamma+1)^{2/3}} \tag{2}$$

$$K_v = \frac{1 + (\gamma-1)/Pr}{Re\ \delta^{2/3} M_\infty^{4/3} (\gamma+1)^{2/3}} \tag{3}$$

δ is the thickness to chord ratio of the airfoil and Re and Pr are the Reynolds number and Prandtl number respectively, based on longitudinal viscosity and half-chord length. x,y and ϕ are suitably non-dimensionalized variables.

Boundary conditions are

$$\frac{\partial \phi}{\partial y}(x,o) = \frac{df}{dx} \quad , \quad |x| \leq 1 \tag{4}$$

$$= 0 \quad , \quad |x| > 1$$

$$\begin{aligned} &\text{As } x \to -\infty \ , \quad \phi \to 0 \text{ and } \phi_{xx} \to 0 \\ &\text{As } x \to +\infty \ , \quad \phi_{xx} \to 0 \\ &\text{As } y \to \infty \ , \quad \phi \to 0 \end{aligned} \tag{5}$$

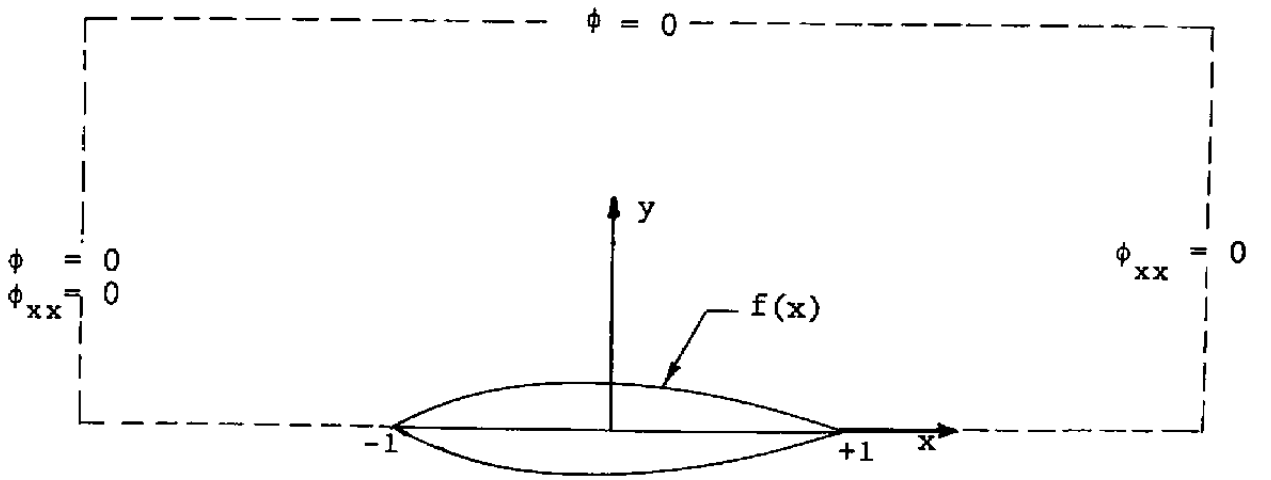

Introducing $U = \phi_x$ and $W = \phi_{xx}$, Equation (1) is written as a system of three equations which have only first order derivatives in x.

$$\begin{aligned} \phi_x &= U \\ U_x &= W \\ (K_v W + K_i U - \tfrac{1}{2}U^2)_x &= -\phi_{yy} \end{aligned} \tag{6}$$

The third equation is written in the divergence form so that the corresponding difference equations would preserve the conservation laws.

Difference Notation:

$$\begin{aligned} x_i &= x_{i-1} + h_i \quad , \quad i = 2,3, \ldots I \\ x_1 &\simeq -\infty \quad , \quad x_I \simeq +\infty \end{aligned} \tag{7}$$

$$y_j = y_{j-1} + g_j \quad , \quad j = 2,3, \ldots,J$$

$$y_{\frac{1}{2}} = 0, \; y_1 = g_1/2, \; y_J \simeq +\infty$$

$$U_{i,j} = U(x_i, y_j)$$

$$U_{i-\frac{1}{2},j} = (U_{i,j} + U_{i-1,j})/2$$

$$D_x U_{i-\frac{1}{2},j} = (U_{i,j} - U_{i-1,j})/h_i \qquad (8)$$

$$D_y U_{i,j-\frac{1}{2}} = (U_{i,j} - U_{i,j-1})/g_j$$

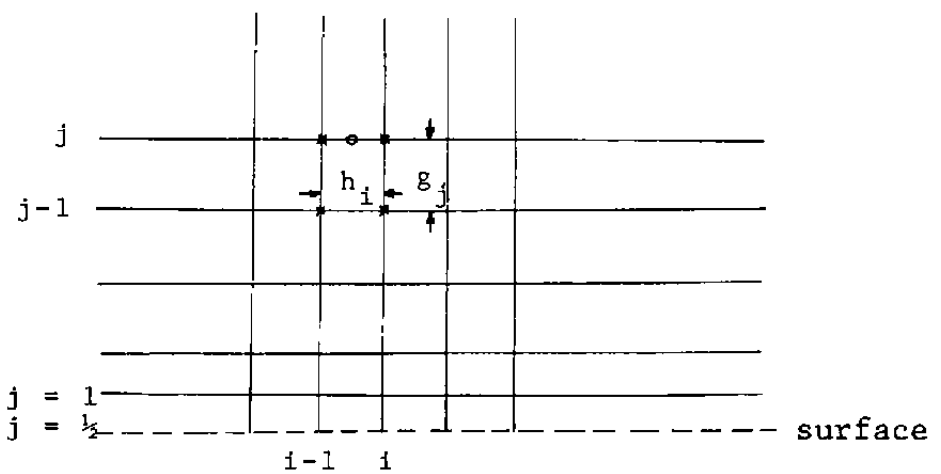

The difference equations corresponding to the equations (6) are written at the point (i-½,j). The difference scheme is second order accurate and the grid spacing is non-uniform in both x and y directions. The difference scheme is given by

$$
\begin{aligned}
D_x\ \phi_{i-\frac{1}{2},j} &= U_{i-\frac{1}{2},j} \\
D_x\ U_{i-\frac{1}{2},j} &= W_{i-\frac{1}{2},j} \\
D_x\ (K_v W + K_i U - \tfrac{1}{2} U^2)_{i-\frac{1}{2},j} &= -\ D_y\ V_{i-\frac{1}{2},j}
\end{aligned}
\qquad (9)
$$

$$i = 2,3, \ldots I$$

$$j = 1,2, \ldots J$$

where

$$D_y V_{i-\frac{1}{2},j} = \frac{2}{(g_j + g_{j+1})} \left(V_{i-\frac{1}{2},j+\frac{1}{2}} - V_{i-\frac{1}{2},j-\frac{1}{2}}\right)$$

$$V_{i-\frac{1}{2},j+\frac{1}{2}} = D_y\ \phi_{i-\frac{1}{2},j+\frac{1}{2}} \quad , \text{ for } j \geq 1$$

and $V_{i-\frac{1}{2},\frac{1}{2}} = \frac{\partial \phi}{\partial y}\left(x_{i-\frac{1}{2}},\ 0\right)$ from equation (4).

This difference scheme which is similar to the "box scheme" developed by Keller (Ref. 32) for parabolic problems, would remain the same in both subsonic and supersonic regions of the flow field, unlike the mixed difference schemes used by most others for inviscid transonic flow computations. The equations (7) together with the boundary conditions are a set of non-linear algebraic equations for ϕ, U and W at all the mesh points (i,j); i = 1, ... I; j = 1,2, ... J. These equations are solved by a horizontal line relaxation method. Assuming some approximation for the solution in the entire region, equations on line j = 1 are solved for obtaining the next approximation for the variables on that line. However, even on this line, equations are non-linear and they themselves are solved by Newton's iteration. While carrying out those Newton iteration steps, structure of the equation matrix which is a tri-diagonal block matrix with additional zeros in some of the blocks, is taken advantage of. Then equations on line j = 2 are solved and so on. One sweep is

completed after the equations on all the horizontal lines are solved. This gives next approximation in the entire field and the next sweep is carried out. It takes several hundred sweeps for the relaxation scheme to converge if the starting approximation is very far from the actual solution. However, when one solution is obtained for certain values of the parameters of the problem, that solution is used as the starting approximation for obtaining solutions for slightly different values of the parameters. Convergence would be rapid in such cases.

In a typical run, about 125 points in the x-direction and about 30 points in the y-direction are used. The mesh spacing is non-uniform and mesh lines are introduced in the field when necessary in regions of strong shocks for better resolution during the computation, and also lines can be taken out of computation when it is desirable.

Nomenclature

a	Sound speed
B	Wall-law intercept
C_f	Skin friction coefficient
C_p	Pressure coefficient
$f(x)$	Cavity or airfoil shape function
G	Clauser's velocity defect parameter
h	Step height
K	Transonic similarity parameter
K_i	Inviscid transonic similarity parameter
K_v	Viscous transonic similarity parameter
ℓ	Cavity length
ℓ_r	Reattachment distance
ℓ_s	Separation distance
L_f	Distance to forward facing step
L_R	Distance to rearward facing step
M	Mach number
p	Pressure
Pr	Prandtl number
r	Recovery factor
$r(x)$	$\{(1-x)/(1+x)\}^{\frac{1}{2}}$
Re	Reynolds number
u	Axial velocity
u_τ	Friction velocity
u^*	van Driest's generalized velocity
x	Axial distance
x_r	Distance downstream from rearward facing step
x_f	Distance upstream from forward facing step
y	Transverse coordinate
$\hat{y}$	Stretched y coordinate, $\delta^{1/3}y$
α	Angle of attack
γ	Specific heat ratio
δ	Boundary layer thickness; cavity depth or airfoil thickness to chord ratio.

δ^*	Boundary layer displacement thickness
δ^*_c	Cole's displacement thickness
η	Integration variable
Δ	Clauser's thickness parameter
θ	Boundary layer momentum thickness
θ_c	Cole's momentum thickness
κ	von Karman constant
μ	Coefficient of viscosity
ν	Coefficient of kinematic viscosity
ξ	Integration variable
$\overline{\pi}$	Cole's profile parameter
ρ	Density
ϕ	Disturbance velocity potential
ω	Wake function

SUBSCRIPTS:

b	Base
e	Edge of boundary layer
i	Characteristic
L_f	Distance to forward facing step
L_R	Distance to rearward facing step
$\ell/2$	Center of cavity
m	Peak
p	Plateau
r	Reattachment
ref	Reference
s	Separation
t	Total
w	Wall
x	Axial distance
δ	Boundary layer thickness
∞	Free stream